

Abstract

Ab Initio Insights Into Substrate Effects, Structural Identification, and Excitonic States in 2D

Materials

Stephen Eltinge

2022

The 21st century has seen enormous growth in the study of two-dimensional (2D) materials, beginning with the isolation of graphene but rapidly expanding to include a wide variety of other compounds. Due to their size, 2D materials have immediate appeal for applications in nanoscale electronics. At the same time, uniquely low-dimensional phenomena such as the quantum spin Hall effect, quantum confinement, and 2D superconductivity are of interest to basic physics researchers. This dissertation presents *ab initio* investigations of three 2D materials. First, we discuss the binding of stanene on various substrates. Stanene, the buckled monolayer form of tin, is predicted to be a 2D topological insulator with symmetry-protected helical edge states. We investigate the effects of strain, chemical functionalization, and substrate–overlayer interactions on the topological band structure of stanene, showing that Al_2O_3 is an ideal substrate for synthesizing a potential quantum spin Hall insulator. Next, we examine the polymorphic structure of borophene sheets, the monolayer form of boron. We report on research that revealed the complex atomic structure of borophene on the $\text{Cu}(111)$ and $\text{Cu}(100)$ surfaces, including the crucial role played by simulated scanning tunneling microscopy (STM) data. We discuss the effect of modulation by the substrate on the occurrence of Dirac cones in the borophene band structure. Finally, we discuss the potential for Mg_2TiO_4 films to host long-lived, strongly bound interlayer excitons. At the DFT level, we obtain the band structure of Mg_2TiO_4 films grown on MgO and show how the polar films have a band offset favorable for interlayer exciton formation. Motivated by this work, we present *GW* and *GW*-BSE calculations of quasiparticle energies, exciton binding energies, and optical absorption spectra. These calculations more clearly characterize the suite of excitons that exist in Mg_2TiO_4 and shed light on the importance of film thickness in controlling their relative binding energies. The materials studied in this dissertation are diverse in chemical identity and properties, but are unified by their 2D structure and the crucial role played by their growth substrates, which are discussed throughout.

Ab Initio Insights Into Substrate Effects, Structural Identification, and
Excitonic States in 2D Materials

A Dissertation

Presented to the Faculty of the Graduate School

of

Yale University

in Candidacy for the Degree of

Doctor of Philosophy

by

Stephen Eltinge

Dissertation Director: Sohrab Ismail-Beigi

December 2021

Copyright © 2022 by Stephen Eltinge

All rights reserved.

Acknowledgments

The image of the lone-genius scientist was always something of a myth, but anyone who works in a physics lab today knows just how much one relies on the help, advice, and collaboration of one's colleagues. It's only right to begin by appreciating some of those people.

First, of course, thanks must go to my advisor, Sohrab Ismail-Beigi. When he teaches PHYS 650/APHY 856, Sohrab begins with a discussion of effective theories and the importance of choosing a relevant scale for one's physical models. True to that spirit, Sohrab has always been willing to offer advice appropriate to any scale I could need, from proposing broad areas of research to immediately recalling the fine details of a particular derivation or physical argument. I learned an enormous amount from Sohrab, and I hope to retain it long after I have left Yale.

My groupmates were also invaluable sources of wisdom, both physics-related and otherwise. Minjung Kim was a kind and helpful mentor when I first joined the group. Arvin Kakekhani taught me to always think about real-life applications of one's work—I know who to alert if I ever figure out how to split water with stanene. Subhasish Mandal was an ever-welcoming officemate through many long, hot summer days. Mehmet Doğan and Alexandru Georgescu reminded me to be passionate about both my work and my extracurricular pursuits. Xin Liang and Alex Lee were always willing to answer my technical questions about pseudopotentials, computer clusters, or anything else. Kayahan Saritaş asks me wise, probing questions about my work. Finally, Zheteng Jin is never without an interesting new paper, which proved especially helpful when I needed to do the band unfolding calculations in Chapter 6.

My work also relied on close collaboration and feedback with several different experimental projects. I thank Stephen Albright, Rongting Wu, Adrian Gozar, and Kida Shin for many long, productive discussions about their experiments, and for their patience as we wrestled with interpreting often-confusing data. Fred Walker, Charles Ahn, and Ivan Božović provided steady leadership and guidance, without which the confusing data would not have existed in the first place.

Finally, I must thank my friends and family, especially Olivia Murton. Neither of us could have handled attending universities in two different states, and the frequent travel that necessitated, without endless patience, love, and support. In the past year and a half, it would have been easy to feel lonely, doubtful, or lost, but I always knew that Olivia was there for me. I'm so grateful for everything she does and is.

For Walter.

Contents

1	Introduction	1
2	Methods	5
2.1	Density functional theory (DFT): Ground-state properties	5
2.1.1	Exchange–correlation functionals	11
2.1.2	Wannier functions	13
2.1.3	Scanning tunneling microscopy (STM)	18
2.1.4	Band unfolding	22
2.2	GW-BSE method: Electronic excitations and interactions	26
2.2.1	Screening in solids	26
2.2.2	The Green’s function	28
2.2.3	The <i>GW</i> approximation	31
2.2.4	Excitons and optical absorption with the Bethe–Salpeter equation .	38
2.2.5	<i>GW</i> calculations	42
2.2.6	Scaling <i>GW</i> calculations to large systems	45
3	Epitaxial binding and strain effects in monolayer stanene on the $\text{Al}_2\text{O}_3(0001)$ surface	55

3.1	Introduction	56
3.2	Methods	57
3.3	Results	59
3.3.1	Free-standing stanene monolayers	59
3.3.2	Bound low-buckled structure	59
3.3.3	Binding energy and van der Waals functionals	62
3.3.4	Commensurate versus incommensurate binding	64
3.3.5	Dumbbell stanene	65
3.3.6	Free-standing and bound stanene band structures	66
3.4	Discussion and outlook	71
3.5	Appendix: Additional calculations	72
4	Identifying chemical reactions at the interface of stanene on $\text{Bi}_2\text{Te}_3(0001)$	74
4.1	Introduction	75
4.2	Experimental methods	77
4.3	X-ray photoelectron spectroscopy	79
4.4	Synchrotron x-ray diffraction	82
4.5	Theoretical results and discussion	87
4.6	Conclusions	91
5	Structure and binding of large-area borophene sheets on $\text{Cu}(111)$ surfaces	92
5.1	Introduction	93
5.2	Methods	95
5.3	Experimental results	96
5.4	Theoretical structure search	102

5.5	Conclusion	108
6	Long-wavelength modulation of borophene sheets on Cu(100) surfaces	110
6.1	Introduction	111
6.2	Methods	114
6.3	Experimental results	115
6.4	Structural identification and theoretical analysis	120
6.5	Band unfolding	127
6.6	Conclusion	130
7	Structural analysis of 2D inverse spinel Mg_2TiO_4 on $\text{MgO}(001)$ for hosting excitons	132
7.1	Introduction	133
7.2	Design considerations for oxides with interlayer exciton states	135
7.3	Electronic structure of $\text{Mg}_2\text{TiO}_4/\text{MgO}$ from DFT calculations	137
7.4	Mg_2TiO_4 growth using reactive MBE	141
7.5	Structural characterization using CTR measurements	143
7.6	Polarity-driven displacements at the interface	145
7.7	Conclusion	147
8	Further study of excitons in Mg_2TiO_4 on MgO via the <i>GW</i>-BSE method	149
8.1	Introduction	149
8.2	Methods	150
8.3	Convergence and scaling tests	153
8.4	Polarity and structural properties	154

8.5	Quasiparticle calculations	158
8.6	Excitonic and absorption calculations	161
8.7	Discussion	166
8.8	Conclusion	169
9	Summary and outlook	171
9.1	Stanene	171
9.2	Borophene	172
9.3	Mg ₂ TiO ₄	173
	Bibliography	175

List of Figures

2.1	Demonstration of band folding for a simple two-dimensional crystal.	22
2.2	Flowchart of steps for performing a <i>GW</i> -BSE calculation.	43
2.3	Low- <i>q</i> behavior of the inverse dielectric matrix.	53
3.1	Top and side views of the bare $\text{Al}_2\text{O}_3(0001)$ slab and of the two most stable registry choices for stanene on Al_2O_3	60
3.2	LDOS and PDOS of stanene on $\text{Al}_2\text{O}_3(0001)$ slab.	63
3.3	Side view of stanene on alumina showing positive (yellow) and negative (cyan) isosurfaces for electron redistribution.	64
3.4	Evolution of band gap and band structures of bare stanene (green), fluorinated stanene SnF (magenta), and hydrogenated stanene SnH (black) as a function of lattice parameter.	67
3.5	Band structure plots showing the change of topological character via band inversions in bare stanene (top row), fluorinated stanene SnF (middle row), and hydrogenated stanene SnH (bottom row).	68
3.6	Band structure plot for epitaxial stanene on alumina.	70
3.7	Orbital-projected hybrid (HSE06) band structures of stanene and SnF.	73
3.8	Substrate thickness dependence of the stanene-on-alumina band structure.	73

4.1	Crystal structure of stanene and Bi_2Te_3	76
4.2	XPS data showing the growth of Sn on Bi_2Te_3	79
4.3	Integrated intensity of Sn^0 and $\text{Sn}^{2+} 3d_{5/2}$, and Bi^{3+} and $\text{Bi}^0 4f_{7/2}$ transitions as a function of stanene deposited.	80
4.4	Ratios of integrated intensities of Bi^{3+} to Sn^0 and Sn^{2+} , and Sn^{2+} to Sn^0 and Bi^0 at take-off angles of 90° and 45°	81
4.5	Anomalous x-ray scattering data at the Sn K-edge.	83
4.6	Experimental and simulated Sn scattering strength from anomalous x-ray scattering.	85
4.7	Ternary phase diagram for thin-film structures of Sn, Bi, and Te.	88
5.1	Structure of borophene grown on Ag(111) surfaces.	97
5.2	Growth dynamics of borophene on Cu(111) surface.	99
5.3	Domain structure of borophene on Cu(111) revealed by selected area diffrac- tion.	101
5.4	Structure of borophene on Cu(111) as revealed by STM data and DFT simulations.	103
5.5	Atomic positions for a relaxed borophene structure with hexagonal vacancy concentration $\eta = 2/15$	104
5.6	Atomic positions for proposed and alternative borophene structures on Cu(111).	106
5.7	Charge-transfer interaction between borophene and Cu(111) surface.	107
6.1	Growth dynamics of borophene on the Cu(100) surface.	116
6.2	Single-crystal domains of borophene revealed by dark-field LEEM images.	118

6.3	Topography of borophene islands revealed by STM.	121
6.4	Atomic structure of β_{13} borophene as revealed by STM measurements and <i>ab initio</i> DFT calculations.	122
6.5	Electronic bands of β_{13} borophene on the Cu(100) surface.	124
6.6	Dirac cones of β_{13} borophene on the Cu(100) surface.	126
6.7	Wannier functions and the supercell–primitive cell relationship in the borophene sheet.	128
6.8	Electronic band structure of the modulated β_{13} borophene sheet accounting for the stripe modulation.	131
7.1	Structures of Mg_2TiO_4 in bulk phase and on $\text{MgO}(001)$	136
7.2	Band offset in Mg_2TiO_4 on $\text{MgO}(001)$	138
7.3	PDOS and band-edge electron localization in Mg_2TiO_4 on $\text{MgO}(001)$	139
7.4	Reflection high-energy electron diffraction images of Mg_2TiO_4 growth. . .	142
7.5	Structure fitting to CTR data.	144
7.6	Tetrahedral Mg atom displacement in Mg_2TiO_4 on $\text{MgO}(001)$	146
8.1	Convergence of the <i>GW</i> quasiparticle band gap as a function of cutoff energy for bulk MgO , bulk rutile TiO_2 , and an $\text{MgO}(001)$ slab.	152
8.2	Projected density of states (PDOS) for one layer of Mg_2TiO_4 on $\text{MgO}(001)$. .	154
8.3	PDOS for two layers of Mg_2TiO_4 on $\text{MgO}(001)$	155
8.4	PDOS for three layers of Mg_2TiO_4 on $\text{MgO}(001)$	155
8.5	PDOS for four layers of Mg_2TiO_4 on $\text{MgO}(001)$	156
8.6	PDOS for six layers of Mg_2TiO_4 on $\text{MgO}(001)$	156
8.7	Quasiparticle energies for Mg_2TiO_4 -based materials.	159

8.8	Absorption spectra for Mg_2TiO_4 -based materials calculated with both the RPA and the BSE.	162
8.9	Intralayer (surface) and interlayer excitons for Mg_2TiO_4 on MgO	163
8.10	Schematic picture of how band edges and exciton binding energies are expected to evolve as Mg_2TiO_4 film thickness increases	167

List of Tables

2.1	Optimal memory distribution for the BerkeleyGW <code>epsilon</code> code in both the low-parallelization ($N_p < N_c/N_v$) and high-parallelization ($N_p \gg N_c/N_v$) limits.	47
3.1	Structural data for free-standing stanene in its bare, hydrogenated, and fluorinated forms.	59
3.2	Structural and energetic information for the two most favorable registries of stanene on Al_2O_3	61
4.1	Bulk heats of reaction for Sn deposited on various substrates.	90
8.1	Number of bands required for GW calculations in materials treated in this chapter.	152
8.2	Potential difference and DFT band gaps for $\text{MgO} + \text{Mg}_2\text{TiO}_4$ slabs of varying thickness.	157
8.3	Comparison of DFT and GW band gaps for Mg_2TiO_4 materials.	160
8.4	Convergence of exciton binding energies (in eV) with coarse and fine grids for Mg_2TiO_4 materials.	164

Chapter 1

Introduction

In 2004, Andre Geim and Konstantin Novoselov showed that graphene, the two-dimensional (2D) hexagonal form of carbon, could be prepared by using tape to repeatedly peel layers off of a sample of graphite [1]. Though graphite had long been known to have a layered structure, the isolated graphene monolayer had previously been presumed to be unstable. Geim and Novoselov demonstrated that this was not the case, sparking a flurry of interest in graphene that soon spread to the study of other 2D materials. Today, well-characterized 2D materials include not only graphene (a semimetal) but also hexagonal boron nitride (a wide-gap insulator), MoS_2 (a semiconductor), and other transition metal dichalcogenides (TMDs). 2D materials can be studied on their own, or they can be stacked into loosely-bound “van der Waals heterostructures”; the latter have been proposed as a way of realizing exotic types of field-effect transistors, optoelectronic devices, and other futuristic consumer electronics [2].

Equally important to modern physics is the tremendous growth in the development of first-principles (*ab initio*) computational tools, whose use is now ubiquitous. The most widespread of these tools is density functional theory (DFT). The foundations of DFT

were laid in the 1960s [3, 4], but its surge in popularity came with the broad availability of powerful computers. In 2014, more than 16,000 papers were published about DFT, a number that has only continued to grow [5]. *Ab initio* calculations are used by researchers ranging from chemical spectroscopists to theoretical physicists engaged in materials discovery. Of particular relevance to this dissertation is their use by experimental physicists and their collaborators; in this context, *ab initio* calculations can help guide, interpret, and confirm efforts at materials synthesis and characterization.

In this dissertation, we present and analyze *ab initio* calculations of three materials: stanene, borophene, and a thin film of Mg_2TiO_4 . These materials exemplify both of the trends mentioned above: in addition to being two-dimensional, each one is believed to exhibit exciting new physics that was initially predicted from first principles [6, 7, 8]. Furthermore, the properties of each of these materials are shaped by the substrate on which it is grown. Substrates are crucial to accurately describing 2D materials: they can strain a material by enforcing an epitaxial lattice match, saturate its orbitals by forming chemical bonds, dope it by donating electrons, or modify its electronic properties by screening electric fields. As a third throughline in our research, we aim to clearly identify and explicate these substrate effects wherever they impact properties of interest.

Throughout this work, we have attempted to be methodologically flexible, learning and using whatever theoretical methods are appropriate for the task at hand. Our various projects have used overlapping but distinct sets of tools from *ab initio* theory, including Wannier functions, hybrid functionals, and the *GW* method for self-energy calculations. The collected suite of methods we use is outlined in some detail in Chapter 2, with cross-references to the relevant research chapters where each method makes an appearance.

In Chapters 3 and 4, we discuss work on stanene, a buckled hexagonal monolayer of

elemental tin. Stanene is predicted to be a gapped 2D topological insulator (also known as a quantum spin Hall insulator), hosting topologically protected edge states even at room temperature [6]. However, its properties are highly sensitive to the choice of substrate. In Chapter 3, we present theoretical calculations of the binding of stanene to the (0001) crystal surface of alumina (Al_2O_3), a wide-gap insulator with a good lattice match. We carefully investigate the effects of strain and dispersion forces, including the delicate interplay between strain and functionalization of the stanene monolayer. We argue that Al_2O_3 presents a promising substrate for synthesizing gapped, topologically nontrivial stanene, and briefly discuss implications for device applications. In Chapter 4, we report on a collaboration with experimentalists who grew tin films on Bi_2Te_3 . Bi_2Te_3 is itself a 3D topological insulator. Our primary contribution to this work was a theoretical investigation of the chemical Sn–Bi–Te phase diagram, showing that Sn films on Bi_2Te_3 can be expected to spontaneously decompose into films of SnTe and elemental Bi.

In Chapters 5 and 6, we move left along the periodic table to borophene, the monolayer form of boron. To a physicist borophene is, depending on one’s perspective, either a dream or a nightmare. Boron sheets are expected to host a veritable zoo of exotic physical behavior, including high- T_c superconductivity [7], massless Dirac fermions [9], and Dirac nodal lines [10]. However, boron’s electron deficiency makes borophene highly polymorphic [11, 12, 13], with a large variety of nearly degenerate possible structures. It is therefore not surprising that the borophene ground state is sensitive to the choice of substrate; this sensitivity is a major challenge for borophene synthesis and characterization [14, 15]. These chapters reflect an extended collaboration with experimentalists who grew borophene on the (111) and (100) surfaces of copper (Chapters 5 and 6, respectively). In each chapter, we discuss a cross-correlation of experimental diffraction and STM data with theoretical

structural relaxations and STM simulations to resolve the borophene structure on an atomic scale. We quantify the effect of the substrate on the borophene sheet, both by doping the Fermi level and by inducing periodic modulations of the atomic structure and band energies.

In Chapters 7 and 8, we discuss a third collaboration with experimentalists, this one concerning excitons in transition metal oxide films. An exciton is a bound state formed from an optically excited electron and the hole it leaves behind in the valence band; stable, long-lived excitons have potential applications in quantum computing. From a structural perspective, this project represents a graduation from 2D materials (*i.e.*, atomic monolayers) to “quasi-2D” materials with meaningful physical extent in the z -direction. Methodologically, Chapter 8 also requires a step up in complexity, supplementing the ground state methods of DFT with many-body techniques that can handle various kinds of excited quasiparticles. In Chapter 7, we show how a polar Mg_2TiO_4 film, grown on $\text{MgO}(001)$ via widely-used fabrication techniques, has an ideal band alignment for the production of long-lived interlayer excitons. In Chapter 8, we extend this research with an analysis of how this material’s properties vary with thickness and a quantitative treatment of its electronic excitations and optical absorption spectrum. This project is ongoing, and we conclude by discussing both its current status and our future research plans.

In Chapter 9, we briefly recap the dissertation and present a research outlook for each topic covered.

Chapter 2

Methods

This chapter introduces the computational methods used throughout the rest of the dissertation. Its contents are intended to be instructive for non-experts, especially the detailed discussion of scaling the *GW* method to large systems in Section 2.2.6. Most of the tools we discuss are fairly well-established, but we highlight modifications we have made to existing techniques and software where appropriate.

2.1 Density functional theory (DFT): Ground-state properties

The main workhorse of electronic structure calculations is density functional theory (DFT), a simple and widely-used tool for computing ground-state properties of materials. DFT is motivated by the task of solving the Schrödinger equation of an N -electron system in the Born–Oppenheimer approximation, which takes the form

$$H\Psi(\{\mathbf{r}_i\}) = [T + V_{ee} + V_{ei}] \Psi(\{\mathbf{r}_i\}) = E_0\Psi(\{\mathbf{r}_i\}). \quad (2.1)$$

Here, T is the kinetic energy operator, V_{ee} is the Coulombic electron–electron potential, V_{ei} is the Coulombic potential due to the material’s positively charged ionic cores, and E_0 is the ground-state energy. In atomic units ($\hbar = 1$, $|e| = 1$, $m_e = 1$), the operators take the form

$$T = -\frac{1}{2} \sum_{j=1}^N \nabla_j^2, \quad V_{ee} = \frac{1}{2} \sum_{j \neq k}^N \frac{1}{|\mathbf{r}_j - \mathbf{r}_k|}, \quad V_{ei} = \sum_{j=1}^N v(\mathbf{r}_j), \quad (2.2)$$

where $v(\mathbf{r})$ is the ionic potential energy felt by a single electron:

$$v(\mathbf{r}) = - \sum_J \frac{Z_J}{|\mathbf{r} - \mathbf{R}_J|} \quad (2.3)$$

for ions with charges Z_J at positions \mathbf{R}_J . The many-body wavefunction $\Psi(\{\mathbf{r}_i\})$ is an anti-symmetric function of N continuous position variables. The dimension of the Hilbert space in which it lives grows exponentially with the number of electrons, so explicitly solving Equation 2.1 rapidly becomes intractable for even modestly-sized systems.

Fortunately, many properties of a system’s ground state can be extracted from an alternative formulation of the same problem that demands much less information to solve. Following Hohenberg and Kohn [3], we write the ground-state energy as the expectation value of the Hamiltonian in the ground state:

$$E_0 = \langle \Psi | T + V_{ee} + V_{ei} | \Psi \rangle = \langle \Psi | T + V_{ee} | \Psi \rangle + \int d\mathbf{r} n(\mathbf{r}) v(\mathbf{r}), \quad (2.4)$$

where $n(\mathbf{r})$ is the ground-state electron density, given by

$$n(\mathbf{r}) = N \int d\mathbf{r}_2 \cdots d\mathbf{r}_N |\Psi(\mathbf{r}, \mathbf{r}_2, \dots, \mathbf{r}_N)|^2. \quad (2.5)$$

Equation 2.4 is a useful decomposition of the problem because the first term on the right-hand side depends only on the electronic wavefunction (not the ionic potential or any external perturbations), while the second term is expressed in terms of the total electron density, a much less complex beast than the many-body wavefunction. In fact, the calculation of any ground-state property of an N -electron system, including its total energy, can be formulated as a variational problem in the electron density. This insight is the basis for DFT.

The transition to DFT is usually framed in terms of the two *Hohenberg–Kohn theorems*. The first theorem states that, given a fixed number of electrons N , and assuming that the ground state is non-degenerate [16],

[H–K 1] There is a one-to-one correspondence between the ground-state electron density $n(\mathbf{r})$ and the external potential $v(\mathbf{r})$.

One direction of the proof is trivial: given a potential $v(\mathbf{r})$, we can construct the Hamiltonian in Equation 2.1, solve for $\Psi(\{\mathbf{r}_i\})$, and calculate the electron density from Equation 2.5. The other direction is a straightforward proof by contradiction presented in [3]: one imagines two potentials that yield the same density and shows via the variational principle that they must be identical everywhere. The first Hohenberg–Kohn theorem dramatically simplifies the problem of solving Equation 2.1. It allows us to define a functional $|\Psi_0[n]\rangle$ that gives the ground-state *wavefunction* of a system with ground-state electron density $n(\mathbf{r})$ —effectively inverting Equation 2.5. We can go further and speak of an energy functional

$$\mathcal{E}[n; v] \equiv \underbrace{\langle \Psi_0[n] | T + V_{ee} | \Psi_0[n] \rangle}_{F[n]} + \int d\mathbf{r} n(\mathbf{r}) v(\mathbf{r}), \quad (2.6)$$

where $F[n]$ is a universal functional that is the same for all N -electron systems. Note that

$n(\mathbf{r})$ and $v(\mathbf{r})$ do not necessarily correspond to one another, but if they *do*, then we see by comparison to Equation 2.4 that $\mathcal{E}[n; v]$ gives the ground-state energy of the system. The second Hohenberg–Kohn theorem strengthens that relation:

[H–K 2] For a given potential $v(\mathbf{r})$, the functional $\mathcal{E}[n; v]$ is minimized at the corresponding ground-state electron density, and its value is the ground-state energy.

This proof, too, follows immediately from the variational principle [3].

The next step was made by Kohn and Sham [4], who further simplified the problem by mapping a system of interacting electrons onto an equivalent system of non-interacting electrons with the same density. The first Hohenberg–Kohn theorem applies equally well to non-interacting particles (*i.e.*, those with $V_{ee} = 0$), so we can define a functional

$$T_{\text{KS}}[n] = \langle \Psi_{\text{KS}}[n] | T | \Psi_{\text{KS}}[n] \rangle = -\frac{1}{2} \sum_j \langle \psi_j | \nabla_j^2 | \psi_j \rangle, \quad (2.7)$$

where $|\Psi_{\text{KS}}[n]\rangle$ is a Slater determinant of non-interacting electrons that has electron density $n(\mathbf{r})$, and $|\psi_j\rangle$ are orthonormal single-particle *Kohn–Sham orbitals* that make up $|\Psi_{\text{KS}}[n]\rangle$.

In terms of the Kohn–Sham orbitals, the electron density is

$$n(\mathbf{r}) = \sum_j |\psi_j(\mathbf{r})|^2. \quad (2.8)$$

We write the universal functional $F[n]$ of the *interacting* system in terms of the *non-interacting* kinetic energy term:

$$F[n] = T_{\text{KS}}[n] + V_{\text{H}} + E_{\text{xc}}[n], \quad (2.9)$$

where V_H is the Hartree energy,

$$V_H[n] = \frac{1}{2} \int d\mathbf{r} d\mathbf{r}' \frac{n(\mathbf{r}) n(\mathbf{r}')}{|\mathbf{r} - \mathbf{r}'|} = \frac{1}{2} \sum_{jk} \int d\mathbf{r} d\mathbf{r}' \frac{|\psi_j(\mathbf{r})|^2 |\psi_k(\mathbf{r}')|^2}{|\mathbf{r} - \mathbf{r}'|}, \quad (2.10)$$

and $E_{xc}[n]$ is the *exchange–correlation functional*. By definition, the exchange–correlation functional captures all terms not included in T_{KS} or V_H , including a correction to the kinetic energy for interacting electrons, the Fock exchange term for identical particles, and “correlation” effects arising from the non-independent nature of the electron distribution. (For example, the fact that the electron pair density $P(\mathbf{r}, \mathbf{r}')$, the probability density of finding two electrons at \mathbf{r} and \mathbf{r}' , is not simply the independent product $n(\mathbf{r})n(\mathbf{r}')$ is a correlation effect.) With these definitions, we can write everything in Equation 2.6 in terms of the Kohn–Sham orbitals:

$$\begin{aligned} \mathcal{E}[n; v] = & -\frac{1}{2} \sum_j \int d\mathbf{r} \psi_j^*(\mathbf{r}) \nabla^2 \psi_j(\mathbf{r}) + \frac{1}{2} \sum_{jk} \int d\mathbf{r} d\mathbf{r}' \frac{|\psi_j(\mathbf{r})|^2 |\psi_k(\mathbf{r}')|^2}{|\mathbf{r} - \mathbf{r}'|} \\ & + \sum_j \int d\mathbf{r} |\psi_j(\mathbf{r})|^2 v(\mathbf{r}) + E_{xc}[n]. \end{aligned} \quad (2.11)$$

To minimize this functional, we apply a variational method with respect to small changes $\delta\psi_j$ and $\delta\psi_j^*$ in the orbitals and their complex conjugates. Setting $\delta\mathcal{E} = 0$ and solving for the coefficients of the variational parameters yields the *Kohn–Sham equations*:

$$\left[-\frac{\nabla^2}{2} + v(\mathbf{r}) + \int d\mathbf{r}' \frac{n(\mathbf{r}')}{|\mathbf{r} - \mathbf{r}'|} + v_{xc}(\mathbf{r}) \right] \psi_j(\mathbf{r}) = \epsilon_j \psi_j(\mathbf{r}), \quad (2.12)$$

where

$$v_{xc}(\mathbf{r}) \equiv \frac{\delta E_{xc}[n]}{\delta n(\mathbf{r})} \quad (2.13)$$

is a functional derivative of $E_{\text{xc}}[n]$ known as the *exchange–correlation potential*. Formally, the ϵ_j are a set of Lagrange multipliers that enforce orthonormality of the Kohn–Sham orbitals, but they are interpreted as single-particle energy levels due to the Schrödinger-like form of Equation 2.12. The total ground-state energy is given exactly in terms of Kohn–Sham quantities by [16]

$$E_0 = \sum_j \epsilon_j - \frac{1}{2} \sum_{jk} \int d\mathbf{r} d\mathbf{r}' \frac{n(\mathbf{r}) n(\mathbf{r}')}{|\mathbf{r} - \mathbf{r}'|} + E_{\text{xc}}[n] - \int d\mathbf{r} n(\mathbf{r}) v_{\text{xc}}(\mathbf{r}), \quad (2.14)$$

where the sums range over the N lowest-energy Kohn–Sham orbitals.

Since the Kohn–Sham orbitals appear implicitly in the bracketed term on the left-hand side of Equation 2.12, the system of equations is *self-consistent*. It cannot generally be solved in one shot; rather, an initial guess for the orbitals is made, the density and exchange–correlation potential are calculated from that guess, and the Kohn–Sham equations are solved to yield an improved set of orbitals. This procedure is iterated until it converges to within some numerical tolerance. Various schemes exist for optimizing the stability and convergence of this calculation.

By calculating more than N orthonormal solutions to Equation 2.12, one can obtain single-particle orbitals and energies for *unoccupied* states of the system. Or, in a periodic crystal, one could calculate states at a particular point in \mathbf{k} -space by specifying Kohn–Sham orbitals that are Bloch functions, with $\psi_j(\mathbf{r} + \mathbf{R}) = e^{i\mathbf{k} \cdot \mathbf{R}} \psi_j(\mathbf{r})$ for any lattice vector \mathbf{R} . However, it is important to note that the ϵ_j are not energy levels of the interacting system in any rigorous sense. Treating them as such typically yields a reasonable description of band dispersion, but band gaps of semiconductors and insulators are systematically underestimated. Various methods for handling this issue exist, some of which we describe

later in this chapter.

2.1.1 Exchange–correlation functionals

In order to solve Equation 2.12, we need to calculate the exchange–correlation functional $E_{\text{xc}}[n]$. This functional can be written down exactly for simple systems like a uniform gas of electrons, but in general it is unknown. Various practical approximations have been developed. In this section, we briefly describe three of them: the *local density approximation*, the *generalized gradient approximation*, and the *hybrid functional*.

The local density approximation (LDA) is derived by assuming that the electron density $n(\mathbf{r})$ varies slowly in space. In that case, any small region of space $d\mathbf{r}$ resembles a uniform electron gas of density $n(\mathbf{r})$, so we can estimate that

$$E_{\text{xc}}[n] \approx E_{\text{xc}}^{\text{LDA}}[n] \equiv \int d\mathbf{r} n(\mathbf{r}) \varepsilon_{\text{xc}}^{\text{LDA}}(n(\mathbf{r})), \quad (2.15)$$

where $\varepsilon_{\text{xc}}^{\text{LDA}}(n)$ is the exact exchange–correlation energy per electron of a uniform gas of interacting electrons with density n . The exchange–correlation potential is given by

$$v_{\text{xc}}(\mathbf{r}) \equiv \frac{\delta E_{\text{xc}}^{\text{LDA}}[n]}{\delta n(\mathbf{r})} = \varepsilon_{\text{xc}}^{\text{LDA}}(n(\mathbf{r})) + n(\mathbf{r}) \left. \frac{d\varepsilon_{\text{xc}}^{\text{LDA}}(n)}{dn} \right|_{n=n(\mathbf{r})}. \quad (2.16)$$

This expression simplifies Equation 2.14, with a cancellation between the two exchange–correlation terms reducing them to one:

$$E_0 = \sum_j \epsilon_j - \frac{1}{2} \sum_{jk} \int d\mathbf{r} d\mathbf{r}' \frac{n(\mathbf{r}) n(\mathbf{r}')}{|\mathbf{r} - \mathbf{r}'|} - \int d\mathbf{r} n^2(\mathbf{r}) \left. \frac{d\varepsilon_{\text{xc}}^{\text{LDA}}(n)}{dn} \right|_{n=n(\mathbf{r})}. \quad (2.17)$$

$\varepsilon_{\text{xc}}^{\text{LDA}}(n)$ has been carefully tabulated [17] and parametrized [18]. The LDA is widely used

in DFT calculations of materials with weak electron correlation. In this dissertation, we use the Perdew–Zunger exchange–correlation functional for the borophene-on-Cu calculations in Chapters 5 and 6.

In systems with stronger electron correlation (e.g., *d*-band solids) or rapidly-varying electron density (e.g., molecules), the assumptions of the LDA fail. In this case, it is intuitive to build a model that depends on not only the local density, but also derivatives of the density. Exchange–correlation functionals of the form

$$E_{\text{xc}}[n] = \int d\mathbf{r} n(\mathbf{r}) \varepsilon_{\text{xc}}^{\text{GGA}}(n(\mathbf{r}), \nabla n(\mathbf{r})) \quad (2.18)$$

are called *generalized gradient approximations* (GGAs). There is no universal choice for $\varepsilon_{\text{xc}}^{\text{GGA}}$; in solid-state physics, widely-used GGAs include the PW91 functional by Perdew and Wang [19] and the PBE functional by Perdew, Burke, and Ernzerhof [20]. GGAs generally yield more accurate values for cohesive and binding energies than the LDA. In this dissertation, we use the PBE GGA in Chapters 3, 4, 7, and 8.

The LDA and GGA are, respectively, *local* and *semilocal*: at a particular point in space they depend on physical properties at that point and (in the case of the GGA) its immediate surroundings. Electron–electron interactions are not necessarily local, though, a fact that often contributes to errors when calculating band gaps, bond lengths, vibrational frequencies, and other properties with local functionals. To tackle this problem, Becke [21] proposed replacing some fraction of the exchange–correlation functional with the exchange energy term E_{x} used in Hartree–Fock theory:

$$E_{\text{x}} = -\frac{1}{2} \sum_{jk} \int d\mathbf{r} d\mathbf{r}' \frac{\psi_j^*(\mathbf{r}) \psi_k^*(\mathbf{r}') \psi_k(\mathbf{r}) \psi_j(\mathbf{r}')}{|\mathbf{r} - \mathbf{r}'|}. \quad (2.19)$$

The resulting functional is called a *hybrid functional*. Widely used hybrid functionals in solid-state physics include the PBE0 functional of Perdew, Burke, and Ernzerhof, who argued for replacing exactly 1/4 of their PBE functional’s exchange term with exact exchange [22]:

$$E_{\text{xc}}^{\text{PBE0}} = E_{\text{xc}}^{\text{PBE}} + \frac{1}{4} \left(E_{\text{x}} - E_{\text{x}}^{\text{PBE}} \right), \quad (2.20)$$

where $E_{\text{x}}^{\text{PBE}}$ is the portion of the PBE functional that describes exchange. This functional accurately calculates chemical properties of interest, often obtaining band gaps in better agreement with experiment than LDA or GGA. However, since the exact exchange cannot be expressed purely in terms of electron density, hybrid calculations are often expensive. Heyd, Scuseria, and Ernzerhof (HSE) introduced a less costly version of the PBE0 functional that uses a screened Coulomb potential, expediting convergence of the calculation without sacrificing accuracy [23]. In this dissertation, we use a revised version of the HSE functional [24] in Chapters 3 and 7.

2.1.2 Wannier functions

In a periodic crystal, the Kohn–Sham equations generate Bloch wavefunctions $\psi_{n\mathbf{k}}(\mathbf{r})$ that are wave-like and thus delocalized within a material. Bloch functions are useful for many purposes, since they share the periodicity of the crystal lattice and they diagonalize the Hamiltonian. However, they are often poorly suited for describing intrinsically local processes like chemical bonding, polarization, and magnetism. Wannier functions, first described in 1937 [25], repackage the information of Bloch functions in a localized form, with the states $\psi_{n\mathbf{k}}$ for a band n being replaced by a set of Wannier functions, one per unit cell. Like atomic orbitals, to which they often bear a qualitative resemblance, Wannier

functions can be used as basis functions for tight-binding models. However, unlike atomic orbitals, Wannier functions are orthonormal, they preserve the crystal symmetries of their material, and they can be used to exactly reconstruct the DFT bands from which they are built.

The simplest case to consider is that of a single isolated band n . The textbook definition of a set of Wannier functions $|\mathbf{R}n\rangle$, where \mathbf{R} is a real-space lattice vector, is in terms of a Fourier transform of the band's Bloch functions:

$$|\mathbf{R}n\rangle = \frac{1}{\sqrt{N}} \sum_{\mathbf{k}} e^{-i\mathbf{k}\cdot\mathbf{R}} |\psi_{n\mathbf{k}}\rangle, \quad (2.21)$$

where N is the number of points in the \mathbf{k} -mesh being used to cover the Brillouin zone. Wannier functions are orthonormal ($\langle \mathbf{R}n | \mathbf{R}'n \rangle = \delta_{\mathbf{R}\mathbf{R}'}$), and they form a complete basis for the same subspace spanned by the band's Bloch functions:

$$P_n \equiv \sum_{\mathbf{k}} |\psi_{n\mathbf{k}}\rangle \langle \psi_{n\mathbf{k}}| = \sum_{\mathbf{R}} |\mathbf{R}n\rangle \langle \mathbf{R}n|. \quad (2.22)$$

Most importantly, they are translations of one another in real space:

$$W_{n\mathbf{R}}(\mathbf{r}) \equiv \langle \mathbf{r} | \mathbf{R}n \rangle = \langle \mathbf{r} - \mathbf{R} | \mathbf{0}n \rangle = W_{n\mathbf{0}}(\mathbf{r} - \mathbf{R}), \quad (2.23)$$

where $|\mathbf{r}\rangle$ is a δ -function state that we use here to obtain the wavefunction of a ket. This fact can be shown easily using Equation 2.21 and the periodicity of Bloch functions, which satisfy $\psi_{n\mathbf{k}}(\mathbf{r} - \mathbf{R}) = e^{-i\mathbf{k}\cdot\mathbf{R}} \psi_{n\mathbf{k}}(\mathbf{r})$ if \mathbf{R} is a lattice vector. Even in the single-band case, Wannier functions are not unique. This fact comes from the gauge freedom that we have to assign an arbitrary phase to each Bloch function: $\psi_{n\mathbf{k}}(\mathbf{r}) \rightarrow e^{i\varphi_n(\mathbf{k})} \psi_{n\mathbf{k}}(\mathbf{r})$, for $\varphi_n(\mathbf{k})$

periodic in \mathbf{k} -space. Altering the phase convention alters the Wannier functions; generally, to obtain highly localized Wannier functions, one should choose a smoothly-varying phase convention [26].

The above gauge freedom is actually just a special case of the gauge freedom that arises for a set of multiple bands. Consider a set of J bands that are separated in energy from higher or lower bands, but may have band crossings or degeneracies among themselves. The subspace spanned by these bands is also spanned by any set of states $|\tilde{\psi}_{n\mathbf{k}}\rangle$ defined by

$$|\tilde{\psi}_{n\mathbf{k}}\rangle = \sum_{m=1}^J U_{mn}^{(\mathbf{k})} |\psi_{m\mathbf{k}}\rangle, \quad (2.24)$$

where $U_{mn}^{(\mathbf{k})}$ is a family of unitary matrices, one for each \mathbf{k} , that is periodic in reciprocal space. In general $|\tilde{\psi}_{n\mathbf{k}}\rangle$ are not eigenstates of the Hamiltonian, though one could imagine nontrivial unitary transformations among states, e.g., in the presence of degeneracies. Nevertheless, they can still be used to define a set of Wannier functions for the whole manifold:

$$|\mathbf{R}n\rangle = \frac{1}{\sqrt{N}} \sum_{\mathbf{k}} e^{-i\mathbf{k}\cdot\mathbf{R}} |\tilde{\psi}_{n\mathbf{k}}\rangle = \frac{1}{\sqrt{N}} \sum_{\mathbf{k}} \sum_{m=1}^J e^{-i\mathbf{k}\cdot\mathbf{R}} U_{mn}^{(\mathbf{k})} |\psi_{m\mathbf{k}}\rangle. \quad (2.25)$$

Indeed, the best-localized Wannier functions often involve nontrivial mixing of a system's Bloch functions.

The ambiguities that arise in defining Wannier functions likely contributed to their relative disuse for several decades after their initial discovery [26]. However, researchers in the 1990s made major advances in selecting well-chosen Wannier functions, culminating in Marzari and Vanderbilt's 1997 proposal of the maximally localized Wannier function (MLWF) scheme [27]. The MLWF procedure is based on minimizing a *spread functional*

Ω , defined as

$$\Omega = \sum_n [\langle \mathbf{0}n | r^2 | \mathbf{0}n \rangle - \langle \mathbf{0}n | \mathbf{r} | \mathbf{0}n \rangle^2] = \sum_n [\langle r^2 \rangle_n - \bar{\mathbf{r}}_n^2], \quad (2.26)$$

which intuitively captures the spatial extent of each Wannier function about its charge center.

It is common to decompose the spread functional into two terms: $\Omega = \Omega_I + \tilde{\Omega}$, where

$$\Omega_I = \sum_n \left[\langle \mathbf{0}n | r^2 | \mathbf{0}n \rangle - \sum_{\mathbf{R}m} |\langle \mathbf{R}m | \mathbf{r} | \mathbf{0}n \rangle|^2 \right], \quad (2.27)$$

$$\tilde{\Omega} = \sum_n \sum_{\mathbf{R}m \neq \mathbf{0}n} |\langle \mathbf{R}m | \mathbf{r} | \mathbf{0}n \rangle|^2. \quad (2.28)$$

Both terms are individually positive definite, but Ω_I is also gauge invariant for a given set of bands. Marzari and Vanderbilt defined a straightforward iterative procedure to select the set of transformations $U_{mn}^{(\mathbf{k})}$ that minimize $\tilde{\Omega}$; the Wannier functions obtained from such a gauge choice are deemed *maximally localized*. The only ingredients needed for the minimization scheme are a set of Bloch functions and an set of overlap matrices $M_{mn}^{(\mathbf{k}, \mathbf{b})} = \langle u_{m\mathbf{k}} | u_{n\mathbf{k}+\mathbf{b}} \rangle$, where $u_{n\mathbf{k}}(\mathbf{r}) = e^{-i\mathbf{k} \cdot \mathbf{r}} \psi_{n\mathbf{k}}(\mathbf{r})$ is the cell-periodic part of $\psi_{n\mathbf{k}}$.

The discovery of MLWFs has greatly expanded the uses of Wannier functions. Soluyanov and Vanderbilt [28] proposed a method that uses “hybrid” functions, which are Wannierized along one dimension but not others, to compute the Z_2 topological invariant of systems without inversion symmetry. Their approach works by tracking how the Wannier charge centers $\mathbf{r}_n = \langle \mathbf{0}n | \mathbf{r} | \mathbf{0}n \rangle$ evolve as a function of wave vector \mathbf{k} in a non-Wannierized direction. It is conceptually related to the Berry-phase-based “modern theory of polarization” developed by King-Smith and Vanderbilt [29, 30] and based on earlier work by Resta [31]. Wannier functions can also be used to affordably interpolate band structures when a full

DFT calculation at each point along the \mathbf{k} -path is infeasible. Briefly, a set of Wannier functions $|\mathbf{R}n\rangle$ is constructed from a DFT calculation on a coarse \mathbf{k} -grid. The Hamiltonian matrix elements $\langle \mathbf{0}n | \hat{H} | \mathbf{R}m \rangle$ in this basis are computed, and taken to be the hopping and on-site terms of a tight-binding model. The bands of this tight-binding model can then be calculated at an arbitrary point \mathbf{k} by defining a new Bloch Hamiltonian

$$\hat{H}_{\mathbf{k},nm}^W = \sum_{\mathbf{R}} e^{i\mathbf{k}\cdot\mathbf{R}} \langle \mathbf{0}n | \hat{H} | \mathbf{R}m \rangle \quad (2.29)$$

and diagonalizing it. Effectively, we have performed a double Fourier transform from the Bloch basis to the Wannier basis and back again; mathematically, this is often referred to as “Fourier interpolation.” The procedure depends on the smoothness of the Hamiltonian in \mathbf{k} space, which directly stems from the locality (*i.e.*, short-ranged nature) of the Wannier functions and matrix elements $\langle \mathbf{0}n | \hat{H} | \mathbf{R}m \rangle$.

The desire to calculate band structures for complex materials motivates the final Wannier-function topic we will discuss, that of *disentangling* bands. Often, we want to build a model for a subset of bands in an entangled manifold; for example, we might want to isolate the p_z -like orbitals from monolayer graphene or borophene, or the surface states of a slab material. The relevant bands may mix with or cross over irrelevant bands that we want to exclude. To build suitable Wannier functions for this purpose, we need a prescription to choose which bands are relevant at each \mathbf{k} -point. Souza et al. [32] addressed this issue by noting that, while $\tilde{\Omega}$ captures the smoothness of individual Wannier functions, Ω_I captures the “smoothness” of the Hilbert space in which those functions live, considered as a function of \mathbf{k} . Given a set of $\mathcal{J}_{\mathbf{k}} \geq J$ Bloch states at each \mathbf{k} -point, they defined an iterative procedure to select the J -dimensional subspace at each \mathbf{k} that minimizes Ω_I . Often, the search is

further constrained by defining a “frozen” energy window in which all bands are necessarily retained; this can help to define the character of the desired bands so that they can be readily selected outside of the frozen window.

This dissertation uses maximally localized Wannier functions constructed using the Wannier90 package [33]. In Chapter 3, we use these functions and the WannierTools package [34] to compute topological invariants of materials without inversion symmetry using the method of Soluyanov and Vanderbilt [28]. In Chapter 6, we use tight-binding models built from Wannier functions to unfold electronic band structures (see Section 2.1.4).

2.1.3 Scanning tunneling microscopy (STM)

Scanning tunneling microscopy (STM) is a commonly used technique for high-resolution real-space imaging of atomically structured surfaces. First developed in 1981 at IBM [35], the STM technique led its developers, Gerd Binnig and Heinrich Rohrer, to share a portion of the 1986 Nobel Prize in Physics. Since then, STM has been used to image a wide variety of metals, insulators, and molecules, even being used to manipulate individual xenon atoms on a nickel surface to spell out “IBM” [36].

The active element of a scanning tunneling microscope is an atomically sharp conducting metal tip, which is brought into near contact with a surface of interest and held at a specified bias voltage. When the tip is sufficiently close to the surface, electrons quantum tunnel between surface and tip, producing an electric current that is measured by the microscope. The tip scans laterally over the surface, being held either at a constant height or at a constant tunneling current. The latter mode is implemented by a piezoelectric feedback mechanism that moves the tip towards the surface when the tunneling current is lower than the desired set point, and farther from the surface when the opposite is true. In this way, a high-

resolution topographic image of the surface is produced. By adjusting the bias voltage, different near- E_F states can be imaged, producing information about the system's electronic structure as well.

Tersoff and Hamann introduced a simple widely-used approach to theoretical STM calculations in the mid-1980s, shortly after the development of the STM technique itself [37, 38]. They built on earlier work by Bardeen [39], who showed generally that the tunneling current I can be expressed in terms of the tunneling matrix element $M_{\mu\nu}$ by

$$I = \frac{2\pi e}{\hbar} \sum_{\mu,\nu} f(E_\mu) [1 - f(E_\nu + eV)] |M_{\mu\nu}|^2 \delta(E_\mu - E_\nu), \quad (2.30)$$

where $f(E)$ is the Fermi function, V is the bias voltage (the voltage of the surface with respect to the tip), and E_μ and E_ν are the energies of the tip and surface states, respectively. Bardeen further showed that the tunneling matrix element can be computed in terms of the initial and final wavefunctions ψ_μ, ψ_ν as

$$M_{\mu\nu} = \frac{\hbar^2}{2m} \int d\vec{S} \cdot (\psi_\mu^* \nabla \psi_\nu - \psi_\nu \nabla \psi_\mu^*), \quad (2.31)$$

where the integral is taken over a surface within the vacuum separating the initial and final regions.

Tersoff and Hamann made two crucial simplifying assumptions: first, that the wavefunctions for electrons in the metal tip are spherically symmetric with respect to the center of the tip (*i.e.*, they are s -type states), and second, that the work functions of the surface and the tip are identical: $\phi_{\text{surface}} = \phi_{\text{tip}} \equiv \phi$. Under these assumptions, they expressed the

tip wavefunctions ψ_μ and surface wavefunctions ψ_ν as

$$\psi_\mu(\mathbf{r}) = \frac{c_t}{\Omega_t^{1/2}} \frac{\kappa R e^{\kappa R}}{\kappa |\mathbf{r} - \mathbf{r}_0|} \exp[-\kappa |\mathbf{r} - \mathbf{r}_0|], \quad (2.32)$$

$$\psi_\nu(\mathbf{r}) = \frac{1}{\Omega_s^{1/2}} \sum_{\mathbf{G}} a_{\mathbf{G}} \exp\left[-(\kappa^2 + |\mathbf{k}_\parallel + \mathbf{G}|^2)^{1/2} z\right] \exp[i(\mathbf{k}_\parallel + \mathbf{G}) \cdot \mathbf{x}], \quad (2.33)$$

where \mathbf{r}_0 is the tip's center of curvature, R is its radius of curvature, $a_{\mathbf{G}}$ are the expansion coefficients of ψ_ν in a plane-wave basis with reciprocal lattice vectors \mathbf{G} , and $\kappa = \sqrt{2m\phi}/\hbar$ is a decay constant set by the vacuum work function. In the low-temperature limit, the Fermi functions in Equation 2.30 can be replaced by step functions, and the requisite integrals carried out to obtain

$$I = \frac{32\pi^3 e}{\hbar} \frac{R^2 \phi^2}{\kappa^4} \int_0^{eV} d\epsilon D_t(E_F + \epsilon) \underbrace{\sum_\nu |\psi_\nu(\mathbf{r}_0)|^2 \delta(E_\nu - (E_F - eV + \epsilon))}_{\rho(\mathbf{r}_0; E_F - eV + \epsilon)}, \quad (2.34)$$

where $D_t(\epsilon)$ is the tip density of states. The local behavior is captured by the underbraced expression, which is the *surface* local density of states evaluated at the *tip* center of curvature, $\rho(\mathbf{r}_0, \epsilon)$. This quantity can be easily calculated from *ab initio* calculations, readily allowing for accurate simulation of STM experiments. If the bias voltage is sufficiently small that each system's density of states is roughly constant over the relevant range, then the integral in Equation 2.34 can be carried out to obtain

$$I = \frac{32\pi^3 e^2 V}{\hbar} \frac{R^2 \phi^2}{\kappa^4} D_t(E_F) \rho(\mathbf{r}_0, E_F). \quad (2.35)$$

Tersoff and Hamann used their crude *s*-wave approximation for the tip wavefunctions partly because the physical nature of the STM tip was not well understood in the early

1980s. Subsequent research revealed that these assumptions may have been ill-founded; in particular, p - and d -type states play a major role in the near- E_F tip states [40, 41]. Chen [40] revisited the problem of STM calculations using a more general Green’s function approach. Chen’s results replicate the Tersoff–Hamann result in the case of an s -wave tip, but find that $\ell \neq 0$ states contribute terms to the tunneling matrix element that depend on *derivatives* of surface wavefunctions:

$$M_s \propto \psi_v(\mathbf{r}_0), \quad M_{p_i} \propto \frac{1}{\kappa} \left. \frac{\partial \psi_v}{\partial r_i} \right|_{\mathbf{r}_0}, \quad i = x, y, z. \quad (2.36)$$

Thus, the tunneling current contains terms proportional to the squares of derivatives of surface states, as well as the surface LDOS term of Equation 2.35. Subsequent researchers have noted that these terms are especially important when the STM tip is *functionalized* by adding a single molecule with non- s -wave tunneling orbitals [42]. For example, in experiments with a CO-functionalized tip in a vertical configuration, the $2\pi^*$ orbitals open a tunneling channel described by a rotationally-invariant combination of p_x - and p_y -wave states [41]:

$$I_{p_x+p_y} \propto \sum_v \left[\left| \frac{\partial \psi_v}{\partial x} \right|^2 + \left| \frac{\partial \psi_v}{\partial y} \right|^2 \right] \delta(E_v - E_F) \quad (2.37)$$

In this dissertation, STM calculations were carried out using Quantum ESPRESSO’s post-processing executable `pp.x`, which calculates the s -wave STM current from the Tersoff–Hamann formula. We modified the code to also calculate p_z -wave STM currents and the rotationally-invariant $p_x + p_y$ current described above.

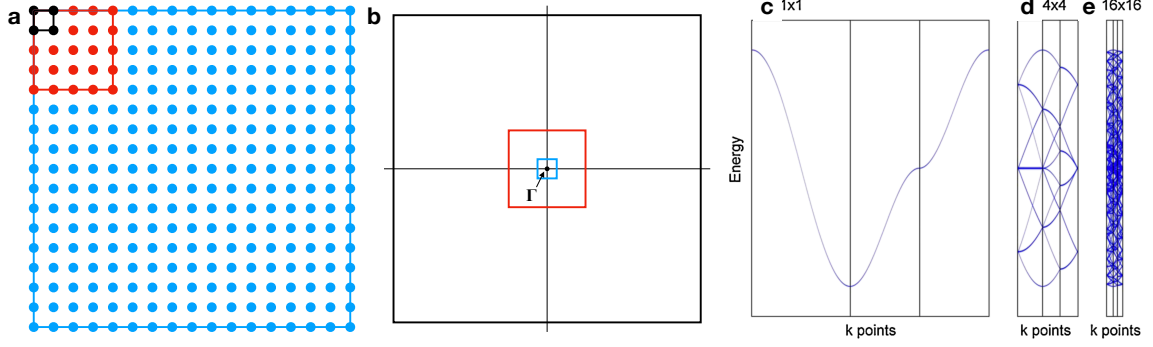


Figure 2.1: Demonstration of band folding for a simple two-dimensional crystal. For the 4×4 (red) and 16×16 (blue) supercells of the black primitive cell depicted in (a), the first Brillouin zone is reduced to the sizes shown in (b). (c) Band structure of a one-band tight-binding model in the primitive cell. (d,e) The band structure from (c), folded into the first Brillouin zone of the supercells. Panels (c-e) are adapted from [43].

2.1.4 Band unfolding

One powerful application of density functional theory is to compute a material’s electronic band structure, which encodes information that is useful for analyzing transport, optical, and scattering properties. This can be done easily using the Kohn–Sham equations, which describe the one-particle energy levels at any arbitrary \mathbf{k} -point in the Brillouin zone. For a crystalline material with a small unit cell and perfect periodicity, this procedure is conceptually simple and quite tractable. Often, though, one wants to study the effects of localized defects or long-period modulations in crystal structure. These structures can be studied by simulating a large “supercell” containing many copies of the primitive unit cell, which is then perturbed to include the imperfection of interest. In such a system, the size of the Brillouin zone is dramatically reduced, resulting in bands that are “folded” over themselves (Figure 2.1). These band structures can be made easier to interpret by “unfolding” them back into the larger primitive Brillouin zone.

Various band unfolding schemes exist; in this dissertation, we use and expand on a

technique described by Ku, Berlijn, and Lee [43], with occasional support from a similar method proposed shortly afterward by Popescu and Zunger [44]. The procedure of Ku et al. uses maximally localized Wannier functions [27] to map states from a commensurate supercell onto a smaller primitive cell. Our extension applies this technique to cases where the primitive cell–supercell relation is not perfectly commensurate and examines the ways in which the band unfolding procedure is still meaningful.

Properly speaking, the quantity calculated by band unfolding is not the band structure but rather the spectral function, most generally defined as $A(\omega) = -\frac{1}{\pi} \text{Im } G(\omega)$, where G is the retarded one-electron Green’s function. For a system with well-defined quasiparticles, the spectral function is nearly diagonal in momentum–energy space and exhibits δ -function peaks. For example, the spectral function for a crystalline system of non-interacting fermions in reciprocal space is

$$A(\mathbf{k}, \omega) = \sum_j \delta(E_{\mathbf{k}j} - \omega), \quad (2.38)$$

where $E_{\mathbf{k}j}$ is the energy of the j th band at \mathbf{k} . For a given path through \mathbf{k} -space, a heat map of this function on (\mathbf{k}, ω) axes perfectly overlaps with a plot of the energy bands (perhaps with some energy broadening applied to make the spectral function easily visible).

Before continuing, we define some terminology and notation. Bloch states in the primitive cell are denoted $|\mathbf{k}j\rangle$, where \mathbf{k} is a point in the primitive Brillouin zone (PBZ) and j is a band index. In the supercell, Bloch states are denoted $|\mathbf{K}J\rangle$ for a supercell Brillouin zone (SBZ) point \mathbf{K} . A SBZ point \mathbf{K} is said to *unfold into* a PBZ point \mathbf{k} if there is a supercell reciprocal lattice vector \mathbf{G} such that $\mathbf{k} = \mathbf{K} + \mathbf{G}$. In the primitive cell (supercell), we can also introduce a basis of Wannier functions $|\mathbf{r}n\rangle$ ($|\mathbf{R}N\rangle$), where \mathbf{r} (\mathbf{R}) is a real-space lattice vector and n (N) is an orbital index. For well-localized Wannier functions and a

weak perturbation, it is expected that supercell Wannier functions can be approximated by correctly indexed primitive cell Wannier functions:

$$|\mathbf{R}N\rangle \approx |\mathbf{r} = \mathbf{R} + \mathbf{r}'(N), n = n'(N)\rangle \quad (2.39)$$

for maps \mathbf{r}' and n' that can be constructed by inspection. It is also useful to define Fourier-transformed Wannier functions:

$$|\mathbf{k}n\rangle = \sum_{\mathbf{r}} |\mathbf{r}n\rangle \langle \mathbf{r}n | \mathbf{k}n \rangle = \frac{1}{\sqrt{l}} \sum_{\mathbf{r}} |\mathbf{r}n\rangle e^{i\mathbf{k}\cdot\mathbf{r}}, \quad (2.40)$$

where l is the number of \mathbf{k} -points in the PBZ, and likewise for supercell Wannier functions.

In the primitive cell, we define the *unfolded spectral function*

$$A(\mathbf{k}, \omega) = \sum_{Jj} |\langle \mathbf{k}j | \mathbf{K}J \rangle|^2 \delta(E_{\mathbf{K}J} - \omega), \quad (2.41)$$

where \mathbf{K} is the SBZ point that unfolds into \mathbf{k} . This function can also be expressed in terms of Fourier-transformed Wannier functions:

$$A(\mathbf{k}, \omega) = \sum_{Jn} |\langle \mathbf{k}n | \mathbf{K}J \rangle|^2 \delta(E_{\mathbf{K}J} - \omega). \quad (2.42)$$

A simple calculation detailed in [43] shows that the matrix elements $\langle \mathbf{k}n | \mathbf{K}J \rangle$ can be expressed purely in terms of Bloch states and Wannier functions in the *supercell*:

$$\langle \mathbf{k}n | \mathbf{K}J \rangle = \sqrt{\frac{L}{l}} \sum_N e^{-i\mathbf{k}\cdot\mathbf{r}'(N)} \delta_{n,n'(N)} \delta_{[\mathbf{k}],\mathbf{K}} \langle \mathbf{K}N | \mathbf{K}J \rangle, \quad (2.43)$$

where $\delta_{[\mathbf{k}],\mathbf{K}} = 1$ if and only if \mathbf{K} unfolds into \mathbf{k} . Thus, the unfolded spectral function can be computed simply by constructing Wannier functions in the supercell and defining a coherent mapping between primitive cell and supercell sites.

In the standard picture of band unfolding, the supercell is *commensurate* to the primitive cell; that is, the primitive cell basis vectors \mathbf{a}_i and supercell basis vectors \mathbf{A}_i are related by a matrix of integers [44]:

$$\begin{pmatrix} \mathbf{A}_1 \\ \mathbf{A}_2 \\ \mathbf{A}_3 \end{pmatrix} = \begin{pmatrix} m_{11} & m_{12} & m_{13} \\ m_{21} & m_{22} & m_{23} \\ m_{31} & m_{32} & m_{33} \end{pmatrix} \cdot \begin{pmatrix} \mathbf{a}_1 \\ \mathbf{a}_2 \\ \mathbf{a}_3 \end{pmatrix} \quad m_{ij} \in \mathbb{Z}. \quad (2.44)$$

However, in Chapter 6, we discuss a borophene structure with a domain-wall dislocation that defines a supercell for which some m_{ij} are non-integer rational numbers. In this system, SBZ points can still be unfolded into PBZ points, and supercell Wannier functions sites can still be mapped to primitive cell sites. In principle, the latter map depends on the choice of origin and shape for the real-space unit cells, but the difference is only meaningful in the vicinity of the domain-wall boundary. More details on the procedure and results for this calculation are available in Section 6.5.

In this dissertation, band unfolding calculations were performed using a basis of maximally localized Wannier functions constructed with the Wannier90 code [33]. The construction of the spectral function itself was carried out by code written in MATLAB.

2.2 *GW*-BSE method: Electronic excitations and interactions

The DFT-based methods outlined in Section 2.1 describe ground-state properties of interacting electrons in solids. They are much less successful at describing excited-state properties such as band gaps and optical absorption spectra. Hybrid functionals like those described in Section 2.1.1 can yield more accurate band gaps, but fundamentally they still only produce single-particle energy levels. To properly describe quasiparticles, excitons and light–matter interactions, a more elaborate many-body theory is necessary. One such approach, the *GW* method for quasiparticle properties, was developed first for the electron gas by Hedin [45] and applied to real materials in a modern form by Hybertsen and Louie [46, 47]. We outline its basics in this section.

2.2.1 Screening in solids

To describe how electrons in materials interact with both one another and optical probes, we need a framework for describing electric fields and potentials in solids. For example, consider the simple case of a uniform (or at least slowly-varying) applied electric field \mathbf{E}_{ext} . In the presence of this field, a solid’s ions and electrons rearrange to produce a polarization \mathbf{P} that screens (*i.e.*, reduces) the net electric field \mathbf{E} within the solid. The relation between these three vectors is $\mathbf{E}_{\text{ext}} = \mathbf{E} + 4\pi\mathbf{P}$. Often, the polarization is linear in the internal electric field, so we can write $\mathbf{E}_{\text{ext}} = \epsilon\mathbf{E}$. The quantity ϵ is called the *dielectric constant*.

We can think about the same phenomenon in terms of the screening of electric potentials, rather than fields. Consider adding an electron to an insulating solid at a point \mathbf{r} . If the

screening in the solid is isotropic and uniform, then the screened potential $W(\mathbf{r}, \mathbf{r}')$ at a point \mathbf{r}' due to the electron will take the form

$$W(\mathbf{r}, \mathbf{r}') = \frac{v(\mathbf{r}, \mathbf{r}')}{\epsilon}, \quad (2.45)$$

where $v(\mathbf{r}, \mathbf{r}') = 1/|\mathbf{r} - \mathbf{r}'|$ is the unscreened Coulomb potential. In reality, screening in materials at the microscopic level is more complicated. Valence electrons are often highly localized to bonding orbitals, and so they screen potentials in an inhomogeneous manner. We must consider a nonlocal model that takes into account the variability of the polarization response at all third points \mathbf{r}'' :

$$W(\mathbf{r}, \mathbf{r}') = \int d\mathbf{r}'' \epsilon^{-1}(\mathbf{r}, \mathbf{r}'') v(\mathbf{r}'', \mathbf{r}'). \quad (2.46)$$

The response function here, no longer constant, is often called the *dielectric function*. In full generality, this expression is difficult to work with, so for crystalline systems it is more productive to take a Fourier transform and work in reciprocal space. We use the following conventions:

$$W(\mathbf{r}, \mathbf{r}') = \sum_{\mathbf{q}, \mathbf{G}, \mathbf{G}'} e^{i(\mathbf{q}+\mathbf{G})\cdot\mathbf{r}} W_{\mathbf{G}\mathbf{G}'}(\mathbf{q}) e^{-i(\mathbf{q}+\mathbf{G}')\cdot\mathbf{r}'}, \quad (2.47)$$

$$\epsilon^{-1}(\mathbf{r}, \mathbf{r}') = \sum_{\mathbf{q}, \mathbf{G}, \mathbf{G}'} e^{i(\mathbf{q}+\mathbf{G})\cdot\mathbf{r}} \epsilon_{\mathbf{G}\mathbf{G}'}^{-1}(\mathbf{q}) e^{-i(\mathbf{q}+\mathbf{G}')\cdot\mathbf{r}'}, \quad (2.48)$$

$$v(\mathbf{r}, \mathbf{r}') = \sum_{\mathbf{q}, \mathbf{G}} v(\mathbf{q} + \mathbf{G}) e^{i(\mathbf{q}+\mathbf{G})\cdot(\mathbf{r}-\mathbf{r}')}, \quad (2.49)$$

where \mathbf{G} and \mathbf{G}' are reciprocal lattice vectors and \mathbf{q} is a wave vector in the first Brillouin zone. The Fourier transform of the bare Coulomb potential has the well-known form

$v(\mathbf{q}) = 4\pi/q^2$. After Fourier transforming Equation 2.46, we obtain

$$W_{\mathbf{G}\mathbf{G}'}(\mathbf{q}) = \epsilon_{\mathbf{G}\mathbf{G}'}^{-1}(\mathbf{q}) v(\mathbf{q} + \mathbf{G}'). \quad (2.50)$$

It is important to note that $W_{\mathbf{G}\mathbf{G}'}(\mathbf{q})$ and $\epsilon_{\mathbf{G}\mathbf{G}'}^{-1}(\mathbf{q})$ are now matrices, with rows and columns labeled by reciprocal lattice vectors. When there are nonzero off-diagonal ($\mathbf{G} \neq \mathbf{G}'$) elements, termed *local-field effects*, it will not generally be the case that $\epsilon_{\mathbf{G}\mathbf{G}'}^{-1} = 1/\epsilon_{\mathbf{G}\mathbf{G}'}$. This becomes relevant when consider spatially-averaged *macroscopic* quantities, for which the relevant dielectric function is not $\epsilon_{\mathbf{0}\mathbf{0}}(\mathbf{q})$ but rather $\epsilon_{\text{mac}}(\mathbf{q}) \equiv 1/\epsilon_{\mathbf{0}\mathbf{0}}^{-1}(\mathbf{q})$.

Our discussion so far has concerned static perturbations, but when treating light–matter interactions, we are often interested in the response to a harmonically varying field at frequency ω . Assuming that time-translation invariance holds, we can treat individual frequencies separately and write

$$W_{\mathbf{G}\mathbf{G}'}(\mathbf{q}, \omega) = \epsilon_{\mathbf{G}\mathbf{G}'}^{-1}(\mathbf{q}, \omega) v(\mathbf{q} + \mathbf{G}'). \quad (2.51)$$

to describe the response to photons of energy $E = \hbar\omega$. We work in $\hbar = 1$ units, so we can use E and ω interchangeably. Below, we will generally use E to emphasize our focus on electronic band structures and quasiparticle energies.

2.2.2 The Green's function

Information about a system's excitation spectrum is encoded in an object called the *Green's function*. The general theory of Green's functions is a rich mathematical topic, and there are many subtly different objects referred to as Green's functions. In Sections 2.2.2 and

2.2.3, we discuss the time-ordered one-particle Green's function [48]:

$$iG(\mathbf{r}, t, \mathbf{r}', t') = \langle N | T[\hat{\psi}(\mathbf{r}, t) \hat{\psi}^\dagger(\mathbf{r}', t')] | N \rangle = \begin{cases} \langle N | \hat{\psi}(\mathbf{r}, t) \hat{\psi}^\dagger(\mathbf{r}', t') | N \rangle & \text{for } t > t', \\ -\langle N | \hat{\psi}^\dagger(\mathbf{r}', t') \hat{\psi}(\mathbf{r}, t) | N \rangle & \text{for } t < t', \end{cases} \quad (2.52)$$

where $|N\rangle$ is the N -particle ground state, and the field operator $\hat{\psi}(\mathbf{r}, t)$ removes an electron from position \mathbf{r} at time t . This object describes the amplitude for (if $t > t'$) an electron to be created at position \mathbf{r}' and time t' , propagate to (\mathbf{r}, t) , and be destroyed, or (if $t < t'$) a hole to be created at (\mathbf{r}, t) and propagate to (\mathbf{r}', t') . For a time-independent system, we can Fourier-transform to an energy representation of the Green's function, $G(\mathbf{r}, \mathbf{r}'; E)$. In the case of a non-interacting system with a local one-particle Hamiltonian $\hat{H}(\mathbf{r})$, this object is the function that produces a δ -function response at energy E [49]:

$$[E - \hat{H}(\mathbf{r})] G(\mathbf{r}, \mathbf{r}'; E) = \delta(\mathbf{r} - \mathbf{r}'). \quad (2.53)$$

In its *spectral representation* or *Lehmann representation*, the Green's function also encodes information about the system's wavefunctions ψ_i and energies E_i [48, 49]:

$$G(\mathbf{r}, \mathbf{r}'; E) = \sum_i \frac{\psi_i(\mathbf{r}) \psi_i^*(\mathbf{r}')}{E - E_i}. \quad (2.54)$$

Here, i indexes an intermediate eigenstate with an added electron or hole, the addition and removal amplitudes are $\psi_i(\mathbf{r}) = \langle N | \hat{\psi}(\mathbf{r}) | N + 1, i \rangle$ for an electron state and $\psi_i^*(\mathbf{r}) = \langle N - 1, i | \hat{\psi}(\mathbf{r}) | N \rangle$ for a hole state, $E_i = E_{N+1,i} - E_N$ for an electron, and $E_i = E_N - E_{N-1,i}$ for a hole. This is an exact formula, but for physically well-defined quasiparticles with very long lifetimes, the index i corresponds to the usual band index for real energies E_i with

orthornomal one-particle states $\psi_i(\mathbf{r})$.

For a typical many-body problem of interacting fermions, Equation 2.53 takes the modified form [45, 48]

$$[E - T - V_{\text{ext}}] G(\mathbf{r}, \mathbf{r}'; E) - \int d\mathbf{r}'' M(\mathbf{r}, \mathbf{r}''; E) G(\mathbf{r}'', \mathbf{r}; E) = \delta(\mathbf{r} - \mathbf{r}'), \quad (2.55)$$

where M is a *mass operator* that couples the Green's function across space. The mass term can be decomposed into the Hartree potential V_H and a remainder called the *self-energy* that is denoted $\Sigma(\mathbf{r}, \mathbf{r}'; E)$:

$$[E - T - V] G(\mathbf{r}, \mathbf{r}'; E) - \int d\mathbf{r}'' \Sigma(\mathbf{r}, \mathbf{r}''; E) G(\mathbf{r}'', \mathbf{r}; E) = \delta(\mathbf{r} - \mathbf{r}'), \quad (2.56)$$

where $V \equiv V_{\text{ext}} + V_H$.

If we denote the Green's function for $\Sigma = 0$ by G_0 , then in the time domain G satisfies a form of the Dyson equation:

$$G(1, 2) = G_0(1, 2) + \int d(34) G_0(1, 3) \Sigma(3, 4) G(4, 2), \quad (2.57)$$

where $1 \equiv (\mathbf{r}_1, t_1)$, etc. Hedin [45] derived a further set of coupled equations for relevant physical quantities:

$$\Sigma(1, 2) = i \int d(34) G(1, 3^+) W(1, 4) \Lambda(3, 2, 4), \quad (2.58)$$

$$\Lambda(1, 2, 3) = \delta(1 - 2) \delta(2 - 3) + \int d(4567) \frac{\partial \Sigma(1, 2)}{\partial G(4, 5)} G(4, 6) G(7, 5) \Lambda(6, 7, 3), \quad (2.59)$$

$$W(1, 2) = v(1, 2) + \int d(34) v(1, 3) P(3, 4) W(4, 2), \quad (2.60)$$

where $\Lambda(1, 2, 3) \equiv -\delta G^{-1}(1, 2)/\delta V(3)$ is the *vertex function*, $W(1, 2)$ is the screened Coulomb potential, $\epsilon^{-1}(1, 2) \equiv \delta V(1)/\delta V_{\text{ext}}(2)$ is the inverse dielectric function, v is the bare Coulomb interaction, and $P(1, 2) \equiv \delta \rho(1)/\delta V(2)$ is the *irreducible polarizability* [47]. Equations 2.57–2.60 can be greatly simplified by truncating at first order in the screened Coulomb interaction, just as an introductory perturbation theory problem might involve working to first order in some bare interaction. This is equivalent to retaining only the first term on the right-hand side of Equation 2.59. Plugging that result back into Equation 2.58 yields the *GW approximation*:

$$\Sigma(1, 2) = i G(1, 2) W(1, 2). \quad (2.61)$$

Transforming back to the energy domain, this can be written

$$\Sigma(\mathbf{r}, \mathbf{r}'; E) = \frac{i}{2\pi} \int dE' e^{-i\delta E'} G(\mathbf{r}, \mathbf{r}'; E - E') W(\mathbf{r}, \mathbf{r}'; E'), \quad (2.62)$$

where $\delta = 0^+$. This is the form in which the self-energy can be most lucratively manipulated.

2.2.3 The *GW* approximation

The self-energy enters into the eigenvalue equation for quasiparticle energies in the following form:

$$[T + V_{\text{ext}} + V_{\text{H}}] \psi_i(\mathbf{r}) + \int d\mathbf{r}' \Sigma(\mathbf{r}, \mathbf{r}'; E) \psi_i(\mathbf{r}') = E_i \psi_i(\mathbf{r}). \quad (2.63)$$

The self-energy plays an analogous role to the exchange–correlation functional in DFT. Its real part contributes a term to quasiparticle energies, while its imaginary part gives the quasiparticle lifetime. In this work, we focus on the real part.

It is fruitful to express the screened Coulomb potential W in its own spectral representation [48]:

$$W(\mathbf{r}, \mathbf{r}'; E) = v(\mathbf{r}, \mathbf{r}') + \int_{-\infty}^0 dE' \frac{D(\mathbf{r}, \mathbf{r}'; E)}{E - E' - i\delta} + \int_0^{\infty} dE' \frac{D(\mathbf{r}, \mathbf{r}'; E)}{E - E' + i\delta}, \quad (2.64)$$

where

$$D(\mathbf{r}, \mathbf{r}'; E) = -\frac{1}{\pi} \text{Im} [W(\mathbf{r}, \mathbf{r}'; E) - v(\mathbf{r}, \mathbf{r}')] \text{sgn}(E). \quad (2.65)$$

This decomposition is particularly useful because it enables the real part of the self-energy to be split into two physically meaningful parts, the *screened exchange* term Σ_{SX} and the *Coulomb hole* term Σ_{CH} : $\text{Re } \Sigma = \Sigma_{\text{SX}} + \Sigma_{\text{CH}}$. Using Equations 2.54, 2.62, and 2.64, we can define them as follows:

$$\Sigma_{\text{SX}}(\mathbf{r}, \mathbf{r}'; E) = - \sum_i^{\text{occ}} \psi_i(\mathbf{r}) \psi_i^*(\mathbf{r}') \text{Re } W(\mathbf{r}, \mathbf{r}'; E - E_i), \quad (2.66)$$

$$\Sigma_{\text{CH}}(\mathbf{r}, \mathbf{r}'; E) = \sum_i \psi_i(\mathbf{r}) \psi_i^*(\mathbf{r}') P \int_0^{\infty} d\omega' \frac{D(\mathbf{r}, \mathbf{r}'; E')}{E - E_i - E'}. \quad (2.67)$$

The meaning of “screened exchange” is straightforward enough: it is the typical Fock exchange energy term with the bare Coulomb interaction replaced with a screened potential. To elucidate the meaning of the “Coulomb hole” term, suppose that we are interested in an energy scale much lower than the pole of the screened interaction, which appears near the material’s plasma frequency. This assumption is well-justified for states near the Fermi level. It allows us to set $E - E_i \approx 0$ in Equation 2.67 and compute the principal value with

the Kramers–Kronig relation, yielding

$$\begin{aligned}\Sigma_{\text{CH}}(\mathbf{r}, \mathbf{r}'; E \approx E_F) &= \sum_i \psi_i(\mathbf{r}) \psi_i^*(\mathbf{r}') \frac{1}{2} [W(\mathbf{r}, \mathbf{r}'; 0) - v(\mathbf{r}, \mathbf{r}')] \\ &= \frac{1}{2} \delta(\mathbf{r} - \mathbf{r}') [W(\mathbf{r}, \mathbf{r}'; 0) - v(\mathbf{r}, \mathbf{r}')] .\end{aligned}\tag{2.68}$$

In the second line, we used a completeness relation for the wavefunctions to replace them with a δ -function. We see that the Coulomb hole represents a local response to the rearrangement of nearby electrons that screens the Coulomb potential (in this static limit).

Having somewhat demystified the self-energy, the next task is to actually compute the screened Coulomb potential. Screening in insulators is a complex, highly inhomogeneous process that must be studied at short length scales, or equivalently, over a large region of reciprocal space. It is described quantitatively by the inverse dielectric function $\epsilon^{-1}(\mathbf{r}, \mathbf{r}'; E)$ of Section 2.2.1, whose results can be framed in the notation of Equations 2.57–2.60 in the following way:

$$W(1, 2) = \int d(3) \epsilon^{-1}(1, 3) v(3, 2).\tag{2.69}$$

For our purposes, it will be more useful to Fourier-transform to reciprocal space, as we did in Section 2.2.1. Then, the above convolution becomes simple multiplication:

$$W_{\mathbf{G}\mathbf{G}'}(\mathbf{q}; E) = \epsilon_{\mathbf{G}\mathbf{G}'}^{-1}(\mathbf{q}; E) v(\mathbf{q} + \mathbf{G}'),\tag{2.70}$$

where \mathbf{G} and \mathbf{G}' are reciprocal lattice vectors and \mathbf{q} is a wave vector in the first Brillouin zone. The choice in the previous section to retain only one term in the vertex function, which was called the *GW* approximation there, is equivalent to making a *random phase approximation* (RPA) for the dielectric function. Under this approximation, the (normal,

non-inverse) dielectric function can be written

$$\epsilon_{\mathbf{G}\mathbf{G}'}(\mathbf{q}; E) = \delta_{\mathbf{G}\mathbf{G}'} - v(\mathbf{q} + \mathbf{G}) P_{\mathbf{G}\mathbf{G}'}(\mathbf{q}; E), \quad (2.71)$$

where P is the *irreducible polarizability*. In the RPA, the static limit of the irreducible polarizability was derived independently by Adler [50] and Wiser [51]:

$$P_{\mathbf{G}\mathbf{G}'}(\mathbf{q}; E = 0) = \sum_{n,n',\mathbf{k}} \langle n\mathbf{k} + \mathbf{q} | e^{i(\mathbf{q}+\mathbf{G})\cdot\mathbf{r}} | n'\mathbf{k} \rangle \langle n'\mathbf{k} | e^{-i(\mathbf{q}+\mathbf{G}')\cdot\mathbf{r}'} | n\mathbf{k} + \mathbf{q} \rangle \frac{f(E_{n,\mathbf{k}+\mathbf{q}}) - f(E_{n',\mathbf{k}})}{E_{n,\mathbf{k}+\mathbf{q}} - E_{n',\mathbf{k}}}, \quad (2.72)$$

where $f(E)$ is a Fermi occupation function. For semiconductors and insulators, the Fermi factors become 0 or 1, and we can restrict the n and n' sums to range over either occupied or empty bands:

$$P_{\mathbf{G}\mathbf{G}'}(\mathbf{q}; E = 0) = 2 \sum_n^{\text{occ}} \sum_{n'}^{\text{emp}} \sum_{\mathbf{k}} \frac{\langle n\mathbf{k} + \mathbf{q} | e^{i(\mathbf{q}+\mathbf{G})\cdot\mathbf{r}} | n'\mathbf{k} \rangle \langle n'\mathbf{k} | e^{-i(\mathbf{q}+\mathbf{G}')\cdot\mathbf{r}'} | n\mathbf{k} + \mathbf{q} \rangle}{E_{n,\mathbf{k}+\mathbf{q}} - E_{n',\mathbf{k}}}. \quad (2.73)$$

We can plug this into Equation 2.71 to obtain the static dielectric function:

$$\epsilon_{\mathbf{G}\mathbf{G}'}(\mathbf{q}; 0) = \delta_{\mathbf{G}\mathbf{G}'} - \frac{8\pi}{|\mathbf{q} + \mathbf{G}|^2} \sum_n^{\text{occ}} \sum_{n'}^{\text{emp}} \sum_{\mathbf{k}} \frac{\langle n\mathbf{k} + \mathbf{q} | e^{i(\mathbf{q}+\mathbf{G})\cdot\mathbf{r}} | n'\mathbf{k} \rangle \langle n'\mathbf{k} | e^{-i(\mathbf{q}+\mathbf{G}')\cdot\mathbf{r}'} | n\mathbf{k} + \mathbf{q} \rangle}{E_{n,\mathbf{k}+\mathbf{q}} - E_{n',\mathbf{k}}}. \quad (2.74)$$

The next step is to build a model for the dielectric function at nonzero energies. The simplest standard approach is the generalized plasmon pole (GPP) model of Hybertsen and Louie [47]. The imaginary part of the screened Coulomb potential is known to exhibit a strong peak at the plasmon frequency; the GPP model assumes that this is the only important feature of the spectrum. Since self-energy calculations typically involve integrating the screened Coulomb potential over a large energy range, this is a reasonable assumption.

Hybertsen and Louie postulated that the imaginary part of the inverse dielectric function takes the form

$$\text{Im } \epsilon_{\mathbf{G}\mathbf{G}'}^{-1}(\mathbf{q}; E) = A_{\mathbf{G}\mathbf{G}'}(\mathbf{q}) \{ \delta[E - \tilde{\omega}_{\mathbf{G}\mathbf{G}'}(\mathbf{q})] - \delta[E + \tilde{\omega}_{\mathbf{G}\mathbf{G}'}(\mathbf{q})] \} \quad (2.75)$$

for two unknown parameters $A_{\mathbf{G}\mathbf{G}'}(\mathbf{q})$ and $\tilde{\omega}_{\mathbf{G}\mathbf{G}'}(\mathbf{q})$. We need two constraints to solve for these parameters. The first comes from requiring that the dielectric function be causal and applying a Kramers–Kronig relation at zero energy:

$$\text{Re } \epsilon_{\mathbf{G}\mathbf{G}'}^{-1}(\mathbf{q}; 0) = \delta_{\mathbf{G}\mathbf{G}'} + \frac{2}{\pi} P \int_0^\infty dE \frac{\text{Im } \epsilon_{\mathbf{G}\mathbf{G}'}^{-1}(\mathbf{q}; E)}{E}. \quad (2.76)$$

The second is a version of the f -sum rule from linear response theory derived in [47]:

$$\int_0^\infty dE \text{Im } \epsilon_{\mathbf{G}\mathbf{G}'}^{-1}(\mathbf{q}; E) = -\frac{\pi}{2} \underbrace{\omega_p^2 \frac{(\mathbf{q} + \mathbf{G}) \cdot (\mathbf{q} + \mathbf{G}')}{|\mathbf{q} + \mathbf{G}|^2} \frac{\rho(\mathbf{G} - \mathbf{G}')}{\rho(\mathbf{0})}}_{\Omega_{\mathbf{G}\mathbf{G}'}^2(\mathbf{q})}, \quad (2.77)$$

where $\omega_p = \sqrt{4\pi\rho(\mathbf{0})e^2/m}$ is the bulk plasma frequency and $\rho(\mathbf{G})$ is a Fourier component of the ground-state charge density. The underbraced term defines a \mathbf{q} -dependent *effective bare plasma frequency* $\Omega_{\mathbf{G}\mathbf{G}'}(\mathbf{q})$. Using these constraints, the amplitude $A_{\mathbf{G}\mathbf{G}'}(\mathbf{q})$ and mode frequency $\tilde{\omega}_{\mathbf{G}\mathbf{G}'}(\mathbf{q})$ can be determined with no further adjustable parameters:

$$\tilde{\omega}_{\mathbf{G}\mathbf{G}'}^2(\mathbf{q}) = \frac{\Omega_{\mathbf{G}\mathbf{G}'}^2(\mathbf{q})}{\delta_{\mathbf{G}\mathbf{G}'} - \epsilon_{\mathbf{G}\mathbf{G}'}^{-1}(\mathbf{q}; E = 0)}, \quad (2.78)$$

$$A_{\mathbf{G}\mathbf{G}'}(\mathbf{q}) = -\frac{\pi}{2} \frac{\Omega_{\mathbf{G}\mathbf{G}'}(\mathbf{q})}{\tilde{\omega}_{\mathbf{G}\mathbf{G}'}(\mathbf{q})}, \quad (2.79)$$

and the real part of the inverse dielectric function can be written as

$$\text{Re } \epsilon_{\mathbf{G}\mathbf{G}'}^{-1}(\mathbf{q}; E) = \delta_{\mathbf{G}\mathbf{G}'} + \frac{\Omega_{\mathbf{G}\mathbf{G}'}^2(\mathbf{q})}{\omega^2 - \omega_{\mathbf{G}\mathbf{G}'}^2(\mathbf{q})}. \quad (2.80)$$

For materials with inversion symmetry, the GPP matrix elements of the screened exchange and Coulomb hole self-energies can now be written down explicitly:

$$\begin{aligned} \langle n\mathbf{k} | \Sigma_{\text{SX}}(\mathbf{r}, \mathbf{r}'; E) | n'\mathbf{k} \rangle &= - \sum_{n''}^{\text{occ}} \sum_{\mathbf{q}\mathbf{G}\mathbf{G}'} \langle n\mathbf{k} | e^{i(\mathbf{q}+\mathbf{G})\cdot\mathbf{r}} | n''\mathbf{k} - \mathbf{q} \rangle \langle n''\mathbf{k} - \mathbf{q} | e^{-i(\mathbf{q}+\mathbf{G}')\cdot\mathbf{r}'} | n'\mathbf{k} \rangle \\ &\quad \times \left[\delta_{\mathbf{G}\mathbf{G}'} + \frac{\Omega_{\mathbf{G}\mathbf{G}'}^2(\mathbf{q})}{(E - E_{n'',\mathbf{k}-\mathbf{q}})^2 - \tilde{\omega}_{\mathbf{G}\mathbf{G}'}^2(\mathbf{q})} \right] v(\mathbf{q} + \mathbf{G}'), \end{aligned} \quad (2.81)$$

$$\begin{aligned} \langle n\mathbf{k} | \Sigma_{\text{CH}}(\mathbf{r}, \mathbf{r}'; E) | n'\mathbf{k} \rangle &= \frac{1}{2} \sum_{n''} \sum_{\mathbf{q}\mathbf{G}\mathbf{G}'} \langle n\mathbf{k} | e^{i(\mathbf{q}+\mathbf{G})\cdot\mathbf{r}} | n''\mathbf{k} - \mathbf{q} \rangle \langle n''\mathbf{k} - \mathbf{q} | e^{-i(\mathbf{q}+\mathbf{G}')\cdot\mathbf{r}'} | n'\mathbf{k} \rangle \\ &\quad \times \frac{\Omega_{\mathbf{G}\mathbf{G}'}^2(\mathbf{q})}{\tilde{\omega}_{\mathbf{G}\mathbf{G}'}(\mathbf{q}) [E - E_{n'',\mathbf{k}-\mathbf{q}} - \tilde{\omega}_{\mathbf{G}\mathbf{G}'}(\mathbf{q})]} v(\mathbf{q} + \mathbf{G}'). \end{aligned} \quad (2.82)$$

For materials without inversion symmetry, $\Omega_{\mathbf{G}\mathbf{G}'}^2(\mathbf{q})$ and $\tilde{\omega}_{\mathbf{G}\mathbf{G}'}(\mathbf{q})$ are not necessarily real, so slight corrections must be made to obtain real-valued eigenvalues [52, 53]. The basic structure holds, however: the screened exchange involves a sum over occupied bands, while the Coulomb hole involves an infinite sum over all bands in the system.

Having set up this machinery, we return to our actual goal: calculating quasiparticle energies and states. In principle, Equation 2.63 is entirely self-consistent, and swapping out the exchange–correlation functional for the self-energy produces a new set of wavefunctions. One could solve for them by starting with an initial guess based on DFT wavefunctions, constructing and diagonalizing the resulting energy-dependent Hamiltonian in some manner, and iterating until self-consistency is achieved, as is done for the electron density and Kohn–Sham wavefunctions in DFT (see Section 2.1). However, for most systems, the DFT

wavefunctions are a very good approximation to the quasiparticle wavefunctions [47], and it suffices to correct their energies by computing matrix elements of the *GW* Hamiltonian in the DFT basis:

$$E_{n\mathbf{k}}^{\text{QP}} = E_{n\mathbf{k}}^{\text{DFT}} + \langle n\mathbf{k} | \Sigma(E_{n\mathbf{k}}^{\text{QP}}) - V_{\text{xc}} | n\mathbf{k} \rangle. \quad (2.83)$$

This approach is a diagonal-only approximation to the Dyson equation. Typically, it is combined with the *single-shot GW* or G_0W_0 approach, in which both the Green's function and the screened Coulomb potential are constructed from the input (DFT) wavefunctions. The low number of self-energy matrix elements and the fact that the calculation is done in one shot combine to substantially reduce the required workload. The self-energy still depends self-consistently on the quasiparticle energies, but this dependence is close to linear [47] and can be well-approximated by taking a first-order expansion around the DFT energy values:

$$E_{n\mathbf{k}}^{\text{QP}} \approx E_{n\mathbf{k}}^{\text{DFT}} + \langle n\mathbf{k} | \Sigma(E_{n\mathbf{k}}^{\text{DFT}}) - V_{\text{xc}} | n\mathbf{k} \rangle + (E_{n\mathbf{k}}^{\text{QP}} - E_{n\mathbf{k}}^{\text{DFT}}) \left. \frac{\partial \langle n\mathbf{k} | \Sigma(E) | n\mathbf{k} \rangle}{\partial E} \right|_{E=E_{n\mathbf{k}}^{\text{DFT}}}. \quad (2.84)$$

Solving for the quasiparticle energies, we obtain

$$E_{n\mathbf{k}}^{\text{QP}} = E_{n\mathbf{k}}^{\text{DFT}} + \frac{1}{1 - \left. \frac{\partial \Sigma(E)}{\partial E} \right|_{E=E_{n\mathbf{k}}^{\text{DFT}}}} \langle n\mathbf{k} | \Sigma(E_{n\mathbf{k}}^{\text{DFT}}) - V_{\text{xc}} | n\mathbf{k} \rangle. \quad (2.85)$$

Up to a question of where to evaluate it along the energy axis, the prefactor $\left[1 - \frac{\partial \Sigma}{\partial E}\right]^{-1}$ is the quasiparticle renormalization factor Z of Fermi liquid theory [47]. We should always have $Z < 1$; when Z is close to 1, energy corrections are large and the system's collective excitations are well-described by the particle-like picture we are using here.

2.2.4 Excitons and optical absorption with the Bethe–Salpeter equation

Having discussed the use of the GW method to calculate quasiparticle energies, we now turn to the question of describing optical phenomena. The GW method does an excellent job of describing *single-particle* experiments such as X-ray or ultraviolet photoemission spectroscopy (XPS or UPS), in which an electron is removed from or added to a single energy level in a system [47]. However, optical absorption processes at lower energies often promote an excited electron to the conduction band, leaving a positively charged hole in the band that the electron vacates. Since the electron and hole have nonzero and opposite charges, they may form a bound state known as an *exciton*. Such two-particle processes are not fully treated by the one-body Green’s functions of Sections 2.2.2 and 2.2.3. As a result, theoretical absorption spectra computed within the RPA are often quite poor, even when corrected with GW quasiparticle energy levels [54].

The source of these problems is the correlation between the quantum states of the electron and the hole. We account for this correlation quantitatively using the *two-body* Green’s function, generally denoted by G_2 or, for historical reasons, L . L has a spectral representation analogous to Equation 2.54:

$$L(12; 1'2'; E) = i \sum_S \left[\frac{\chi_S(\mathbf{x}_1, \mathbf{x}'_1) \chi_S^*(\mathbf{x}'_2, \mathbf{x}_2)}{E - \Omega_S} - \frac{\chi_S(\mathbf{x}_2, \mathbf{x}'_2) \chi_S^*(\mathbf{x}'_1, \mathbf{x}_1)}{E + \Omega_S} \right], \quad (2.86)$$

where S indexes a set of electron–hole excitations with energies Ω_S whose two-particle wavefunctions can be expanded in terms of single-particle electron and hole states as

follows:

$$\chi_S(\mathbf{x}, \mathbf{x}') = \sum_v^{\text{occ}} \sum_c^{\text{emp}} \sum_{\mathbf{k}} \left[A_{vc\mathbf{k}}^S \psi_{c\mathbf{k}}(\mathbf{x}) \psi_{v\mathbf{k}}^*(\mathbf{x}') + B_{vc\mathbf{k}}^S \psi_{v\mathbf{k}}(\mathbf{x}) \psi_{c\mathbf{k}}^*(\mathbf{x}') \right]. \quad (2.87)$$

In the non-interacting case, the spectrum includes all possible valence–conduction transitions, and the non-interacting Green’s function L_0 can be written directly in terms of single-particle states:

$$L_0(12; 1'2'; E) = i \sum_{v,c} \left[\frac{\psi_c(\mathbf{x}_1) \psi_v^*(\mathbf{x}'_1) \psi_v(\mathbf{x}_2) \psi_c^*(\mathbf{x}'_2)}{E - (E_c - E_v)} - \frac{\psi_v(\mathbf{x}_1) \psi_c^*(\mathbf{x}'_1) \psi_c(\mathbf{x}_2) \psi_v^*(\mathbf{x}'_2)}{E + (E_c - E_v)} \right]. \quad (2.88)$$

L is subject to a Dyson equation analogous to Equation 2.57 called the Bethe–Salpeter equation (BSE):

$$L(12; 1'2') = L_0(12; 1'2') + \int d(3456) L_0(14; 1'3) K(35; 46) L(62; 52'), \quad (2.89)$$

in which the role previously held by the self-energy is played by the *interaction kernel* K . In the basis of the single-particle states of Equation 2.87, the kernel has a block-diagonal structure, with blocks K^{AA} and K^{BB} describing interactions among $A_{vc\mathbf{k}}^S$ terms and among $B_{vc\mathbf{k}}^S$ terms, respectively, and blocks K^{AB} and K^{BA} describing cross-couplings. However, the off-diagonal blocks are typically negligible in strength, so it is common to apply the Tamm–Dancoff approximation of setting $K^{AB} = K^{BA} = 0$ [54]. In this case, the information provided by the $B_{vc\mathbf{k}}^S$ terms turns out to be redundant, so we ignore them and focus on the

$A_{v\mathbf{c}\mathbf{k}}^S$ terms. Under these simplifications, the BSE is rendered as an eigenvalue problem:

$$(E_{c\mathbf{k}} - E_{v\mathbf{k}})A_{v\mathbf{c}\mathbf{k}}^S + \sum_{v'\mathbf{c}'\mathbf{k}'} K_{v\mathbf{c}\mathbf{k},v'\mathbf{c}'\mathbf{k}'}^{AA}(\Omega_S) A_{v'\mathbf{c}'\mathbf{k}'}^S = \Omega_S A_{v\mathbf{c}\mathbf{k}}^S, \quad (2.90)$$

where

$$K_{v\mathbf{c}\mathbf{k},v'\mathbf{c}'\mathbf{k}'}^{AA}(\Omega_S) \equiv i \int d(3456) \psi_{v\mathbf{k}}(\mathbf{x}_4) \psi_{c\mathbf{k}}^*(\mathbf{x}_3) K(35, 46; \Omega_S) \psi_{v'\mathbf{k}'}^*(\mathbf{x}_5) \psi_{c'\mathbf{k}'}(\mathbf{x}_6). \quad (2.91)$$

In the limit that $K = 0$, we see that Equation 2.90 is already diagonalized, with eigenvalues simply consisting of interband transition energies (which could be DFT energies or quasi-particle energies obtained from GW). The kernel is responsible for coupling between these transitions to produce correlated exciton states.

The BSE kernel can be calculated as a functional derivative of the Coulomb and self-energy interaction terms with respect to the one-particle Green's function [54]:

$$K(35; 46) = \frac{\delta [V_{\text{Coul}} \delta(3, 4) + \Sigma(3, 4)]}{\delta G(6, 5)}. \quad (2.92)$$

Applying the GW approximation and further assuming that the screened Coulomb interaction W is independent of G , this expression can be decomposed into two terms:

$$\begin{aligned} K(35; 46) = & -i \delta(3, 4) \delta(5^-, 6) v(3, 6) \\ & + i \delta(3, 6) \delta(4, 5) W(3^+, 4). \end{aligned} \quad (2.93)$$

These terms are labeled the *exchange term* K^x and the *direct term* K^d , respectively. The direct term provides most of the electron-hole attraction that produces bound states, while

the exchange term is spin-dependent and results in a splitting between singlet and triplet excitations. In the static limit, which is usually sufficient for describing solids but not necessarily atoms or molecules, the matrix elements are given by

$$K_{vc\mathbf{k},v'c'\mathbf{k}'}^{AA,x} = \int d\mathbf{x} d\mathbf{x}' \psi_{c\mathbf{k}}^*(\mathbf{x}) \psi_{v\mathbf{k}}(\mathbf{x}) v(\mathbf{r}, \mathbf{r}') \psi_{c'\mathbf{k}'}(\mathbf{x}') \psi_{v'\mathbf{k}'}^*(\mathbf{x}'), \quad (2.94)$$

$$K_{vc\mathbf{k},v'c'\mathbf{k}'}^{AA,d} = - \int d\mathbf{x} d\mathbf{x}' \psi_{c\mathbf{k}}^*(\mathbf{x}) \psi_{c'\mathbf{k}'}(\mathbf{x}) \psi_{v\mathbf{k}}(\mathbf{x}') \psi_{v'\mathbf{k}'}^*(\mathbf{x}') W(\mathbf{r}, \mathbf{r}'; E = 0). \quad (2.95)$$

However, upon transforming to a basis that decouples spin singlets and triplets, the kernel reduces to just K^d for each triplet state and $K^d + 2K^x$ for the singlet state, explaining the origin of the spin splitting.

Once constructed, Equation 2.90 can be diagonalized to obtain the exciton eigenstates $A_{vc\mathbf{k}}^S$ and their corresponding energy eigenvalues Ω_S . There is physical insight to be gained by studying the exciton wavefunctions in either real space or reciprocal space, but their most immediate experimental use is in the construction of a more accurate formula for the system's optical absorption spectrum, given by the imaginary part $\epsilon_2(\omega)$ of its dielectric function. In the RPA, the optical spectrum is given by [54]

$$\epsilon_2^{(0)}(\omega) = \frac{8\pi^2 e^2}{\omega^2} \sum_{vc\mathbf{k}} |\mathbf{e} \cdot \langle v\mathbf{k} | \mathbf{v} | c\mathbf{k} \rangle|^2 \delta(\omega - (E_{c\mathbf{k}} - E_{v\mathbf{k}})), \quad (2.96)$$

where \mathbf{e} is the polarization of the impinging light and $\mathbf{v} = i[H, \mathbf{r}]$ is the single-particle velocity operator. As mentioned, this spectrum is often qualitatively inconsistent with experiment. The absorption spectrum obtained from the BSE is analogous in structure but

encodes information about transitions to exciton states:

$$\epsilon_2(\omega) = \frac{8\pi^2 e^2}{\omega^2} \sum_S |\mathbf{e} \cdot \langle 0|\mathbf{v}|S\rangle|^2 \delta(\omega - \Omega_S), \quad (2.97)$$

where the excitonic optical transition matrix is computed in terms of hole–electron transitions:

$$\langle 0|\mathbf{v}|S\rangle = \sum_{v\mathbf{k}} A_{v\mathbf{k}}^S \langle v\mathbf{k}|\mathbf{v}|c\mathbf{k}\rangle. \quad (2.98)$$

There are several ways to compute the non-interacting transition matrix elements, but in crystals the simplest derives from $\mathbf{k} \cdot \mathbf{p}$ perturbation theory. For a small but finite reciprocal-space shift \mathbf{q} , the matrix elements are given by

$$\langle v\mathbf{k}|\mathbf{v}|c\mathbf{k}\rangle = (E_{c\mathbf{k}} - E_{v\mathbf{k}}) \lim_{\mathbf{q} \rightarrow 0} \frac{\langle v\mathbf{k} + \mathbf{q}|e^{i\mathbf{q}\cdot\mathbf{r}}|c\mathbf{k}\rangle}{q}. \quad (2.99)$$

Other schemes are possible, but they must account for subtleties involving the commutator $[V_{\text{ps}}, \mathbf{r}]$ of the possibly-nonlocal pseudopotential with the position operator, as well as a renormalization of the transition matrix element that appears when quasiparticle energy corrections are applied [54]. These corrections are handled implicitly in $\mathbf{k} \cdot \mathbf{p}$ theory.

2.2.5 *GW* calculations

GW and *GW*-BSE calculations yield accurate results, but at substantial computational cost. The computational work of a DFT calculation generally scales with N^3 , where N is the number of atoms in the system. In contrast, the work needed for the *GW* method typically scales with N^4 , while post-processing with the BSE often scales with N^6 . In practice, the *GW* step is usually the more expensive of the two, since the number of bands it requires

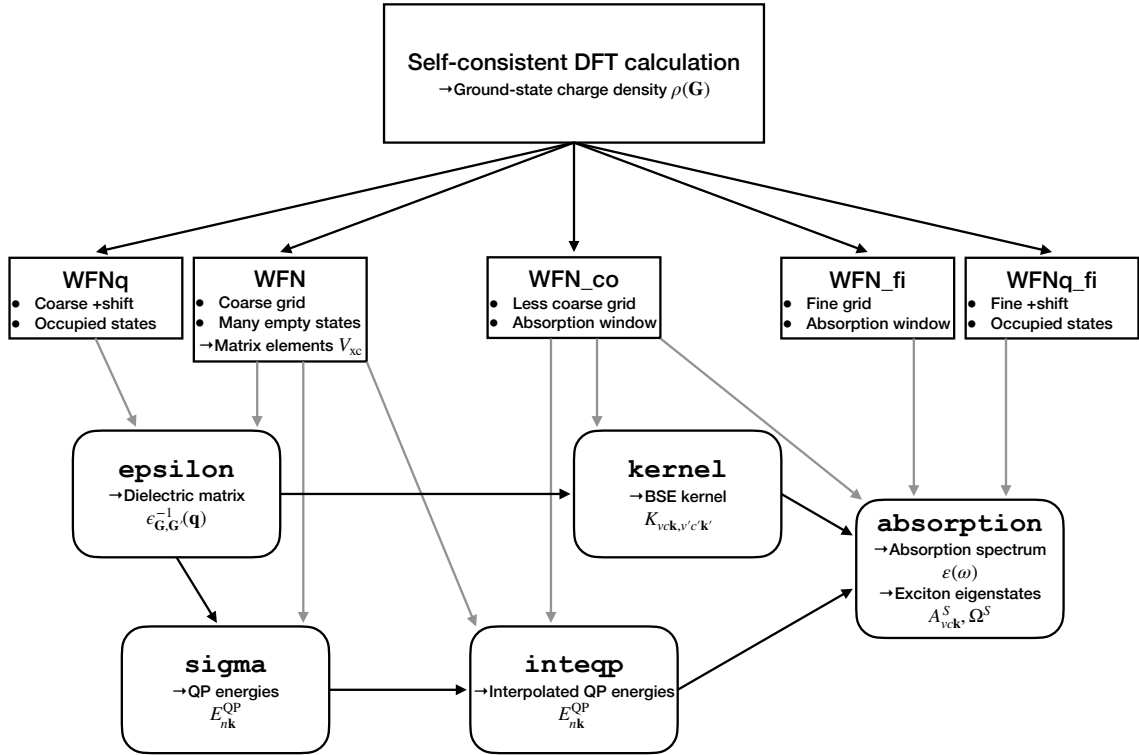


Figure 2.2: Flowchart of steps for performing a *GW*-BSE calculation. A mean-field technique such as DFT should be used to generate the WFN, WFNq, WFN_fi, WFNq_fi, and (optionally) WFN_co files. Quasiparticle energies are generated using the `epsilon`, `sigma`, and (optionally) `inteqp` executables, while *GW*-BSE calculations are done with the `kernel` and `absorption` executables.

can be orders of magnitude higher. Even so, the rapid scaling of the BSE step may mean that only a few eV of an absorption spectrum can be satisfactorily converged without a very expensive calculation.

In Chapter 8, we perform *GW* and *GW*-BSE calculations on systems with up to 45 atoms. Some of these systems are 2D slabs that require vacuum spacing at least as large as the slab itself (see discussion of Coulomb truncation below). Since the number of \mathbf{G} -vectors in the system scales with the total unit cell volume, these 2D systems effectively have ~ 100 atoms for the purposes of some terms in the *GW* calculation. To handle these calculations, we use BerkeleyGW [53], a software package designed to scale efficiently to massively parallel calculations.

BerkeleyGW breaks the *GW*-BSE workflow down into four main executables:

1. `epsilon` calculates $\epsilon_{\mathbf{G}\mathbf{G}'}(\mathbf{q})$ and $\epsilon_{\mathbf{G}\mathbf{G}'}^{-1}(\mathbf{q})$ via the Adler–Wiser polarizability sum of Equation 2.73. Minimally, it computes the static $\omega = 0$ dielectric matrix, but it can also do finite- ω calculations.
2. `sigma` calculates quasiparticle energies $E_{n\mathbf{k}}^{\text{QP}}$ from an expression such as Equation 2.85, using Equations 2.81 and 2.82 (or equivalent expressions for a frequency model other than the GPP) to compute the self-energy. In addition to interpolating with Equation 2.85, `sigma` can apply a static “scissors” shift to DFT energies or be run multiple times to achieve self-consistency.
3. `kernel` calculates the matrix elements $K_{v\mathbf{k},v'\mathbf{c}'\mathbf{k}'}$ of the BSE kernel on a coarse grid of \mathbf{k} -points using reciprocal-space forms of Equations 2.94 and 2.95.
4. `absorption` interpolates the BSE kernel to a finer grid of \mathbf{k} -points, diagonalizes it to obtain exciton states $A_{v\mathbf{k}}^S$ and energies Ω_S , and computes the optical absorption

spectrum $\epsilon_2(\omega)$.

Figure 2.2 shows how these steps interact with one another, as well as with preceding DFT calculations. Both `epsilon` and `sigma` use a large number of unoccupied DFT states on a relatively coarse **k**-grid. `epsilon` also uses occupied states on a slightly shifted coarse grid to calculate its $\mathbf{q} \rightarrow \mathbf{0}$ terms in a non-divergent way, while `sigma` depends on the DFT calculation to provide V_{xc} matrix elements for Equation 2.85 and the charge density $\rho(\mathbf{G})$ for the GPP. `kernel` can use the same coarse grid as the *GW* steps, but if the *GW* step is prohibitively expensive, it may be useful to run `sigma` on a very coarse grid and then interpolate to an intermediate grid (WFN_co in Figure 2.2) using the auxiliary `inteqp` executable. In that case, `epsilon` and `kernel` must be run on the intermediate grid. `absorption` uses DFT calculations on both the grid used by `kernel` and the finer grid to which it interpolates the kernel; in each case it needs enough unoccupied states to capture all interband transitions in the intended energy window of the absorption spectrum. Finally, `absorption` also uses a shifted set of occupied states to calculate the RPA matrix elements from Equation 2.99.

2.2.6 Scaling *GW* calculations to large systems

This section reviews various considerations that are important for efficiently performing plane-wave *GW* calculations in large-scale systems.

Memory usage

The limiting factor in large-scale *GW* calculations is often not processor time, but rather the memory needed to store the calculation’s enormous wavefunctions, polarizability matrices, and Bethe–Salpeter kernels. Therefore, we want to take a moment to discuss how memory

usage in BerkeleyGW depends on parallelization of the calculation. Some steps, such as the summation in Equation 2.73 that computes the polarizability, are distributed over the entire set of CPUs in a block-cyclic manner [53]. This requires intermittent MPI communication between cores but allows the total memory usage to be essentially fixed. As a result, the memory per core needed for this step decreases linearly with the number of cores.

Other steps are more complicated, however. The `epsilon` executable provides a case study in large-scale parallelization [53]. The first task carried out by `epsilon` is to compute a large number of matrix elements of the following form:

$$M_{nn'}(\mathbf{k}, \mathbf{q}, \mathbf{G}) = \langle n\mathbf{k} + \mathbf{q} | e^{i(\mathbf{q}+\mathbf{G})\cdot\mathbf{r}} | n'\mathbf{k} \rangle, \quad (2.100)$$

where n is the index of an occupied band, n' is the index of an unoccupied band, \mathbf{k} and \mathbf{q} are points in the Brillouin zone, and \mathbf{G} is a reciprocal lattice vector. These matrix elements first appear when evaluating Equation 2.73, but are used at several points throughout the *GW* calculation. The computation is distributed among the N_p processors by grouping them into P_v “pools,” each of which is responsible for a fraction of the valence bands. Each of the $P_c = N_p/P_v$ processors in a pool is then assigned some share of the conduction bands. If there are N_v valence bands and N_c conduction bands ($N_c \gg N_v$), then each processor must compute matrix elements that couple roughly N_v/P_v valence bands to N_c/P_c conduction bands. If the memory required to store a single band is m_0 , then the memory needed to store a single processor’s wavefunctions is

$$M_p = m_0 \left(\frac{N_v}{P_v} + \frac{N_c}{P_c} \right) = m_0 \left(\frac{N_v}{P_v} + \frac{N_c P_v}{N_p} \right), \quad (2.101)$$

Table 2.1: Optimal memory distribution for the BerkeleyGW `epsilon` code in both the low-parallelization ($N_p < N_c/N_v$) and high-parallelization ($N_p \gg N_c/N_v$) limits.

	$N_p < N_c/N_v$	$N_p \gg N_c/N_v$
Number of valence pools, P_v	1	$\sqrt{\frac{N_v N_p}{N_c}}$
Average memory per processor, M_p	$m_0 \left(N_v + \frac{N_c}{N_p} \right)$	$2m_0 \sqrt{\frac{N_v N_c}{N_p}}$
Total memory, M_{tot}	$m_0 (N_v N_p + N_c)$	$2m_0 \sqrt{N_v N_c N_p}$

and the total memory used is

$$M_{\text{tot}} = N_p M_p = m_0 \left(\frac{N_v N_p}{P_v} + N_c P_v \right). \quad (2.102)$$

For a large, fixed number of processors, the memory usage per processor is minimized when

$$\frac{dM_p}{dP_v} = m_0 \left(-\frac{N_v}{P_v^2} + \frac{N_c}{N_p} \right) = 0, \quad (2.103)$$

which yields

$$P_v \approx \sqrt{\frac{N_v N_p}{N_c}}. \quad (2.104)$$

This choice splits the memory each processor evenly between valence and conduction bands.

However, it is only a coherent prescription for $N_p > N_c/N_v$; otherwise we are obligated to choose $P_v = 1$.

The memory per processor and total memory in each regime are shown in Table 2.1. We see that M_p scales roughly with $1/N_p$ for small N_p , but the scaling softens to $1/\sqrt{N_p}$ as N_p becomes larger. In addition, the total memory usage is not fixed, but grows with N_p even for a small number of processors. Therefore, when performing a calculation on an entire node, a choice must be made between efficient memory usage (distributing the

node's entire memory to just a few processors) and performance (using more of the node's processors).

Converging sums with the static Coulomb hole remainder

In principle, both the static dielectric matrix (Equation 2.74) and the Coulomb hole portion of the self-energy (Equation 2.82) involve infinite sums over unoccupied states, which converge slowly with the number of terms in the sum. Various approaches have been developed to alleviate this problem. Some authors have proposed linear-response methods that avoid the need to sum over empty states altogether [55, 56], while other have proposed schemes for approximating the contribution from the truncated remainder in closed form [57, 58, 59]. In this dissertation, we use a particularly simple and effective remainder term first proposed by Deslippe et al. called the static Coulomb hole (CH) approximation [60]. With this remainder added, sums can be converged with an order of magnitude fewer explicitly included terms, greatly reducing the cost of calculations.

The static CH approximation focuses on the Coulomb hole self-energy sum, since it generally converges more slowly than the dielectric screening matrix. It is based on the “static” (energy-independent) expression for the Coulomb hole, whose first N terms are

$$\begin{aligned} \langle n\mathbf{k} | \Sigma_{\text{CH}}^{\text{Coh}/N}(\mathbf{r}, \mathbf{r}'; 0) | n'\mathbf{k} \rangle &= \frac{1}{2} \sum_{n''}^N \sum_{\mathbf{q}\mathbf{G}\mathbf{G}'} \langle n\mathbf{k} | e^{i(\mathbf{q}+\mathbf{G})\cdot\mathbf{r}} | n''\mathbf{k} - \mathbf{q} \rangle \langle n''\mathbf{k} - \mathbf{q} | e^{-i(\mathbf{q}+\mathbf{G}')\cdot\mathbf{r}'} | n'\mathbf{k} \rangle \\ &\quad \times [\epsilon_{\mathbf{G}\mathbf{G}'}^{-1}(\mathbf{q}; E=0) - \delta_{\mathbf{G}\mathbf{G}'}] v(\mathbf{q} + \mathbf{G}'). \end{aligned} \quad (2.105)$$

The key insight is that, when $N \rightarrow \infty$, the sum over n'' can be eliminated by applying a

completeness relation:

$$\langle n\mathbf{k} | \Sigma_{\text{CH}}^{\text{Coh}/\infty}(\mathbf{r}, \mathbf{r}') | n'\mathbf{k} \rangle = \frac{1}{2} \sum_{\mathbf{q}\mathbf{G}\mathbf{G}'} \langle n\mathbf{k} | e^{i(\mathbf{G}-\mathbf{G}')\cdot\mathbf{r}} | n'\mathbf{k} \rangle [\epsilon_{\mathbf{G}\mathbf{G}'}^{-1}(\mathbf{q}; 0) - \delta_{\mathbf{G}\mathbf{G}'}] v(\mathbf{q} + \mathbf{G}'). \quad (2.106)$$

This fact was already discussed in Section 2.2.3 to provide a physical interpretation for the name “Coulomb hole.” The difference between Equations 2.106 and 2.105 is the static remainder—the contribution that the omitted bands would have made to the Coulomb hole energy had they been included. Since the matrix elements in Equation 2.105 must already be computed for the GPP Coulomb hole self-energy, this remainder can be calculated in a non-static calculation at essentially no additional cost. The static CH correction that results is the following, where Σ_{CH}^N is the standard GPP self-energy from Equation 2.82 with N terms evaluated:

$$\begin{aligned} \langle n\mathbf{k} | \Sigma_{\text{CH}}^{\infty}(\mathbf{r}, \mathbf{r}'; E) | n'\mathbf{k} \rangle &= \langle n\mathbf{k} | \Sigma_{\text{CH}}^N(\mathbf{r}, \mathbf{r}'; E) | n'\mathbf{k} \rangle \\ &+ \frac{1}{2} \left(\langle n\mathbf{k} | \Sigma_{\text{CH}}^{\text{Coh}/\infty}(\mathbf{r}, \mathbf{r}'; 0) | n'\mathbf{k} \rangle - \langle n\mathbf{k} | \Sigma_{\text{CH}}^{\text{Coh}/N}(\mathbf{r}, \mathbf{r}') | n'\mathbf{k} \rangle \right). \end{aligned} \quad (2.107)$$

The factor of $1/2$ is included for consistency with previous work by Kang and Hybertsen [59].

In our experience, including the static Coulomb hole remainder brings convergence of the CH summation roughly in line with the convergence of the dielectric function. It is used in all the GW calculations cited in this dissertation.

State generation with simple approximate physical orbitals (SAPOs)

The cost of calculating sums over unoccupied states can be further reduced if the wave-functions themselves can be generated cheaply. To construct N states in DFT, we must

extract the N lowest eigenvalues and their eigenstates from the Kohn–Sham equations at every \mathbf{k} -point of interest. As N grows into the thousands for large systems treated with GW , this task becomes daunting even if efficient iterative diagonalization techniques are used. Fortunately, this is overkill. The states high in the continuum that must be accounted for in GW calculations are well approximated by individual plane waves, even in the vicinity of ionic cores [61]. As a result, various schemes have been proposed to simply replace them with plane waves in GW calculations. We discuss one of these schemes, dubbed the simple approximate physical orbital (SAPO) approach by its creators [61].

In solid materials, the SAPO approach supplements a modest number of explicitly-calculated DFT states with plane-wave continuum orbitals. The energy of the plane-wave state $\psi_{n\mathbf{k}}(\mathbf{r}) = \exp[i(\mathbf{k} + \mathbf{G}) \cdot \mathbf{r}]$, where \mathbf{k} lies in the first Brillouin zone and \mathbf{G} is a reciprocal lattice vector, is initially estimated by

$$\varepsilon_{n\mathbf{k}} = \langle V_{\text{DFT}} \rangle + (\mathbf{k} + \mathbf{G})^2, \quad (2.108)$$

where $\langle V_{\text{DFT}} \rangle$ is the averaged DFT potential and $(\mathbf{k} + \mathbf{G})^2$ is the plane wave’s kinetic energy in Rydberg atomic units. When combined with the actual DFT states, these states form an overcomplete basis, so they must be orthogonalized. The collection of states is sorted by energy eigenvalue and the Gram–Schmidt process is applied to produce a new set of orthonormal wavefunctions $\Psi_{n\mathbf{k}}$. This set includes both the original DFT states and a new orthogonalized set of plane-wave-like states, the latter of which are the technique’s namesake SAPOs. To assign energies to the new states, two assumptions are made: (1) the energies $\varepsilon_{n\mathbf{k}}$ assigned in Equation 2.108 are the matrix elements of the Hamiltonian in the plane-wave basis, $\langle \psi_{n\mathbf{k}} | \hat{H} | \psi_{n\mathbf{k}} \rangle = \varepsilon_{n\mathbf{k}}$, and (2) the new wavefunctions $\Psi_{n\mathbf{k}}(\mathbf{r})$ are eigenstates

of the Hamiltonian. Neither of these assumptions is exactly true, but assuming them allows one to assign a reasonable value for the SAPO energy eigenvalues:

$$\begin{aligned}
E_{n\mathbf{k}} &= \langle \Psi_{n\mathbf{k}} | H | \Psi_{n\mathbf{k}} \rangle \\
&= \varepsilon_{n\mathbf{k}} + \frac{\sum_{m=1}^{n-1} |\langle \Psi_{m\mathbf{k}} | \psi_{n\mathbf{k}} \rangle|^2 (\varepsilon_{n\mathbf{k}} - E_{m\mathbf{k}})}{1 - \sum_{m=1}^{n-1} |\langle \Psi_{m\mathbf{k}} | \psi_{n\mathbf{k}} \rangle|^2}.
\end{aligned} \tag{2.109}$$

As long as enough DFT wavefunctions are included to account for states with substantial atomic character, this procedure accurately reproduces energy eigenvalues. It also allows converged *GW* results to be obtained for dramatically less computational cost in the DFT step.

In this dissertation, SAPOs are used in all *GW* calculations with more than ~ 10 atoms. Typically, at least 15 Ry of DFT states are calculated by iterative diagonalization of the Kohn–Sham Hamiltonian, and SAPOs are used for the remaining states.

Handling low-dimensional systems with Coulomb truncation and nonuniform neck subsampling (NNS)

The materials described in this dissertation are either two-dimensional (2D) or quasi-two-dimensional (quasi-2D), surrounded in principle by a semi-infinite substrate beneath and a semi-infinite vacuum above. However, they are treated in plane-wave DFT and *GW* calculations by assuming periodic boundary conditions, meaning that they are surrounded by an infinite number of copies of themselves in the vertical direction. It is important to ensure that these periodic copies do not interact in unphysical ways. Electronic wavefunctions decay exponentially in vacuum, so overlap between electronic states can be eliminated with a modest amount of layer spacing. However, long-range Coulomb interactions can be

substantial, especially when describing spatially separated holes and electrons.

The typical remedy is to truncate the Coulomb interaction in the confined direction. For a slab geometry this takes the form

$$v^{\text{sl}}(\mathbf{r}) = \frac{\theta(z_c - |z|)}{r} \quad (2.110)$$

for some truncation length z_c . Sharp truncations like this can present problems in reciprocal space due to ringing effects. For example, the Fourier transform of Equation 2.110 is

$$v^{\text{sl}}(\mathbf{k}) = \frac{4\pi}{k^2} \left\{ 1 + e^{-k_{xy}z_c} \left[\frac{k_z}{k_{xy}} \sin(k_z z_c) - \cos(k_z z_c) \right] \right\}, \quad (2.111)$$

where $k_{xy} = \sqrt{k_x^2 + k_y^2}$. For general z_c , this expression diverges for $k_z \neq 0$ and $k_{xy} \rightarrow 0$, whereas before the potential only diverged for $k \rightarrow 0$. Ismail-Beigi [62] noted that this problem can be avoided by choosing $z_c = L_z/2$, where L_z is the periodicity in the z -direction. This is because when \mathbf{k} is a reciprocal lattice vector we have $k_z = \pi n_z / z_c = 2\pi n_z / L_z$ for some integer n_z , and hence $\sin(k_z z_c) = 0$. The problematic term in Equation 2.111 drops out, and we have

$$v^{\text{sl}}(\mathbf{k}) = \frac{4\pi}{k^2} \left[1 - e^{-k_{xy}z_c} \cos(k_z z_c) \right], \quad (2.112)$$

This expression is finite as $k_{xy} \rightarrow 0$ for $k_z \neq 0$, and diverges as $1/k$ for $k_z = 0$, a softer divergence than the $1/k^2$ behavior seen in the 3D case. Thus, calculations using the Ismail-Beigi truncation scheme are generally well-behaved.

However, slab Coulomb truncation does not fully handle anomalous 2D behavior. The “neck” elements of the inverse dielectric matrix $\epsilon_{\mathbf{G}\mathbf{G}'}^{-1}(\mathbf{q})$ (*i.e.*, elements for reciprocal lattice vectors $\mathbf{G}_\perp, \mathbf{G}'_\perp$ in the confined direction) display sharp structure as $q \rightarrow 0$. In particular,

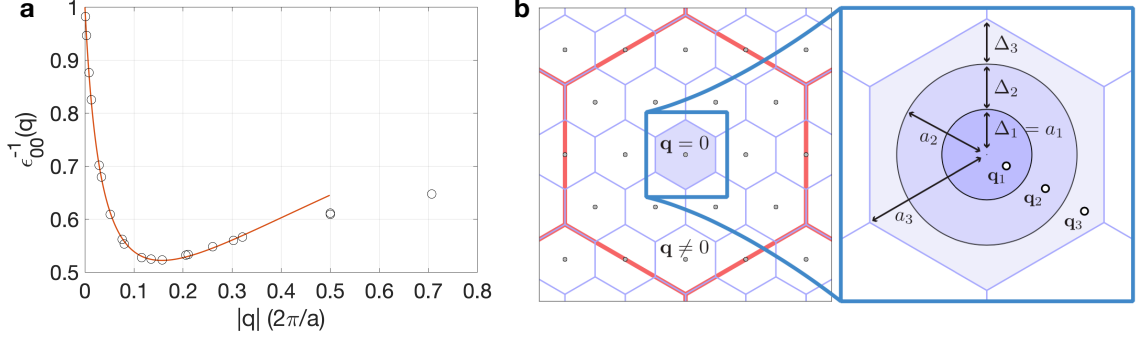


Figure 2.3: Low- q behavior of the inverse dielectric matrix. **(a)** Static inverse dielectric constant $\epsilon_{00}^{-1}(\mathbf{q})$ plotted as a function of $|\mathbf{q}|$ for a slab of Mg_2TiO_4 on an MgO substrate (see Chapter 8). The blue line is a fit of the form $1/\epsilon_{00}^{-1}(\mathbf{q}) = 1 + \gamma|\mathbf{q}|^2 v^{\text{sl}}(\mathbf{q}) \exp(-\alpha|\mathbf{q}|)$ used in [62]. As in all 2D materials, the inverse dielectric constant is exactly 1 at $\mathbf{q} = \mathbf{0}$, but for finite \mathbf{q} it quickly drops by nearly 50% before recovering. **(b)** Schematic of the subsampling scheme used to partition the $\mathbf{q} = \mathbf{0}$ Voronoi cell into annuli, taken from [63].

the $\mathbf{G} = \mathbf{G}' = \mathbf{0}$ entry exhibits a steep drop and local minimum at low q (Figure 2.3(a)).

As a result, GW observables like quasiparticle energies and ionization potentials converge slowly with the size of the \mathbf{k} -grid.

da Jornada, Qiu, and Louie [63] proposed a clever solution to this issue that involves *subsampling* the Voronoi cell of the Brillouin zone surrounding $\mathbf{q} = \mathbf{0}$. Their procedure divides the $\mathbf{q} = \mathbf{0}$ cell into N_s annular regions and selects a point \mathbf{q}_s within each region at which $\epsilon_{\mathbf{G}\mathbf{G}'}(\mathbf{q}_s)$ is calculated (Figure 2.3(b)). Then, the $\mathbf{q} = \mathbf{0}$ neck matrix elements of the screened Coulomb potential are calculated by

$$W_{\mathbf{G}\mathbf{G}'}^{\text{sub}}(\mathbf{q} = \mathbf{0}, \omega) = \sum_{s=1}^N w_s \epsilon_{\mathbf{G}\mathbf{G}'}^{-1}(\mathbf{q}_s, \omega) v(\mathbf{q}_s + \mathbf{G}'), \quad (2.113)$$

where w_s is a weight equal to the fraction of the Voronoi cell area covered by annulus s .

This procedure, dubbed “nonuniform neck subsampling,” or NNS, accelerates convergence with respect to \mathbf{q} -grid size in a dramatic fashion. For bilayer MoSe_2 , the band gap can be converged to within 10 meV using a $6 \times 6 \times 1$ \mathbf{q} -grid with $N_s = 10$ subsampled points [63].

For comparison, a uniform calculation on a $36 \times 36 \times 1$ requires two orders of magnitude more computer time to get a result with 40 meV of error.

In this dissertation, the Ismail-Beigi slab truncation scheme is used for all GW calculations on two-dimensional materials. We note when we use nonuniform neck subsampling, and compare the results to those obtained using a uniform \mathbf{q} -grid where appropriate.

Chapter 3

Epitaxial binding and strain effects in monolayer stanene on the $\text{Al}_2\text{O}_3(0001)$ surface

This chapter is adapted from an article originally entitled “Structure and binding of stanene on the $\text{Al}_2\text{O}_3(0001)$ surface” co-authored with Sohrab Ismail-Beigi that has been submitted for publication [64]. I performed the calculations and did the analysis, and SIB provided guidance.

Stanene, the two-dimensional monolayer form of tin, has been predicted to be a 2D topological insulator due to its large spin-orbit interaction. However, a clear experimental demonstration of stanene’s topological properties has eluded observation, in part because of the difficulty of choosing a substrate on which stanene will remain topologically nontrivial. In this chapter, we present first-principles density functional theory (DFT) calculations of epitaxial monolayer stanene grown on the (0001) surface of alumina, Al_2O_3 , as well as free-standing decorated stanene under strain. By describing the energetics and nature of how monolayer stanene binds to alumina, we show a strong energetic drive for the monolayer to be coherently strained and epitaxial to the substrate. By analyzing the electronic structure of strained stanene, we find it to be a quantum spin Hall insulator on Al_2O_3 .

3.1 Introduction

Two-dimensional topological insulators (2DTIs) have received attention in recent years due to their potential for hosting robust symmetry-protected current-carrying edge states [65]. The buckled hexagonal monolayer form of tin, known as stanene, is of particular interest [66, 67] since its band gap (~ 0.1 eV) is large enough for room-temperature applications [68, 6]. Stanene's band gap can be further enhanced by functionalization, in particular with halogen atoms. Proposed uses of stanene include spintronic nanoribbon devices [69, 70], tunable field-effect transistors [71], a surface for adsorption of molecules including CH_2O , CH_4 , CO , NO , N_2O , and NH_3 [72, 73], and the possibility of room-temperature demonstration of the quantum spin Hall effect [6, 74] and quantum anomalous Hall effect [75, 76, 77].

However, the electronic structure of epitaxial stanene is sensitive to both strain and surface interactions, so choosing an appropriate substrate is vital [78]. Stanene is metallic on many substrates, including $\text{Ag}(111)$ [79, 80], $\text{Au}(111)$ [81, 82], $\text{Sb}(111)$ [83], and $\text{Bi}_2\text{Te}_3(111)$ [84, 85, 86]. Ultraflat stanene grown on $\text{Cu}(111)$ shows evidence of nontrivial edge states but is metallic overall [87], while buckled stanene on $\text{PbTe}(111)$ is gapped but is topologically trivial (*i.e.*, non-topological) due to in-plane compressive strain [88]. $\text{InSb}(111)$ is a promising substrate for globally gapped topological stanene, though reported results remain somewhat inconclusive [89, 90]. A larger suite of potential stanene substrates is important to enable robust continued work.

Alumina (Al_2O_3) is a wide-gap insulator whose growth is well-characterized and commonly performed. Cleaved along its (0001) surface, alumina has a surface lattice parameter within a few percent of the free-standing stanene lattice parameter. Previous work has

examined one possible structure for stanene on Al_2O_3 and elucidated basic aspects of the resulting electronic bands [91, 92]. In this chapter, we describe several critical results regarding the structure, stability, and topological character of stanene on alumina: hexagonal stanene (the assumed structure in the prior works) is indeed stabilized on stanene compared to other structures that are favored as isolated 2D sheets, the strength of the binding of stanene to the alumina surface turns out to be surprisingly large, the binding is strong enough to create an epitaxial 2D layer of stanene on alumina, and the resulting electronic bands of the heterostructure show a large gap as well as the desired topological character of a quantum spin Hall insulator. We end with an outlook for the potential of stanene synthesis on alumina.

3.2 Methods

We performed density functional theory (DFT) calculations using the Quantum ESPRESSO software package [93, 94]. We used fully relativistic projector augmented-wave (PAW) pseudopotentials with spin-orbit interaction, along with the Perdew-Burke-Ernzerhof (PBE) generalized gradient approximation to the exchange-correlation functional [20]. We used a plane-wave basis set with a wavefunction energy cutoff of 680 eV and a charge density plane wave cutoff of 6,800 eV, and we relaxed atomic positions until all axial forces were below 2.5×10^{-3} eV/Å. We performed additional calculations with the same parameters and a hybrid exchange-correlation functional using the VASP software [95, 23, 24]. We performed calculations at the theoretical relaxed lattice parameters of bulk alumina; however, since the Quantum ESPRESSO version we used does not perform automated variable-cell relaxations with fully relativistic pseudopotentials, those lattice parameters were found by

atomically relaxing bulk structures on a grid of lattice parameter values and fitting to find the minimum in energy. We estimate that this is equivalent to performing an automated variable-cell relaxation until all uniaxial stresses are below 5 kbar. Calculations used a $12 \times 12 \times 1$ \mathbf{k} -point mesh and 14 meV of Gaussian thermal broadening.

We carried out substrate-based calculations on an Al-terminated slab of Al_2O_3 cleaved along the (0001) surface. In-plane lattice parameters were taken from a theoretical relaxation of bulk Al_2O_3 , which yielded a lattice parameter of 4.792 Å. We included four stoichiometric layers of the Al_2O_3 slab to ensure convergence in atomic positions and formation energies. We placed monolayers of stanene on both surfaces of a symmetric alumina slab to retain inversion symmetry and avoid the need for a dipole correction in the vacuum. We used the Grimme DFT-D2, DFT-D3, and Becke–Johnson XDM semiempirical functionals to investigate the robustness of our results against noncovalent interactions between the substrate and the stanene overlayer [96, 97, 98, 99, 100].

For isolated 2D tin-based monolayers, we computed topological characters from occupied band parities at time-reversal invariant momenta using the method of Fu and Kane [101]. To compute the topological invariant for bound stanene, we removed one stanene monolayer from one side of the alumina slab and used the Wannier charge center method of Soluyanov and Vanderbilt [28], as implemented in the WannierTools package [34] using maximally localized Wannier functions from the Wannier90 package [33]. This approach breaks the inversion symmetry that was present before, but the resulting electric dipole is quite small and does not affect the states near the Fermi energy.

Table 3.1: Structural data for free-standing stanene in its bare, hydrogenated, and fluorinated forms.

	Bare stanene	Hydrogenated stanene	Fluorinated stanene
Lattice parameter a (Å)	4.68	4.72	5.02
Sn–Sn buckling b (Å)	0.85	0.82	0.53
Sn–Sn bond length d (Å)	2.83	2.85	2.95
Band gap (eV)	0.069	0.214	0.306
Topological insulator?	YES	NO	YES

3.3 Results

3.3.1 Free-standing stanene monolayers

We performed variable-cell structural relaxations for free-standing monolayers of bare stanene, as well as fully functionalized fluorinated stanene (SnF) and hydrogenated stanene (SnH). In each calculation, both the lattice parameter and the atomic positions were relaxed to minimize stresses and forces. Each structure is “low-buckled,” with a unit cell containing two vertically-displaced Sn atoms. The optimal structural parameters and DFT-PBE band gap, shown in Table 3.1, are in good agreement with previous results [6]. According to the Fu–Kane method [101], bare and fluorinated stanene are topological insulators, while hydrogenated stanene is a trivial insulator. The topological properties of each of these freestanding materials are examined in greater detail in Section 3.3.6 below.

3.3.2 Bound low-buckled structure

For our substrate-bound calculations, we focused on undecorated stanene. When bound epitaxially to alumina, low-buckled stanene retains its basic structure but is under $\sim 2.4\%$ tensile strain. We found that the most stable structures are obtained when Sn atoms are

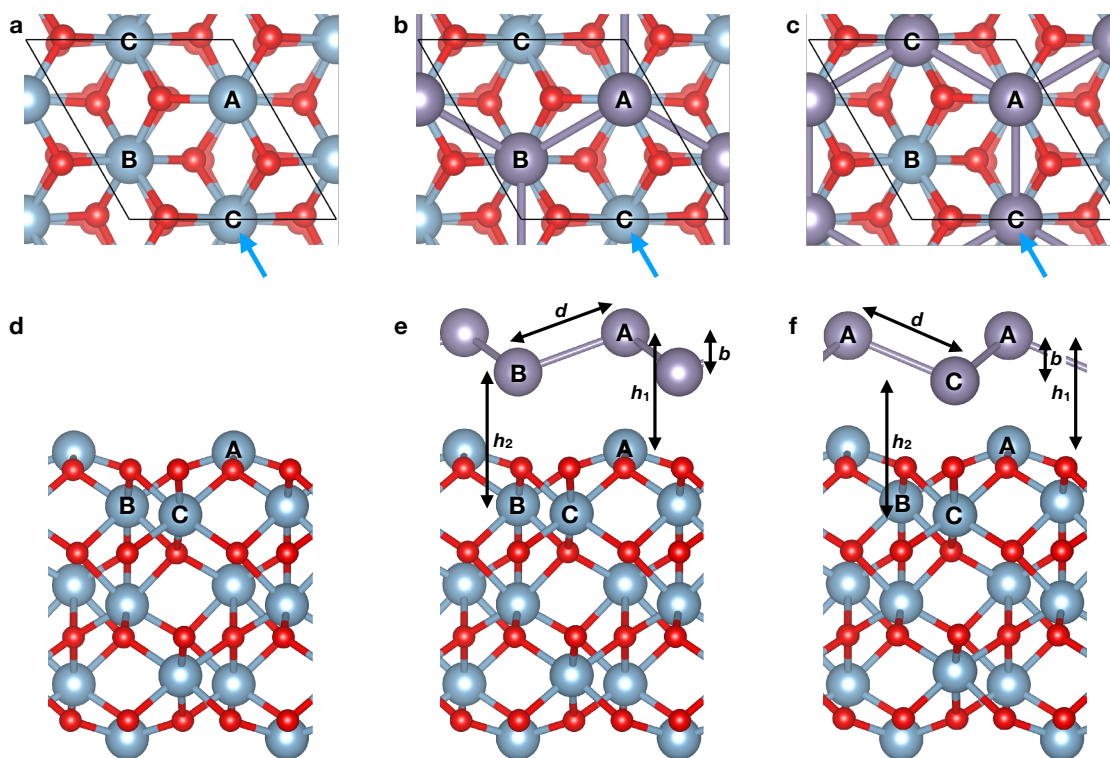


Figure 3.1: (a,d) Top (a) and side (d) views of the bare $\text{Al}_2\text{O}_3(0001)$ slab used as a substrate. The three inequivalent exposed Al atoms are labeled A, B, and C. The blue arrow in (a) indicates the viewing direction of panels (d-f). (b,e) Top (b) and side (e) views of second-most-stable registry choice A/B for stanene on Al_2O_3 , placing the upper and lower Sn atoms in positions A and B, respectively. Black arrows in (e) label the bond length d , the buckling b , and the vertical binding distances h_1 and h_2 , whose values are found in Table 3.2. (c,f) Top (c) and side (f) views of the most stable registry choice A/C for stanene on Al_2O_3 , placing the upper and lower Sn atoms in positions A and C, respectively.

Table 3.2: Structural and energetic information for the two most favorable registries of stanene on Al_2O_3 . See Figure 3.1 for definitions of b , d , h_1 and h_2 .

	A/B structure	A/C structure
Buckling b (Å)	1.03	1.18
Bond length d (Å)	2.95	3.01
Binding distance h_1 (Å)	3.06	2.90
Binding distance h_2 (Å)	3.43	3.47
Binding energy E_b per unit cell (eV):		
no van der Waals functional	0.31	0.50
Grimme DFT-D2 functional [96]	1.02	1.23
Grimme DFT-D3 functional [98]		0.84
XDM functional [99, 100]		1.16
Band gap (eV)	0.247	0.263

placed atop Al atoms.

The Al-terminated alumina slab has three exposed aluminum atoms per unit cell, which are labeled A, B, and C in Figure 3.1(a). Atom A terminates the slab, while atoms B and C are roughly coplanar (~ 0.2 Å vertical separation) and located under a layer of oxygen atoms. We examined a 3×3 grid of possibly registry alignments for stanene within the alumina unit cell, each of which permits two structures that are obtained by swapping the up-buckled and down-buckled Sn atoms. We relaxed the atomic positions in each of these 18 inequivalent stanene-on-alumina registries. The two most favorable registries, shown in Figures 3.1(b) and 3.1(c), place the upper tin atom directly over atom A and the lower tin atom directly over either atom B or C. The structural parameters, binding energies, and DFT-PBE band gaps of the two favorable structures are found in Table 3.2. The A/C structure is the most energetically favored by a margin of at least 0.24 eV per two-atom stanene unit cell. This structure, which was predicted by similar previous work [91, 92], will be taken as the ground state structure.

3.3.3 Binding energy and van der Waals functionals

The binding energy E_b equals the total energy of the bound stanene-substrate complex E_{bound} , minus the sum of the energies of the free-standing stanene layer E_{stanene} and the bare alumina slab $E_{\text{Al}_2\text{O}_3}$:

$$E_b = E_{\text{bound}} - (E_{\text{stanene}} + E_{\text{Al}_2\text{O}_3}) . \quad (3.1)$$

To assess the importance of noncovalent interactions in the binding, we calculated E_b both with and without van der Waals dispersion corrections. We checked three van der Waals functionals implemented in Quantum ESPRESSO: the common Grimme DFT-D2 functional [96]; its DFT-D3 revision, which incorporates three-body interactions [98]; and the Becke–Johnson exchange-hole dipole-moment (XDM) model [99, 100]. We found that including a van der Waals functional modifies the interatomic distances listed in Table 3.2 by less than 0.5%, indicating that the physical structure is determined largely by chemical rather than van der Waals interactions. However, the binding energy, which is 0.50 eV per stanene unit cell without dispersion effects, increase to 0.84–1.23 eV per unit cell depending on the dispersion functional used. The largest binding occurs with the DFT-D2 functional, which is known to overbind solids [98], so we expect that the true binding energy lies within the range between the bare and DFT-D2 calculations. A previous study using the optB86b-vdW functional found a binding energy of 1.11 eV per unit cell, which is well within this range [91]. This suggests that both noncovalent and covalent interactions are needed to fully describe the absolute magnitude of the binding energy of stanene to alumina.

The fact that the chemical binding is quite substantial at 0.50 eV/unit cell requires some explanation: naively, one might expect a wide-gap material such as alumina to be relatively inert. To identify the chemical interaction that drives the binding, we plotted the density

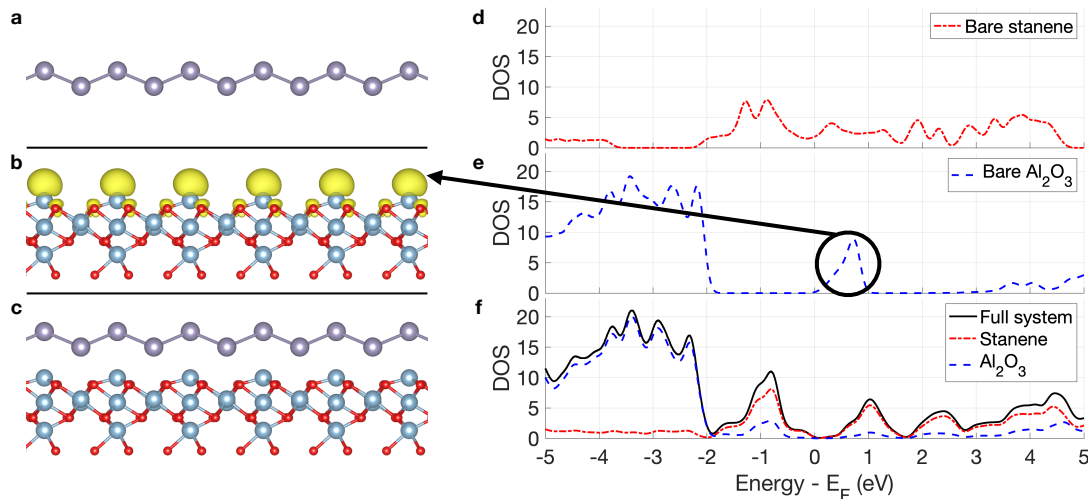


Figure 3.2: **(a,c)** Side view of free-standing stanene layer and stanene bound to the Al₂O₃(0001) slab, respectively. **(b)** Side view of bare alumina slab. The yellow features are an isosurface of the local density of states (LDOS) integrated from the Fermi level (E_F) to 1.0 eV above E_F . **(d-f)** Density of states (DOS) plots for free-standing stanene, bare alumina, and bound stanene on alumina, respectively. In the plot for the full system, the DOS is also projected onto the Löwdin orbitals of the tin atoms (stanene) and the aluminum/oxygen atoms (Al₂O₃).

of states (DOS) of the free-standing stanene layer, the bare alumina slab, and the stanene-substrate complex (Figures 3.2(d-f)). The bare alumina slab displays a peak in the DOS just above the Fermi level, which represents a surface state localized to “dangling” orbitals on the top layer of exposed Al atoms (left panel of Figure 3.2(b)). This state vanishes upon the binding of stanene—as can be seen from Figure 3.2(f), the states of the full complex near the Fermi level are dominated by Sn orbitals. The unoccupied alumina orbital hybridizes with various Sn orbitals, spreading out in energy over the former alumina gap. In particular, a portion of this orbital forms a new bonding orbital between -2 and 0 eV in Figure 3.2(f).

We confirmed that the originally empty “dangling” states of the alumina slab remain localized to the vicinity of the exposed Al atom by examining the redistribution of electron density shown in Figure 3.3. During binding, electron density redistributes from the cyan

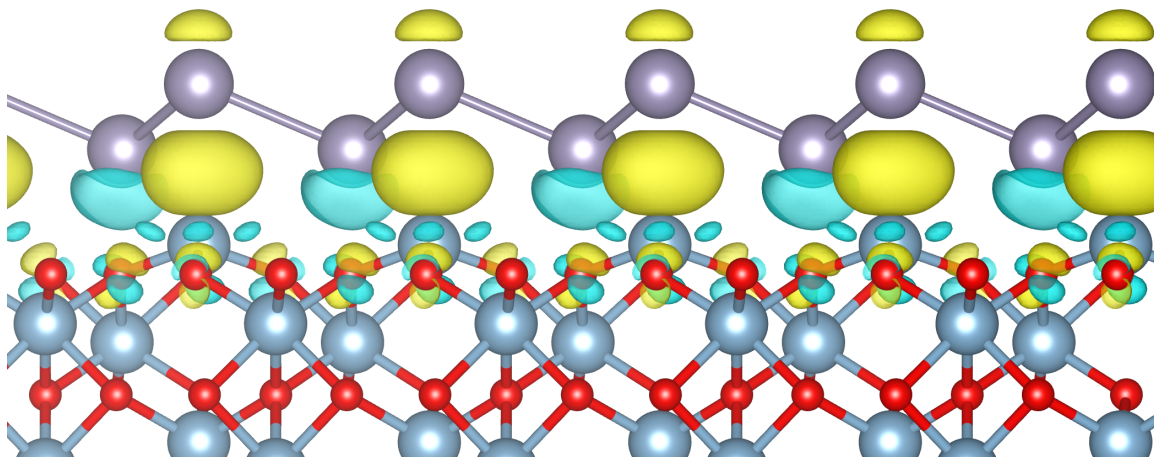


Figure 3.3: Side view of stanene on alumina showing positive (yellow) and negative (cyan) isosurfaces for electron redistribution. For regions in yellow, the electron density of stanene on alumina is greater than the sum of the electron density of the bare slab and that of the free-standing stanene monolayer, indicating an increase in electron density during binding. For regions in cyan, the reverse is true.

regions to the yellow regions, including a large σ -like region between the surface Al atom and the Sn atom above it. This indicates that the formerly-vacant Al orbital becomes filled as it moves lower in energy and hybridizes with nearby Sn orbitals: a heteropolar covalent bond has formed, explaining the substantial binding energy of 0.50 eV even without van der Waals interactions.

3.3.4 Commensurate versus incommensurate binding

Since stanene must be placed under 2.4% tensile strain to bind epitaxially to the $\text{Al}_2\text{O}_3(0001)$ surface, we checked for the possibility of incommensurate rather than epitaxial binding. In a case of incommensurate binding at the free-standing lattice parameter, the Sn monolayer will be unstrained, but most of the monolayer's area will not attain its preferred registry with respect to the alumina substrate. Therefore, the competition between epitaxial and incommensurate binding depends on a comparison of the strain energy of the stanene

monolayer to the energy penalty for placing the monolayer on a non-optimal registry.

The energy to strain a free-standing stanene monolayer from its equilibrium lattice parameter of $a = 4.68 \text{ \AA}$ to the theoretical Al_2O_3 lattice parameter of $a = 4.792 \text{ \AA}$ is 25 meV per unit cell. For low strain, an incommensurate overlayer on a substrate can be treated as a long-wavelength superlattice, with each unit cell of the superlattice sampling a different registry. If we label the in-plane position of the lower Sn atom (Sn atoms B or C in Figure 3.1) by $\mathbf{x} = u_1 \mathbf{a}_1 + u_2 \mathbf{a}_2$, then the average energy of a single unit cell in such an incommensurate overlayer is approximately

$$E_{\text{incomm}} = \int_0^1 \int_0^1 E(u_1 \mathbf{a}_1 + u_2 \mathbf{a}_2) du_1 du_2, \quad (3.2)$$

where $E(\mathbf{x})$ is the energy of a single commensurate unit cell with a lower Sn atom placed at \mathbf{x} . We estimate this integral using the registry calculations performed earlier, considering only the 3×3 grid of structures that are lateral shifts of the optimal A/C structure. The incommensurate energy penalty is 333 meV per unit cell with no van der Waals functional employed, 458 meV per unit cell with the Grimme DFT-D2 functional, and 339 meV per unit cell with the Grimme DFT-D3 functional. In all cases, the incommensurate energy is an order of magnitude greater than the strain energy, so we conclude that the incommensurate structure is irrelevant and that stanene will bind epitaxially on the alumina substrate.

3.3.5 Dumbbell stanene

We considered the “dumbbell” stanene structure proposed by Tang et al., which contains 10 Sn atoms in a multilayered analogue of a 2×2 stanene supercell [102]. In an isolated monolayer, out-of-plane sp^3 hybridization renders dumbbell stanene lower in energy than

low-buckled stanene by 0.18 eV per Sn atom [102]. However, we find that dumbbell stanene binds only weakly to Al_2O_3 , collapsing into a disorderly structure that is 0.46 eV per Sn atom higher in energy than the bound low-buckled configuration. This occurs because the highly buckled dumbbell structure prevents a close wetting interaction between Sn atoms and the substrate. Therefore, dumbbell stanene is not a relevant phase when considering epitaxial stanene on alumina.

3.3.6 Free-standing and bound stanene band structures

Next, we performed a thorough investigation of the band structures and topological indices of free-standing stanene and its derivatives. Figure 3.4(a) shows the evolution of the band gaps of free-standing bare stanene, fluorinated stanene, and hydrogenated stanene as a function of lattice parameter, highlighting regimes in which each material is a topological insulator, a topological material with negative gap (defined below), and a trivial metal. For metallic stanene layers, the band structures exhibit a semimetallic negative gap since the conduction band minimum drops below the valence band maximum compared to nearby insulating structures, and for them we compute the topological index that we would obtain if the valence and conduction bands were pulled apart far enough to create a global gap without further modification of the electronic structure. Figures 3.4(b-d) show the equilibrium band structures of free-standing stanene, fluorinated stanene SnF , and hydrogenated stanene SnH (also called stanane [6]).

The band structure plots in Figure 3.5 illustrate how the bands of each material evolve under strain. In the case of bare stanene (top row), the valence band at Γ sits well above the Dirac cone at K when compressive strain is applied ($a = 4.50 \text{ \AA}$), resulting in a negative-gap semimetal. As the lattice parameter increases ($a = 4.68 \text{ \AA}$), the gaps at Γ and K line up,

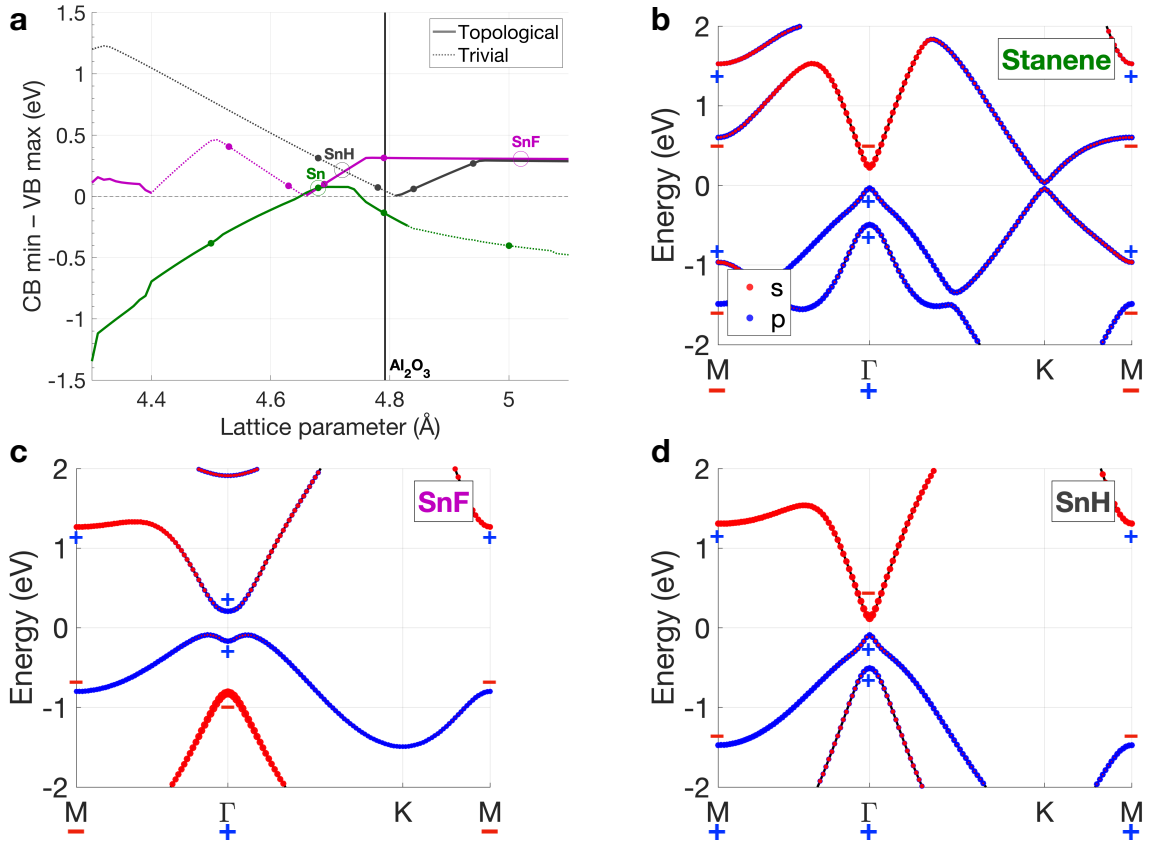


Figure 3.4: **(a)** Evolution of the band gap of bare stanene (green), fluorinated stanene SnF (magenta), and hydrogenated stanene SnH (black) as a function of lattice parameter. The band gap is defined as the signed energy difference between the conduction band (CB) minimum and the valence band (VB) maximum, meaning that it is negative for semimetallic materials. The theoretical equilibrium lattice parameter of Al₂O₃ is indicated with a vertical black line. For each structure, a dashed line indicates a trivial material with a topological index of $Z_2 = 0$, while a solid line indicates a topological material with $Z_2 = 1$. Each material's equilibrium lattice parameter is marked with a large open circle, while the band structures plotted in Figure 3.5 correspond to the points marked with small filled circles. **(b-d)** Band structures of bare stanene, fluorinated stanene SnF, and hydrogenated stanene SnH at their equilibrium lattice parameters. Bands are colored by their s -orbital (red) and p -orbital (blue) characters, and labeled with their parities at time-reversal invariant momenta (TRIMs). On the x -axis, each TRIM is labeled with the product of all of its band parities, the quantity called δ_i in the Fu–Kane treatment [101]. The zero of band energy is the Fermi level E_F .

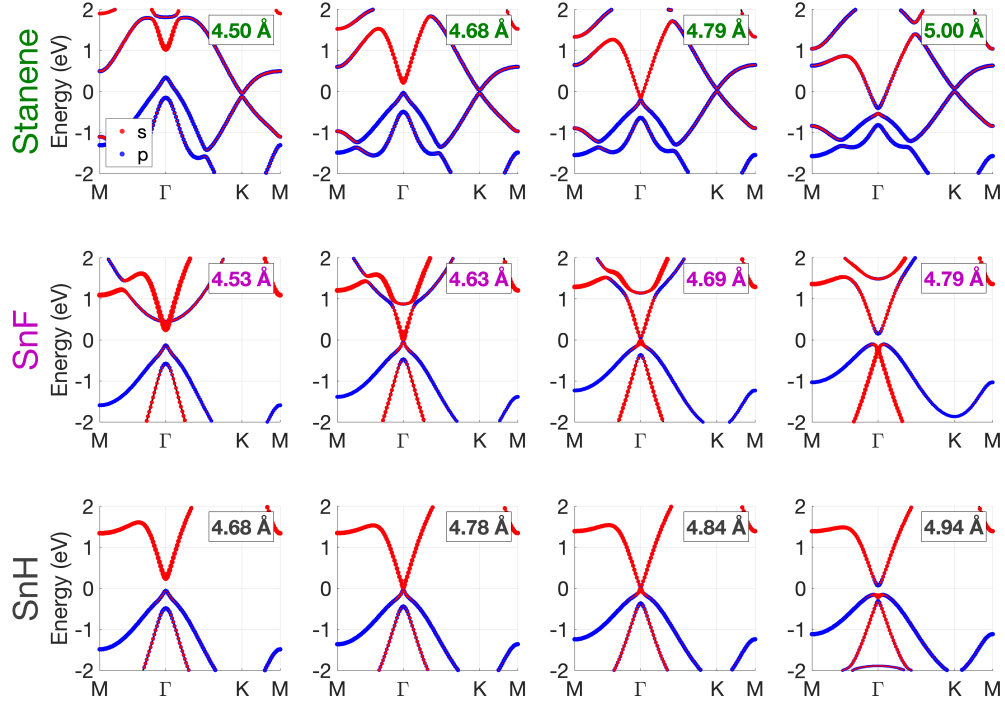


Figure 3.5: Band structure plots showing the change of topological character via band inversions in bare stanene (top row), fluorinated stanene SnF (middle row), and hydrogenated stanene SnH (bottom row). The zero of energy in each plot is the Fermi level E_F . In each case, a negative-parity s -band crosses down from the conduction band into the valence band as the lattice parameter increases. Due to their different equilibrium lattice parameters, free-standing stanene ($a = 4.68 \text{ \AA}$) and SnF ($a = 5.02 \text{ \AA}$) are topological insulators, while SnH ($a = 4.72 \text{ \AA}$) is a trivial insulator, but each material can be tuned to the other regime using strain.

forming a globally gapped topological insulator. For small tensile strain ($a = 4.79 \text{ \AA}$), the gap at Γ is pushed below the Dirac cone at K: this is the regime of strain relevant for stanene on Al_2O_3 , so the substrate is necessary to open the global band gap (we will see that is also sufficient below). Finally, for tensile strain somewhat larger than that applied by Al_2O_3 ($a = 5.00 \text{ \AA}$), the gap closes between the negative-parity s -type conduction band at Γ and the positive-parity p -type valence band (*i.e.*, a band inversion occurs at Γ). The resulting parity exchange renders free-standing stanene non-topological above a lattice parameter of roughly 4.83 \AA .

The story is slightly different for SnF and SnH. At their equilibrium lattice parameters, SnF is a topological insulator while SnH is a trivial insulator. However, the two materials are actually quite similar electronically: both materials are trivial insulators under sufficient compressive strain and topological insulators under sufficient tensile strain. The difference between them at equilibrium is simply due to the relative ordering of the lattice parameter of the topological transition and the equilibrium lattice parameter. This can be seen clearly in the middle-row and bottom-row band structures of Figure 3.5, which depict the topological phase transitions in the two materials. In each case, a negative-parity antibonding band constructed from Sn s orbitals moves down through the conduction band, and crosses over to the valence band at Γ , inducing a band inversion and leading to a nontrivial topological index.

Since each topological phase transition is controlled by a band inversion across the gap at Γ , it is reasonable to ask whether our results break down in a treatment that accounts better for electron–electron interactions which typically renormalize the band gap substantially. To check this, we calculated the band structure of relaxed stanene and SnF with VASP [95] using the HSE06 hybrid functional [23, 24]. Our results, available in the Appendix, are

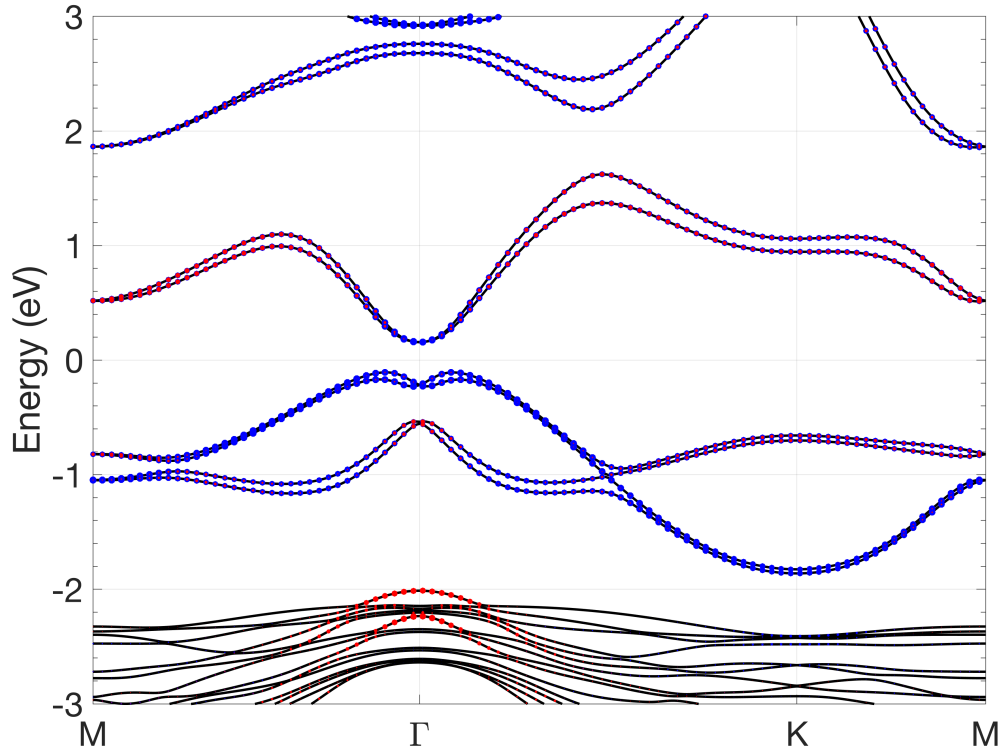


Figure 3.6: Band structure plot for epitaxial stanene on alumina. Bands are colored by their Sn s -orbital (red) and Sn p -orbital (blue) characters. The DFT band gap is calculated to be 0.263 eV.

qualitatively very similar to the results obtained with the PBE functional.

Figure 3.6 shows the the band structure of the full stanene-on-alumina system. It differs from the bare-stanene band structure (Figure 3.4(b)) in several important ways. First, the presence of the substrate breaks inversion symmetry, which, when combined with the spin-orbit interaction, leads to a Rashba splitting of the conduction bands away from the Γ point. We computed the band structures for stanene on alumina slabs of different thickness and confirmed that the k -dependent energy splitting of bands away from the Γ point is due to inversion symmetry breaking (rather than evanescent coupling between the two surfaces of the alumina slab). This data is available in the Appendix.

In addition, the Dirac cone at K has vanished due to the partial saturation of the stanene p_z orbitals by the alumina surface, and the ordering of s -type and p -type orbitals at Γ has become inverted, yielding a band structure remarkably similar to the free-standing SnF band structure. These features are necessary for the existence of topological behavior in stanene on a substrate [6]. Indeed, we confirmed that stanene on alumina is topological using the Wannier charge center method.

3.4 Discussion and outlook

The combination of strong epitaxial binding with band inversion at Γ and p_z -orbital saturation at K indicates that alumina is a promising substrate for the synthesis of bare monolayer stanene. Such a material offers an opportunity for experimental observation of the quantum spin Hall effect [6, 74] as well as a substrate for a variety of technological applications [69, 70, 71, 72, 73]. In addition, the spin separation in the conduction band due to the Rashba splitting can be harnessed for applications in spintronics and topological superconductivity [103].

Controlled functionalization, e.g., by hydrogen or fluorine, is also an important avenue of stanene research, since functionalization both enhances the band gap and protects against unwanted environmental interactions with Sn p_z orbitals [6]. Generally speaking, two-dimensional materials can be synthesized either by epitaxial deposition or by the exfoliation of multilayered van der Waals materials [65]. The latter method is attractive since it is flexible and modular, but is impractical for materials like bare stanene whose 3D bulk phase (α -tin) is not intrinsically layered. However, the epitaxial growth of stanene on alumina should kinetically trap the tin atoms in the 2D hexagonal stanene structure, perhaps making

it possible to functionalize the monolayer *in situ*. The functionalized sheet, now weakly bound to the alumina, could be exfoliated for use in heterostructure and device applications.

In summary, we have shown that monolayer stanene binds strongly and epitaxially to the $\text{Al}_2\text{O}_3(0001)$ surface, with a buckled structure and a sizable global band gap. We have examined the chemical character of the binding and verified the topological nature of stanene on alumina. With its wide surface band gap and relative inertness, alumina is a promising substrate for future experimental fabrication and characterization.

3.5 Appendix: Additional calculations

Figure 3.7 shows the band structures of bare and fluorinated stanene computed using the HSE06 hybrid functional. Bands are labeled by their s (red) and p (blue) character to demonstrate that the band ordering that ensures the topological character of each material is preserved, even when better accounting for nonlocal electron–electron interactions.

Figure 3.8 compares the band structures of stanene on 4-, 6-, and 8-layer alumina slabs. Below around -2 eV, an increasing density of bulk bands can be seen, but the near- E_F states, localized to the tin overlayer, are unaffected by the thickness of the substrate.

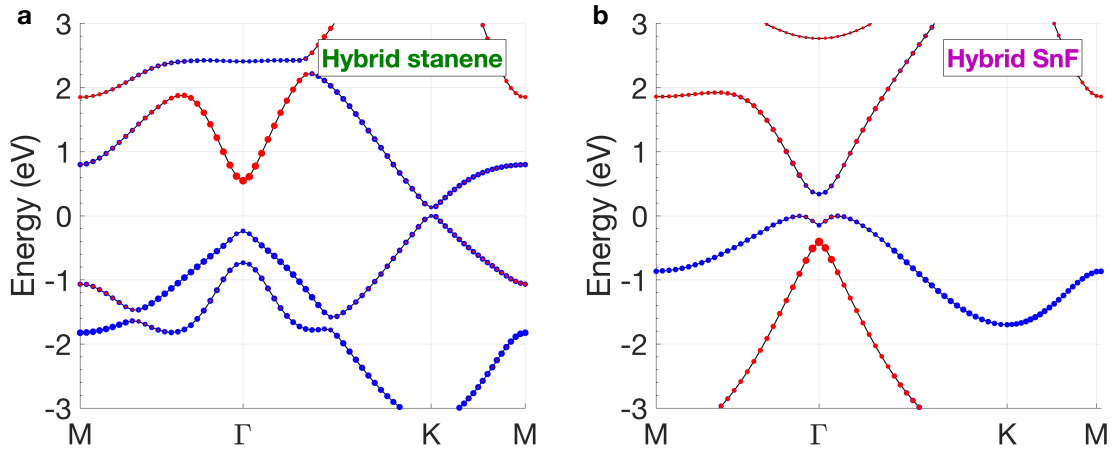


Figure 3.7: Orbital-projected hybrid (HSE06) band structures of **(a)** stanene and **(b)** SnF; the analogous non-hybrid calculations are shown in Figures 3.4(b-c). The zero of energy is the Fermi level E_F .

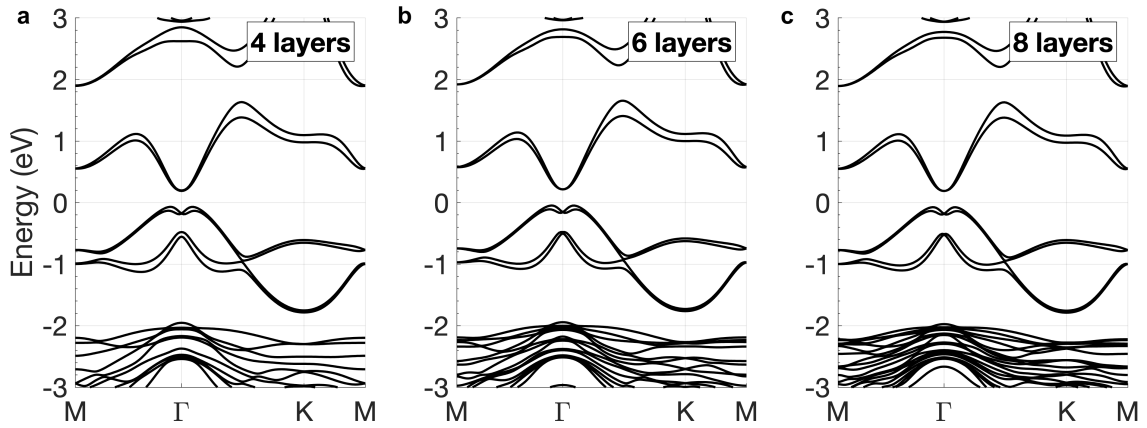


Figure 3.8: Substrate thickness dependence of the stanene-on-alumina band structure: electronic bands for **(a)** 4, **(b)** 6, and **(c)** 8 layers of Al_2O_3 .

Chapter 4

Identifying chemical reactions at the interface of stanene on $\text{Bi}_2\text{Te}_3(0001)$

This chapter is adapted from an article entitled “Identifying crystal structures and chemical reactions at the interface of stanene on Bi_2Te_3 ” by Stephen D. Albright, Ke Zou, Claudia Lau, Stephen Eltinge, Hawoong Hong, Sohrab Ismail-Beigi, Frederick J. Walker, and Charles H. Ahn that was published in the Journal of Applied Physics [104]. Additional experimental data in support of this chapter can be found in the Supplementary Information of that article, and is referenced where appropriate. SA, KZ, CL, and HH did the experimental work, I did the theoretical work, and SIB, FW, and CA provided guidance.

Synthesizing monolayers and heterostructures is an enabling approach to extract new physical phenomena from bulk materials. Among the structures amenable to this approach is stanene, which is a monolayer of tin, similar to graphene, and has been predicted to host one-dimensional topological states at its edges. Stanene can be tuned by decorating with different adatoms, which makes it a promising platform on which to engineer topological devices. In this chapter, we report on a collaboration with experimentalist colleagues who deposited Sn on Bi_2Te_3 and characterized the growth using anomalous synchrotron x-ray scattering and x-ray photoelectron spectroscopy (XPS). We include their experimental results for background; the discussion of our theoretical calculations begins in Section 4.5. Their x-ray diffraction data reveal the formation of epitaxial Sn-based structures, along

with penetration of Sn into the Bi_2Te_3 , with Sn intercalating between the upper 10 Bi_2Te_3 quintuple layers. Additionally, XPS data show deposited Sn reacting to form SnTe and Bi at the Bi_2Te_3 surface. We computed the phase diagram for thin-film structures of Sn, Bi, and Te, at the level of density functional theory, confirming this reaction in the compositional regime probed by the experiment. Using thermodynamic calculations as a guide, we identify several candidate substrates that can stabilize the stanene phase, including the Al_2O_3 substrate discussed in the previous chapter.

4.1 Introduction

The strong interfacial interactions and confinement effects that arise when monolayers or heterostructures of layered materials are synthesized provide a platform to access a wide range of novel physical phenomena [105, 106, 107, 108, 109, 110, 111, 112, 113, 114, 115, 116, 117]. With the high degree of control in contemporary synthesis methods, the field of monolayer materials is rapidly expanding and has produced a number of important developments, such as high-mobility semiconductors [105, 106, 107], enhanced T_c superconductors [108, 109, 110, 111, 112, 113], and switchable topological insulators and quantum spin Hall materials [114, 115, 116, 117]. There are even more possibilities in engineering interfaces of materials from multiple classes, to potential build topological transistors [118, 119, 120] or observe Majorana fermions in topological insulator–superconductor heterostructures [121].

There has been a surge of interest in heterostructures based on chalcogenides or pnictides due to the many novel behaviors in these classes of materials [107, 109, 110, 111, 112, 113, 114, 115, 116, 117, 118, 119, 120, 121, 122]. With the expanding chemical landscape, an important consideration, in addition to crystalline compatibility (*i.e.*, crystal orientation and

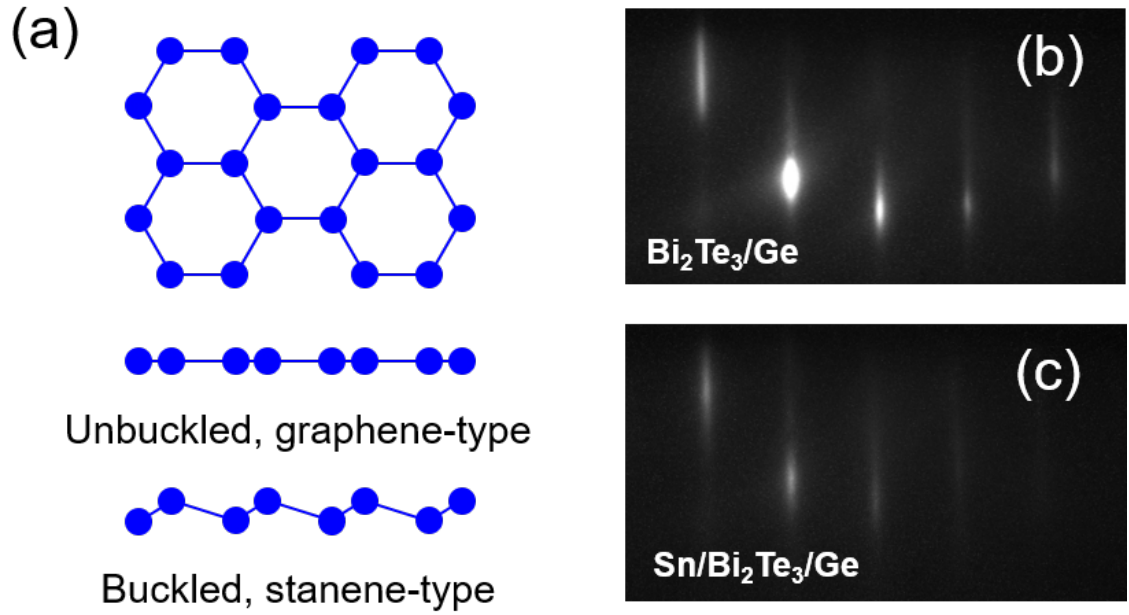


Figure 4.1: (a) Honeycomb crystal structure from above (upper) and the side (lower), as seen for C atoms (graphene)—an unbuckled lattice—and for Sn atoms (stanene)—a buckled lattice. RHEED images measured along the $\langle 10 \rangle$ Bi₂Te₃ direction for Bi₂Te₃ (b) after decapping and (c) after deposition of 1 monolayer stanene.

lattice parameter), is the chemical compatibility between substrate and deposited materials when designing a system for a particular functionality.

Here, our colleagues characterize the growth process for stanene on Bi₂Te₃ substrates. Stanene, a monolayer of buckled hexagonal tin, similar to graphene (Figure 4.1(a)), is predicted to have a wider band gap than other topological materials and host topological edge states [6, 78, 102]. The properties of stanene are also predicted to be tunable by strain, substrate bonding, and decoration with halides or hydroxide, making stanene a promising system for topological devices [6, 78, 123].

Multiple theoretical and experimental attempts to understand the conditions necessary to achieve stanene have revealed the difficulty in synthesizing a continuous stanene monolayer [84, 124, 91, 125, 77, 67]. A few substrates have been shown to host uniform and topological

stanene monolayers, most notably on Ag(111), where stanene sits atop a reacted Ag_2Sn interface [79], and on $\text{PbTe}/\text{Bi}_2\text{Te}_3/\text{Si}(111)$ heterostructures, where bi- and tri-layer stanene have been observed to be superconducting, making possible the observation of Majorana particles [126, 127]. These examples highlight the need to understand the crystal structure, chemical conditions, and growth process for stanene deposited on substrates selected for different applications.

4.2 Experimental methods

Bi_2Te_3 is hexagonal with a stable (0001) surface and an in-plane lattice parameter (4.38 Å) closely matched to stanene (4.68 Å). The unit cell of Bi_2Te_3 consists of hexagonal quintuple layers (QLs), each bonded by van der Waals forces along the $\langle 0001 \rangle$ direction. In this work, thick Bi_2Te_3 films were grown by molecular beam epitaxy (MBE) on $\text{Si}(111)-7\times 7$ and $\text{Ge}(111)-c(2\times 8)$ reconstructions, the most stable atomic reconstructions for the Si and Ge(111) surfaces [128, 129, 130, 131, 132]. The reconstructions can be observed by reflection high-energy electron diffraction (RHEED), seen in Supplementary Figure S1 in [104].

Once the reconstruction is achieved in RHEED, 20 QL Bi_2Te_3 films were grown by co-depositing molecular Bi and Te, with a $\sim 10\times$ overpressure of Te. RHEED confirmed high-quality crystal growth (Figure 4.1(b) and Supplementary Figure S1 in [104]) of strain-relaxed Bi_2Te_3 on both Ge (4.00 Å in-plane lattice parameter, 9.5% mismatch with Bi_2Te_3) and Si (3.86 Å lattice parameter, 13.5% mismatch) substrates. Following deposition, Bi_2Te_3 was capped with an amorphous layer of Te or Sn at a substrate temperature below 50 °C to protect the Bi_2Te_3 from oxidation while transferring to external chambers for stanene

growth and measurement.

The procedure for stanene growth is based on that used previously [84] and optimized in the same MBE deposition chamber used for Bi_2Te_3 growth. Our colleagues explored the growth process for substrate temperatures between 25 and 200 °C and found that RHEED patterns of stanene films grown with the substrate at 100 °C (Figure 4.1(c)) produce the highest intensity diffraction. All the data reported here are for Sn grown on Bi_2Te_3 at a substrate temperature of 100 °C.

To understand the growth process of stanene on Bi_2Te_3 , Sn growth was performed in a custom x-ray photoelectron spectroscopy (XPS) chamber that allows in situ measurements during Sn deposition. The deposition rate was calculated by depositing Sn on a quartz disc and measuring absorption of a laser ($\lambda = 633 \text{ nm}$) before and after growth. The coverage of Sn on Bi_2Te_3 corresponding to 1 monolayer is $1.2 \times 10^{15} \text{ atom/cm}^2$. Bi_2Te_3 films used for XPS measurements were capped with Te and subsequently decapped in the XPS chamber by annealing to 350 °C. To verify the cap has been removed, XPS was measured during heating and the sample was cooled once the Bi and Te core level intensities stop changing. XPS spectra before and after anneal (Supplementary Figure S2 in [104]) show the emergence of Bi^{3+} peaks following the anneal.

To extract the crystal structure of Sn deposited on Bi_2Te_3 , the same growth process was performed in an MBE growth chamber mounted for in situ synchrotron x-ray diffraction (XRD) at the 33ID-E beamline at the Advanced Photon Source, Argonne National Laboratory. The deposition rate was measured using a quartz crystal microbalance. Bi_2Te_3 substrates prepared for XRD measurements were capped with Sn, then decapped by argon sputtering in the XRD chamber. Following sputtering, Bi_2Te_3 was annealed at 250 °C to recover an atomically smooth surface, indicated by a strong RHEED pattern (Figure 4.1(b)).

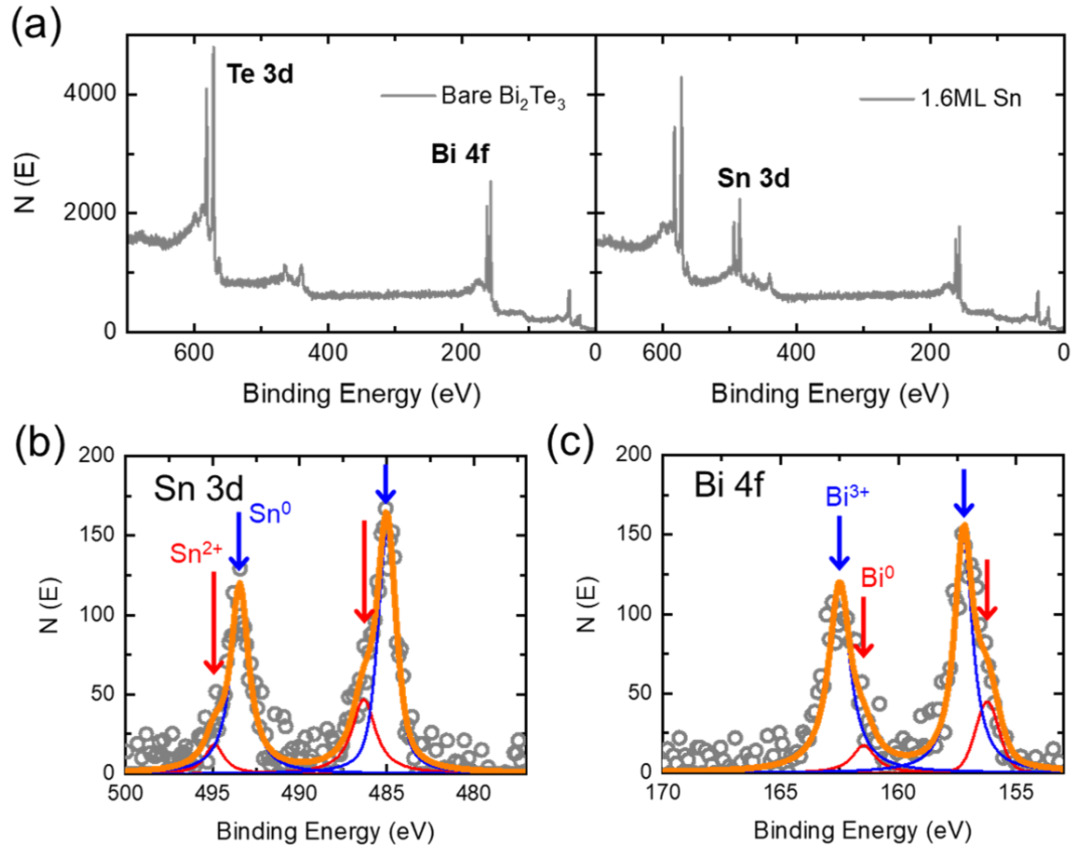


Figure 4.2: (a) XPS surveys for bare Bi₂Te₃ and following 1.6 monolayers Sn growth. Spectra (grey) with fits (individual peak fits in red and blue, total in orange) of (b) Sn 3d and (c) Bi 4f peaks at 0.8 monolayer Sn show multiple Sn and Bi valences.

Sn, which has a lower vapor pressure than Te, was chosen as a cap for XRD measurements due to the extended time necessary to transport the samples to the beamline.

4.3 X-ray photoelectron spectroscopy

Our colleagues grew Sn at 0.5 monolayers/min and measure XPS continuously during growth so that spectra of all constituent elements are measured each 0.4 monolayers. In addition, they paused growth at 1.6, 3.2, and 16 monolayers to perform longer measurements to improve the signal to noise ratio. The energy of each scan was calibrated to the valence

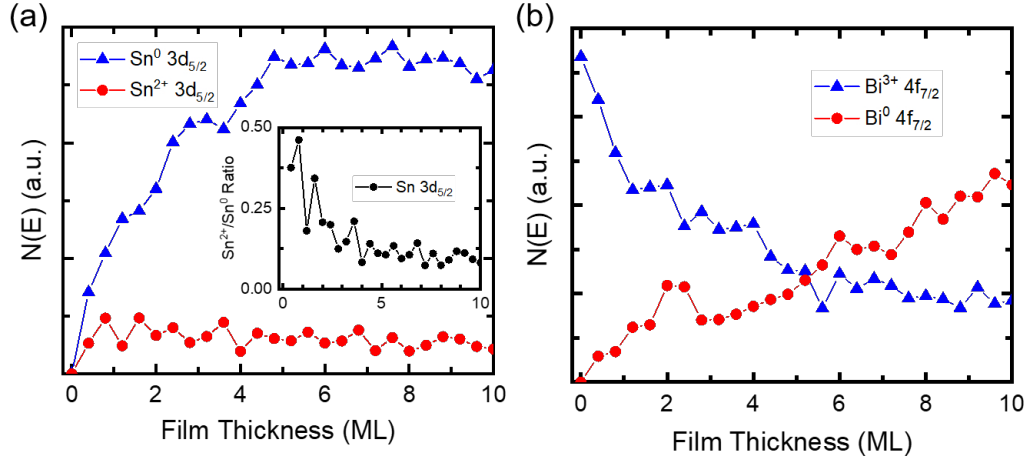


Figure 4.3: Integrated intensity of (a) Sn^0 and Sn^{2+} $3d_{5/2}$ and (b) Bi^{3+} and Bi^0 $4f_{7/2}$ transitions as a function of stanene deposited. Inset of panel (a) displays ratio of Sn^{2+} to Sn^0 intensity as a function of film thickness. In the inset of panel (a), the data point at Film Thickness = 0 is excluded; there is initially no XPS peak for Sn^0 and Sn^{2+} .

band edge. The spectra for bare Bi_2Te_3 and 1.6 monolayers deposited Sn are shown in Figure 4.2(a), with a clear appearance of Sn peaks following growth.

Beginning at 0.4 monolayer coverage, the spectra for Bi and Sn show multiple peaks (Bi $4f$ and Sn $3d$ transitions at 0.8 monolayer shown in Figures 4.2(b-c)), which is a sign of multiple valences in the Bi and Sn atoms. Our colleagues identified Bi^{3+} $4f_{7/2}$ and Sn^0 $3d_{5/2}$, at 157.3 and 485.1 eV, respectively, which correspond to the binding energies expected for Bi_2Te_3 and elemental Sn [133, 134]. They also identified binding energies corresponding to Bi^0 $4f_{7/2}$ and Sn^{2+} $3d_{5/2}$, at 156.3 and 486.4 eV, respectively, which suggests the reaction of Bi_2Te_3 and stanene to Bi and SnTe [134, 135]. Other recent work to recreate stanene on Bi_2Te_3 showed similar evidence of this reaction in XPS [85].

To understand the chemical reaction during growth, our colleagues extracted the integrated intensity of each transition as a function of film thickness (Figure 4.3). Immediately upon depositing Sn, $3d_{5/2}$ peaks corresponding to both Sn^0 and Sn^{2+} appear, with the Sn^0 peak becoming increasingly dominant as growth continues (Figure 4.3(a)). The ratio of

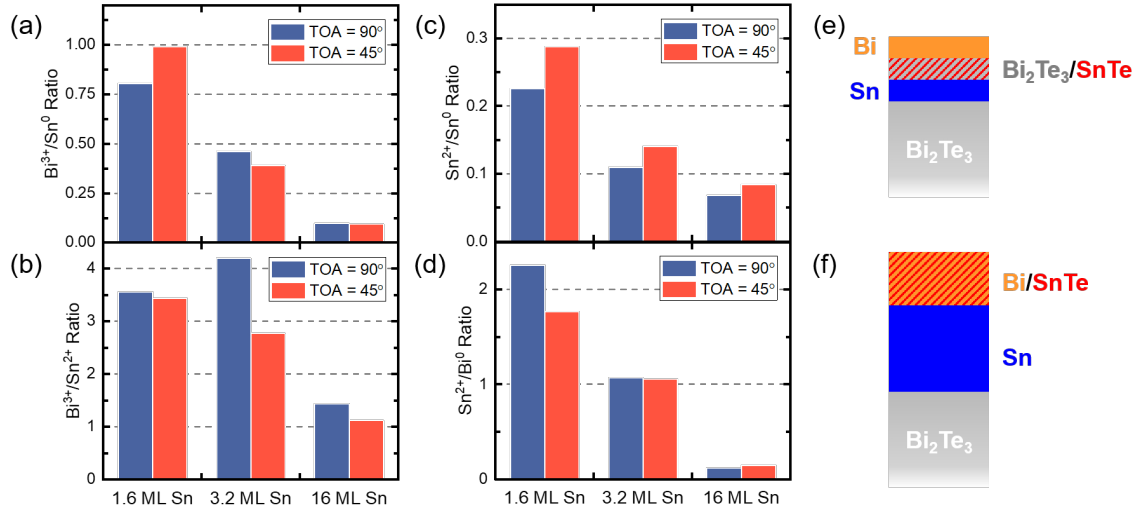


Figure 4.4: Ratios of integrated intensities of Bi^{3+} to (a) Sn^0 and (b) Sn^{2+} , and Sn^{2+} to (c) Sn^0 and (d) Bi^0 at take-off angles of 90° and 45° . Intensities of $\text{Sn } 3d_{5/2}$ and $\text{Bi } 4f_{7/2}$ transitions are used to calculate ratios. (e,f) Film profile for (e) ≤ 1.6 monolayers deposited Sn and (f) ≥ 3.2 monolayers deposited Sn, deduced from XPS measurements.

$\text{Sn}^{2+}/\text{Sn}^0$, plotted in the inset of Figure 4.3(a), shows that as Sn is initially deposited, approximately half as much Sn^{2+} forms as Sn^0 . This suggests that half as much SnTe forms as elemental Sn at the beginning of growth. This chemical reaction is reflected in the intensity of Bi as well (Figure 4.3(b)). Initially, Bi^{3+} from the bulk Bi_2Te_3 dominates the $\text{Bi } 4f_{7/2}$ signal, and as growth proceeds, Bi^0 grows in intensity as Sn and Bi_2Te_3 react into SnTe and Bi.

Considering the reaction that occurs when Sn is deposited on Bi_2Te_3 , a uniform stanene layer may not form at this interface. XPS results suggest an inhomogeneous film profile, consisting of Bi_2Te_3 , Sn, Bi, and SnTe . To better understand the structure that develops, our colleagues performed XPS at different take-off angles (TOAs) from the film plane, which varies the depths probed by the electron analyzer. They measured spectra with $\text{TOA} = 45^\circ$ (more surface sensitive) and 90° (more bulk sensitive), and computed the ratios of relevant elemental transitions to extract their layering order (Figure 4.4).

Beginning at 1.6 monolayers Sn, the ratio of Bi^{3+} to Sn^0 is greater at 45° , suggesting more Bi_2Te_3 is located at the surface than elemental Sn (Figure 4.4(a)). Considering also that the Bi^{3+} to Sn^{2+} ratio is approximately equal at both angles for 1.6 monolayers (Figure 4.4(b)), these results suggest that Sn initially reacts with subsurface Bi_2Te_3 , creating an upper layer of Bi_2Te_3 , SnTe and Bi. The $\text{Sn}^{2+}/\text{Sn}^0$ and $\text{Sn}^{2+}/\text{Bi}^0$ ratios further indicate that SnTe is located above the deposited Sn, and Bi above the SnTe at 1.6 monolayers (Figures 4.4(c-d)). This profile for films ≤ 1.6 monolayers thick is shown in Figure 4.4(e). For films ≥ 3.2 monolayers thick, the upper Bi_2Te_3 layer has fully reacted. The profile consists of the following layers: intermixed SnTe and Bi, elemental Sn, and the Bi_2Te_3 substrate (Figures 4.4(a-d), profile in Figure 4.4(f)). At an atomic level, multiple compounds intermixed in the same layer may manifest in a variety of ways—separate lateral domains or alternating layering, for example—but techniques beyond XPS and XRD are necessary to go beyond our identification of the layer order of atomic valences. This ordering is likely due to compounds of low surface energy, *i.e.*, Bi and Bi_2Te_3 , migrating towards the surface, effectively wetting the other compounds with higher surface energies. Bi is a well-known surfactant [132, 136] and $\text{Bi}_2\text{Te}_3(0001)$ should have low surface energy because of the dominant van der Waals bonding between QLs.

4.4 Synchrotron x-ray diffraction

While the Sn/ Bi_2Te_3 interface consists of several intermixed materials, it is possible to examine stanene on the surface, as has been done with STM studies of hexagonal stanene [84]. To quantitatively study stanene on the surface, our colleagues performed in situ synchrotron x-ray diffraction at the Advanced Photon Source. Previous studies suggest

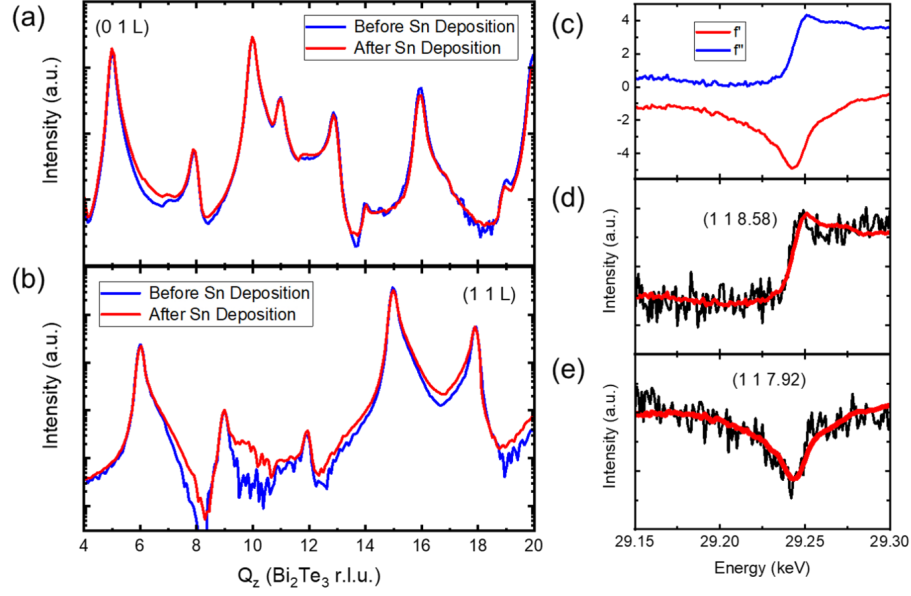


Figure 4.5: Bi_2Te_3 (a) $(0\ 1\ L)$ and (b) $(1\ 1\ L)$ CTRs before and after Sn deposition. (c) Energy dependent Sn atomic form factor components f' and f'' across the Sn K-edge. (d-e) Spectra measured at $(1\ 1\ 8.58)$ and $(1\ 1\ 7.92)$, respectively, with fits (red) to Equation 4.1, demonstrating interference between f' and f'' .

stanene is strained coherently to the Bi_2Te_3 substrate, and thus they examined stanene signals along the Bi_2Te_3 crystal truncation rods (CTRs).

Our colleagues observed clear differences between Bi_2Te_3 CTRs measured before and after deposition of 1 monolayer Sn (grown at 0.2 monolayers/min), shown in Figures 4.5(a-b), indicating that the deposition of Sn has created a film structure coherently strained to the Bi_2Te_3 lattice. However, from XPS we know that SnTe and Bi are both present in addition to Sn, and both may possess hexagonal structures that may grow coherently strained to Bi_2Te_3 . Any difference they observed along Bi_2Te_3 CTRs could be due to stanene, SnTe, or Bi, meaning one cannot distinguish between deposited stanene, SnTe, and Bi with scans along Q_z alone.

To elucidate more structural information of the stanene film, our colleagues perform anomalous x-ray scattering at the Sn K-edge to extract the diffraction of Sn atoms from

the entire system, allowing one to probe for only stanene. As the energy of the incoming photons crosses an absorption edge, the atomic form factor has a significant complex energy dependent term, $f'(E) + i f''(E)$, where f'' is the absorption and f' is related to f'' by the Kramers–Kronig relation. The values of f' and f'' for Sn, calculated by measuring the absorption of x-rays through a 58 μm Sn foil, are shown in Figure 4.5(c).

Using anomalous scattering to extract the Sn signal of the stanene films, our colleagues moved along Bi_2Te_3 CTRs and scanned the beam energy across the Sn K-edge (29.3 keV). They fit the resulting spectra to an expression for the scattered intensity taking into account the energy dependent terms f' and f'' :

$$I(\mathbf{q}, E) = \left| A_{\text{Sn}}(\mathbf{q}) (f_{\text{Sn}}(\mathbf{q}) + f'(E) + i f''(E)) + A_{\text{BT}}(\mathbf{q}) e^{-i\varphi} \right|^2 \quad (4.1)$$

where $A_{\text{Sn}}(\mathbf{q}) (f_{\text{Sn}}(\mathbf{q}) + f'(E) + i f''(E))$ is the structure factor for Sn, A_{BT} is the structure factor for all forms of Bi and Te (Bi_2Te_3 , Bi, and Te in SnTe), f_{Sn} is the energy-independent atomic form factor for Sn, and φ is the phase difference between the Sn and Bi_2Te_3 structure factors. We refer to A_{Sn} as the Sn scattering strength.

Following the deposition of 1 monolayer Sn, our colleagues observed a strong energy dependence along the (1 1 L) Bi_2Te_3 CTR (Figures 4.5(d-e)), which they fit to Equation 4.1 to extract the Sn scattering strength. Performing these fits along the CTR extracts diffraction from only Sn, shown in Figure 4.6(a). The extracted scattering strength of Sn along the (1 1 L) CTR, which consists of two features: a broad peak centered at $Q_z = 8$ and a sharper, more intense peak centered at $Q_z = 8.7$, can be analyzed to extract the structure of the coherently strained Sn. Simulations of 1 monolayer buckled and unbuckled stanene (structure in Figure 4.1(a)) do not exhibit peaks in this range of Q_z (Figure 4.6(b)). However,

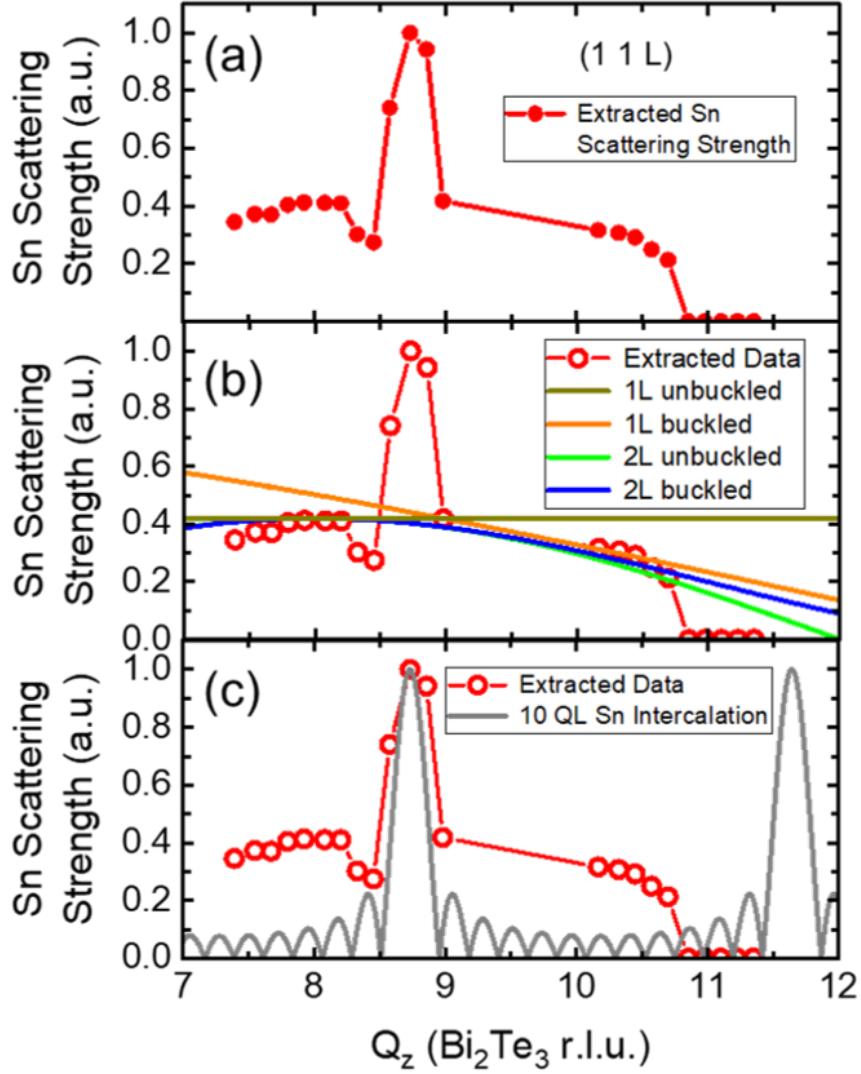


Figure 4.6: (a) Sn scattering strength, A_{Sn} , extracted from spectra measured along the Bi₂Te₃ (1 1 L) CTR. (b) Simulated Sn scattering strength for 1 and 2 monolayers of un buckled and buckled stanene. (c) Simulated Sn scattering strength for Sn intercalated between the top 10 QL along the $\langle 0001 \rangle$ direction. Data are normalized to the maximum peak intensity and simulations are normalized to match the intensity of the respective features.

assuming an AB graphene-like stacking, both an unbuckled stanene bilayer with a gap between layers of 3.81 Å and a buckled stanene bilayer with a buckling distance of 0.93 Å and layer gap of 3.51 Å, which is similar to the structure of (111) α -Sn, can reproduce the broad peak centered at $Q_z = 8$ (Figure 4.6(b)). This bilayer stacking is consistent with previous STM measurements of stanene, which observe an AB-stacked second stanene layer forming before achieving full coverage of a single monolayer [84]. Considering the documented favorability for buckled stanene in previous work [6, 78, 84], the buckled bilayer stanene is the likely source for the peak centered at $Q_z = 8$, though measurement over more of reciprocal space is needed to confirm the presence of buckled monolayer stanene. Furthermore, since the analysis of anomalous scattering extracts all Sn diffraction signal, this CTR may still contain contributions from SnTe. XRD of stanene grown on a less reactive substrate should yield a more conclusive stanene structure.

The narrow peak width of the second feature at $Q_z = 8.7$, which corresponds to a film feature 10 nm thick, cannot be accounted for by the deposited film of stanene or Sn reacted to SnTe, and thus another structure, in addition to the stanene bilayer, must be present. The source of this peak is intercalation into the Bi_2Te_3 substrate, which would give a similarly wide peak at $Q_z = 9$. Assuming a structure where Sn atoms intercalate between Bi_2Te_3 QLs, fitting the measured peak width indicates Sn is intercalated into the upper 10 QLs. The shift in Q_z to 8.7 Bi_2Te_3 r.l.u. indicates a 3% expansion along the c -axis of the Bi_2Te_3 .

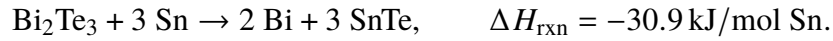
A random in-plane intercalation structure would give Bragg peaks every integer in Q_z , so the presence of an intercalation peak near $Q_z = 9$ but absence near $Q_z = 8$ suggests a high-symmetry in-plane structure. Our colleagues deduced an intercalated Sn structure consisting of a single Sn atom per unit cell between each QL at locations shown in Supplementary Figure S3 in [104], similar to structures observed in previous works studying the intercalation

of Sn [137, 138]. Simulating this intercalation with the c -axis expansion generates a close match to the sharp peak observed in the extracted scattering strength (Figure 4.6(c)).

By comparing the extracted Sn scattering strength at the intercalation peak to the intensity of strong Bi_2Te_3 Bragg peaks at (0 1 20) and (0 1 23), normalized to their respective structure factors, our colleagues estimate that the upper 10 QLs of Bi_2Te_3 contain 10-17% of a stanene monolayer intercalated between each QL, which is more total Sn than deposited during stanene growth. This indicates that the intercalation mostly occurs as a result of the sputter removal of the Sn cap, as opposed to deposition. This process of deposition followed by sputtering and annealing may provide a novel method for intercalating Sn into thin films of Bi_2Te_3 or other materials, contrasting the solid state crystal growth or penetration through crystal steps observed in previous work [137, 138].

4.5 Theoretical results and discussion

Our observations that Sn deposited on Bi_2Te_3 forms a mix of SnTe, Bi, and Sn instead of pure stanene reveals that Bi_2Te_3 induces inhomogeneity during stanene growth. The favorability of this reaction is consistent with a calculation of the heat of reaction, ΔH_{rxn} , from the bulk literature values of reactant and product heats of formation:



This sign of ΔH_{rxn} indicates this reaction is exothermic. We also performed first principles calculations of the bulk formation energies that are consistent with this thermodynamic observation.

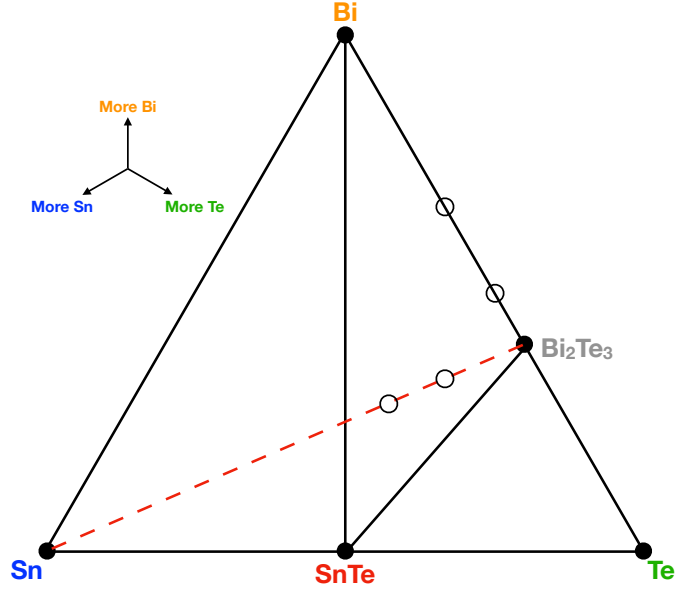


Figure 4.7: Ternary phase diagram for thin-film structures of Sn, Bi, and Te. Structures on the convex hull (*i.e.*, those that are thermodynamically stable) are marked with filled circles, while other structures included in the calculation set are marked with open circles. All unstable structures in the calculation set lie on or within the portion of the hull bounded by Bi, SnTe, and Bi_2Te_3 , and would be expected to decompose into those three structures.

While this heat of reaction is similar in magnitude to those of Cu or Ni forming Cu_3Si and NiSi with Si (-11.6 kJ and -42.4 kJ, respectively), both of which occur at low temperatures when those elements are deposited on Si [139, 140], bulk thermodynamic calculations may not always predict the surface structure. There are examples of stable monolayer films on substrates where a reaction should take place, such as Sr on Si(001) [141]. The layered nature of Bi_2Te_3 suggests that the surface and interface energies could prevent a bulk-like reaction, though our colleagues' experiments suggest the low surface energy of Bi may dominate.

To verify this, we perform additional first principles calculations considering a variety of possible surface structures of Sn, Bi, and Te on a Bi_2Te_3 substrate. We used fully relativistic projector augmented-wave (PAW) pseudopotentials with spin-orbit interaction, and for polar surface structures, we applied a self-consistent dipole correction in the vacuum

to avoid unphysical electric fields arising from periodic boundary conditions [142]. We fixed the surface lattice parameter to the bulk Bi_2Te_3 value of 4.383 Å and allowed atomic positions to relax until all axial forces were less than 1.0×10^{-4} Ry/ a_0 . We used a $3 \times 3 \times 1$ \mathbf{k} -point mesh, and confirmed our results by spot-checking against a denser $6 \times 6 \times 1$ \mathbf{k} -mesh.

We investigated the stability of each of the following surface structures by placing them on 2 QLs of Bi_2Te_3 :

- 4 bulk-like atomic layers of each of Bi, Sn, and Te,
- an additional QL of Bi_2Te_3 ,
- 4 bulk-like atomic layers of $\text{SnTe}(111)$ in both the Sn-interfacial and Te-interfacial and configurations,
- a single-layer triangular lattice of Sn,
- a buckled hexagonal lattice of stanene, equivalent to two layers of a triangular lattice,
- and several structures intercalating one or two atomic layers of Sn^0 into the substrate, either between two Bi_2Te_3 QLs or within a single QL.

We computed the energy of each surface structure and then constructed the convex hull for ternary mixtures of Bi, Sn, and Te (Figure 4.7). Compounds that appear at a vertex on the convex hull are stable, while those in the interior of a triangle are energetically unstable against decomposing into the three compounds on its triangle's corners. Adding a small amount of Sn to a Bi_2Te_3 substrate corresponds to moving along the dashed red line in Figure 4.7; all such systems have a thermodynamic tendency to decompose into bulk Bi, Bi_2Te_3 , and SnTe . These results are consistent with most elements of the picture presented in Figures 4.4(e-f). They do not address the possibility of Sn^0 buried deep within the Bi_2Te_3

Table 4.1: Bulk heats of reaction for Sn deposited on various substrates. All potential substrates have a hexagonal (0001) surface and provide a close lattice match to stanene.

Substrate	Products of reaction with Sn	ΔH_{rxn} (kJ/mol Sn)
Bi ₂ Te ₃	2 Bi + 3 SnTe	−30.9
BaTe	Ba + SnTe	−68.4
CdTe	Cd + SnTe	33.4
PbTe	Pb + SnTe	11.6
InSb	In + SnSb	43.1
	Sn + InSn ₂	1.9
Cu	Cu ₃ Sn	−7.5
Au	AuSn	−15.8
Ag	Ag ₃ Sn	−4.1
Al ₂ O ₃	2 Al + 3 SnO ₂	534.5
AlN	2 Al + Sn ₃ N ₂	211.2
BN	2 B + Sn ₃ N ₂	166.5
GaN	2 Ga + Sn ₃ N ₂	228.0

substrate. However, we do note that of all the intermixed structures, the most stable was a single Sn layer intercalated between two intact Bi₂Te₃ QLs, lying only 0.12 eV per atom above the convex hull.

The agreement between our observation of mixed growth and the unfavorable bulk heat of reaction provides an efficient method for checking the suitability of potential substrates for stanene growth with criteria that extend beyond favorable lattice constants and topological properties. To evaluate alternative substrates for stanene, we calculate the ΔH_{rxn} for other potential substrates that have been identified in the literature (Table I) [84, 124, 91, 125, 79, 126, 85, 143, 87, 144, 145, 146, 81, 82, 86, 90]. In addition to deposition attempts on Bi₂Te₃, recent work depositing Sn on Au and Ag also presented evidence of substrate alloying with Sn, in agreement with the calculated heat of reaction [79, 82]. There are a few substrates that offer a more favorable energy landscape, such as InSb and PbTe, consistent with previous results [126]. Table 4.1 points to Al₂O₃ or (Al,B,Ga)N as being particularly chemically stable for stanene growth. First principles calculations also confirm the stability

of Al_2O_3 as a substrate for stanene [64]. Considering monolayer stanene has rarely been synthesized on scales larger than hundreds of nanometers [84, 79, 87, 81, 82, 90], this work may provide important guidance to finding more appropriate substrates for large area, thin film deposition of this material.

4.6 Conclusions

In summary, we find that bulk thermodynamics promotes a reaction of Sn with Bi_2Te_3 . We also find that Sn can intercalate in Bi_2Te_3 up to 10-17% stanene monolayers per quintuple layer, which may have interesting properties in the topological insulator Bi_2Te_3 . We predict other hexagonal materials that may serve as suitable, inert substrates for stanene growth.

Chapter 5

Structure and binding of large-area borophene sheets on Cu(111) surfaces

This chapter is adapted from an article entitled “Large-area single-crystal sheets of borophene on Cu(111) surfaces” by Rongting Wu, Ilya K. Drozdov, Stephen Eltinge, Percy Zahl, Sohrab Ismail-Beigi, Ivan Božović, and Adrian Gozar that was published in Nature Nanotechnology [147]. Additional experimental data in support of this chapter can be found in the Supplementary Information of that article, and is referenced where appropriate. RW, ID, PZ, and AG did the experimental work, I did the theoretical work, and SIB and IB provided guidance.

Borophene, a theoretically proposed two-dimensional boron allotrope [11, 148, 12], has attracted much attention [149, 150] as a candidate material platform for high-speed, transparent, and flexible electronics [151, 13, 152, 153]. It has been recently synthesized on Ag(111) substrates [154, 155] and studied by tunneling and electron spectroscopy [156]. However, the exact crystal structure is still controversial, the nanometer-size single-crystal domains produced so far are too small for device fabrication, and the structural tunability via substrate-dependent epitaxy is yet to be proven. In this chapter, we report on a synthesis of borophene by experimentalist colleagues, monitored in situ by low-energy electron microscopy, diffraction, and scanning tunneling microscopy, and modeled by us using *ab initio* calculations. Our colleagues resolve the crystal structure and phase diagram of borophene

on Ag(111) but find that the domains remain nanoscale for all growth conditions. However, by growing borophene on Cu(111) surfaces, our colleagues obtained large single-crystal domains, up to $100 \mu\text{m}^2$ in size. The crystal structure is a novel triangular network with $\eta = 1/5$ concentration of hexagonal vacancies. Our colleagues' experimental data and our first principles calculations indicate charge-transfer coupling to the substrate without significant covalent bonding. Our work sets the stage for fabricating borophene-based devices and substantiates the idea of borophene as a model for artificial 2D materials development.

5.1 Introduction

Metallic sheets of atomically thin borophene are expected to enable new functionalities of two-dimensional (2D) materials and open applications in flexible electronics and near-visible plasmonics [150, 15]. The polymorphism of borophene also opens up concrete paths for engineering structural and electronic properties of anisotropic 2D metallic sheets [11, 150, 151, 13], by choosing different substrates or growth conditions. Atomic boron planes isostructural to graphene already stand out by providing a high critical superconducting temperature ($T_c \approx 40$ K) in MgB_2 , making the prospect of discovering other boron-based 2D superconducting compounds promising [7].

Using Ag(111) substrates and molecular beam epitaxy, a pioneering work demonstrated successful synthesis of atomically thin 2D boron layers organized in islands tens of nanometers in size [154, 155]. Indications for persisting Dirac fermions are present in photoemission data [156, 9] of this boron sheet and their existence is supported by theoretical calculations in several polymorphs [7]. To the extent that simple tight binding approximations provide a good parametrization for *ab initio* band structure calculations in borophene, it is notable that

within nearest-neighbor interaction the degeneracy at graphene K points and the presence of associated Dirac cones are preserved for an arbitrary distribution of “impurity” atoms filling the hexagonal centers of any type of super-cell of a honeycomb lattice. This remains true in higher order hopping for several of the theoretically stable sheets of borophene, with the concomitant appearance of flat or weakly dispersive bands arising from localized orbitals of the center atoms. This peculiarity of the honeycomb lattice is interesting because flat bands can engender strange, non-Fermi-liquid metals, and perhaps open a path to room-temperature superconductivity [157]. In order to realize this potential, it is pressing to explore synthesis of borophene on other substrates and study the ensuing crystal structures.

Notwithstanding the promises for unique electronic and mechanical properties, the lateral extent of borophene domains produced so far makes them amenable to study by only few techniques and is far below the limits required for device fabrication. This is an impediment for gaining access to key properties, such as resistivity, Hall effect, magnetoresistance, etc., because micron-sized single-crystal flakes are needed for such measurements. Here, our colleagues solved this challenge by growing borophene on a different substrate (copper), producing single-crystal domains $10\text{--}100\ \mu\text{m}^2$ in size. Elemental borophene may now be used as a material platform to make devices and study fundamental physics.

The interest in borophene encounters substantial theoretical and experimental challenges. The prediction and targeted synthesis of borophene is a delicate affair because of the existence of many states with energies very close to the overall minimum [11, 148, 12, 13, 152]. Furthermore, it has been predicted that the already-rich phase space for 2D borophene sheets in vacuum can be easily modified by the interaction with the substrate of choice [15]. 2D phases are found to be stabilized by the existence of boron vacancies in a triangular lattice but theory predicts a disconnect between the stable patterns of vacancies

in free-standing and metal-supported borophene [15]. This is important for the transfer of sheets from metallic to device-compatible substrates.

5.2 Methods

Growth of borophene on single crystal Cu(111) and Ag(111) substrates were performed in an ultrahigh-vacuum LEEM system augmented with molecular beam epitaxy (MBE) capability. Real-time monitoring of in-situ growth and of the atomic deposition rate were used to achieve synthesis of high-quality single crystals and precise control of coverage. Single-crystal Cu(111) and Ag(111) were cleaned by repeated cycles of argon ion sputtering and post-annealing, until a clean and broad terraced structure, with corresponding bright and sharp LEED pattern, was observed. Boron was evaporated by an electron-beam evaporator focused onto a pure boron rod. The growth was further characterized using x-ray photoemission (XPS) and atomic force microscopy (AFM) measurements, the details of which are available in the published paper [147].

Scanning tunneling microscopy (STM) data were acquired with a customized Createc scanning tunneling and non-contact atomic force microscope (NC-AFM/STM) system operating in ultra-high vacuum and at a nominal temperature of $T = 5$ K. The Pt/Ir tip was mounted on a qPlus sensor [158] operating at 32 kHz that was used for detection of NC-AFM signals. Pt/Ir tips were prepared by in-situ field emission on clean Au or Cu single crystal surfaces. In-situ boron deposition on sputtered/annealed Cu(111) surfaces at $T \sim 600$ °C was done in a preparation chamber equipped with a LN₂ cooled manipulator and a LEED system. Enhanced spatial resolution was achieved by metal tip functionalization, which was realized by in-situ dosing of carbon-monoxide (CO) molecules and subsequent vertical

manipulation. The measurements were performed using an open-source GXSM SPM control system (P. Zahl, T. Wagner “GXSM - Smart & Customizable SPM Control” Imaging & Microscopy (GIT), Jan. 26, 2015. <http://gxsm.sourceforge.net/>).

Ab initio density functional theory calculations were performed using the Quantum ESPRESSO package [93, 94], using pseudopotentials generated with the Perdew–Zunger local density approximation to the exchange–correlation functional [18]. A plane-wave basis set with an energy cutoff of 476 eV was used. For structural relaxations, the Brillouin zone was sampled at the Γ point, and for DOS calculations a $9 \times 9 \times 1$ Monkhorst–Pack \mathbf{k} -point grid was used [159]. Boron atoms were relaxed until forces were less than 2.5×10^{-3} eV/Å. For calculations on a copper surface, the borophene sheet was relaxed on a two-layer slab of copper at its experimental bulk lattice parameter. STM calculations were performed using the Tersoff–Hamann formalism, with p -type orbitals described using the derivative rule of Chen [37, 40].

5.3 Experimental results

In this work our colleagues utilized the capabilities of low-energy electron microscopy (LEEM) for simultaneous real-time monitoring of dynamics of borophene nucleation and growth, as well as k -space structural characterization by low-energy electron diffraction (LEED) [160, 161, 162, 163]. A setup employing a customized electron-beam evaporation source along with other sample preparation capabilities enables precise control of deposition rates, which is essential for producing crystalline 2D sheets. In order to determine the structure of borophene on Cu(111), our colleagues performed high-resolution scanning tunneling microscopy (STM) measurements [158] using functionalized tips [41, 164] in

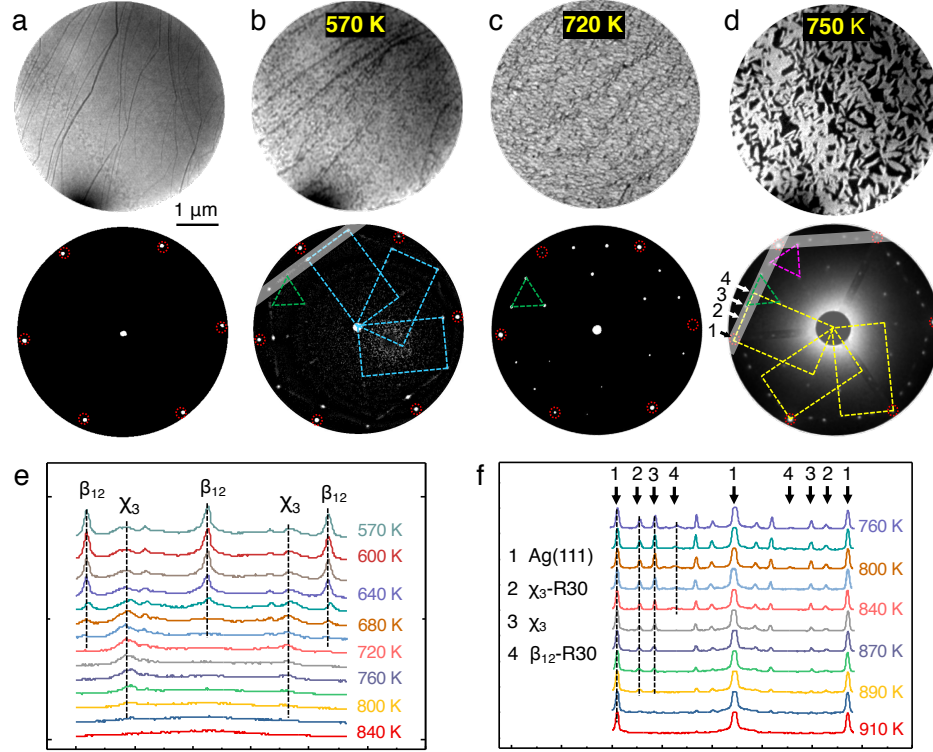


Figure 5.1: Structure of borophene grown on Ag(111) surfaces. (a) The top, real-space image, shows the terraced surface of the pristine Ag substrate revealed by LEEM phase contrast. The corresponding LEED pattern is shown at the bottom. (b) LEEM image of surface morphology (top) for 1 ML coverage and the corresponding LEED pattern (bottom) showing that borophene growth at $T = 570$ K yields primarily the β_{12} structure (blue rectangles) with a weak contribution from χ_3 domains (green triangle). (c) LEEM and LEED images as in panel (b) for borophene growth at $T = 720$ K which yields only the χ_3 structure. The diffraction pattern (green triangle in the bottom panel) shows that the χ_3 UC corresponds to a 3×3 reconstruction of the Ag(111) surface. (d) LEEM and LEED images for borophene growth at $T = 750$ K which generates both β_{12} and χ_3 structures. Two additional UC orientations rotated by 30° with respect to LEED images in panels (b) and (c) appear at this temperature. The rotated structures, denoted by β_{12} -R30 and χ_3 -R30, are shown as yellow rectangles and purple triangles, respectively. (e) Temperature-dependent intensity of the diffraction peaks across the white shaded line profile at the bottom of panel (b). The data show the evolution of borophene structures during heating from $T = 570$ K to 840 K. (f) Temperature-dependent diffraction peak intensities along the white lines in the bottom of panel (d). The data show the evolution with heating from $T = 760$ K to 910 K.

conjunction with our own *ab initio* density functional theory (DFT) calculations [93, 37, 40].

Our colleagues first studied the growth and stability of borophene on Ag(111) surfaces in detail. Previous work used STM data in combination with DFT to infer the crystal structure [154, 155]. For a given 2D borophene sheet, the parameter η is defined [11] as the ratio of vacant hexagon-center sites to the number of triangular lattice sites in a unit cell (UC). An “empty” honeycomb (graphene-like) lattice has $\eta = 1/3$, and a putative all-boron triangular lattice has $\eta = 0$. For borophene on Ag(111), two structures denoted β_{12} and χ_3 have been proposed, corresponding to $\eta = 1/6$ and $\eta = 1/5$, respectively. Our colleagues have synthesized borophene layers on Ag(111) at various substrate temperatures (Figure 5.1). Both β_{12} and χ_3 phases were indeed identified by LEED, and they confirmed that the former is favored at lower growth temperatures, $550 \text{ K} \lesssim T \lesssim 600 \text{ K}$. Nevertheless, weak diffraction peaks corresponding to the χ_3 phase are also present, indicating phase coexistence in this temperature range. Growth at an elevated temperature, $650 \text{ K} \lesssim T \lesssim 720 \text{ K}$, renders only the χ_3 phase (Figure 5.1(c)). Further increasing the substrate temperature generates additional orientations for χ_3 domains, rotated by 30° , as well as a re-entrance of the β_{12} phase, also with domains rotated by 30° (see Figure 5.1(d) and Supplementary Figures S1 and S2 in [147]). In-situ post-growth temperature ramps in the 550–850 K and 750–910 K ranges (Figure 5.1(e,f)) both show that the χ_3 phase is more stable than the β_{12} counterpart.

Figures 5.1(b,c) show bright-field LEEM and LEED images of borophene on Ag(111). The size of single-crystal domains is only in the range of tens of nm. The domains do not coalesce and the average size does not change even at complete monolayer (ML) coverage. These results are further confirmed by atomic force microscopy (AFM) (Supplementary Figure S3 in [147]). The higher nucleating density on Ag surfaces along with a tendency for

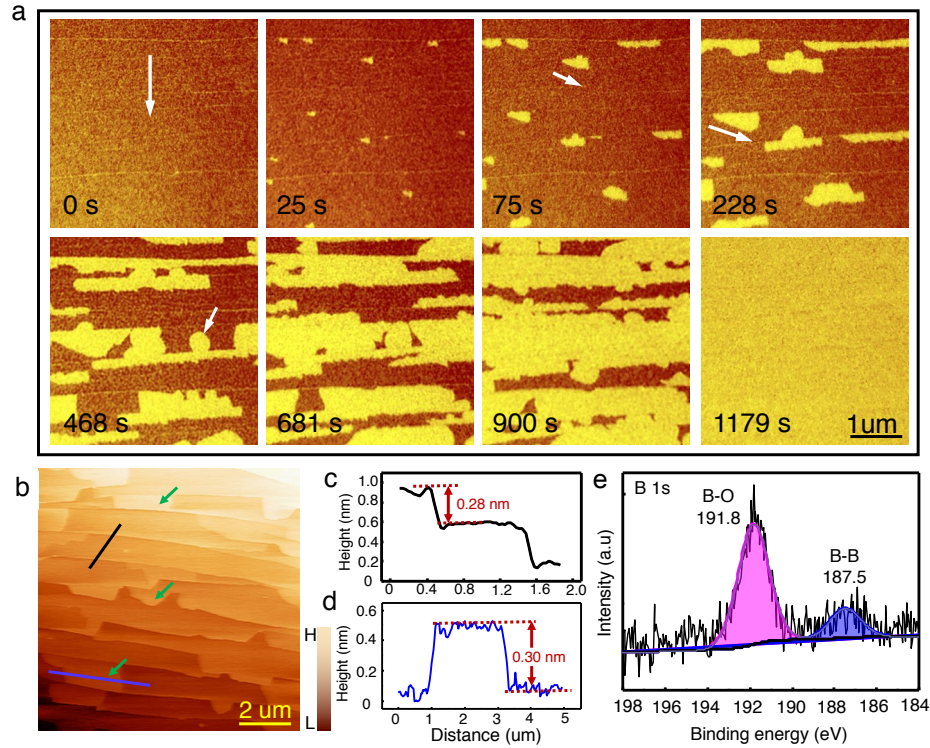


Figure 5.2: Growth dynamics of borophene on Cu(111) surface. (a) Sequence of bright-field LEEM images at $T = 770$ K reveal that borophene islands prefer to nucleate from the down-step edge of Cu terraces (*i.e.*, the direction marked by the arrow in the first, $t = 0$ s, panel) and that growth proceeds faster along the step-edge direction: ~ 97 Å/s compared to ~ 20 Å/s for the perpendicular direction (see also Supplementary Figure S5 in [147]). Snapshots taken at 75 s and 228 s illustrate that at this stage of growth borophene flakes display sharp edges along low-index directions of the substrate, as shown by the white arrows (see also Supplementary Movie “B-Cu111 Triangular Islands” in [147]). These two panels along with the snapshot at 468 s also show that down-step nucleation is followed by borophene growth across the upper step edge. In contrast to the down-step growth, up-step growth generates arc-shaped islands, indicating more isotropic growth kinetics; see the white arrow in the 468 s panel. A continuous monolayer (ML) emerges, reproducing faithfully the Cu(111) terrace structure. The growth rate was ~ 0.05 ML/min (see also Supplementary Movie “B-Cu111 Film Growth” in [147]). (b) Topographic atomic force microscopy (AFM) image around 0.1 ML coverage. The surface RMS is 0.24 Å on Cu(111) terraces and 0.43 Å on borophene islands (green arrows), respectively. (c) Line profile corresponding to the black line in panel (b) showing a 2.8 Å tall atomic step of the Cu substrate. (d) Line profile corresponding to the blue line in panel (b) showing that the thickness of the borophene sheet in ambient conditions is around 3.0 Å. (e) Ex-situ x-ray photoemission (XPS) spectra from a B/Cu(111) sample. The data indicate that after one hour exposure to air about 80% of borophene has been oxidized; see also Supplementary Figure S9 in [147].

boron clustering could be a limiting factor for the average domain size. Indeed, continuing deposition beyond one full ML coverage leads to a reduction of crystallinity (dark areas in Figure 5.1(d)). The bright areas in the same panel correspond to regions where nanosized β_{12} -30°, χ_3 -30° and χ_3 domains are found to coexist and, occasionally, even overlap with each other spatially (dark-field images in Supplementary Figure S4 in [147]).

In order to produce larger domains, we have explored candidate substrates less inert than Ag, *i.e.*, potentially able to promote growth of larger domains, but not so reactive as to form metal boride compounds. Our data support the notion that Cu substrates achieve this balance. Figure 5.2 illustrates nucleation and growth of a large area ML film of borophene on a single-crystal Cu(111) substrate, at $T = 770$ K and at the rate of 0.05 ML/min (see the Supplementary Movie “B-Cu(111) Film Growth” in [147]). The growth on lower terraces of Cu step edges is anisotropic and proceeds at a rate that is about five times faster along the step edge than in the perpendicular direction (Supplementary Figure S5 in [147]). Nucleation on upper terraces follows subsequently and displays more isotropic growth kinetics. Growth of single crystals ensues once the density of nucleation sites reaches a saturation value observed to be around $0.75/\mu\text{m}^2$. Ambient AFM data (Figure 5.2(b-d)) corroborate the growth of one-atom-thick borophene islands.

LEED and dark-field LEEM images in Figure 5.3 show that the borophene sheets are composed of large single-crystal domains. The domain length along the terrace directions can exceed $10\ \mu\text{m}$. Domain widths in the perpendicular direction can be limited by the terrace width, typically $1\text{--}3\ \mu\text{m}$ and determined by the angle of surface miscut with respect to the Cu(111) plane. Nevertheless, boundaries of borophene domains do not always follow the Cu terraces, and it is common to find borophene flakes that cross many steps edges (Supplementary Figure S6 in [147]). In spite of the large number of Bragg peaks in the

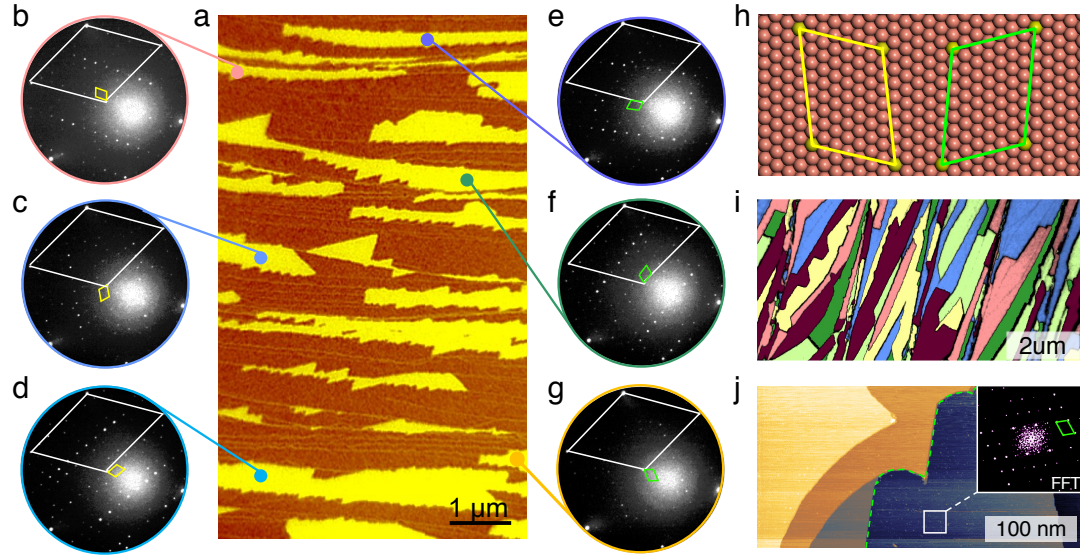


Figure 5.3: **Domain structure of borophene on Cu(111) revealed by selected area diffraction.** (a) Bright-field LEEM image for borophene on Cu(111) at about 0.4 ML surface coverage. Borophene appears in yellow color. (b-d) Selected area LEED patterns taken from single-crystal domains of borophene using an electron beam focused to $1.5\ \mu\text{m}$. The three different LEED patterns orientations correspond to three domain orientations which can be connected by the 120° rotations. The large white rhombus corresponds to the Cu(111) substrate unit cell (UC) while smaller yellow rhomboid defines the borophene UC. (e-g) Selected-area LEED patterns for the three remaining domains which are mirror-symmetric with respect to those depicted in panels (b-d). The reciprocal UC of borophene is shown in green. The six domains in panels (b-g) share the same structure and exhaust the observed domain orientation variety for borophene on Cu(111). (h) The two mirror symmetric UCs of borophene correspond to a $(\sqrt{73} \times \sqrt{39})R \pm 5.8^\circ$ superstructure on Cu(111). Yellow and green rhomboids are the real-space correspondents of the reciprocal UCs shown in (b-d) and (e-g), respectively. (i) Combined dark-field images of a multi-domain flake of borophene. The color coding from panels (b-g) is carried through in panel (i). (j) A large-area Scanning Tunneling Microscope (STM) image at about 0.5 ML borophene coverage. The boundary of a single domain (dark blue) is marked by a green dashed line. Other areas in this panel correspond to terraces of uncovered Cu(111). The inset shows a Fourier transform of the STM signal from the area marked by white rectangle inside the borophene domain. The reciprocal space information obtained in this way is in agreement with electron diffraction data.

LEED data, our colleagues observe that many of them “light up” the same domain structure. Our colleagues elucidate this domain structure by performing μ LEED. Figure 5.3 and Supplementary Figure S6 in [147] demonstrate that the entire ML is made out of six domain types. They are obtained by 120° rotations of two types of UCs with different chiralities (Figure 5.3(i)), and correspond to a single structural phase. The UC of our structure is $21.84 \text{ \AA} \times 15.96 \text{ \AA}$ in size, larger than those corresponding to β_{12} and χ_3 sheets, and is rotated by a small angle ($\pm 5.8^\circ$) with respect to the [100] direction of the Cu(111) surface (Figure 5.3(h)). While domain sizes are generally correlated with substrate step edges, large individual Cu terraces also allow faceted island growth (Supplementary Figure S7 and Supplementary Movie “B-Cu111 Faceted Islands” in [147]). Important and delicate questions involving possible boride formation, B–Cu solubility or the role of evaporation and sub-surface dissolution are also elegantly solved using LEEM capabilities: our colleagues are able to induce subsurface dissolution and resurfacing of crystalline borophene sheets by thermal cycling the Cu(111) substrate covered by a full ML of borophene (see Supplementary Figure S8 and Supplementary Movie “B-Cu(111) Miscibility” in [147]).

5.4 Theoretical structure search

To decipher the internal structure of the UC, we performed STM measurements and *ab initio* density functional theory (DFT) calculations. Figure 5.3(j) and Figures 5.4(a,b) show large area topographic STM images of a borophene domain on Cu terraces. The Fourier transform of the topographic signal is in very good agreement with LEED results indicating that the same borophene structure is preserved at $T = 5 \text{ K}$. STM tip functionalization with carbon monoxide molecules [158, 41] dramatically improves the spatial resolution compared to

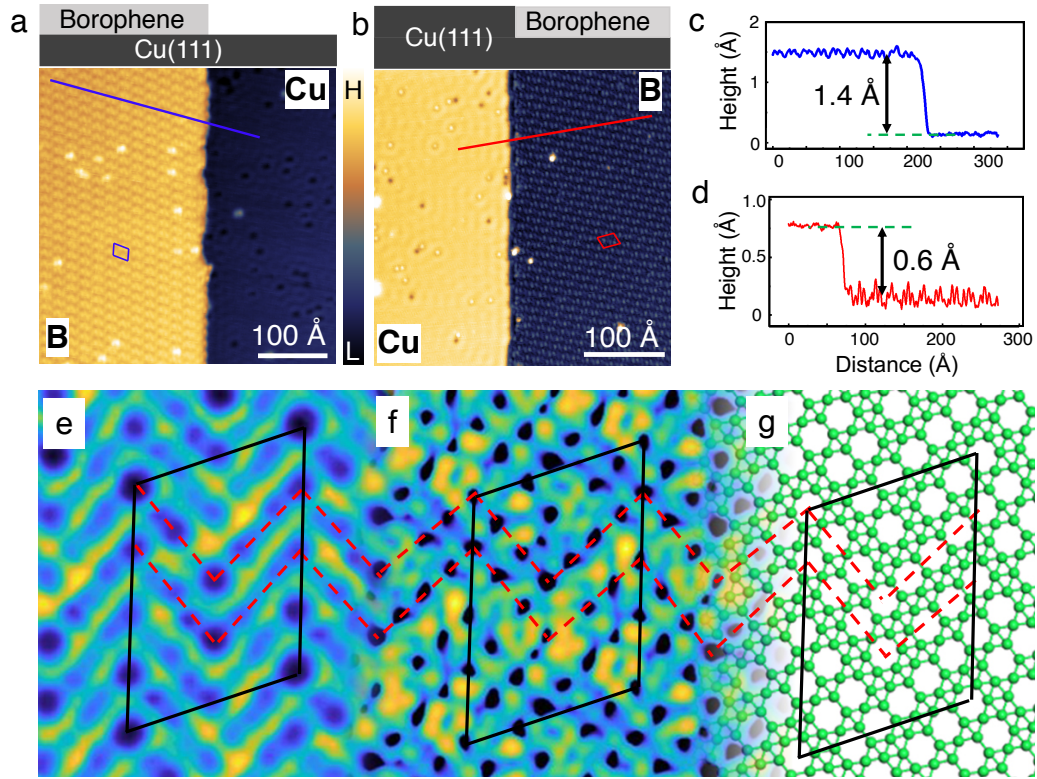


Figure 5.4: **Structure of borophene on Cu(111) as revealed by STM data and DFT simulations.** (a) Large area STM topographic image of a borophene-Cu step edge (setpoint parameters: $I_s = 10$ pA and $V_b = +100$ mV). Color coding: borophene appears in yellow (higher z -values) and is identified by the UC motif, displayed as a small blue rhomboid; Cu appears in dark blue (lower z -values). The top drawing illustrates this layering sequence. (b) Same as panel (a) but for a different z -stacking: here the scanning captures a borophene domain which most likely nucleated from a down step edge of a Cu terrace; see discussion in Figure 5.2. (c,d) Profiles across the blue and red lines in panels (a) and (b), respectively. The height difference between borophene and the top Cu layer is 1.4 Å in panel (a) and -0.6 Å in panel (b), indicating a reduced density of states (DOS) in borophene with respect to Cu. (e) Ultra-high resolution STM data of borophene (setpoint parameters: $I_s = 50$ pA and $V_b = +20$ mV). The rhomboid corresponds to the borophene UC and the red dashed lines are guides along the zig-zag pattern characteristic of all STM data, see Supplementary Figure S10 in [147]. (f) DFT-simulated constant tunneling current isosurface of the proposed borophene structure, assuming a p_z tunneling state for the tip [40]. (g) Pictorial view of the borophene structure with B atoms and bonds shown in green. The red dashed lines continue the basic zig-zag motif from panel (e) through the DFT simulations (panel (f)) and the proposed balls-and-sticks structure (panel (g)).

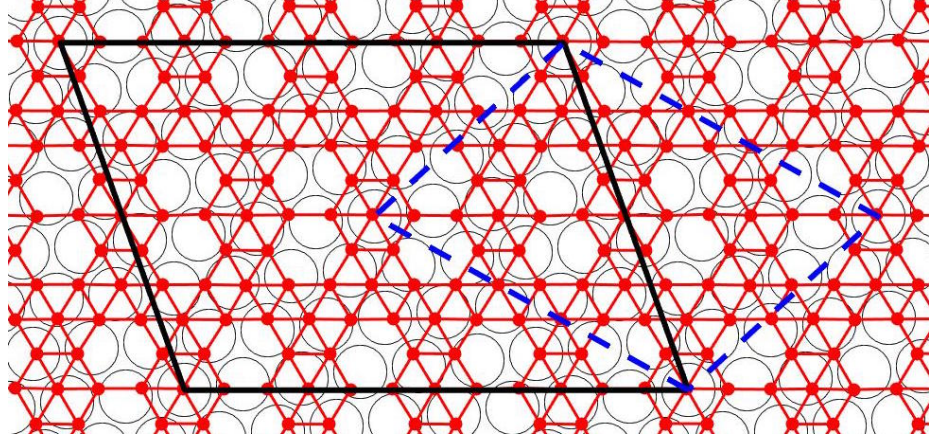


Figure 5.5: **Atomic positions for a relaxed borophene structure with hexagonal vacancy concentration $\eta = 2/15$.** Large empty circles represent the top layer of the Cu(111) surface. Filled red dots are B atoms and red lines are bonds between them. The black solid line represents the borophene unit cell (UC), depicted also in Figure 5.4. The blue dashed line is the UC of the $\eta = 2/15$ structure as obtained by DFT and is half the size of the one determined by electron diffraction because of centering (note also that the center of the UC determined by DFT is also an inversion symmetry point). We found that none of the starting $\eta = 2/15$ arrangements used in simulations was able to break the symmetry of the smaller (dashed blue) UC. Although the energy differences between the initial and relaxed structures were relatively small (~ 0.03 eV/atom), they would always converge towards the centered lattice. This robust result allowed us to rule out the $\eta = 2/15$ structure as a possible candidate.

what is typically achieved with bare metallic tips (Supplementary Figure S10 in [147]). Such ultra-resolved STM data allow us to propose an array of potential planar borophene sheets, whose stabilities are subsequently found by DFT calculations and relaxations [93, 37]. Figure 5.4(e-g) summarizes this procedure and display our proposed structure of borophene on Cu(111) substrates, which is also the one with the largest binding energy of all the sheets investigated. The good agreement between the experimental (Figure 5.4(e)) and DFT simulated structure using tunneling states with p_z character [40] for the functionalized STM tip (Figure 5.4(f)) supports this assignment. The proposed structure has a boron vacancy density of $\eta = 1/5$ (the same as the χ_3 structure).

Our search for borophene structures compatible with both LEED (Figure 5.3) and high

resolution STM data (Figure 5.4) was guided by the constraints of preserving average B–B distances within a 1.7 ± 0.1 Å window as well as by matching the zig-zag pattern seen in the STM data (see Figure 5.4(e)) to low index azimuths of the underlying honeycomb lattice, *i.e.*, along B–B directions and 30° away from them. We generated a library of potential structures and, after applying these constraints, narrowed them down to eight candidates. We analyzed all of them in detail by performing full atomic relaxations on Cu(111). The one with the largest binding energy is the one shown in Figure 5.4(g).

In addition to these eight structures, we investigated the vacuum and on Cu(111) stability of more than a dozen of various other types of borophene layers that could be, in principle, compatible with either the CO-functionalized data or lower-resolution STM data obtained with metallic Pt/Ir tip. All candidates were found to be stable as sheets in vacuum, but many were found to be unstable on our specific substrate. An example of an $\eta = 2/15$ structure that is stable both in vacuum and on Cu(111) but was rejected on account of being at odds with electron diffraction data is shown in Figure 5.5. This structure was stable on Cu(111), but invariably preserved the symmetry of the smaller unit cell indicated in dashed blue lines, rather than the larger black experimental unit cell. As a result, it could not replicate the high-resolution STM data, so we ruled it out.

Another example is shown in Figure 5.6. In this case, a honeycomb “backbone” is preserved in the free-standing sheet but disrupted once the borophene layer is bound to the substrate. It is interesting to note that stable 2D B/Cu(111) structures can accommodate relatively large amount of (typically anisotropic) strain, up to almost 10% compared to B–B bond lengths of relaxed sheets in vacuum. The proposed structure in Fig. 4 is under $\sim 6.5\%$ and $\sim 2\%$ anisotropic strain in the directions of its long and short axes, respectively. This suggests that charge transfer and potential chemical interactions with the substrates have a

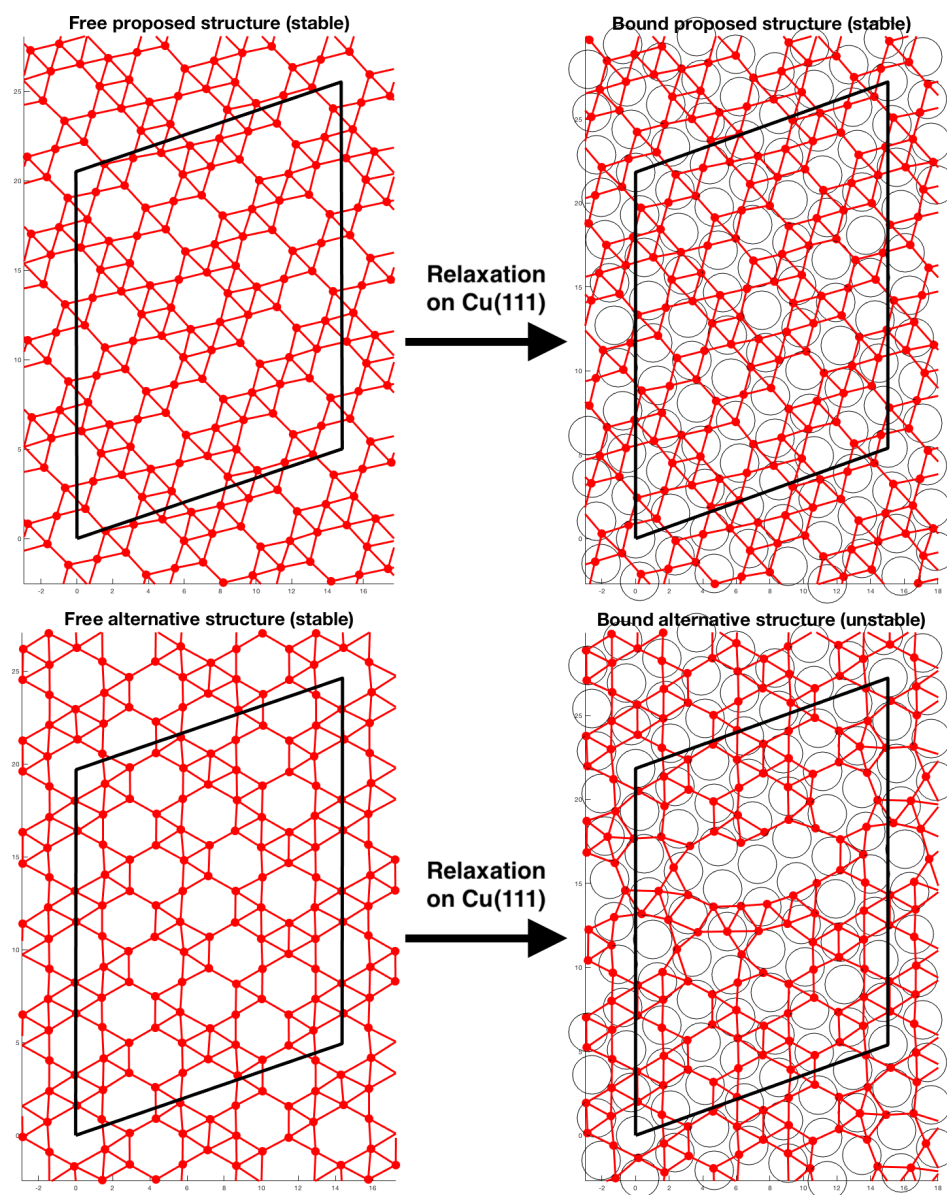


Figure 5.6: **Atomic positions for proposed and alternative borophene structures on Cu(111).** This figure provides an illustration of other types of structures we considered. Symbols have the same meaning as in Figure 5.5. The upper two images show a schematic of the proposed structure (also shown in Figures 5.4(e-f)), while the lower two images show an alternative structure that was considered and rejected as unstable on Cu(111). In each pair, the left-hand image shows the free-standing borophene layer, with both its unit cell and its atomic positions relaxed in vacuum. The right-hand image shows the borophene layer strained to the experimentally determined unit cell and bound to the Cu(111) surface. The proposed structure (top panels) is stable upon binding to the substrate, while the alternative structure (lower panels) is stable in vacuum but becomes substantially deformed upon binding to Cu(111).

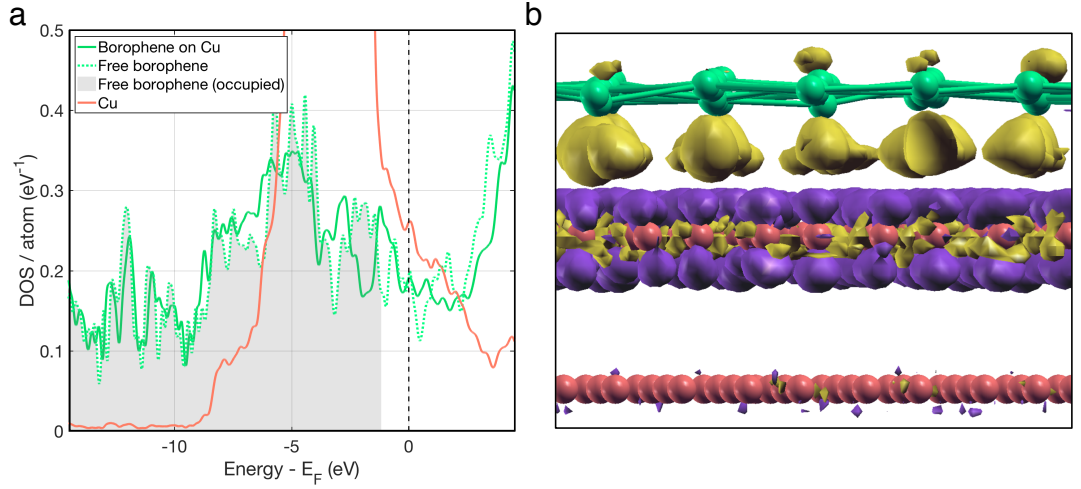


Figure 5.7: Charge-transfer interaction between borophene and Cu(111) surface. (a) Electronic DOS for the relaxed borophene sheet on Cu (green solid curve), for the same structure relaxed in vacuum (“free” borophene – green dotted curve) and for Cu (pink curve). Shaded area corresponds to the occupied states for the undoped free borophene. DFT calculations show that relaxed B/Cu(111) is electron doped by 0.23 e/B atom. The vertical dashed marks the Fermi level (E_F) in B/Cu(111) as well as that of the isolated borophene if it were electron doped by 0.23 e/atom (this doping amount shifts E_F of the isolated borophene by 1.18 eV). The high similarity between the green curves indicates that the interaction between borophene and Cu is of a charge-transfer type with a minor degree of covalence. (b) Isosurface plot of charge redistribution between Cu planes (pink atoms) and relaxed borophene (green atoms) along the (100) direction of the underlying honeycomb lattice. Electron depletion is shown in purple and accumulation in yellow: electrons move from Cu d_{z^2} - into B p_z -like orbitals. This real-space image further confirms the charge-transfer scenario and the lack of significant covalent bonding between borophene and Cu.

more prominent role in determining the actual structure [154].

Our *ab initio* calculations reveal a rather flat sheet of relaxed borophene with a z -corrugation of only 0.43 Å, consistent with prior theoretically investigated structures on Cu(111) with smaller UCs [15, 165]. The average boron-boron bond length is 1.72 Å, with a spread < 0.2 Å, which indicates that the sheet on Cu(111) is under anisotropic, $\approx 4\%$ on the average, tensile strain compared to the corresponding structure relaxed in vacuum. More details on other borophene structures we investigated can be found in Section 4 of

the Supplementary Information in [147]. We investigated the film-substrate interaction, a relevant parameter for prospective sheet transfer and device fabrication (Figure 5.7). The calculations show that our borophene structure in Figure 5.4 is electron doped via charge transfer with no significant covalent bonding. The value of $\eta = 1/5$ can be understood if one takes into account that the self-doping mechanism [12, 166] in conjunction with the electron transfer from Cu to B is expected to increase η above $\eta \approx 1/9$ (maximum stability for isolated sheets). Our findings are generally in agreement with the predicted behavior of 2D boron on Cu(111) surfaces [15, 165] and confirm the predictive power and capabilities of *ab initio* calculations for guiding future choices of material substrates for structural and electronic engineering of 2D sheets of borophene.

5.5 Conclusion

Data on both Cu and Ag substrates indicate that the formation of atomically thin 2D boron sheets is a self-limiting process; this is advantageous for synthesis of heterostructures based on atomically thin layers. Indeed, beyond 1 ML coverage, the growth rate on Cu and Ag decreases dramatically, even if the boron flux is substantially increased. Next, our study illustrates several other differences brought about by the material choice for the substrate. Growth dynamics, the influence of incoming atomic flux or substrate temperature on the structure, film adhesion and rippling [154, 155, 167, 168] are shown to be very different on the two substrates. This is crucial from the device fabrication perspective, because synthesis of large-size domains is required for engineering heterostructures. Our results underscore the importance of borophene-substrate interactions and the choice of substrate materials. Simultaneous real- and k -space mapping is shown to be very useful for controlled synthesis

and characterization of new 2D phases, and in conjunction with several elemental sources can also be used to visualize heterostructure growth.

Chapter 6

Long-wavelength modulation of borophene sheets on Cu(100) surfaces

This chapter is adapted from an article entitled “Borophene on Cu(100) surface” by Rongting Wu, Stephen Eltinge, Ilya K. Drozdov, Adrian Gozar, Percy Zahl, Jerzy T. Sadowski, Sohrab Ismail-Beigi, and Ivan Božović that has been accepted for publication in Nature Chemistry. Additional experimental data in support of this chapter can be found in the Supplementary Information of that article when it becomes available, and is referenced where appropriate. RW, ID, AG, PZ, and JS did the experimental work, I did the theoretical work, and SIB and IB provided guidance.

In the previous chapter, we discussed a project in which we characterized the physical and electronic structure of two-dimensional borophene on the Cu(111) surface. In this chapter, we report on a followup study with the same collaborators concerning borophene on the Cu(100) surface. On this surface, borophene takes on a new crystal structure, with ten boron atoms and two hexagonal vacancies in the unit cell. First-principles calculations indicate that charge transfer rather than covalent bonding binds 2D boron to the copper surface. Intriguingly, the electronic band structure features multiple anisotropic tilted Dirac cones, indicating the potential co-existence of type-I and type-II Dirac and Weyl fermions.

6.1 Introduction

The electronic band structure of graphene features isotropic gapless Dirac cones that host massless fermionic quasiparticles [1, 169]. This has triggered an intense search for new quantum 2D materials to realize other exotic quasiparticles, such as the analogs of massless Dirac, Majorana, and Weyl fermions. Honeycomb-lattice 2D sheets have been synthesized of various group-IV elements: silicene [170, 171], germanene [172, 173], and stanene [84, 87]. They were shown to feature exotic properties absent in their 3D counterparts, promising new applications.

Borophene can be realized by periodically adding extra boron atoms at the centers of hexagons in a honeycomb-like boron lattice, or equivalently, as a triangular boron lattice with some sites vacant. By choosing different vacancy patterns, borophene with different in-plane structures can be envisaged. Many of these structures are predicted to have similar energies, giving rise to intrinsic polymorphism [11, 12, 13]. This suggests that by choosing the substrate and the synthesis recipe, one can engineer various borophene atomic structures, thus tailoring the electronic properties. Of particular interest is the potential for 2D superconductivity, given the small atomic mass of boron in conjunction with the predicted strong electron-phonon coupling [174, 7]. Experimentally, MgB_2 —a stack of 2D honeycomb boron sheets separated by magnesium atoms—is indeed a superconducting compound with a relatively high critical temperature ($T_c \approx 40$ K). Borophene has also been predicted to support massless Dirac fermions [10, 9, 175] and to find applications in flexible electronics [153], energy storage [176] and sensors [177].

Unlike carbon, boron by itself does not form layered structures in nature—the 3D boron structure is more stable than any of the conjectured 2D boron polymorphs [151, 178].

However, it was predicted that 2D boron sheets may be epitaxially stabilized on appropriate substrates that have low boron solubility and do not form borides [154], e.g., gold, silver and copper.

Following these suggestions, borophene was successfully synthesized on Ag(111) surfaces, with an island size on the scale of tens of nanometers [154, 155]. Two borophene structures were identified: the β_{12} phase with vacancy fraction $\eta = 1/6$ (the ratio of vacant to total number of sites in the triangular boron lattice), and the χ_3 phase with $\eta = 1/5$, respectively. Dirac-cone dispersion was predicted from theory [10] and observed experimentally by angle-resolved photoemission spectroscopy (ARPES) [9, 175]. Anticipating borophene integration in nanoelectronics, self-assembly of line defects [168] and borophene-based heterostructures [179, 180] has been pioneered. However, nanoscale flakes of borophene on Ag(111) surfaces are too small for transport measurements. This motivated us to undertake synthesis of borophene on the “stickier” Cu(111) surface [147, 181]. In this way, the lateral extent of borophene islands was increased by two orders of magnitude; single-crystal domains up to $100 \mu\text{m}^2$ -sized were reproducibly obtained. In the pioneering work [154, 155, 147], (111) substrates were initially chosen because these surfaces have the same symmetry as that of the boron lattice; however, the emerging borophene sheets contain vacancies that are ordered in patterns that often display lower symmetry. This, in turn, gives rise to the formation of domains and domain boundaries, which are typically unwanted since they could affect the material’s transport properties and degrade the device’s performance. In principle, substrates with lower symmetry could favor energetically and select one over the other of domain orientations, thus suppressing the formation of domain boundaries. Moreover, by creating incommensurate coordination between borophene and the substrate, borophene-substrate interactions could be reduced. This is somewhat analogous to the ven-

erated case of twisted bilayer graphene and twisted bilayers of other quantum 2D materials. These have been found to display moiré patterns, flat bands, strongly-correlated electron properties including Mott insulator state, electronic nematicity, emergent magnetism and superconductivity, and much more. In the present chapter, we have chosen the Cu(100) substrate, because it has a flat surface with a square lattice that could incommensurately modulate the adsorbed hexagonal boron lattice and alter the vacancy patterns in novel and surprising ways. The Cu(100) substrate thus appeared to be a promising candidate to examine the influence of the substrate symmetry on the resulting borophene structure, clarify the corresponding structure-property relations, and search for novel emergent physics. The challenge was to find the proper balance between the two competing requirements—we wish the substrate–borophene interaction to be weak enough to sustain incommensurate structures of interest, yet strong enough to stabilize borophene by sufficient charge transfer needed to alleviate the electron deficiency.

In the work on which this chapter is based, our colleagues utilized molecular beam epitaxy (MBE) synthesis enlightened by monitoring of the growing film surface using LEEM and LEED in real time. They developed a process to fabricate large-scale, high-quality borophene sheets on Cu(100) surface. By controlling deposition of boron and substrate topography, they can choose to synthesize isolated faceted micrometer-size borophene islands or to achieve full monolayer coverage. Using micro-LEED and dark-field LEEM techniques, they identified the occurrence of four rotational borophene domains and imaged their distribution. They have used in-situ X-ray photoemission spectroscopy to discern the chemical signatures of copper and boron before and after borophene growth. Combining LEED, high-resolution STM measurements with CO-functionalized tips [41, 164], and *ab initio* density functional theory (DFT) calculations [93, 94], we have determined the atomic

structure of borophene on the Cu(100) surface. We have found that this new borophene phase has a small (roughly $5 \times 6 \text{ \AA}^2$) rectangular unit cell that contains ten boron atoms and two hexagonal vacancies. DFT calculations reveal four different Dirac cones in its electronic band structures. Some of these cones are anisotropic and tilted, indicating the possibility to host type-II Dirac and Weyl fermions.

6.2 Methods

As described in the previous chapter, borophene was synthesized on a single-crystal copper substrate using an MBE coupled to an Elmitec LEEM-III system. The material's growth and final state were characterized using x-ray photoemission (XPS), atomic force microscopy (AFM), and scanning tunneling microscopy (STM) measurements. The experimental procedure is broadly outlined in Section 5.2. Further details are available in the published versions of the previous chapter [147] and in the forthcoming paper corresponding to this chapter.

Ab initio DFT calculations were performed using the Quantum ESPRESSO package [93, 94] with pseudopotentials generated with the Perdew–Zunger local-density approximation to the exchange–correlation functional [18]. A plane-wave basis set with an energy cutoff of 476 eV was used. For relaxations, the Brillouin zone was sampled at the Γ point, and a Monkhorst–Pack grid with a spacing of 0.1 \AA^{-1} between points was used for DOS calculations [159]. Boron atom positions were relaxed until the forces were less than $2.5 \times 10^{-3} \text{ eV \AA}^{-1}$. For calculations on a copper surface, the borophene sheet was relaxed on a three-layer slab of copper, assuming its experimental bulk lattice parameter. STM calculations were performed using the Tersoff–Hamann formalism, with *s*-type or *p*-type

orbitals described using the derivative rule of Chen [37, 40]. 2D Gaussian filtering of the calculated STM image with a standard deviation $\sigma = 1.0 \text{ \AA}$ was performed to simulate a resolution comparable to that in the experimental STM image.

6.3 Experimental results

Borophene was synthesized by slowly depositing boron atoms onto a hot Cu(100) surface, with the growing process illustrated by a sequence of bright-field LEEM images in Figures 6.1(a-h). The initial nucleation of borophene islands happens at the down-step edges of the Cu(100) terraces, as highlighted by the green arrows in Figure 6.1(b). The nucleus density is around $1.25 \mu\text{m}^{-2}$. As more boron is deposited, borophene islands start to grow, first along the step edges, and then covering a single terrace without nucleation of new islands (Figure 6.1(c,d)). Subsequently, borophene islands keep growing continuously across multiple terraces (Figure 6.1(e,f)), eventually reaching up to several micrometers in size. Finally, all borophene islands merge together, forming a continuous monolayer film covering the entire surface, as shown in Figure 6.1(g,h). Our colleagues found that at $T = 753 \text{ K}$, borophene growth on the Cu(100) surface is self-limiting; once the full monolayer is deposited, subsequent boron atoms do not stick and a second borophene layer does not form.

X-ray photoemission spectroscopy data, with a focus on copper $3p$ and boron $1s$ core levels, were taken before and after borophene growth, and are shown in Figures 6.1(i-k). In Figure 6.1(i), upper panel, the two peaks at binding energies of $E = 75.1 \text{ eV}$ and $E = 77.3 \text{ eV}$ correspond to the $3p^{3/2}$ and $3p^{1/2}$ orbitals, respectively, of the pristine copper substrate. After borophene growth (Figure 6.1(i), lower panel), no new peaks appear, attesting that

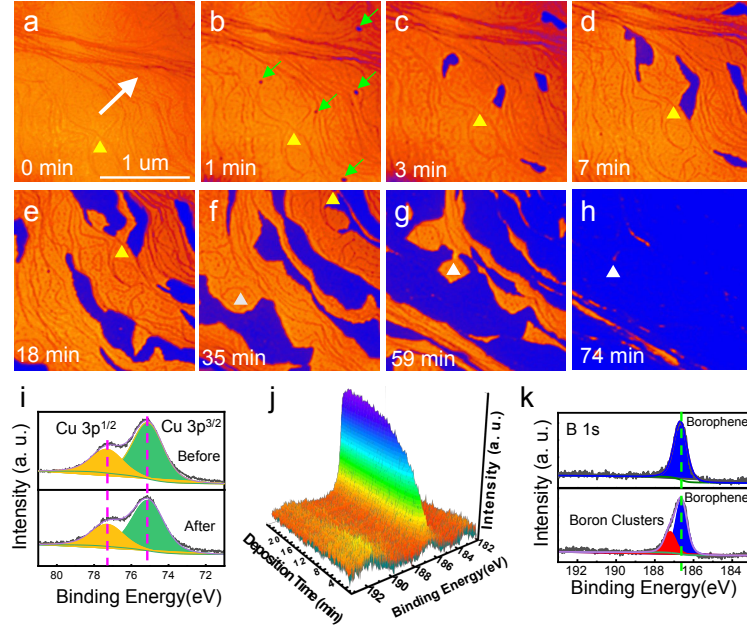


Figure 6.1: Growth dynamics of borophene on the Cu(100) surface. (a,b) The sequence of bright-field LEEM images, recorded at $T = 753$ K, reveals that borophene islands prefer to nucleate from the down-step edges of Cu terraces (highlighted by the green arrows in the second panel, $t = 1$ min). The growth rate was ~ 0.013 ML min^{-1} . (c,d) The growth proceeds initially along the step-edge direction, and then covers the whole terrace. (e-g) Borophene growth on a single terrace is followed by growth across the step edges. (The yellow and white triangles in different panels mark two reference points on the surface.) (h) A continuous monolayer forms and covers most of the Cu(100) surface. (i) In-situ XPS of copper, taken before and after borophene growth. The peak at energy $E = 75.1$ eV corresponds to copper $\text{Cu } 3p^{3/2}$, and the $E = 77.3$ eV peak to $\text{Cu } 3p^{1/2}$ orbitals, respectively. (j) Continuous XPS data showing that a sharp single new boron $1s$ peak related to borophene emerges during boron deposition. (k) Top panel: XPS of boron $1s$ core level, after borophene growth at $T = 753$ K, showing the borophene-related peak at $E = 186.6$ eV. Bottom panel: XPS data of the same sample after more boron was deposited at the room temperature, showing a new peak at $E = 187.2$ eV due to formation of 3D boron clusters.

there is no chemical reaction between the copper substrate and the deposited boron atoms. Figure 6.1(j) shows the evolution in time of the X-ray photoemission spectra taken in situ simultaneously with the borophene growth. One can see a continuously rising sharp boron 1s core level at binding energy of $E = 186.6$ eV. As seen in Figure 6.1(k) (upper panel), once the full monolayer borophene coverage has been reached, this sharp boron 1s core level remains unchanged while additional boron is supplied at $T = 753$ K. However, when the sample was cooled down to the room temperature and extra boron was deposited, a new peak appeared at a slightly higher binding energy, $E = 187.2$ eV (the red peak in Figure 6.1(k), lower panel). This new peak originates from boron clusters or 3D bulk boron. (Analogously, the sp^3 orbital in 3D carbon produces a peak at a slightly higher binding energy than the sp^2 orbital in graphene [182].)

LEED patterns and dark-field LEEM images (in Figure 6.2) reveal that the borophene sheet on Cu(100) consists of single-crystal domains with different orientations. By choosing different LEED spots (indicated by different colors in Figure 6.2(b)) and taking respective dark-field LEEM images, our colleagues established that there are four different borophene domain orientations (highlighted by different colors in Figures 6.2(a), (c), (d), and (e)). The shapes of borophene flakes largely conform to the contours of the copper terraces. The long axis of a single-crystal flake is typically oriented along a step edge in the substrate and reaches up to 5–10 μm . The width of the domains is typically 1–3 μm , perpendicular to the step edges, and for the most part limited by the width of substrate terraces.

In Figure 6.2(b), we show a LEED pattern composed by superposing four patterns taken with the electron energies of $E = 2.5$ eV, 6 eV, 10.5 eV and 25 eV, respectively (individual images available in Supplementary Figure S1 of the forthcoming paper). In this way, we can display simultaneously the diffraction spots from the relatively small borophene unit cells

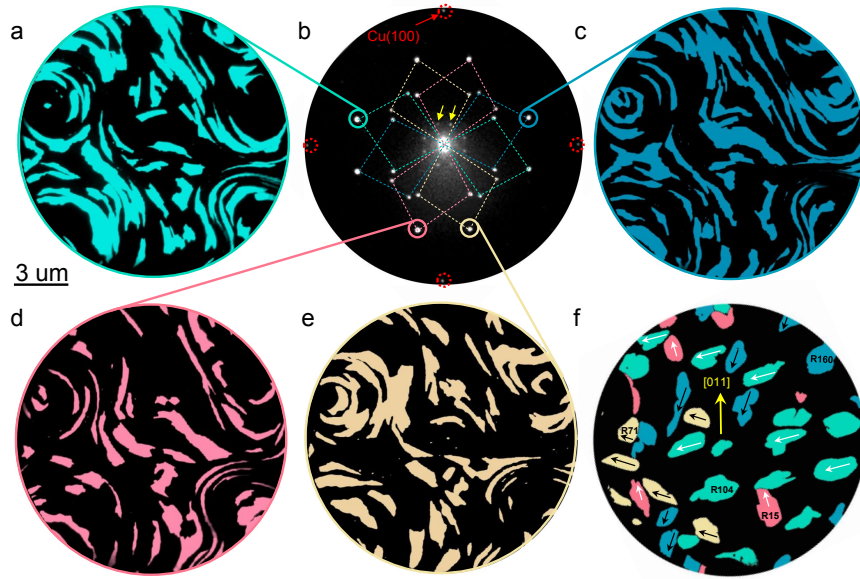


Figure 6.2: **Single-crystal domains of borophene revealed by dark-field LEEM images.** (a) A dark-field LEEM image of borophene taken from the non-specular Bragg spot marked by the green circle in panel (b). The green color highlights the domains contributing to this specific LEED spot. (b) Superposition of the four borophene/Cu(100) LEED patterns taken at the energy of 2.5 eV, 6 eV, 10.5 eV, and 25 eV. The four dashed red circles in the corner highlight the first-order diffraction spots of the Cu(100) substrate itself. The LEED reflections corresponding to different borophene domains are highlighted by differently-colored dashed lines. (c-e) Dark-field LEEM images reveal the distribution of different borophene domains taken from the non-specular Bragg reflection spots marked by blue, pink, and yellow color, respectively. (f) Micrometer-sized, faceted single-crystal borophene islands on a wide Cu(100) terrace. Different orientations are indicated by different colors, and the faceted island edges are highlighted by the white and black arrows. The labels inside select islands specify the angles (counterclockwise) from Cu(011) direction (the yellow arrow) to the direction of the faceted island edge.

(colored dashed lines) and from some large-length-scale super-modulations (yellow arrows near the center). The overall composite LEED pattern is rich and complicated because of the presence of four rotational domains. The rhomboidal reciprocal lattices for different domains are highlighted by different colors. The unit cell size is roughly $5 \text{ \AA} \times 6 \text{ \AA}$ in real space, with the angle of $\sim 83^\circ$ between the two neighboring edges. By rotating 90° or mirror-flipping the unit cells, one can generate the four epitaxially inequivalent rhomboidal lattices, as observed.

On broad terraces, micrometer-sized faceted borophene islands can be created, as seen in dark-field LEEM images (Figure 6.2(f)). Borophene islands with the same orientation exhibit parallel straight edges (highlighted by the white and black arrows). In contrast to the triangular borophene flakes on Cu(111), the facets of the single-crystal islands of borophene on Cu(100) are not oriented along the high-symmetry directions of the substrate. A detailed analysis reveals that these facets mainly follow the zig-zag edges of borophene flakes (Supplementary Figures S6 & S7 of the forthcoming paper), which indicates that here the B–B rather than the B–Cu interactions are playing the dominant role in determining the island shapes.

Our colleagues also investigated the stability of this new borophene phase against heating and oxidization, which is critical for prospective borophene applications. They have established that borophene dissolves when the temperature exceeds 873 K, and that boron atoms resurface forming borophene again once the sample is cooled back down. They also found that this borophene phase can survive for several hours under 10^{-6} Torr partial pressure of oxygen. All of this attests that this new borophene structure is the thermodynamic ground state and not kinetically trapped.

6.4 Structural identification and theoretical analysis

To decipher the atomic structure of this new borophene sheet, we have performed STM measurements and *ab initio* DFT calculations. Figure 6.3(a) shows the large-area STM topography of borophene islands on three broad terraces on the Cu(100) surface. In Figure 6.3(b), we show the line profile measured along the green line in Figure 6.3(a). The height of the borophene edges A and C is the same, 1.1 Å, while the height of the copper step edge B is 2.0 Å. This indicates that this boron sheet is an atomic monolayer, and its density of states (DOS) is lower than that of the Cu(100) surface. In Figure 6.3(c), we show an enlarged STM image of the white rectangle area in Figure 6.3(a). On borophene islands, some linear stripes (highlighted in red and blue) with different orientations become visible.

A high-resolution STM image of the area of junction between two borophene monodomains is shown in Figure 6.3(d). Between the linear stripes (blue and red arrows), isolated yellow dots are arranged in a rectangular lattice, with repeat periods of about 5.3 Å and 6.0 Å. Notably, when these rectangular unit cells cross the stripes, they undergo a dislocation (highlighted by the green and pink dashed lines). Figure 6.3(e) shows the fast Fourier transform (FFT) of the high-resolution STM image of a single borophene domain. It coincides with the LEED pattern (Figure 6.3(f)) taken on a single borophene flake, confirming that the two are capturing the same structure. The effect of the periodic striped modulations and the lattice dislocations in STM topography is to generate a small distortion in the basic borophene reciprocal lattice: the basic borophene reciprocal lattice (the green rectangle in Figure 6.3(f)) is shifted by a small wave vector (the yellow arrows in Figure 6.3(f)). In this way, we can reproduce well the final deformed rhomboid reciprocal lattice in the FFT and LEED patterns. (More details are provided in Supplementary Figure

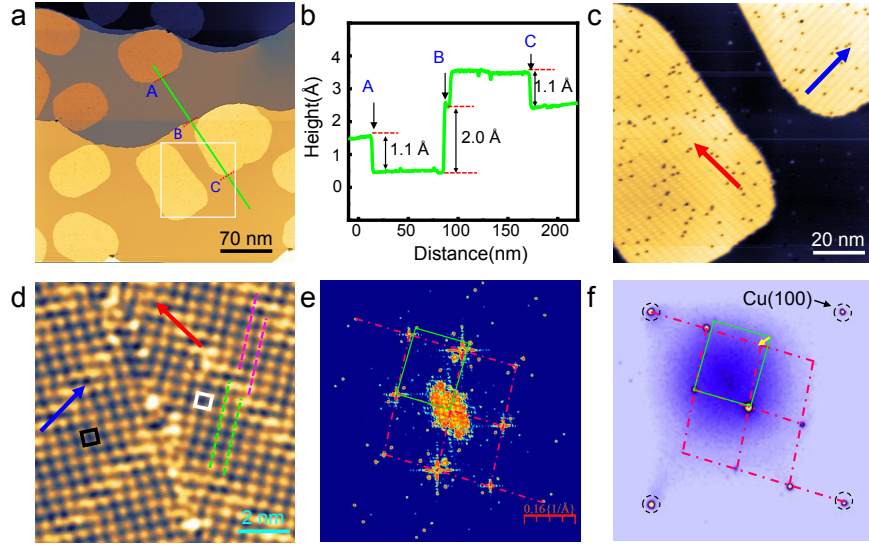


Figure 6.3: Topography of borophene islands revealed by STM. (a) A large scale STM image shows borophene islands grown on the surface of a single-crystal Cu(100) substrate. (b) The cross-section height profile (measured along the green line in the panel (a)) of islands of borophene on Cu(100). (c) The enlarged STM image shows the two borophene islands located within the white rectangle in panel (a). Some straight stripes with different orientations (highlighted by the red and blue arrows) appear in these two islands. (d) A high-resolution STM image shows the junction area where two borophene domains meet. The blue and red arrows indicate the direction of the stripes. Some dots, highlighted by the white and black rectangles, arranged in a rectangular lattice appear between the stripes. The pink and green dashed lines indicate the dislocation of the rectangular unit cells across the stripes. The scanning parameters for STM images are: bias voltage $V_b = +400$ mV, tunneling current $I_t = 30$ pA for (a); $V_b = +400$ mV, $I_t = 30$ pA for (c); $V_b = +500$ mV, $I_t = 200$ pA for (d). (e) Fast Fourier transform (FFT) pattern of a high-resolution STM image of a single-crystal borophene island on Cu(100) surface. (f) A LEED pattern obtained from a single borophene domain. The dashed red lines indicate the reciprocal unit cells. The green rectangle indicates the reciprocal lattice of the real-space unit cells (the black and white rectangles in (d)). The yellow arrow corresponds to the miniature reciprocal lattice generated by the superstructure modulation with a large period in real space.

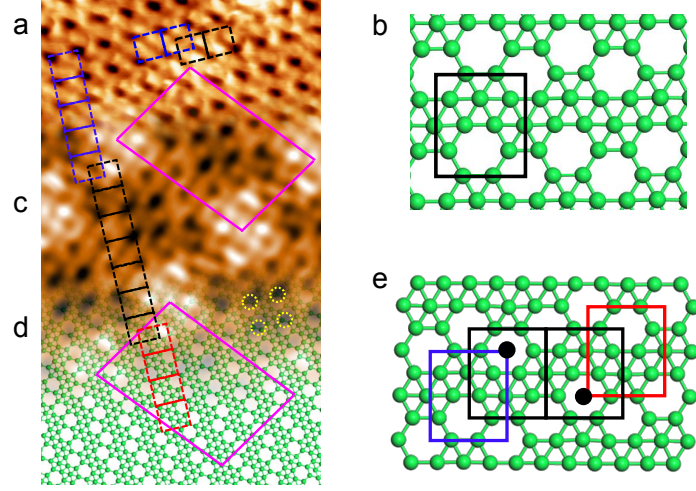


Figure 6.4: **Atomic structure of β_{13} borophene as revealed by STM measurements and *ab initio* DFT calculations.** (a) An ultrahigh-resolution STM image of the borophene surface topography. (The scanning parameters: $I_s = 50$ pA and $V_b = +200$ mV). (b) A pictorial representation of the basic structure of β_{13} borophene, with boron atoms and bonds shown in green. The unit cell contains 10 boron atoms and two vacant sites compared to the ideal triangular lattice. (c) The DFT-simulated, constant-tunneling-current iso-surface of the proposed β_{13} borophene structure on Cu(100). (d) A larger-scale atomistic model that captures the observed superstructure of borophene on Cu(100) surface. The small blue, black and red rectangles correspond to the basic small unit cells, while the big pink rhomboid indicates the large cell of the super-modulation. (e) A schematic of β_{13} borophene lattice with dislocations (highlighted by the blue, black and red rectangles). A continuous dislocation occurs in the middle of two black rectangles.

S5 of the forthcoming paper.)

With higher spatial resolution, our colleagues were able to capture more details of the rectangular unit cell and striped features in the STM topography (see Figure 6.4(a)). The borophene sheet appears as a continuous film with isolated dark spots (“holes”) arranged in a rectangular lattice. In the regular regions away from the white stripes, we typically see that each unit cell contains one dark spot at the corner (the dashed blue rectangle). In the striped areas, a second dark spot appears inside the unit cell, which coincides with the one

at the corner of the neighboring unit cell (the dashed black rectangle) that belongs to the regular area on the other side. In this way, this new borophene phase, with a rectangular unit cell that contains one vacancy at the corner and another one inside, can continuously cross the striped area.

In Figure 6.4(b), we present the atomistic structural model of a new borophene phase, β_{13} , that accounts well for all of our data. It has ten boron atoms and two vacancies, *i.e.*, the vacancy ratio is $\eta = 1/6$. Utilizing DFT calculations, we explored all possible borophene models hosting two boron vacancies in the unit cell of the shape and size close to what is seen in the experiment. As a free-standing sheet, this β_{13} structure is the most stable among such sheets. The optimized unit cell size is $5.04 \text{ \AA} \times 5.82 \text{ \AA}$, as highlighted by the black rectangle. On Cu(100), this unit cell can take four inequivalent orientations; hence, simultaneous nucleation of borophene islands at different locations on the substrate should lead to the formation of domains and domain walls.

A simulated STM image using β_{13} borophene mono-domains as the building blocks on the Cu(100) surface is displayed in Figure 6.4(c). This image is fully consistent with both the real-space STM topography (Figure 6.4(a)) and the atomic model (Figure 6.4(d)). It captures well both the occurrence of single holes in the regular regions and double holes in the striped transition areas. Notably, the dark spots in the STM topography are located halfway between two nearest boron vacancies, as highlighted by the yellow circles. In our *ab initio* calculations and STM simulations for borophene on Cu(100), we have used the large unit cells defined by the super-modulation, highlighted by the pink rhomboids in Figure 6.4. The meaning and the role of the small unit cell are that it is the most stable “local” building block of borophene on the Cu(100) surface. However, it does not fit perfectly on the Cu(100) surface, so some distortion is necessary. But because this small unit cell is so stable, rather

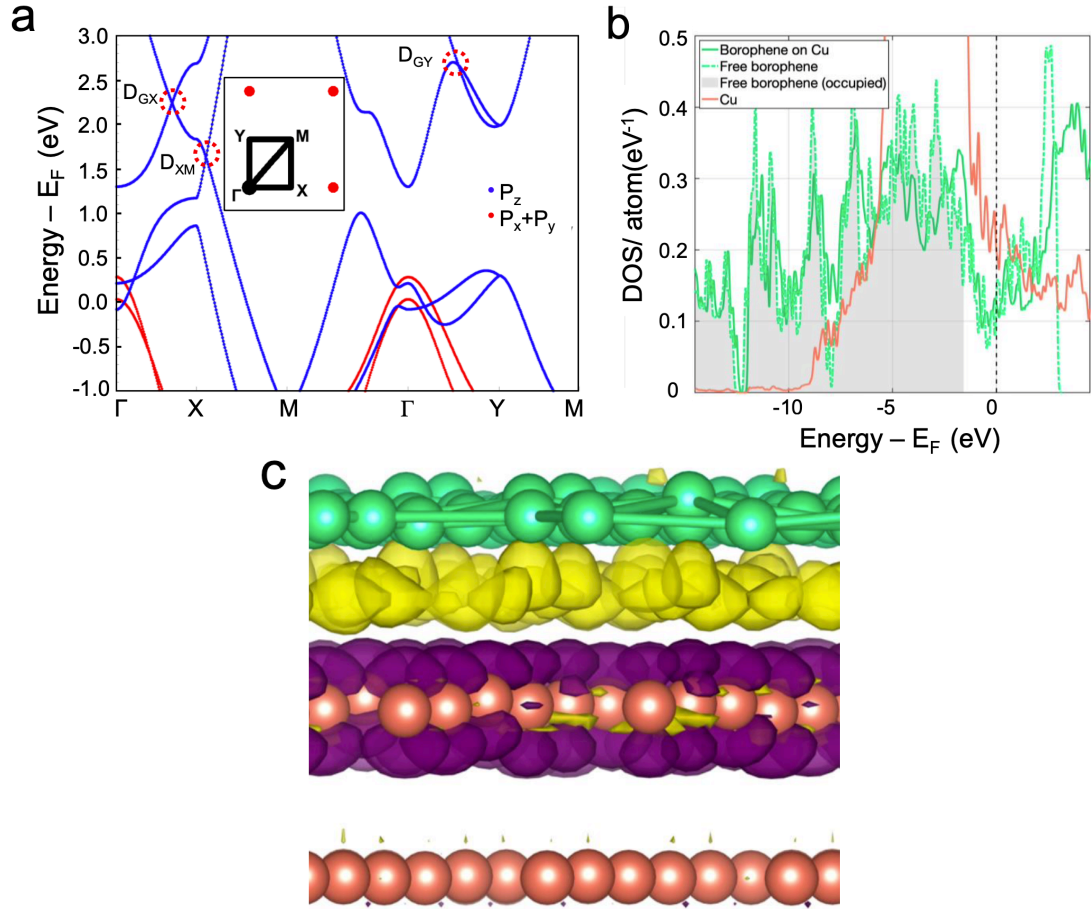


Figure 6.5: **Electronic bands of β_{13} borophene on the Cu(100) surface.** (a) The electronic band structure of free-standing β_{13} borophene, inferred by *ab initio* DFT calculations, along high-symmetry directions, as indicated in the inset (the red dots correspond to the reciprocal lattice). The orbital character is indicated by color: red for p_x and p_y , and blue for p_z . Dirac cones are highlighted by the red dashed circles. (b) Electronic DOS for Cu (the red line), the free borophene relaxed in vacuum (the dotted green line) and for the relaxed borophene sheet on Cu(100) substrate (the solid green line). The shaded area corresponds to the occupied states in the undoped free borophene. The relaxed borophene on Cu(100) is doped by 0.21 electrons per boron atom. The vertical dashed line marks the Fermi level (E_F) in borophene on Cu(100), as well as the Fermi level in isolated borophene if it were doped by 0.21 electrons per atom. (This doping would shift E_F of the isolated borophene upwards by 1.57 eV.) The similarity between the two green curves indicates that the interaction between borophene and Cu is mainly of the charge-transfer type. (c) Constant-density surface plot of the charge redistribution between Cu planes (the pink atoms) and relaxed borophene (the green atoms). Electron depletion is shown in purple and accumulation in yellow. Electrons mainly ($\sim 2/3$) move from the Cu orbitals with $4s$ -like character into p_z -like B orbitals. The out-of-plane d orbitals account for most of the rest of the electron loss and modulate the shape of the electron depletion around each Cu atom. This real-space image reinforces the charge-transfer scenario and the absence of covalent bonding between Cu and B.

than distorting locally, large-scale incommensurate modulations are formed to further lower the total energy. In Figure 6.4(e), we show a model of continuous and nondestructive dislocation around the striped area, as highlighted by the blue, red, and black rectangles.

A DFT calculation of the electronic band structure of free-standing β_{13} borophene along several high-symmetry directions is shown in Figure 6.5(a). The electronic bands from p_z and (p_x, p_y) orbitals are highlighted by blue and red colors, respectively. We have also studied β_{13} borophene on the Cu(100) surface. Our calculations indicate that it is rather flat, with z -axis fluctuations of only 0.31 Å, smaller than in borophene on the Cu(111) surface [147]. Compared to the free-standing β_{13} sheet, borophene on the Cu(100) surface is under substantial anisotropic tension, $\sim 5\%$ on average, with an average boron–boron bond length of 1.74 Å. (More details are provided in Supplementary Figure S6 of the forthcoming paper.)

For the possibility of borophene lift-off, transfer and subsequent device fabrication, it is important to have information on borophene–substrate interactions. Rather than Cu–B covalent bond formation, we have found that β_{13} borophene undergoes considerable electron doping (0.21 electrons per boron atom), coming mainly from the copper 4s orbitals and going to the boron p_z orbital. This is slightly less than the value of 0.23 electrons per boron that we calculated on Cu(111). Combined with the flatter shape of borophene on Cu(100), this indicates that in the latter case the B–Cu interaction is somewhat weaker, promising easier exfoliation. In Figure 6.5(b), we show the electron density of states (DOS) of the free-standing borophene (the dotted green line), borophene on Cu(100) surface (the solid green line), and the pristine copper substrate (the red line), respectively. As seen in Figure 6.5(b), the charge transfer from copper substrate to borophene lifts the Fermi level (E_F) upwards by about 1.57 eV while essentially preserving the DOS of the free-standing borophene. We have reinforced this conclusion by plotting the surfaces of constant electron

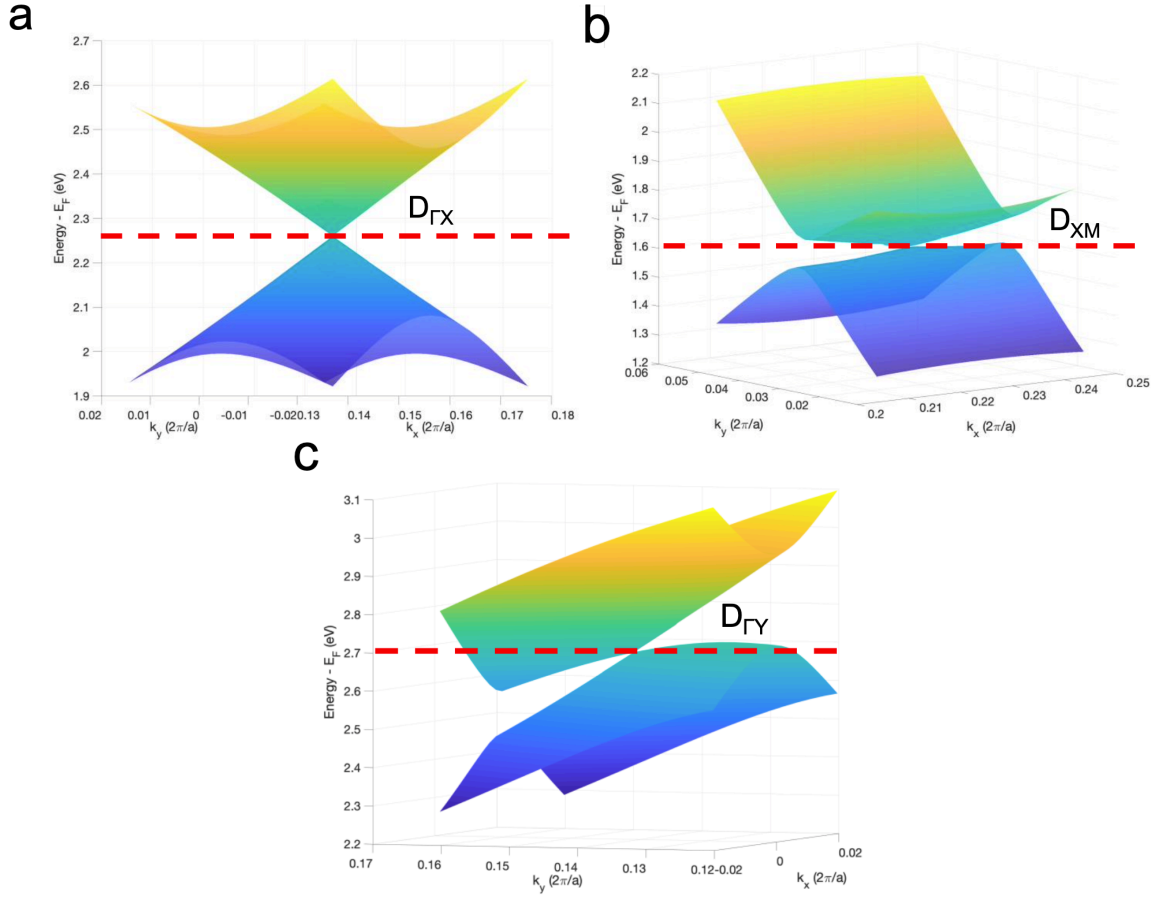


Figure 6.6: **Dirac cones of β_{13} borophene on the Cu(100) surface.** 2D energy surfaces of three Dirac cones, located on the (a) ΓX , (b) XM , and (c) ΓY lines, in free standing β_{13} borophene, as determined by *ab initio* DFT calculations. A fourth Dirac cone, labeled kk , lies in the interior of the Brillouin zone and is discussed in the Supplementary Material of the forthcoming paper.

density and studying electron redistribution between the Cu planes (the pink atoms) and the relaxed borophene (the green atoms). As shown in Figure 6.5(c), electrons are depleted (purple color) mainly from $4s$ -like Cu orbitals and accumulated (yellow) in the p_z -like B orbitals, without any obvious signature of covalent Cu–B bonding.

The electronic band structure (Figure 6.5(a)) features three Dirac cones (marked by the dashed red circles), where the upper and the lower bands touch at a single point. Given their locations in the Brillouin zone, we refer to them as Dirac cones ΓX , XM , and ΓY , respectively. The energy surfaces of these Dirac cones are plotted in Figure 6.6. Dirac cone ΓX (Figure 6.6(a)) mainly originates from the honeycomb (graphene-like) boron lattice. Dirac cone ΓY (Figure 6.6(c)), which primarily stems from the zig-zag chains of boron atoms, is both anisotropic and tilted. Near such an exotic point, massless type-II Dirac/Weyl fermions could emerge, giving rise to some exotic physics [183, 184, 185, 186]. Dirac cone XM (Figure 6.6(b)) largely derives from armchair-shaped chains of boron atoms and is also highly anisotropic. If these Dirac cones could be accessed by doping and without altering the band structure qualitatively, this could open exciting new fields of study.

6.5 Band unfolding

To take into account the stripe modulation, we performed band unfolding calculations using the Wannier function method described in Section 2.1.4. We constructed maximally localized Wannier functions [27] for the free-standing borophene sheet using the Wannier90 package [33]. We used p_z -type orbitals centered at the boron atom positions as initial guesses for the Wannier functions. We used a frozen energy window ranging from 0.2 to 2.4 eV above the Fermi level to aid in disentangling p_z -type orbitals from the full manifold

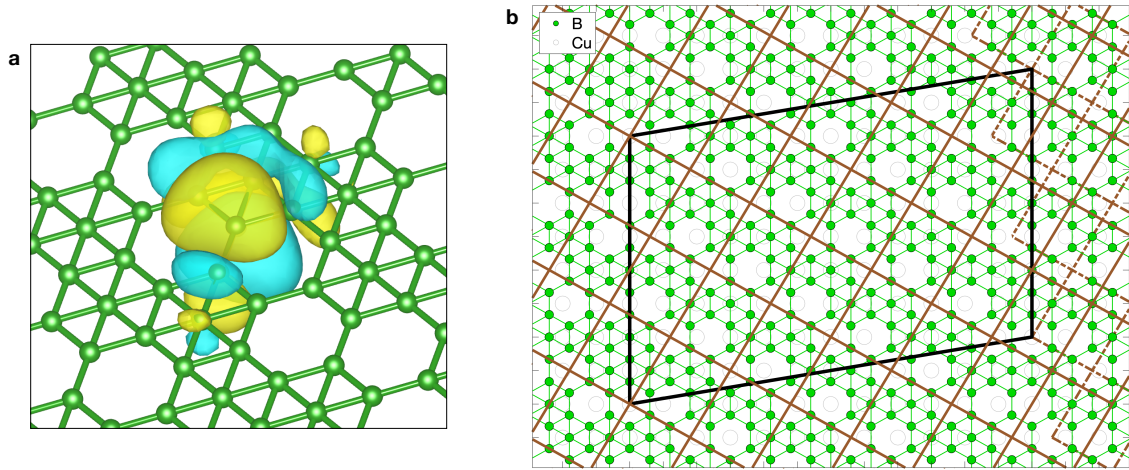


Figure 6.7: **Wannier functions and the supercell–primitive cell relationship in the borophene sheet.** (a) Isosurfaces of a typical Wannier function constructed from boron-centered p_z orbitals. Yellow and blue isosurfaces represent lobes with opposite phase, demonstrating how the p_z character of the Wannier functions is preserved. Moving from the central boron atom to its neighbors, the Wannier function changes in sign and decreases in weight. (b) Relationship between the primitive (small) cell and supercell for the boron sheet. Boron atoms are marked with filled green circles, while the underlying copper lattice is marked with open gray circles. One copy of the supercell is marked as the large black parallelogram, while a possible choice for the primitive cell is marked with solid brown rectangles. Another primitive cell, relevant in the region along the short supercell axis, is marked with dashed brown rectangles on the right-hand side of the figure.

of bands. A typical Wannier function is shown in Figure 6.7(a). It has a node in the plane of the borophene sheet and spreads over a small number of neighboring boron atoms.

To illustrate the band unfolding task, we plot both the primitive cell and supercell of the borophene sheet in Figure 6.7(b). The primitive cell is rectangular, while the supercell is a parallelogram, with a short axis parallel to the vertical Cu(100) lattice direction and a long diagonal axis rotated 9.5° from the horizontal. In terms of area, the supercell is an integer multiple of the primitive cell, containing 200 boron atoms and 40 vacancies to the primitive cell's 10 and 2, respectively. However, the supercell is not commensurate to the primitive cell in the sense of Equation 2.44: the two supercell corners on the left coincide with the corner vacancy of the primitive cell, while the supercell corners on the right coincide with the interior vacancy. The structural result of this fact is that, along the short supercell axis, boron vacancies occur three in a row, unlike the zig-zag pattern observed in the supercell interior.

This fact complicates our use of the band unfolding procedure described in Section 2.1.4. Papers like [43] contemplate perturbations in which a supercell is constructed from copies of a primitive cell, and the atomic structure within one or more of those copies is perturbed. The mapping of orbitals in the supercell to their unperturbed versions in the primitive cell is unambiguous, even if the supercell orbitals experience a variety of environments. In this work, we must *choose* how to assign supercell orbitals to primitive cell orbitals; effectively, we choose whether to treat points along the short supercell axis as belonging to the primitive cells marked with solid lines in Figure 6.7(b) or the shifted cells marked with dashed lines. In the language of Section 2.1.4, this amounts to selecting the maps \mathbf{r}' and n' from supercell to primitive cell Wannier functions that are used in Equations 2.39 and 2.43.

In this work, we map all supercell atoms to primitive cell sites using the solid-line

primitive cells of Figure 6.7(b). Because this choice only affects ~ 10 of the 200 atoms in the supercell, we expect that it has a minimal effect on the unfolded band structure, which is plotted in Figure 6.8(a) and compared to the primitive cell band structure in Figure 6.8(b). Several salient p_z -dominated features, such as the bright dispersive bands along the M– Γ line and near Y, are well-preserved after band unfolding. Dirac cone ΓX appears to be gapped, but in fact has been shifted off the $k_2 = 0$ axis (Figures 6.8(c,d)). The tilted ΓY Dirac cone is also shifted (Figures 6.8(i,j)). Meanwhile, at the XM point, the formerly degenerate bands cross over, and their intersection produces a Dirac nodal line (Figures 6.8(e,f)). These features, which have been predicted in other borophene sheets [10], are associated with topologically protected edge states and other features indicative of interesting new physics.

6.6 Conclusion

The synthesis of micrometer-sized single-crystal flakes of β_{13} borophene monolayers in this work showcases an avenue to engineer in-plane borophene structure by the choice of substrate and its facets. Real-time monitoring of the film topography, diffraction patterns, and chemical composition is shown to be an efficient strategy to pioneer novel high-quality 2D boron sheets and attain comprehensive insights. β_{13} borophene single crystals offer a new platform to explore anisotropic massless Dirac or Weyl fermions and simulate exotic black-hole related physics [185, 186]. We hope that this work will stimulate further experiments on the β_{13} borophene, such as tuning of the chemical potential, photoemission and transport measurements, and study of various potentially exotic quasiparticles.

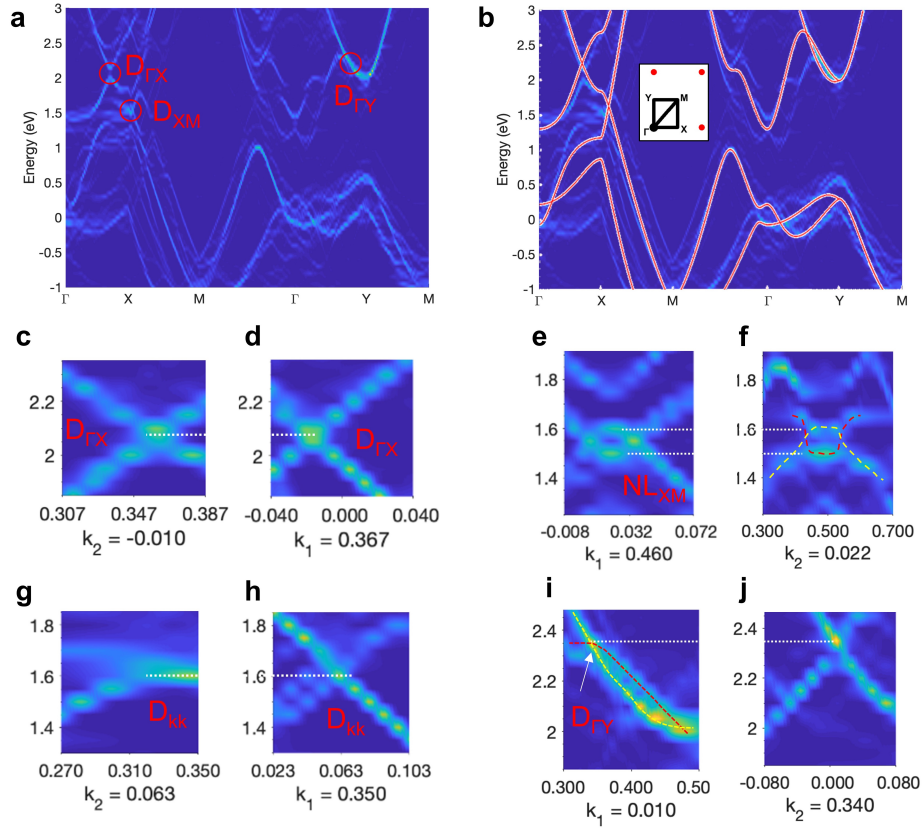


Figure 6.8: Electronic band structure of the modulated β_{13} borophene sheet accounting for the stripe modulation. (a) Electronic band structure of the modulated β_{13} borophene sheet, computed by unfolding the spectral function of the modulated supercell onto the Brillouin zone of the 10-atom small unit cell. The band structure follows the same high-symmetry directions as that in Figure 6.5(a). (b) Superposition of the free-standing (red lines) and modulated β_{13} borophene electronic band structures along high-symmetry directions, as indicated in the inset (the red dots correspond to the reciprocal lattice). (c,d) Crosscut of Dirac cone ΓX along directions parallel to the primitive reciprocal lattice vectors. This Dirac cone is preserved under the striped modulation, and it shifts slightly in energy-momentum space. (e,f) Crosscut of original Dirac cone XM . This Dirac cone evolves into a Dirac nodal line due to the vertical replicas of the two bands at different energies. Moreover, flat band features emerge in the vicinity in the $E-k$ space, as highlighted by the red and yellow dashed lines. (g,h) Crosscut of Dirac cone kk . This Dirac cone is preserved under the striped modulation, and it shifts slightly in energy-momentum space. (i,j) Crosscut of Dirac cone ΓY . This Dirac cone is preserved under the striped modulation, and it shifts slightly in $E-k$ space. Overall, by breaking the translation symmetry of the small unit cell, the striped features indeed have a substantial influence on the band structure of the β_{13} boron sheet. Specifically, band shifts/replicas in $E-k$ space produce gap openings, flat bands, abundant degeneracy points and lines, and make this system a good candidate to explore novel emergent physics.

Chapter 7

Structural analysis of 2D inverse spinel Mg_2TiO_4 on $\text{MgO}(001)$ for hosting excitons

This chapter is adapted from an article entitled “Polarity-driven atomic displacements at 2D $\text{Mg}_2\text{TiO}_4/\text{MgO}(001)$ oxide interface for hosting potential interlayer exciton states” by Kidae Shin, Stephen Eltinge, Sangjae Lee, Hyunki Shin, Juan Jiang, Hawoong Hong, Bruce Davidson, Ke Zou, Sohrab Ismail-Beigi, Charles H. Ahn, and Frederick J. Walker that has been prepared for publication [187]. KS, SL, HS, JJ, HH, BD, and KZ did the experimental work, I did the theoretical work, and SIB, CA, and FW provided guidance.

Interlayer excitons in solid-state systems have emerged as candidates for realizing novel physics, ranging from excitonic transistors and optical quantum bits (qubits) to exciton condensates. Recent investigations of interlayer excitons have been centered around 2D transition metal dichalcogenides (TMDs), owing to their large exciton binding energies and their ability to form van der Waals (vdW) heterostructures. In this chapter, in a collaboration with experimentalist colleagues, we propose that an oxide system consisting of inverse spinel Mg_2TiO_4 on $\text{MgO}(001)$ may also be used to host interlayer excitons. Using a combination of density functional theory (DFT) calculations, molecular beam epitaxy (MBE) growth, and *in situ* crystal truncation rod (CTR) measurements, we show that the $\text{Mg}_2\text{TiO}_4/\text{MgO}$

interface can be precisely controlled to yield a band offset suitable for hosting interlayer excitons. We observe that the atoms in the polar Mg_2TiO_4 layers are displaced to reduce the polarity of the film. Such polarity-driven atomic displacements lead to structural differences between the different layers of Mg_2TiO_4 . We also verify with DFT calculations that the band offset in this material may lead to the localization of photoexcited electrons in the bottom layer and holes in the top layer, which may then bind to form interlayer excitons.

7.1 Introduction

An exciton is a bosonic quasiparticle composed of a bound electron–hole pair. Excitons that can be manipulated electronically and optically are attractive for novel physics applications. For example, optical qubits with ultrafast control and fast excitonic switches have been demonstrated using excitons in InAs quantum dots (QDs), AlAs/GaAs coupled quantum wells (CQWs), and MoS_2 – WSe_2 van der Waals (vdW) heterostructures [188, 189, 190, 191]. Also, signatures of Bose–Einstein condensates of excitons have been reported in materials such as MoSe_2 – WSe_2 heterostructures and GaAs/AlGaAs CQWs, along with the prediction of novel superconductivity in exciton condensates [192, 193, 194, 195]. For practical applications, large exciton binding energies and long lifetimes must be achieved to ensure the stability of the exciton states [188, 196]. To this end, interlayer excitons in transition metal dichalcogenide (TMD) heterostructures have emerged as prominent candidates. 2D TMDs that are a monolayer or bilayer thick can host strongly bound excitons with large binding energies (> 100 meV) [197, 198]. When 2D TMDs of different materials are layered to form heterostructures, photoexcited electrons and holes can be localized in distinct layers that are spatially separated. These electrons and holes can bind to form interlayer excitons,

which can have lifetimes an order of magnitude longer than conventional intralayer excitons [199, 200, 201].

Recently, 2D transition metal oxides (TMOs) have been predicted to exhibit even larger exciton binding energies, on the order of 1 eV [8]. Moreover, it has been reported that TMOs such as anatase TiO_2 can host strongly bound excitons even in the bulk form [202, 203, 204]. TMOs also have the advantages that they are (1) generally robust under ambient conditions, (2) scalable using well established growth techniques, and (3) integrable with both existing metal-oxide technologies and novel complex oxide devices [205, 206, 207, 208, 209]. Along with the advantages, using oxides for hosting interlayer excitons poses unique challenges. Unlike 2D TMDs, for which vdW epitaxy or exfoliation is readily achieved, oxide epitaxy is often complicated by issues such as lattice mismatch and intermixing. Interaction of the film with the substrate leads to atomic-scale structural distortions at the interface, which can alter the electronic properties of the film.

Here, based on density functional theory (DFT) calculations, we propose that a single unit cell (uc) 2D Mg_2TiO_4 on an $\text{MgO}(001)$ substrate can host interlayer excitons. Our colleagues have grown and characterized the $\text{Mg}_2\text{TiO}_4/\text{MgO}$ structure using molecular beam epitaxy (MBE) and *in situ* crystal truncation rod (CTR) measurements. DFT calculations predict that the photoexcited electrons and holes should localize to the bottom and the top Mg_2TiO_4 layers, respectively, and thus potentially form interlayer excitons. This binding is favored by a polarization within the film that is predicted theoretically and inferred experimentally from the displacement of Mg tetrahedral sites at the interface. Through *in situ* CTR measurements, our colleagues confirm such displacements at the interface and resolve the $\text{Mg}_2\text{TiO}_4/\text{MgO}$ structure at the atomic level.

7.2 Design considerations for oxides with interlayer exciton states

The main challenge in creating oxides that can host interlayer excitons is finding a material that has both suitable band alignment and feasible growth conditions. In order to confine the exciton states to the 2D film region, the substrate band gap must be larger than the film band gap. Within the film, different layers must have a type-II band alignment in order to ensure localization of photoexcited electrons and holes to opposite sides [210, 211, 212]. On top of these restrictions, one has to find a latticed-matched substrate and film.

The $\text{Mg}_2\text{TiO}_4/\text{MgO}$ system satisfies all of these conditions. MgO has a large band gap of about 7.9 eV, while Mg_2TiO_4 is reported to have a band gap of about 3.7 eV [213, 214, 215]. In its inverse spinel structure, Mg_2TiO_4 is polar when cleaved along the (001) direction, with alternating positively- and negatively-charged atomic layers. Thus, one can expect that when interfaced with a non-polar material such as $\text{MgO}(001)$, polar layers in the Mg_2TiO_4 will be displaced to reduce the polar discontinuity (*i.e.*, dielectric screening) but the polarity will remain and induce an asymmetric band structure for the different layers of Mg_2TiO_4 . MgO and Mg_2TiO_4 also have a good lattice match, with the lattice constant of Mg_2TiO_4 (8.4400 Å) being almost exactly twice that of MgO (4.2127 Å) [216, 217].

Figure 7.1(a) shows the structures of an ordered and disordered inverse spinel Mg_2TiO_4 . In the ordered inverse spinel, $1/8^{\text{th}}$ of the tetrahedral voids are occupied by Mg atoms (known as Mg-tet sites), $1/4^{\text{th}}$ of octahedral voids by Mg atoms (known as Mg-oct sites), and $1/4^{\text{th}}$ of octahedral voids by Ti atoms (known as Ti-oct sites), while the oxygen sublattice remains similar to that in MgO . In the disordered case, the Mg-oct and Ti-oct sites are mixed. For

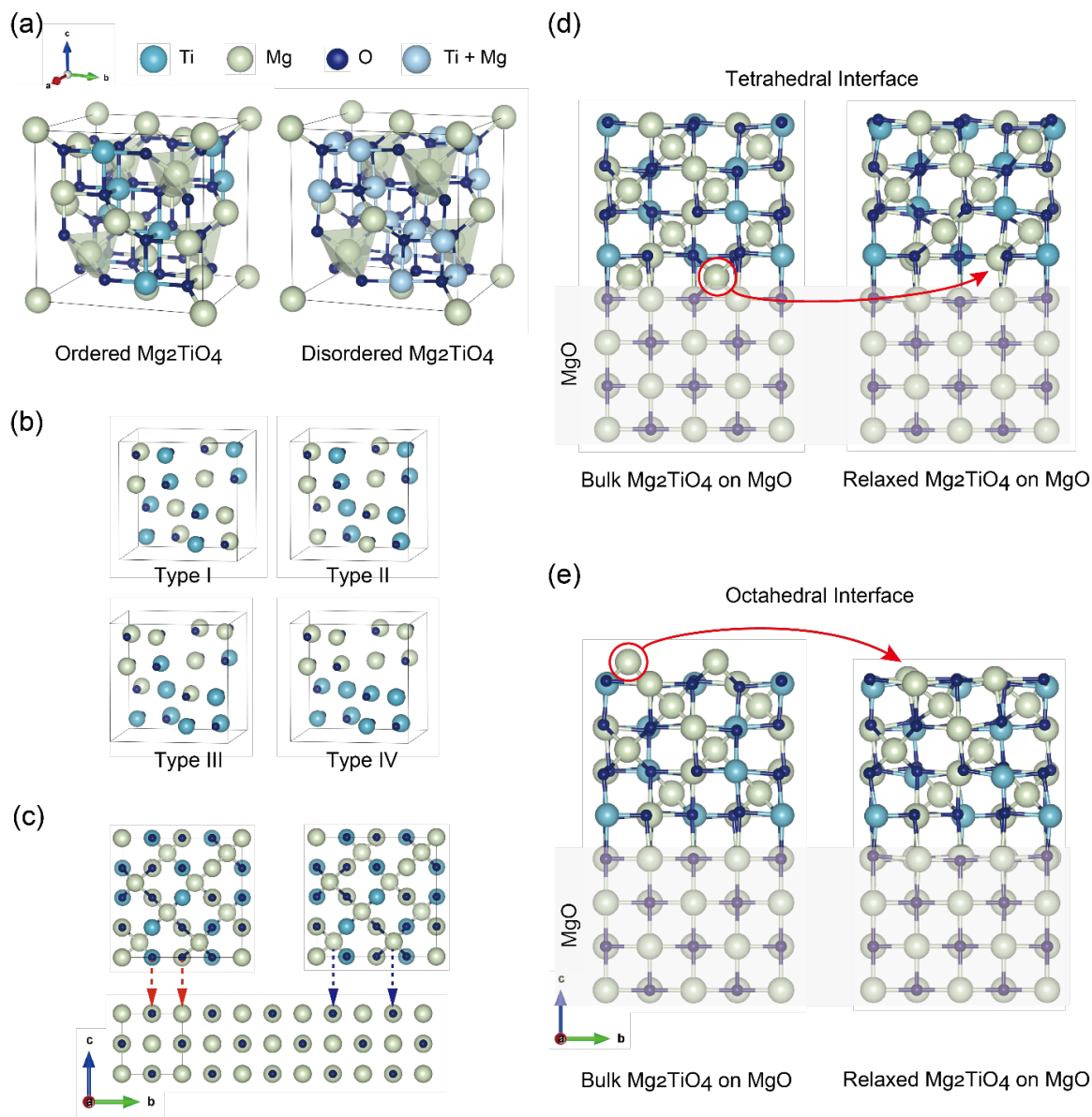


Figure 7.1: **(a)** Crystal structures of the ordered (left) and disordered (right) Mg_2TiO_4 . **(b)** Examples of different types of Mg/Ti-oct site orderings possible for ordered Mg_2TiO_4 . **(c)** Schematics of oxygen sublattice matched registry (red arrows) and oxygen sublattice mismatched registry (blue arrows). **(d)** Structure of bulk-like (left) and 1 uc Mg_2TiO_4 on $\text{MgO}(001)$ relaxed to form the tetrahedral interface (right), as obtained from DFT calculations. The first layer of Mg-tet sites is displaced to fill nearby vacant Mg-oct sites (red arrow). **(e)** Structure of bulk-like (left) and 1 uc Mg_2TiO_4 on $\text{MgO}(001)$ relaxed to form the octahedral interface (right), as obtained from DFT calculations. The last layer of Mg-tet sites is displaced to fill nearby vacant Mg-oct sites (red arrow).

the ordered inverse spinel structure, different cation orderings are possible at the octahedral sites. Type I and II orderings in Figure 7.1(b) are examples of structures in which there are equal number of Mg-oct and Ti-oct atoms for each monolayer of Mg_2TiO_4 . For type III ordering, only two monolayers in a unit cell have equal number of Mg-oct and Ti-oct atoms. In type IV ordered case, the Mg-oct and Ti-oct atoms are all segregated into different layers.

We note that the disordered and the type I, II ordered Mg_2TiO_4 have the same in-plane averaged electron density profile along the c -axis, and thus cannot be distinguished from each other through integer-order X-ray diffraction measurements along Q_z . However, type III and IV structures in which the Mg-oct and Ti-oct sites are distributed inhomogeneously along c -axis can be distinguished from disordered or type I, II ordered Mg_2TiO_4 . The CTR analysis presented in latter parts of the chapter confirms that the Mg_2TiO_4 structure is of type I, II ordered or disordered. Thus, we choose the type I ordered structure as the basis for DFT calculations, based on the assumption that there is no preferential alignment of Mg-oct and Ti-oct sites either in-plane or out-of-plane. Also, we choose the type I structure over the disordered structure to reduce the computational load.

7.3 Electronic structure of $\text{Mg}_2\text{TiO}_4/\text{MgO}$ from DFT calculations

Using DFT calculations, we confirm that $\text{Mg}_2\text{TiO}_4/\text{MgO}$ indeed has a band offset favorable for hosting interlayer excitons. We first consider different ways Mg_2TiO_4 might grow epitaxially on the $\text{MgO}(001)$ surface. Mg_2TiO_4 can stabilize on MgO with either cation octahedral sites on MgO oxygen sites, or Mg-tet sites on MgO oxygen sites. The oxygen sublattices of Mg_2TiO_4 and MgO are matched for the former registry (red arrows in Figure 7.1(c)), while

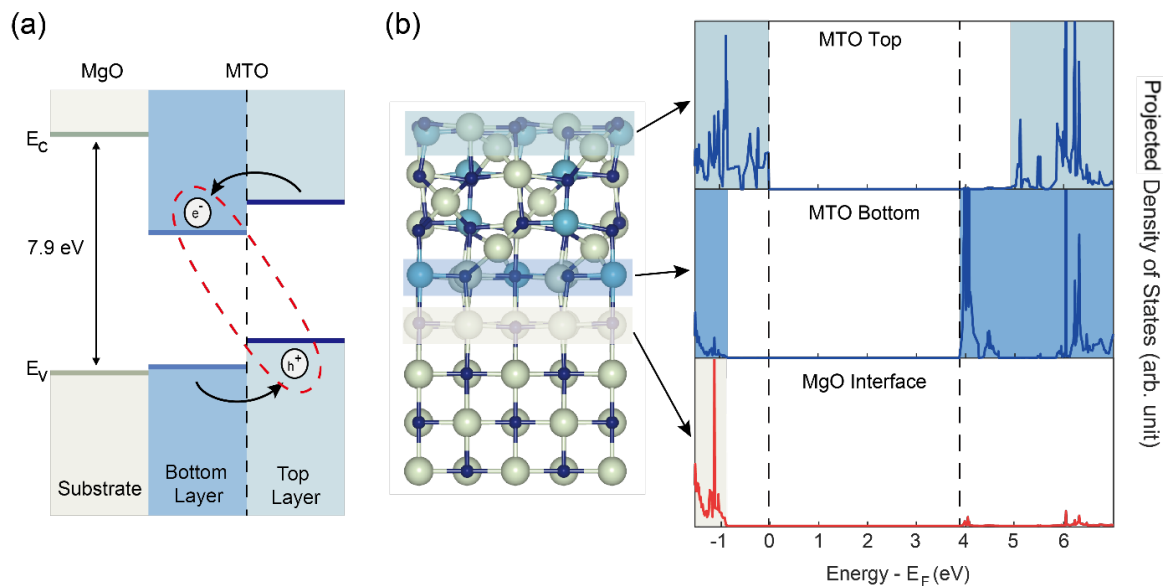


Figure 7.2: **(a)** Schematic of the band offset in 1 uc Mg_2TiO_4 (MTO)/MgO. Upon photoexcitation, electrons are localized to the bottom layer and the holes are localized to the top layer; they can bind to form interlayer excitons. **(b)** Projected density of states (PDOS) for the MTO top, MTO bottom, and MgO interface layers from DFT+HSE06 calculations.

they are mismatched for the latter (blue arrows in Figure 7.1(c)). Preliminary analysis of the CTR data showed a better fit to the oxygen-sublattice-matched registry. Thus, the following DFT calculations are based on the oxygen-sublattice-matched registry only.

Figures 7.1(d) and (e) show the DFT-calculated structures of the relaxed 1 uc Mg_2TiO_4 on MgO. The results show that two types of interfaces are possible. The first starting layer of Mg_2TiO_4 at the interface is the Mg-tet layer for the tetrahedral interface (Figure 7.1(d)), while it is the Mg-oct/Ti-oct layer for the octahedral interface (Figure 7.1(e)). For both the tetrahedral and octahedral interfaces, Mg-tet atoms are displaced during the course of stabilizing the structure. In case of the tetrahedral interface, the Mg-tet atoms in the first layer of Mg_2TiO_4 are displaced to fill nearby octahedral vacancies (Figure 7.1(d)). For the octahedral interface, Mg-tet atoms in the last layer are displaced to fill the nearby octahedral vacancies (Figure 7.1(e)).

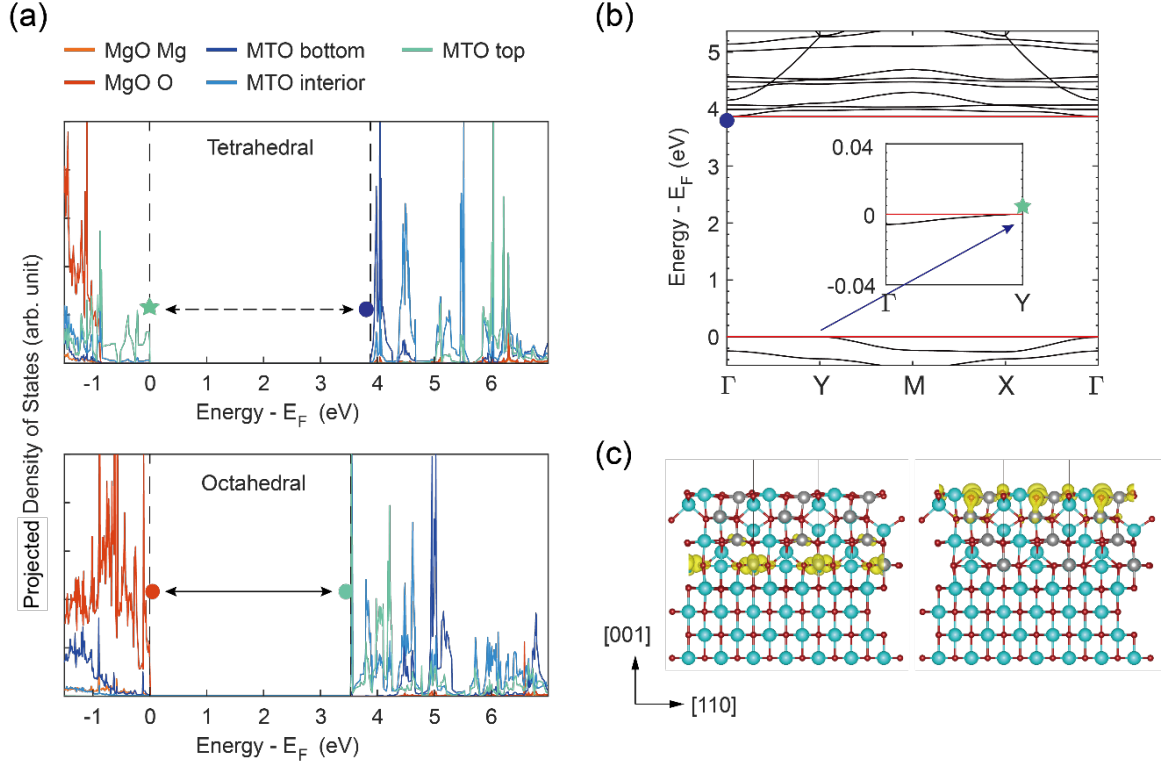


Figure 7.3: **(a)** PDOS of all layers considered in the DFT+HSE06 calculations for the tetrahedral interface (top) and octahedral interface (bottom). For the tetrahedral interface, the valence band maximum (VBM) is in the Mg_2TiO_4 (MTO) top layer, and the conduction band minimum (CBM) is in the MTO bottom layer. For the octahedral interface, the valence band maximum (VBM) is in the MgO substrate layer, and the conduction band minimum (CBM) is in the MTO top and interior layers. **(b)** Band structure of tetrahedrally-interfaced 1 uc MTO/MgO from DFT+HSE06 calculations. The VBM is at the Y point (star) and the CBM is at the Γ point (circle) in the Brillouin zone. The inset shows that the valence band is mostly flat between the Γ and Y points. **(c)** Isosurfaces displaying the Bloch functions for the band-edge states computed in DFT. Electron density is localized mostly to O 2p orbitals in the MTO top layer for the VBM (bottom). For the CBM, electron density is localized mostly to Ti 3d orbitals in the MTO bottom layer (top).

To confirm whether $\text{Mg}_2\text{TiO}_4/\text{MgO}$ exhibits the type-II band offset needed for interlayer excitons, we calculate the projected density of states (PDOS) for each layer in the relaxed Mg_2TiO_4 on MgO . We first consider the tetrahedral interface structure. We employ the HSE06 hybrid functional in the DFT calculations to account for some of the effects of electron–electron interactions neglected by standard DFT, and we obtain a band gap of 3.88 eV, which is slightly larger than the reported bulk Mg_2TiO_4 band gap. Figure 7.2(b) shows the PDOS associated with the Mg_2TiO_4 top and bottom layers, as well as the MgO interface layer. The PDOS plot shows a band offset between the top and bottom layers of the tetrahedral interface Mg_2TiO_4 . Such a band offset is expected to lead to localization of photoexcited holes in the top layer and electrons in the bottom layer, possibly forming interlayer exciton states (Figure 7.2(a)).

A PDOS plot for all 4 layers of Mg_2TiO_4 and 4 layers of MgO substrate considered in the DFT calculation clearly shows that the valence band maximum (VBM) of the system is in the top Mg_2TiO_4 layer, while the conduction band minimum (CBM) is in the bottom Mg_2TiO_4 layer (Figure 7.3(a) top). The VBM states are localized to oxygen $2p$ orbitals in the top layer, and the CBM states are localized to titanium $3d$ orbitals in the bottom layer (Figure 7.3(c)). Also, from the calculated band structure, we determine the band gap to be indirect. The VBM is located at the Y point of the Brillouin zone, whereas the CBM is located at the Γ point (Figure 7.3(b)). This implies that a band-edge electronic transition will require momentum transfer. Thus, we expect optical excitation and recombination to be weak. Essentially, a potential exciton consisting of the VBM and CBM states may not only be an interlayer exciton but also an indirect exciton, with the electron and hole separated in both real space and momentum space. We also note that the VBM of the Mg_2TiO_4 bottom and the MgO interface layers are very close in energy. This is attributed to the Mg-tet sites

in the bottom Mg_2TiO_4 layer filling nearby Mg-oct sites and bringing the net charge of the bottom Mg_2TiO_4 layer close to that of MgO interface. At the same time, the CBM of the Mg_2TiO_4 bottom layer is at significantly lower energy compared to the MgO interface. This is due to the presence of Ti atoms in the Mg_2TiO_4 layer, and is confirmed by the calculated Bloch functions for the CBM states (Figure 7.3(c)).

It is important to note that the above band structure is unique to the tetrahedral interface. DFT+HSE06 calculations show that the octahedral interface structure has a direct band gap of 3.53 eV, with VBM and CBM both at the Γ point. Also, a PDOS plot for the octahedral interface shows that the VBM is in the MgO substrate, with the CBM in the Mg_2TiO_4 interior and top layers (Figure 7.3(a) bottom). Such a band structure is not desirable for hosting long-lived excitons, since the excitons cannot be confined to the film layer. This illustrates the importance of precisely controlling and characterizing the oxide interface. According to our DFT calculations, the relaxed tetrahedral interface structure is about 0.24 eV/uc more stable than the relaxed octahedral interface structure. In the following parts of this chapter, our colleagues confirm experimentally that the tetrahedral interface is indeed achieved.

7.4 Mg_2TiO_4 growth using reactive MBE

Our colleagues successfully grew a single unit cell Mg_2TiO_4 on $\text{MgO}(001)$ using a reactive MBE process [187]. The growth was carried out in the oxide MBE chamber at beamline 33-ID-E at Advanced Photon Source (APS) to allow for *in situ* CTR measurements before and after growth. Our colleagues deposited TiO_2 on MgO using Ti flux from an effusion cell and molecular oxygen. Prior to growth, the MgO substrates were annealed at over 700 °C at an oxygen partial pressure of about 6×10^{-9} Torr to obtain a clean surface. The

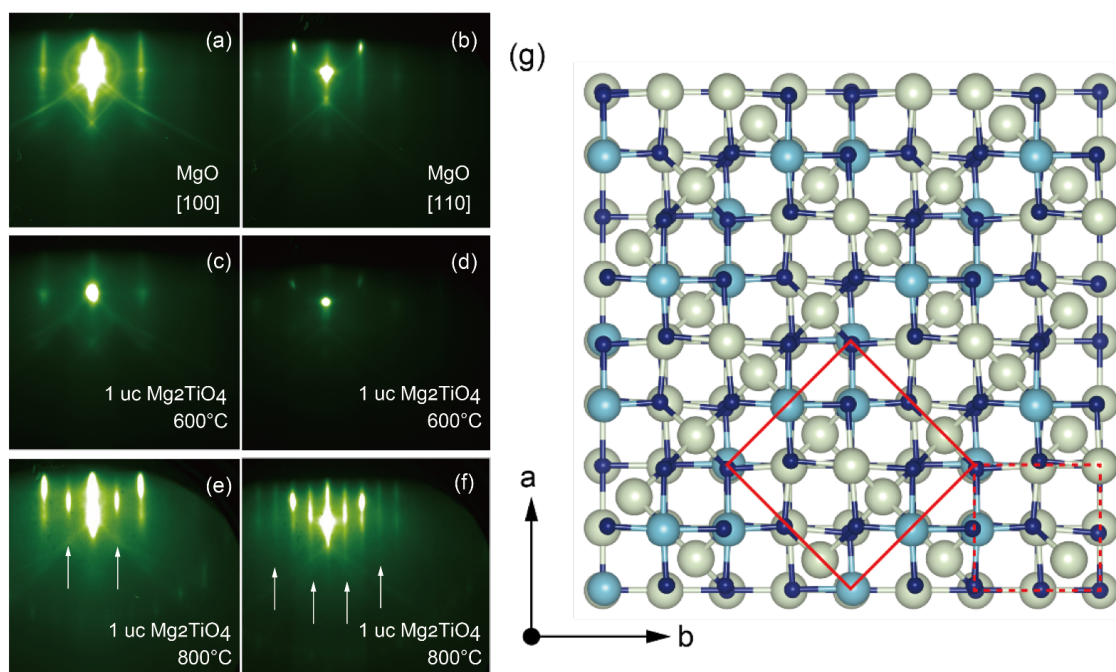


Figure 7.4: Reflection high-energy electron diffraction images along [100] and [110] direction for **(a,b)** oxygen-annealed MgO substrate at 700°C, **(c,d)** 1 uc Mg₂TiO₄ grown on MgO at 600°C, and **(e,f)** 1 uc Mg₂TiO₄ grown on MgO at 800°C. **(g)** Surface of Mg₂TiO₄ film viewed from the top. The surface unit cell of Mg₂TiO₄ (red) is a centered c(2 × 2) reconstructed unit cell of MgO (dashed red).

growth temperature was maintained at about 800 °C. Inter-diffusion of Mg and Ti atoms at the MgO surface leads to formation of Mg_2TiO_4 at high temperatures. Reflection high-energy electron diffraction (RHEED) images show epitaxial growth of the films on MgO (Figure 7.4). Additional diffraction peaks appearing in the RHEED images (white arrows) are attributed to the surface structure of ordered inverse spinel Mg_2TiO_4 (Figure 7.4(e,f)). The Mg_2TiO_4 surface unit cell has a $c(2\times 2)$ symmetry relative to the underlying MgO surface unit mesh (Figure 7.4(g)). Extra half-order rods in RHEED along both the $[100]$ and $[110]$ directions agree with such a surface reconstruction. We also note that the reconstruction appears only when TiO_2 is deposited at high temperatures above 700 °C, or when the film is annealed at elevated temperatures following a lower temperature growth. This is consistent with previously reported formation mechanisms of Mg_2TiO_4 [218, 219, 220]. Thus, based on the above observations, we conclude that the deposition of TiO_2 on MgO at high temperatures results in the epitaxial growth of thin Mg_2TiO_4 on MgO, down to the single unit cell limit.

7.5 Structural characterization using CTR measurements

Our colleagues employed *in situ* CTR measurement to confirm the atomic-scale displacements at the interface predicted by *ab initio* theory [187]. CTR measurements were done immediately after growth in ultra-high vacuum (UHV) without exposing the films to the atmosphere. The 3D electron density maps of the films were obtained using the coherent Bragg peak analysis (COBRA) phase retrieval technique [221, 222, 223, 224]. Since our colleagues use the integer-order diffraction rods along the Q_z direction, information contained in the CTR data is in-plane averaged electron density profile along the c -axis. Therefore,

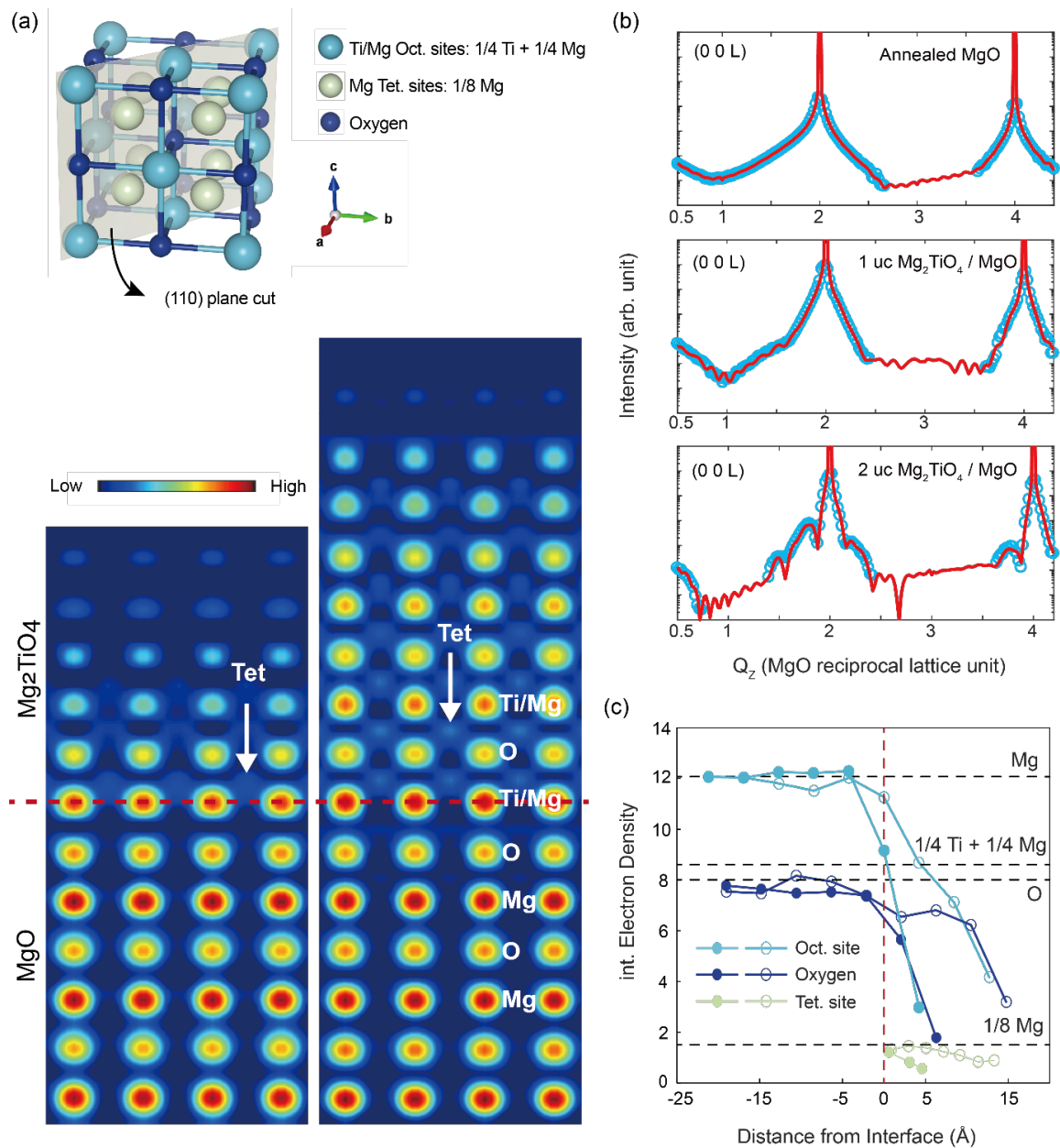


Figure 7.5: (a) Reduced unit cell model of Mg_2TiO_4 used to fit the CTR data (top), and 2D cut of the electron density map along the (110) plane obtained from COBRA (bottom). While 10 layers of MgO substrate was used for COBRA, we show only 6 layers of MgO due to limited space. Red dashed line marks the first layer of Mg_2TiO_4 . (b) Experimental CTR data (sky blue circles) and best fits (red lines). (c) Integrated electron density profile for each Mg/Ti-oct site (teal), oxygen site (blue), and Mg-tet site (light mint). Full and empty circles represent 1 uc and 2 uc films respectively. Dashed black lines show nominal electron densities of Mg, octahedral cation site, oxygen, and tetrahedral site.

they used the reduced structure of Mg_2TiO_4 shown in Figure 7.5(a) to fit the CTR data. The reduced structure has the same unit cell as MgO , but the occupancy of the Mg/Ti-oct sites is 0.25 Ti + 0.25 Mg occupancy, and the Mg-tet sites have 0.125 Mg occupancy. Such a structure has the same in-plane averaged electron density profile along the c -axis as the full type I, II ordered or disordered Mg_2TiO_4 structure. X-ray diffraction spectra calculated using this model structure fits the experimental spectra well (Figure 7.5(b)).

The electron density maps of 1 uc and 2 uc Mg_2TiO_4 on MgO clearly show non-zero electron density at the Mg-tet sites within the Mg_2TiO_4 layers, confirming the structure is indeed Mg_2TiO_4 . The integrated electron densities of these sites are close to $1/8^{\text{th}}$ of the Mg electron density, which agrees with the average electron density of the Mg-tet sites in the Mg_2TiO_4 structure (Figure 7.5(c)). While the number of layers deposited are 4 and 8 for 1 uc and 2 uc films respectively, the electron density maps show 6 and 9 layers, with the top two layers having drastically lower electron densities. Also, the electron densities of the film layers decrease rapidly towards the film-vacuum surface. We attribute these non-ideal features to disorder near the surface and roughness effects.

7.6 Polarity-driven displacements at the interface

A closer look at the electron densities of the Mg/Ti-oct sites at the MgO – Mg_2TiO_4 interface confirms the displacement of Mg-tet atoms. If the Mg-tet atoms in the first layer are displaced to fill nearby Mg/Ti-oct vacancies, the electron density of the first layer Mg/Ti-oct sites will be increased by the amount corresponding to the electron density of the Mg-tet sites. In such case, the electron density of the first layer Mg/Ti-oct sites will be increased to 11.61 (0.5 Mg + 0.25 Ti electron densities) from the nominal value of 8.60

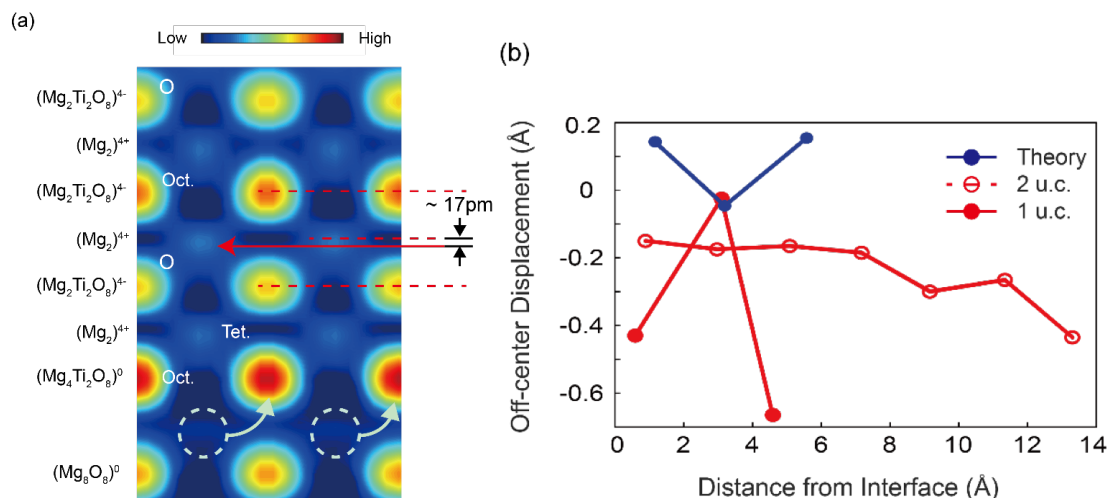


Figure 7.6: **(a)** Valence of each Mg_2TiO_4 layer and displacements of the Mg-tet atoms. Subscripts denote total number of atoms in each layer per Mg_2TiO_4 unit cell and superscripts denote the valence. Red dashed lines indicate the centers of the Mg/Ti-oct and oxygen sites, and the midpoint between them. Red arrow indicates displaced position of Mg-tet atoms, which is off-center by about 17 pm for the marked layer. **(b)** Plot of the Mg-tet atom displacements from its nominal position for 1 uc (red filled circles) and 2 uc (red hollow circles) samples, and the DFT calculated structure of 1 uc Mg_2TiO_4 (blue filled circles).

(0.25 Mg + 0.25 Ti electron densities). Also, one would observe no electron density for the Mg-tet sites immediately above the last MgO oxygen layer. A COBRA electron density map for 2 uc Mg_2TiO_4 indicates that the integrated electron density of the first Mg_2TiO_4 layer Mg/Ti-oct sites is 11.27, in close agreement with the value expected for the DFT-calculated structure of relaxed Mg_2TiO_4 on $\text{MgO}(001)$ (Figure 7.5(c)). The above observation also agrees with the DFT calculation that predicts the tetrahedral interface to be energetically more favorable than the octahedral interface. In the case of the octahedral interface, one would expect finite electron density for the Mg-tet sites immediately above the last MgO oxygen layer and increased electron densities for the Mg/Ti-oct sites in the top Mg_2TiO_4 layer (Figure 7.1(e)), both of which disagree with the COBRA electron density map.

However, although the experiment confirms the tetrahedrally-interfaced Mg_2TiO_4 structure from the theory, picoscale displacements of the Mg-tet sites extracted from the experi-

ment are not consistent with the DFT structure. Our colleagues extracted the displacements of Mg-tet sites from their bulk positions, which would be at a midpoint between the Mg/Ti-oct and oxygen layers (Figure 7.6(a)). The DFT calculation predicts that the Mg-tet sites are mostly displaced upwards from their bulk positions. In contrast, the experiment shows the Mg-tet sites are mostly displaced downwards (Figure 7.6(b)). One possible reason for such a discrepancy is the effect of roughness and disorder near the film surface. The root mean squared (rms) roughness of the 2 uc Mg_2TiO_4 film is 0.752 nm over a $5\text{ }\mu\text{m} \times 5\text{ }\mu\text{m}$ area as measured by atomic force microscopy (AFM), which is about 90% of the Mg_2TiO_4 unit cell thickness. Another possible source of discrepancy is the growth technique. The DFT calculation started with a bulk Mg_2TiO_4 structure on MgO, whereas the experiment consisted of reactive MBE growth depositing only TiO_2 on MgO. The growth process in which all Mg atoms in the Mg_2TiO_4 film are sourced from the MgO substrate below may have caused preferential downward displacements of the Mg-tet sites.

7.7 Conclusion

In conclusion, we propose that the single unit cell Mg_2TiO_4 on $\text{MgO}(001)$ can serve as an oxide platform for exploring interlayer excitons. We also argue that the $\text{Mg}_2\text{TiO}_4/\text{MgO}$ system has the potential to be used for hosting energy-tunable interlayer excitons. In the few-unit-cell limit, Mg_2TiO_4 has a band offset between the top and the bottom layers. By controlling the distance between the top and bottom layers of Mg_2TiO_4 , one may be able to control the spatial size of the interlayer exciton state, thereby controlling the binding energy. This may be achieved simply by varying the thickness of the Mg_2TiO_4 film. See Section 8.7 and especially Figure 8.10 for further discussion.

One area for potential improvement is growing Mg_2TiO_4 through co-deposition of Mg and Ti on MgO. As mentioned in the previous section, reactive MBE growth may be responsible for the observed surface roughness, which amounted to about 90% of the 1 μm Mg_2TiO_4 thickness. Co-deposition may reduce the surface roughness and result in better-quality films. Since the binding energy of a potential interlayer exciton is expected to be related to the thickness of the Mg_2TiO_4 film, large surface roughness can lead to large variation in the binding energies of the observed excitons. Also, a rough surface with large density of atomic steps can reduce the diffusion length of potential interlayer excitons, as they recombine at the step edges where the top layer is abruptly terminated [188]. Thus, it would be ideal to achieve large terraces with small surface roughness through improved growth techniques.

A key enabling factor for potential interlayer excitons in $\text{Mg}_2\text{TiO}_4/\text{MgO}$ is the band offset created by the polarity of the film. A signature of that polarity, in the form of atomic displacements at the inverse spinel interface, has been observed for the first time in this work. We expect that similar band offsets may appear in other polar spinel materials grown on non-polar host material interfaces. This implies that the above scheme for hosting interlayer excitons in oxides can be generalized to other interesting spinel oxides, such as Mg_2SnO_4 and MgGa_2O_4 , which show persistent luminescence [225, 226, 227]. Thus, the merit of this work lies in identifying 2D spinel oxide interfaces as a new class of materials for which exciton physics might be explored. To further confirm the potential of these materials, our colleagues plan to perform optical measurements on these materials in the future.

Chapter 8

Further study of excitons in Mg_2TiO_4 on MgO via the GW -BSE method

In the previous chapter, we described the growth and structural characterization of Mg_2TiO_4 films on MgO . Our *ab initio* work in that chapter used the framework of density functional theory, with nonlocal electron–electron interaction effects treated using hybrid functionals. In this chapter, we apply the GW -BSE method to more accurately describe the quasiparticle energies and absorption spectra of Mg_2TiO_4 . We obtain both intralayer and interlayer excitons with substantial binding energies. We conclude by assessing plausible mechanisms to favor interlayer excitons in experiments.

8.1 Introduction

In Chapter 7, we established using density functional theory that Mg_2TiO_4 films on $\text{MgO}(001)$ have a favorable band alignment for hosting interlayer excitons. The valence band maximum is localized to O $2p$ orbitals on the film’s surface, while the conduction band minimum is localized to the Ti $3d$ orbitals of the film’s interfacial side. The band edges

have a type I alignment with respect to the substrate, a necessary condition for excitons to be isolated to the film. Our analysis in that chapter, while suggestive, is fundamentally incomplete. DFT is not equipped to accurately describe excited electrons, or to treat the dynamic binding interaction between excited electrons and the holes they leave behind in the valence band. To quantitatively describe excitons in Mg_2TiO_4 , we need a many-body formalism.

Our tool of choice is the *GW*-BSE method, which we introduced in some detail in Section 2.2. The reader may wish to refer back to that section for a refresher, but briefly, the *GW* method computes the self-energy of a material’s quasiparticle excitations in terms of the one-body Green’s function G and the screened Coulomb potential W . The self-energy replaces the exchange–correlation functional in the quasiparticle energy eigenvalue equation, providing a self-consistent correction to the single-particle energies obtained in DFT. These quasiparticle energies can be fed into the Bethe–Salpeter equation (BSE), which describes the energies and eigenstates of interacting electron–hole pairs (excitons). The spectrum of exciton energies can then be used to compute the optical absorption spectrum. In this chapter, we will describe the application of this workflow to Mg_2TiO_4 films on MgO.

8.2 Methods

To generate mean-field wavefunctions and energies, we performed density functional theory (DFT) calculations using the Quantum ESPRESSO software package [93, 94]. We used norm-conserving pseudopotentials from the SG15 library generated with the ONCV code [228, 229]. Our exchange–correlation functional was the Perdew–Burke–Ernzerhof (PBE)

generalized gradient approximation [20]. We used a plane-wave basis set with a wave-function energy cutoff of at least 80 Ry. SCF calculations used a Monkhorst–Pack \mathbf{k} -grid [159] with 14 meV of Gaussian thermal broadening, while PDOS plots were generated by additional non-self-consistent calculations using the tetrahedron method of Blöchl et al. [230].

Substrate-bound calculations used a slab geometry, with a surface lattice parameter referenced to a theoretical relaxed bulk MgO parameter of 4.255 Å. Some calculations used for convergence testing were carried out at slightly different lattice parameters. Each slab calculation included vacuum spacing equal to at least the slab thickness—a requirement for slab-geometry Coulomb truncation—plus a buffer of 4 Å to account for the evanescent tails of surface-state wavefunctions. We used a $16 \times 16 \times 1$ \mathbf{k} -point grid. For all polar systems, we used a self-consistent dipole correction in the vacuum to avoid unphysical electric fields arising from periodic boundary conditions [142].

We used the BerkeleyGW software package [53, 47, 54] to carry out single-shot G_0W_0 and BSE calculations, in which the Green’s function and screened Coulomb interaction were constructed from Kohn–Sham DFT states and energies. All GW calculations used the generalized plasmon pole model [47] to describe the frequency-dependent dielectric function and the static remainder term [60] to expedite convergence of the Coulomb hole self-energy. All substrate-bound calculations used a slab Coulomb truncation scheme [62]. All calculations with more than 10 atoms used simple approximate physical orbitals (SAPOs) to account for high-energy unoccupied states [61].

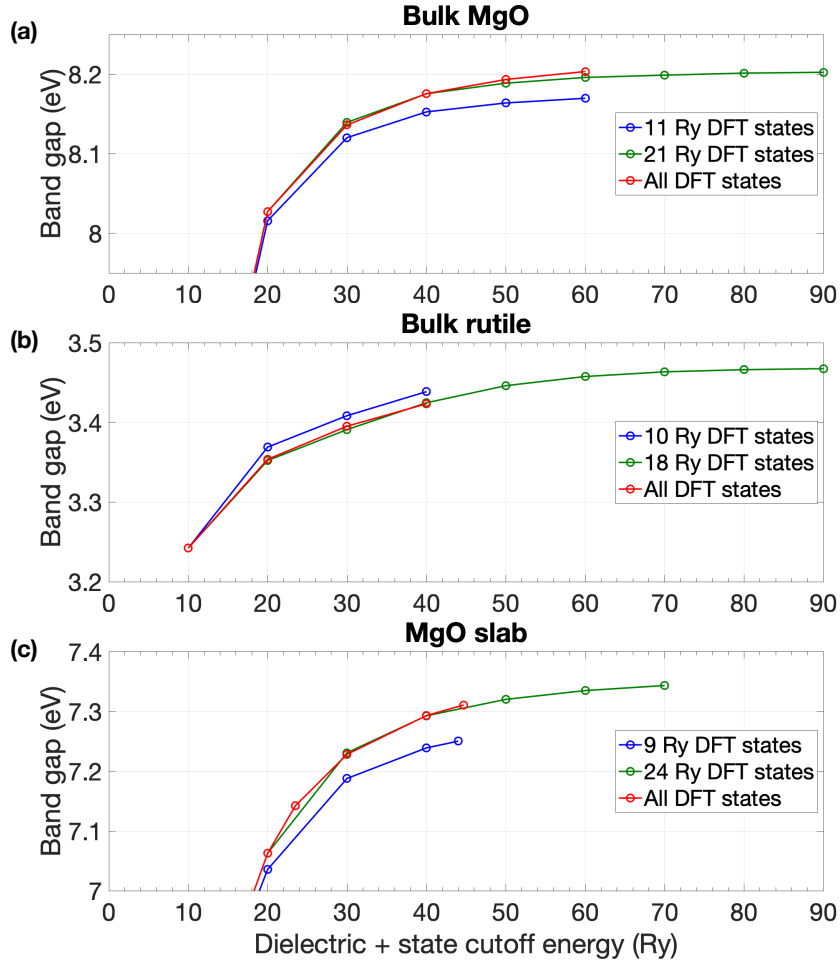


Figure 8.1: Convergence of *GW* quasiparticle band gap as a function of cutoff energy for (a) bulk MgO, (b) bulk rutile TiO_2 , and (c) an MgO(001) slab. Convergence is plotted for calculations with a smaller (blue line) and larger (green line) number of DFT bands—the balance of the bands being provided by SAPOs—as well as for an all-DFT calculation (red line).

Table 8.1: Number of bands required for *GW* calculations in materials treated in this chapter.

Material	Atoms / uc	States to 15 Ry	30 Ry	40 Ry
Bulk MgO	2	142	357	543
Bulk TiO_2 (rutile)	6	452	1187	1848
Bulk Mg_2TiO_4	28	2187	5881	9064
4 MgO layers	8	1016	2684	4252
3 Mg_2TiO_4 layers	21	3227	8895	-
4 MgO + 1 Mg_2TiO_4 layer(s)	39	4757	13005	19997
3 MgO + 3 Mg_2TiO_4 layers	45	6375	17405	-

8.3 Convergence and scaling tests

To determine the parameters needed for our GW calculations, we performed convergence tests on three small systems: bulk MgO, bulk TiO₂ in its rutile form, and a slab of MgO(001) containing four atomic layers. The unit cells of these systems contain 2, 6, and 8 atoms, respectively. For each material, we computed the quasiparticle band gap using both a full set of DFT states and DFT states supplemented with SAPOs. In the calculation of both the polarizability and the Coulomb hole self-energy term, we included all unoccupied states with energy less than or equal to the kinetic energy \mathbf{G} -vector cutoff for the dielectric matrix $\epsilon_{\mathbf{G}\mathbf{G}'}(\mathbf{q})$. The convergence of the quasiparticle band gaps with respect to this single energy parameter is shown in Figure 8.1. From this data, we estimate that a cutoff of 40 Ry is sufficient to converge the band gap of these materials to within 50 meV, while a cutoff of 30 Ry is sufficient for 100 meV accuracy.

Due to resource limitations, we chose a 30 Ry cutoff for our full-size Mg₂TiO₄ calculations. Table 8.1 lists the number of states needed to reach this cutoff for systems of interest. For particles of mass m and quadratic dispersion $E(k) = \hbar^2 k^2 / 2m$ in a box with volume V and periodic boundary conditions, the number of states less than a particular energy is

$$\Omega(E) = \frac{V}{3\pi^2} \left(\frac{2mE}{\hbar^2} \right)^{3/2} \propto V \cdot E^{3/2}. \quad (8.1)$$

Thus, the number of states scales with the volume of the unit cell for bulk materials. For slab materials, the volume includes a vacuum at least as large as the slab, so the number of required states roughly doubles. Where necessary, we computed states up to a 15 Ry cutoff explicitly in DFT and constructed the balance from SAPOs.

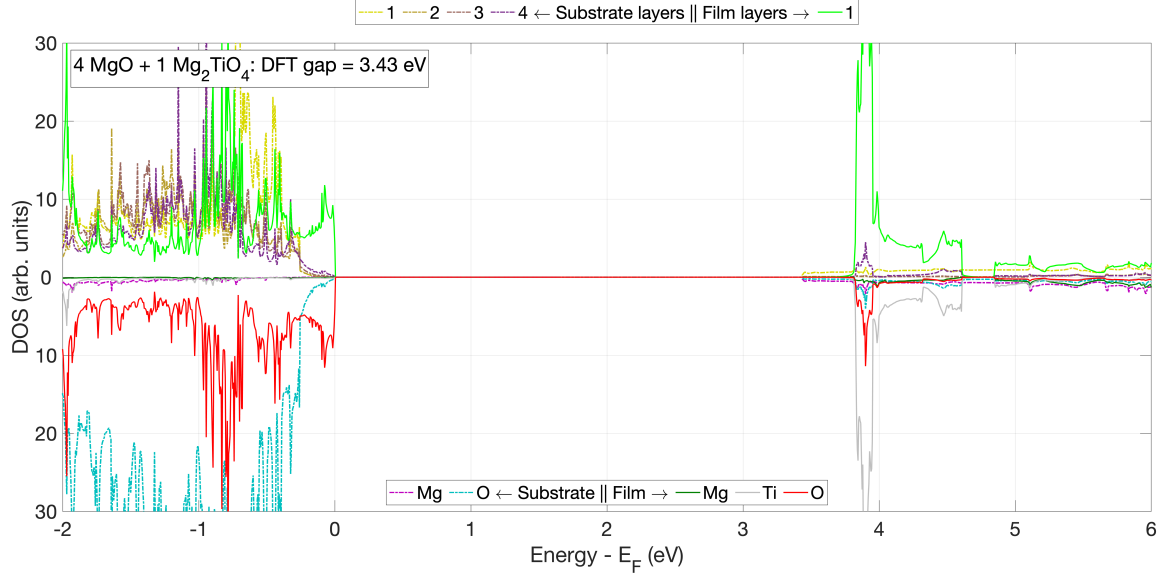


Figure 8.2: Projected density of states (PDOS) for one layer of Mg_2TiO_4 on $\text{MgO}(001)$. The upper panel decomposes the density of states layer-by-layer; Mg_2TiO_4 film layers are marked with solid lines and substrate layers are marked with dash-dotted lines. The lower panel decomposes the DOS by atom. There are observable contributions from the interfacial substrate layer to both band edges. The highly dispersive band from the first substrate layer beginning ~ 3.5 eV above the valence band maximum is an artifact discussed in the text.

8.4 Polarity and structural properties

Excitonic properties in Mg_2TiO_4 depend sensitively on several interrelated factors: the physical proximity of band-edge states in real space, the presence and magnitude of a potential difference across the system, and the band offset between the substrate and the Mg_2TiO_4 film. Therefore, we began at the DFT level by tracking how these properties evolve as the Mg_2TiO_4 film grows layer-by-layer. We relaxed 1, 2, 3, 4, and 6 atomic layers of the tetrahedrally-interfaced Mg_2TiO_4 structure (discussed in the previous chapter) on 4 atomic layers of $\text{MgO}(001)$. The projected densities of states (PDOS) for these materials are plotted in Figures 8.2–8.6. We show both the layer-by-layer decomposition of the density of states and a projection onto atomic orbitals in order to explain both the physical location

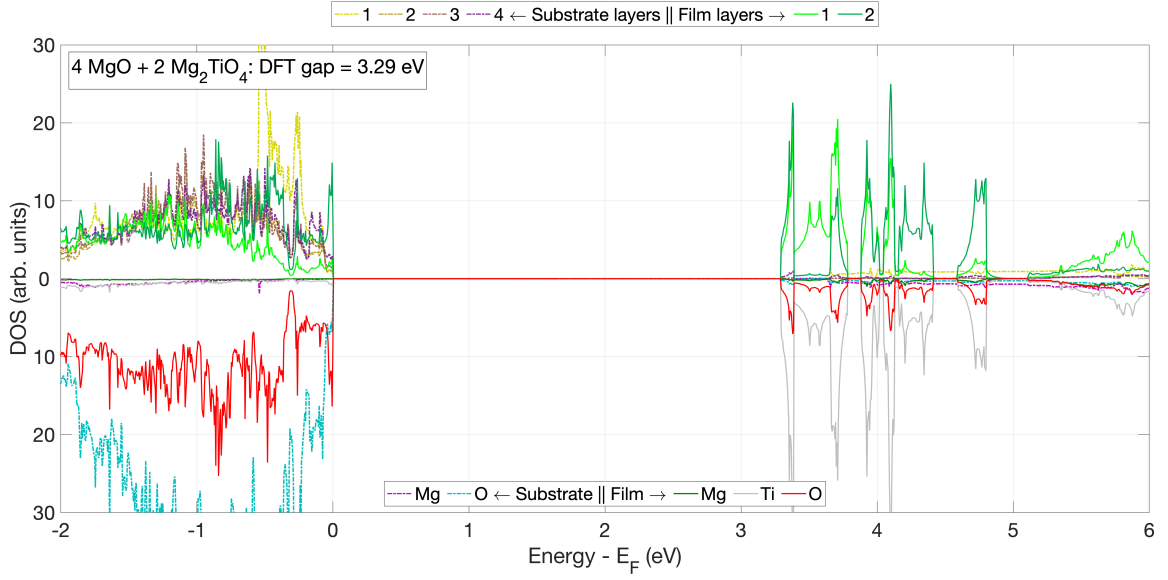


Figure 8.3: PDOS for two layers of Mg_2TiO_4 on $\text{MgO}(001)$. The panels and coloring are the same as in Figure 8.1. There is no appreciable band offset in the valence band, and substantial contributions from both Mg_2TiO_4 layers in the low-lying conduction bands.

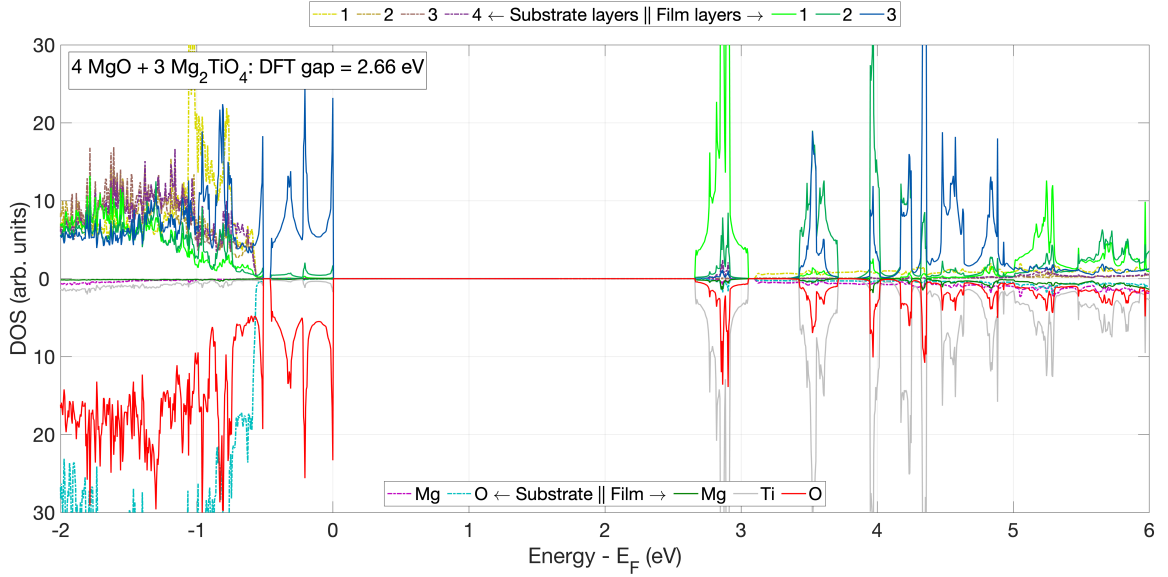


Figure 8.4: PDOS for three layers of Mg_2TiO_4 on $\text{MgO}(001)$. The panels and coloring are the same as in Figure 8.1. There is a type-I band offset between the substrate and the Mg_2TiO_4 , with the valence band maximum dominated by the surface Mg_2TiO_4 layer and the conduction band minimum dominated by the interfacial Mg_2TiO_4 layer.

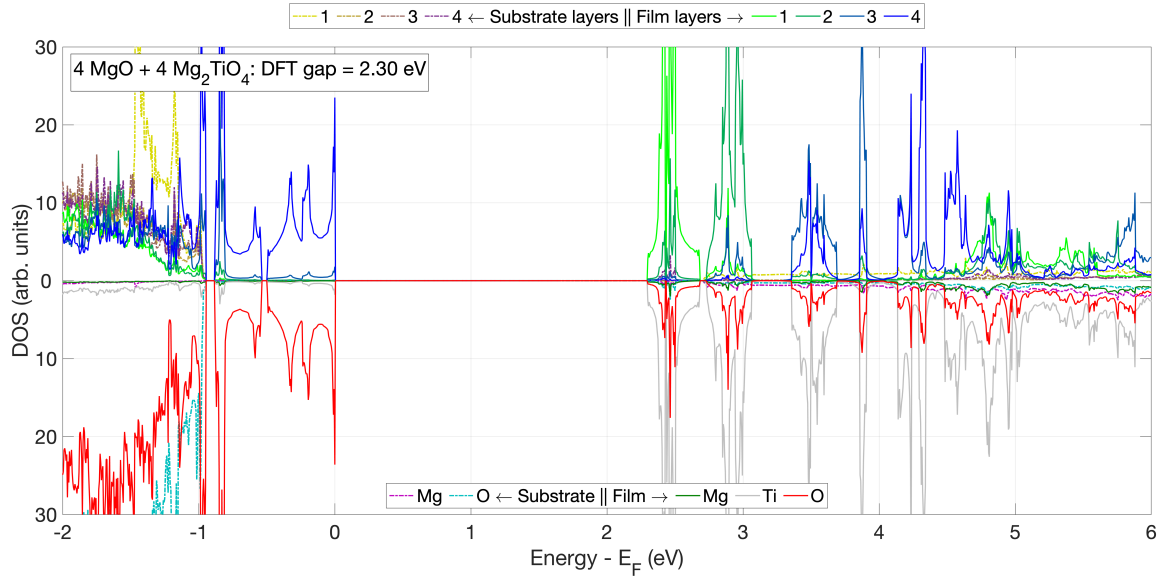


Figure 8.5: PDOS for four layers of Mg_2TiO_4 on $\text{MgO}(001)$. The panels and coloring are the same as in Figure 8.1. Roughly speaking, each of the lower two Mg_2TiO_4 layers contributes a low-lying flat conduction band, with the exterior Mg_2TiO_4 layers contributing in a more mixed fashion.

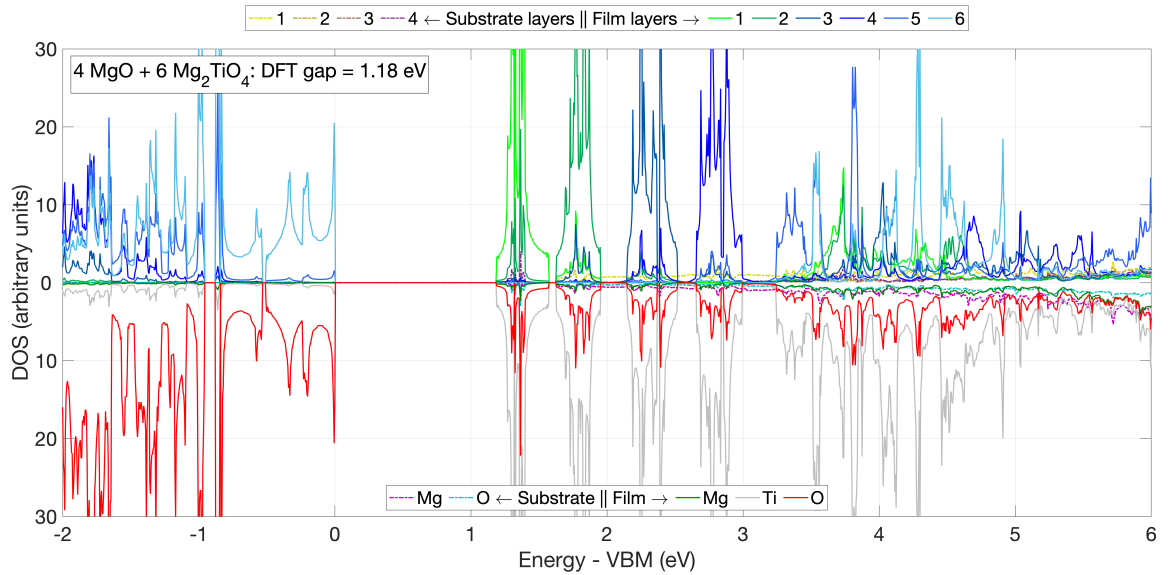


Figure 8.6: PDOS for six layers of Mg_2TiO_4 on $\text{MgO}(001)$. The panels and coloring are the same as in Figure 8.1. The conduction band features four clearly defined flat bands, each originating from a different interior Mg_2TiO_4 layer. The polar nature of the film is clearly illustrated by the dramatically reduced band gap.

Table 8.2: Potential difference and DFT band gaps for MgO + Mg₂TiO₄ slabs of varying thickness, all reported in eV. The bulk Mg₂TiO₄ band gap is also provided for comparison. The “surface gap” is the energy difference between the valence band maximum and the center of the first substantial peak in the surface-layer PDOS (see Figures 8.2–8.6). The reported band gaps consider Mg₂TiO₄ film states only; the unphysical conduction band feature in Figure 8.2 is ignored.

Number of layers	$\Delta\phi$	$\Delta\phi$ / Mg ₂ TiO ₄ layer	Band gap	Surface gap
Bulk Mg ₂ TiO ₄	-	-	3.52	-
3 MgO + 1 Mg ₂ TiO ₄	0.53	0.53	-	-
4 MgO + 1 Mg ₂ TiO ₄	0.51	0.51	3.82	3.90
3 MgO + 2 Mg ₂ TiO ₄	1.00	0.50	3.26	3.36
4 MgO + 2 Mg ₂ TiO ₄	1.00	0.50	3.29	3.38
3 MgO + 3 Mg ₂ TiO ₄	1.75	0.58	2.67	3.52
4 MgO + 3 Mg ₂ TiO ₄	1.76	0.59	2.66	3.53
4 MgO + 4 Mg ₂ TiO ₄	2.10	0.52	2.30	3.49
4 MgO + 6 Mg ₂ TiO ₄	3.17	0.53	1.18	3.54

and chemical character of the band edges. For thin films (1–2 Mg₂TiO₄ layers), there is substantial admixture between the band-edge states of the substrate and the film. Beginning with the 3-layer film, both band edges are dominated by states within the Mg₂TiO₄ film. The sharp onset of the PDOS in both the valence band and the conduction band indicates textbook 2D band dispersion, and the energetic narrowness of the features signals the presence of flat (*i.e.*, non-dispersive) bands. In this case, the valence band maximum is localized to O 2*p* states, while the conduction band minimum is localized to Ti 3*d* states.

As discussed in the previous chapter, the tetrahedrally-terminated Mg₂TiO₄ film is polar and generates a potential difference that grows with film thickness. This is a promising feature for the existence of interlayer excitons, since it tilts the band edges to localize the valence band maximum to the outer surface and the conduction band minimum to the MgO–Mg₂TiO₄ interface. This tilting is accompanied by a reduction in the overall band gap, as shown in Table 8.2. The potential difference cannot grow arbitrarily large without triggering a polar catastrophe leading to a surface reconstruction, so we expect that this structure will

break down for very thick films. This fate is hinted at in the six-layer PDOS presented in Figure 8.6: the outermost Mg_2TiO_4 layer retains a bulk-like band gap of roughly 3.54 eV (see the pale blue feature at that energy in the conduction band), but the global conduction band minimum has marched down to 1.18 eV, with a sequence of flat bands from each preceding layer above it.

There is a substrate feature in Figure 8.2 between 3.5 and 3.8 eV above the Fermi energy that requires explanation. This highly dispersive unoccupied state is composed of Mg $3s$ and O $2p$ states from the lower exposed surface of the MgO substrate slab. Such a state is unphysical in the context of an actual MBE experiment, since the substrate is not suspended in vacuum. In addition, we will find that the GW procedure shifts the energy of this surface state upwards by less than those of the Mg_2TiO_4 film, leading to anomalous values for the quasiparticle band gaps. In principle, this state could be removed from our calculation, perhaps by decorating the bottom edge of the substrate with neutral, electronically repulsive atoms such as He. However, due to its physical separation from the Mg_2TiO_4 overlayer, we find that this state does not couple to the others in absorption calculations, so its contributions can be readily ignored. Except where noted, quasiparticle energies below are reported after removing this state from consideration.

8.5 Quasiparticle calculations

Based on the data in Figures 8.2–8.6, we performed quasiparticle energy calculations on the smallest system that plausibly reflects the required band offset, a slab of three MgO layers and three Mg_2TiO_4 layers. We call this the M3T3 structure. A discussion of how to extrapolate our results to thicker slabs can be found in Section 8.7. We also performed tests

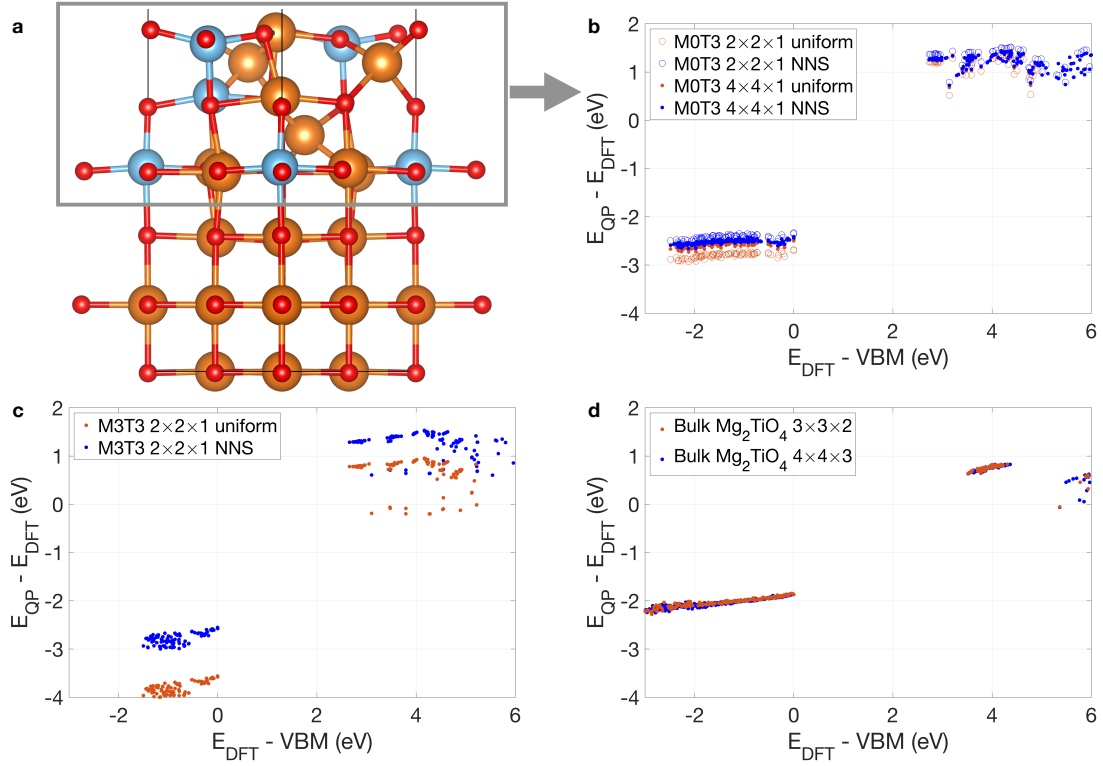


Figure 8.7: Quasiparticle energies for Mg_2TiO_4 -based materials. **(a)** Side view of the atomic structure of the M3T3 slab (three MgO layers + three Mg_2TiO_4 layers). Mg are large orange balls, O are small red balls, and Ti are blue balls. The layers outlined in gray are frozen and isolated in vacuum to produce the M0T3 structure. **(b)** Quasiparticle energies for M0T3, plotted as the DFT energies versus the quasiparticle energy correction. Results are shown for two \mathbf{q} -grids and two procedures for sampling the Brillouin zone. **(c)** Quasiparticle energies for M3T3. Only one \mathbf{q} -grid is used. **(d)** Quasiparticle energies for bulk Mg_2TiO_4 .

Table 8.3: Comparison of DFT and *GW* band gaps for Mg_2TiO_4 materials, all reported in eV. *GW* band gaps are labeled by the \mathbf{q} -grid on which the dielectric matrix was calculated.

Material	DFT	$2 \times 2 \times 1$		$4 \times 4 \times 1$	
		Uniform	NNS	Uniform	NNS
3 Mg_2TiO_4 layers	2.73	6.62	6.43	6.46	6.41
3 MgO + 3 Mg_2TiO_4 layers	2.67	7.00	6.50	-	-
Bulk Mg_2TiO_4	3.52	$3 \times 3 \times 2$		$4 \times 4 \times 3$	
		6.02		6.02	

on a smaller slab of three Mg_2TiO_4 layers frozen to their substrate-bound atomic positions but with the substrate removed (see Figure 8.7(a)), which we denote as M0T3. The dielectric matrix was calculated on a $2 \times 2 \times 1$ coarse \mathbf{q} -grid for both materials and also on a $4 \times 4 \times 1$ \mathbf{q} -grid for the M0T3 slab. In each case, we performed the calculation both on a uniform \mathbf{q} -grid and by subsampling the $\mathbf{q} = \mathbf{0}$ Voronoi cell with $N_s = 6$ radially distributed points (see Section 2.2.6 and [63]). The subsampling direction was chosen to be halfway between the principal polarization axes to maximally expedite convergence [63]. *GW* quasiparticle energies were calculated on a $2 \times 2 \times 1$ \mathbf{k} -grid and then interpolated onto a $4 \times 4 \times 1$ grid using wavefunction projections [53]. The near- E_F bands of this material are quite flat, so we expect the error due to the interpolation procedure to be less than 100 meV even on this coarse grid.

To identify features of our calculations that are unique to the Mg_2TiO_4 film, we also investigated the quasiparticle energies of bulk Mg_2TiO_4 . For this material, we calculated the dielectric matrix on both $3 \times 3 \times 2$ and $4 \times 4 \times 3$ \mathbf{q} -grids, and used each one to calculate quasiparticle energies on an identically-sized \mathbf{k} -grid.

Quasiparticle energies are plotted for each material in Figures 8.7(b-d). The horizontal axis of each plot is the DFT energy referenced to the valence band maximum, while the vertical axis is the difference in *GW* and DFT energies for each state. In general, the

conduction band states are shifted up by a modest amount, while the valence band states are pushed down more dramatically. We see in Figure 8.7(c) that the use of nonuniform Brillouin zone sampling for M3T3 produces a substantial correction to both the band gap (the conduction–valence energy difference) and the absolute quasiparticle energies. For both slab materials, the energy shift is quite rigid, with much of the conduction band being shifted up and much of the valence band being shifted down by roughly fixed amounts. The exceptions are the surface states mentioned in the previous section, which exhibit reduced quasiparticle energy shifts. As noted above, we do not include these unphysical states when reporting *GW* band gaps.

The band gap is substantially enhanced in each material: the DFT and *GW* band gaps calculated using various \mathbf{q}/\mathbf{k} -grids are compared in Table 8.3. For the M0T3 structure, the band gap changes by only 0.02 eV between the $2 \times 2 \times 1$ and $4 \times 4 \times 1$ NNS calculations; we thus expect the band gap in the $2 \times 2 \times 1$ NNS M3T3 calculation to be converged to within 100 meV, if not better. The quasiparticle energy corrections preserve the spatial band offset, but they slightly tilt the flat Γ –Y portion of the valence band seen in Figure 7.3(b). As a result, the band gap is now direct, when it was previously nominally indirect.

8.6 Excitonic and absorption calculations

We performed BSE calculations on the three structures discussed in the previous section: the M0T3 and M3T3 slabs and bulk Mg_2TiO_4 . For both slabs, we included 19 valence bands and 15 conduction bands in the calculation of the BSE kernel; this accounts for the top 1.5 eV of the valence bands and bottom 2.0 eV of the conduction bands in M3T3. In M0T3, the widths of the same energy windows are 2.1 eV and 2.5 eV, respectively. For bulk

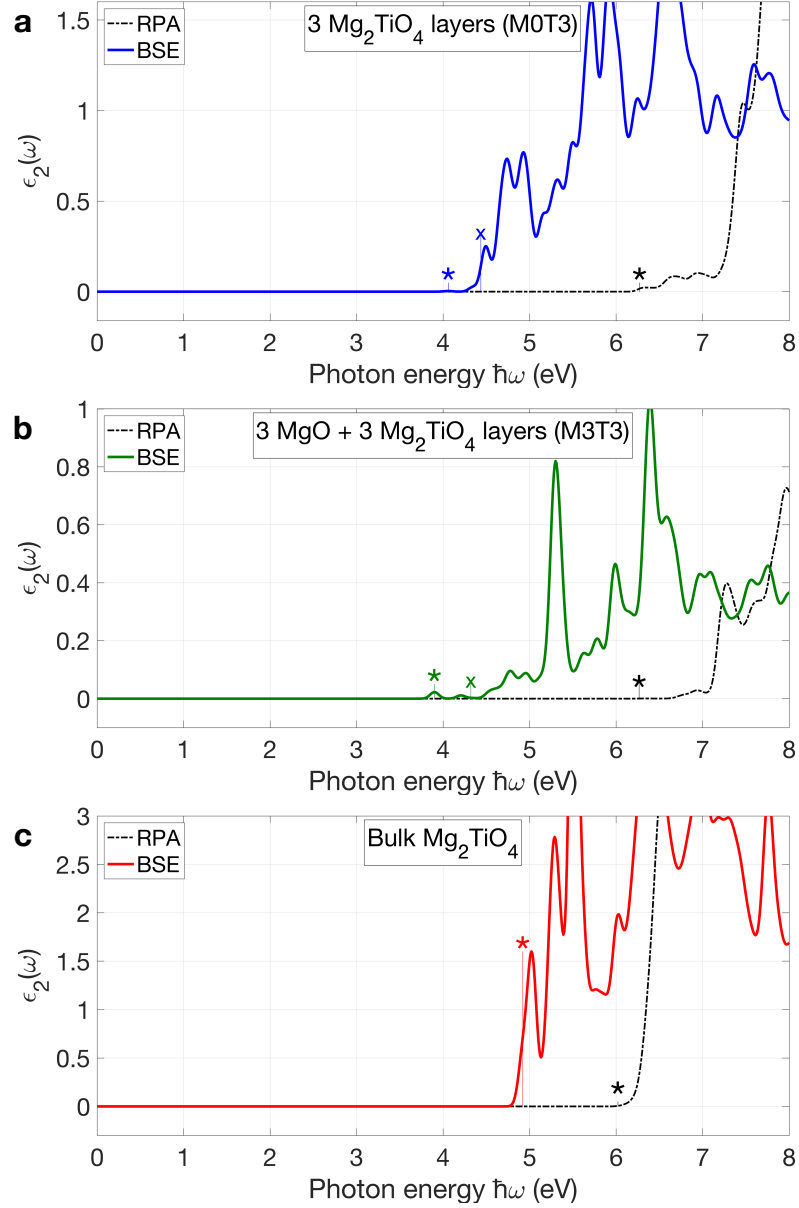


Figure 8.8: Absorption spectra for (a) M0T3, (b) M3T3, and (c) bulk Mg₂TiO₄ calculated with both the RPA and the BSE. The lowest-energy exciton (for BSE) and lowest-energy interband transition (for RPA) are marked with an asterisk; for the slabs, the lowest-energy interlayer exciton is marked with an “x.”

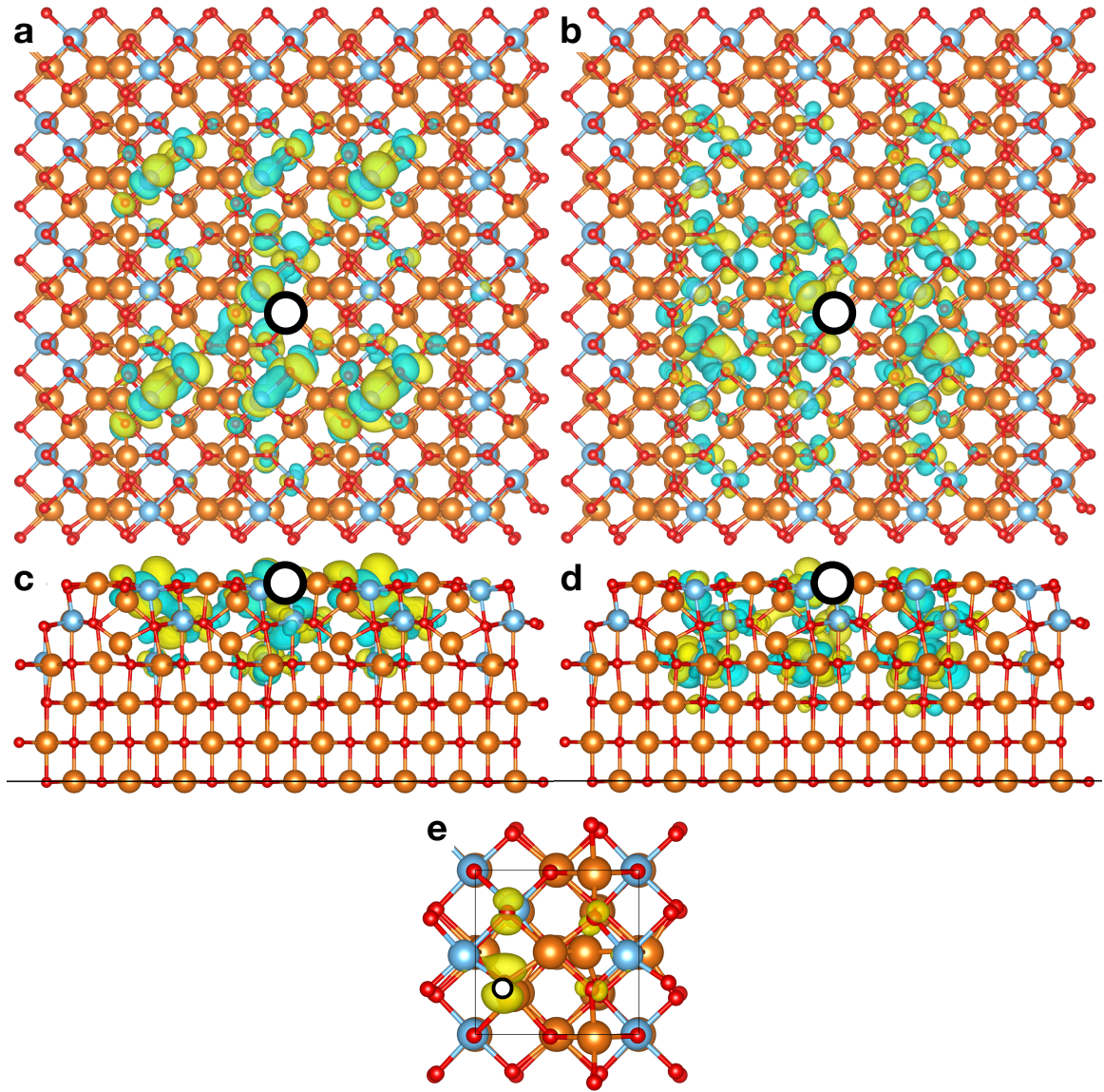


Figure 8.9: Intralayer (surface) and interlayer excitons for Mg_2TiO_4 on MgO . **(a,c)** Top **(a)** and side **(c)** views of the electron distribution $\Psi(\mathbf{r}_e, \mathbf{r}_h)$ for the lowest exciton in M3T3. The electron is primarily localized to the surface. **(b,d)** Top **(b)** and side **(d)** views of the lowest interlayer exciton in M3T3. In all exciton electron distribution plots, the hole location is marked by a white circle with a black border. **(e)** Isosurface of the marginal hole distribution for the surface exciton. The maximum of the distribution occurs at the point marked by a white circle with a black border, which is also the point chosen for the hole position in the other plots.

Table 8.4: Convergence of exciton binding energies (in eV) with coarse and fine grids for Mg_2TiO_4 materials.

Material	Coarse grid \rightarrow Fine grid	Binding energy	
		Largest	Interlayer
3 Mg_2TiO_4 layers (M0T3)	$2 \times 2 \times 1 \rightarrow 8 \times 8 \times 1$	2.77	2.36
	$2 \times 2 \times 1 \rightarrow 16 \times 16 \times 1$	2.92	2.50
	$4 \times 4 \times 1 \rightarrow 8 \times 8 \times 1$	2.21	1.85
	$4 \times 4 \times 1 \rightarrow 16 \times 16 \times 1$	2.35	1.97
3 MgO + 3 Mg_2TiO_4 layers (M3T3)	$2 \times 2 \times 1 \rightarrow 8 \times 8 \times 1$	2.46	2.04
	$2 \times 2 \times 1 \rightarrow 16 \times 16 \times 1$	2.60	2.18
Bulk Mg_2TiO_4	$3 \times 3 \times 2 \rightarrow 6 \times 6 \times 4$	1.09	-
	$3 \times 3 \times 2 \rightarrow 9 \times 9 \times 6$	1.10	-
	$4 \times 4 \times 3 \rightarrow 6 \times 6 \times 4$	1.10	-

Mg_2TiO_4 we included 48 valence bands and 28 conduction bands, accounting for a 4.3 eV valence window and a 5.3 eV conduction window. For solving the BSE and computing absorption spectra, we used fine grids with sizes up to $16 \times 16 \times 1$ for the slabs and $9 \times 9 \times 6$ for bulk Mg_2TiO_4 . On the fine grids, we included 14 valence bands and 12 conduction bands for the slabs, and 25 valence bands and 13 conduction bands for bulk Mg_2TiO_4 .

Figure 8.8 plots two absorption spectra for each of (a) M0T3, (b) M3T3, and (c) bulk Mg_2TiO_4 : the RPA spectrum computed from Equation 2.96 using the GW quasiparticle energies, and the excitonic spectrum computed from Equation 2.97. The difference between the smallest direct intraband transition energy and an exciton's energy is that exciton's binding energy. Table 8.4 shows the largest binding energy in each material for various coarse and fine \mathbf{k} -grid sizes.

The M3T3 absorption spectrum has several features that are promising for engineering long-lived excitons. Both the RPA and the BSE spectra have a range of at least 0.7 eV after onset in which the absorption is quite weak. For the RPA spectrum, the lowest-energy optical transition matrix elements are suppressed by the spatial separation of the surface-localized valence band states and the interfacial conduction band states. The lowest-energy BSE

excitons are similarly “dark.” This is promising for ensuring a long exciton lifetime, since electron–hole pairs that settle in the lowest-energy exciton states will not readily recombine via optical processes. Furthermore, the first exciton involving the unphysical lower-edge surface state appears at 5.40 eV, confirming that the main features of interest are localized to the proper surface of the slab. The binding energy is very large. The cited value of 2.60 eV is likely a substantial overestimate, as 2D BSE calculations converge slowly with respect to \mathbf{k} -grid size [63]. However, the bulk binding energy of 1.10 eV appears better-converged with respect to \mathbf{k} -grid size and is a plausible lower bound for the slab binding energy.

In Figures 8.9(a-d), we provide real-space plots of two M3T3 excitons of interest. The quantity plotted is the real part of the exciton wavefunction $\Psi(\mathbf{r}_e, \mathbf{r}_h)$, defined as

$$\Psi(\mathbf{r}_e, \mathbf{r}_h) = \sum_{v\mathbf{c}\mathbf{k}} A_{v\mathbf{c}\mathbf{k}}^S \psi_{c\mathbf{k}}(\mathbf{r}_e) \psi_{v\mathbf{k}}^*(\mathbf{r}_h). \quad (8.2)$$

This quantity gives the joint probability amplitude to observe an electron at \mathbf{r}_e and a hole at \mathbf{r}_h . To produce plots in real space, we fix the hole at the location that maximizes the marginal hole probability distribution, $P_h(\mathbf{r}_h) = \int d\mathbf{r}_e |\Psi(\mathbf{r}_e, \mathbf{r}_h)|^2$. For low-energy excitons, the hole distribution is made up in large part of unequal contributions from the $2p$ orbitals of surface O atoms, with the global maximum of the distribution being found immediately adjacent to one such atom (Figure 8.9(e)). With the hole fixed at that location, the plotted quantity then represents the spatial distribution of the electron.

The exciton in Figures 8.9(a) and (c) is the lowest-energy M3T3 exciton. It is localized to the vicinity of the hole, which is marked by a white circle with a black border. This partially helps to explain why the calculated binding energy is so large: the Coulomb interaction is very strong, even in the presence of electric field screening. Figures 8.9(b) and (d) show the

fourth-lowest exciton, which is localized much more strongly to the interfacial Mg_2TiO_4 layer. It is the most strongly-bound exciton that can properly be called “interlayer.” Both excitons are localized to the Mg_2TiO_4 layer, and both are associated with dark regions of the absorption spectrum in Figure 8.8(b). Nevertheless, it would be desirable to ensure that the interlayer exciton is the *most* strongly bound exciton in the system. In the following section, we investigate routes to accomplishing that goal.

8.7 Discussion

Our calculations suggest several routes to making the $\text{MgO-Mg}_2\text{TiO}_4$ structure more favorable for interlayer excitons. In general, this goal can be achieved either by weakening the overall scale of the binding energy or by increasing the within-film band offset.

The simplest way to reduce the binding energy is to ensure that the material environment screens electric fields more effectively, thus weakening the electron–hole interaction. One way to do this is to add a dielectric capping layer on top of the Mg_2TiO_4 film, ensuring that fringing fields from above the film are screened out more than in vacuum. Alternatively, or in addition, the substrate could be replaced by another lattice-matched cubic material with a larger optical dielectric constant ϵ_∞ and refractive index n . Options that compare favorably to MgO ($n = 1.7$, $a = 4.21 \text{ \AA}$) might include NiO ($n = 2.4$, $a = 4.18 \text{ \AA}$), CoO ($n = 2.3$, $a = 4.26 \text{ \AA}$), or MnO ($n = 2.2$, $a = 4.45 \text{ \AA}$) [231, 232]. A change in material environment may be accompanied by a change in film structure or band alignment, so more careful analysis is needed before pursuing any of these options.

A complementary approach is to increase the within-film band offset by adjusting the polarity or size of the Mg_2TiO_4 film. We expect that interlayer excitons will become

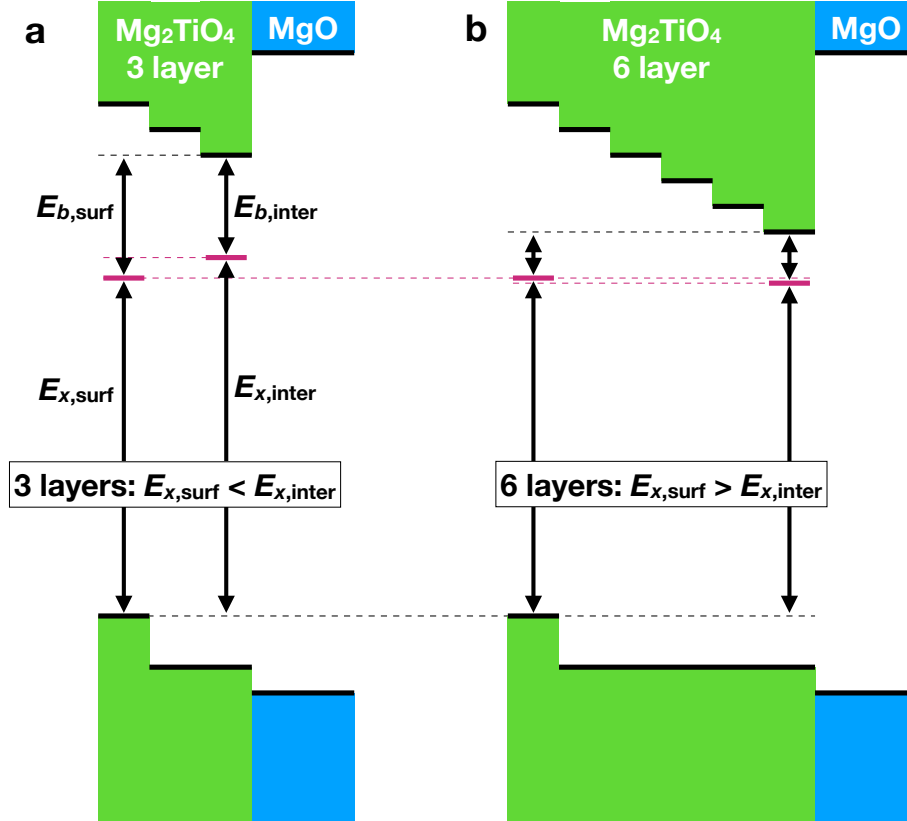


Figure 8.10: Schematic picture of how band edges and exciton binding energies are expected to evolve as Mg_2TiO_4 film thickness increases from (a) 3 layers to (b) 6 layers. In each panel, the horizontal fuschia lines represent the exciton energies E_x for prominent surface (left) and interlayer (right) excitons, measured with respect to the VBM. The energy difference between the CBM and the exciton energy is the binding energy E_b , which will weaken as the spatial separation between hole and electron increases. As discussed in the text, the band offset due to the film polarity is expected to produce an interlayer exciton at lower energy than the surface exciton for sufficiently thick films.

competitive with surface excitons as the Mg_2TiO_4 film becomes thicker, even as the electron and hole become more separated in space (see Figure 8.10). To explain why, we make crude predictions for exciton energies in the $(4 + 6)$ -layer structure of Figure 8.6. We assume that GW corrections shift the near- E_F band energies by a fixed amount (as demonstrated for the $(3 + 3)$ -layer structure in Figure 8.7(c)), that the gap between valence and conduction bands at the surface does not vary with Mg_2TiO_4 film thickness (as demonstrated in Table 8.2), and that the binding energy of an interlayer exciton varies inversely with film thickness (as the electron and hole interact across the thickness). We also assume that all near-onset binding energies for the $(3 + 3)$ structure are overestimated by a fixed amount ΔE_b .

Let the energy of the conduction band minimum at the $\text{MgO-Mg}_2\text{TiO}_4$ interface be E_{ci} , and let the energy of the surface conduction band PDOS peak be E_{cs} . According to Table 8.2, we have $\Delta E_c^{(3+3)} \equiv E_{cs}^{(3+3)} - E_{ci}^{(3+3)} = 0.85 \text{ eV}$ in the $(3 + 3)$ structure, compared to an offset of $\Delta E_c^{(4+6)} \equiv E_{cs}^{(4+6)} - E_{ci}^{(4+6)} = 2.36 \text{ eV}$ for the $(4 + 6)$ structure. We take the energies of the $(3 + 3)$ surface and interlayer excitons with respect to the valence band maximum to be $E_{x,\text{surf}}^{(3+3)} = 3.90 \text{ eV} + \Delta E_b$ and $E_{x,\text{inter}}^{(3+3)} = 4.32 \text{ eV} + \Delta E_b$, respectively. In the $(4 + 6)$ structure, the environment of the surface exciton is essentially unchanged, so we expect to have

$$E_{x,\text{surf}}^{(4+6)} = E_{x,\text{surf}}^{(3+3)} = 3.90 \text{ eV} + \Delta E_b. \quad (8.3)$$

Now let us estimate the interlayer exciton energy $E_{x,\text{inter}}^{(4+6)}$. In terms of our variables, the interlayer exciton binding energy is given by $E_{b,\text{inter}} = E_{ci} - E_{x,\text{inter}}$. For the $(3 + 3)$ structure we have $E_{b,\text{inter}}^{(3+3)} = 2.18 \text{ eV} - \Delta E_b$; we guess that in the $(4 + 6)$ structure this value is renormalized to $E_{b,\text{inter}}^{(4+6)} = \frac{3}{6} \times E_{b,\text{inter}}^{(3+3)} = 1.09 \text{ eV} - \frac{1}{2}\Delta E_b$. Since we assume that $E_{cs}^{(3+3)} = E_{cs}^{(4+6)}$, we can estimate $E_{ci}^{(4+6)}$ from the DFT band offsets and the GW value of

$$E_{ci}^{(3+3)} = 6.50 \text{ eV:}$$

$$\begin{aligned}
E_{x,\text{inter}}^{(4+6)} &= E_{ci}^{(4+6)} - E_{b,\text{inter}}^{(4+6)} \\
&= E_{ci}^{(3+3)} + \Delta E_c^{(3+3)} - \Delta E_c^{(4+6)} - E_{b,\text{inter}}^{(4+6)} \\
&= (6.50 + 0.85 - 2.36 - 1.09) \text{ eV} + \frac{1}{2} \Delta E_b \\
&= 3.90 \text{ eV} + \frac{1}{2} \Delta E_b.
\end{aligned} \tag{8.4}$$

The interlayer exciton should at least be competitive with the surface exciton in a 6-layer film, and may be the energetically favored state if the binding energy correction is substantial. This argument is presented graphically in Figure 8.10.

Future work on refining the above rough estimates will help clarify the situation. In particular, our analysis remains somewhat speculative until the binding energy can be more precisely converged. The obvious next step would be to attempt *GW* calculations on a denser uniform **k**-grid, but the memory needed to store the wavefunctions and dielectric matrices for M3T3 make this not currently practical. However, alternative techniques such as clustered subsampling interpolation (CSI) [63] allow the BSE kernel to be calculated on a finer grid than the original *GW* calculation. This does not require increasing the *GW* grid size, but does require computing $\epsilon_{\mathbf{G}\mathbf{G}'}(\mathbf{q})$ at additional subsampled $\mathbf{q} \approx \mathbf{0}$ points, a task that is feasible within our current resource constraints. We intend to test CSI on the M0T3 and M3T3 slabs in the coming months.

8.8 Conclusion

In this chapter, we have continued and extended our study of Mg_2TiO_4 films on $\text{MgO}(001)$. We have provided more detail on the relation of atomic structure to band offset in Mg_2TiO_4

films of various thickness, and computed the quasiparticle energies and absorption spectra of a representative Mg_2TiO_4 film. We have investigated the competition between surface and interlayer excitons, and discussed research directions to strengthen our conclusions. Our work on this project is ongoing, and proceeds in parallel with continuation of the experimental work described in Chapter 7.

Chapter 9

Summary and outlook

In this dissertation, we have presented *ab initio* calculations of three 2D materials: stanene (Chapters 3 and 4), borophene (Chapters 5 and 6), and a thin film of Mg_2TiO_4 (Chapters 7 and 8). Each of these projects suggests avenues for future research. In this chapter, we summarize the state of affairs for each project and outline some possible future work.

9.1 Stanene

In Chapter 3, we showed that stanene on Al_2O_3 is a gapped, topologically nontrivial insulator. We showed that stanene exhibits strong epitaxial binding, with a gap that is widened by chemical interaction with a dangling unoccupied Al orbital. We studied more broadly the effects of strain on both bare and decorated stanene, with an eye towards device applications. In Chapter 4, we identified a competing mode of tin deposition on Bi_2Te_3 .

Future work on stanene could explicitly consider decorated stanene sheets on substrates. As we showed, decoration with fluorine produces a topological insulator that remains non-trivial over a wide range of strains, while decoration with hydrogen produces a trivial

insulator. Proposed device applications for stanene often envision helical edge states within a single tin sheet at the boundary between two types of decoration [6]. We briefly discussed the potential for *in situ* decoration and exfoliation of stanene sheets in Section 3.4. Future *ab initio* projects could include simulations of that process on Al_2O_3 and other substrates. In addition, future work could consider the effect of half-functionalization, *i.e.*, introducing one adatom per stanene formula unit. This is more immediately plausible than full functionalization on substrates like Al_2O_3 , since we showed that the substrate already partially saturates the Sn p_z orbitals. Different decorations hybridize with stanene's p_z orbitals to produce different electronic properties; one could imagine an even greater range of combinatorial possibilities that arise from examining hybridization with both substrates and decorating groups.

9.2 Borophene

In Chapters 5 and 6, we identified the ground-state atomic structure of borophene on the Cu(111) and Cu(100) surfaces, respectively. We showed in each case that borophene binding is mediated by charge transfer from the metallic copper substrate, and that the structure is modulated by weak interactions with a supercell of the copper lattice. In Chapter 6, we further demonstrated the existence of Dirac cones and nodal lines in the borophene-on-Cu(100) band structure, even in the presence of the aforementioned structural modulation.

Future theoretical work could tackle the question of how to exfoliate borophene from a growth substrate. Proposed device applications often involve enclosing borophene between hexagonal boron nitride sheets to prevent oxygen exposure or combining it with other materials in a van der Waals heterostructure [151]. Clearly, to build these devices, borophene

must be peeled off of its metallic growth substrate, a task that requires overcoming the charge transfer that binds the boron sheet in the first place. Potential avenues to accomplish this task could include functionalizing the boron to weaken the boron–substrate interaction, or picking it up with a transfer material that binds more strongly than the growth substrate. *Ab initio* simulations of various binding and unbinding processes would be useful for devising a practical borophene device fabrication scheme. Since the equilibrium borophene hole fraction varies with the level of charge transfer from the surface [14, 15], *ab initio* studies could also examine how the properties of a borophene monolayer assembled on one substrate change when it is transferred to a different substrate.

9.3 Mg_2TiO_4

In Chapter 7, we showed that the polarity of an inverse spinel Mg_2TiO_4 film on $\text{MgO}(001)$ produces band-edge states that are spatially separated but localized to the Mg_2TiO_4 film, and showed how this band alignment is favorable for hosting interlayer excitons. In Chapter 8, we continued our analysis of Mg_2TiO_4 , calculating the quasiparticle energies of the material’s low-energy excitations and the binding energies of its excitons. We obtained both intralayer and interlayer excitons, and analyzed physical conditions under which interlayer excitons should dominate.

Our own future work will involve refining the calculations presented in Chapter 8 and confirming their convergence. In Section 8.7, we briefly discussed methods for obtaining a more carefully converged BSE kernel without dramatically increasing the computational cost and memory requirements of the *GW* step; those methods should be examined and tested in more detail. Interlayer excitons are believed to be more relevant in thicker (6+

layers) Mg_2TiO_4 films, so future calculations should explicitly treat such systems. If the size of such a system is computationally intractable, a reasonable first approximation could be obtained by calculating an Mg_2TiO_4 film in vacuum, as we did for a 3-layer film in Chapter 8. Future work could also assess the feasibility of encapsulating the Mg_2TiO_4 film with dielectric materials on both sides. In the limit of a thick cap, this calculation is arguably simpler than the ones presented here, since the Mg_2TiO_4 film is embedded in bulk-like MgO rather than resting on a finite-size slab. More broadly, future work could consider alternative substrates and/or transition metal oxide materials, since the existence of polar surfaces and *d*-type conduction bands is certainly not unique to Mg_2TiO_4 .

Bibliography

- [1] K. S. Novoselov, A. K. Geim, S. V. Morozov, D. Jiang, Y. Zhang, S. V. Dubonos, I. V. Grigorieva, and A. A. Firsov. Electric Field Effect in Atomically Thin Carbon Films. *Science*, 306(5696):666–669, October 2004. 1, 111
- [2] A. K. Geim and I. V. Grigorieva. Van der Waals heterostructures. *Nature*, 499(7459):419–425, July 2013. 1
- [3] Pierre Hohenberg and Walter Kohn. Inhomogeneous electron gas. *Physical Review*, 136(3B):B864–B871, 1964. 2, 6, 7, 8
- [4] W. Kohn and L. J. Sham. Self-Consistent Equations Including Exchange and Correlation Effects. *Physical Review*, 140(4A):A1133–A1138, November 1965. 2, 8
- [5] R. O. Jones. Density functional theory: Its origins, rise to prominence, and future. *Reviews of Modern Physics*, 87(3):897–923, August 2015. 2
- [6] Yong Xu, Binghai Yan, Hai-Jun Zhang, Jing Wang, Gang Xu, Peizhe Tang, Wenhui Duan, and Shou-Cheng Zhang. Large-Gap Quantum Spin Hall Insulators in Tin Films. *Physical Review Letters*, 111(13):136804, September 2013. 2, 3, 56, 59, 66, 71, 76, 86, 172
- [7] Evgeni S. Penev, Alex Kutana, and Boris I. Yakobson. Can Two-Dimensional Boron Superconduct? *Nano Letters*, 16(4):2522–2526, April 2016. 2, 3, 93, 111
- [8] Filip A. Rasmussen and Kristian S. Thygesen. Computational 2D Materials Database: Electronic Structure of Transition-Metal Dichalcogenides and Oxides. *The Journal of Physical Chemistry C*, 119(23):13169–13183, June 2015. 2, 134
- [9] Baojie Feng, Osamu Sugino, Ro-Ya Liu, Jin Zhang, Ryu Yukawa, Mitsuaki Kawamura, Takushi Iimori, Howon Kim, Yukio Hasegawa, Hui Li, Lan Chen, Kehui Wu, Hiroshi Kumigashira, Fumio Komori, Tai-Chang Chiang, Sheng Meng, and Iwao

- Matsuda. Dirac Fermions in Borophene. *Physical Review Letters*, 118(9), March 2017. 3, 93, 111, 112
- [10] Sunny Gupta, Alex Kutana, and Boris I. Yakobson. Dirac Cones and Nodal Line in Borophene. *The Journal of Physical Chemistry Letters*, 9(11):2757–2762, June 2018. 3, 111, 112, 130
- [11] Hui Tang and Sohrab Ismail-Beigi. Novel Precursors for Boron Nanotubes: The Competition of Two-Center and Three-Center Bonding in Boron Sheets. *Physical Review Letters*, 99(11):115501, September 2007. 3, 92, 93, 94, 98, 111
- [12] Hui Tang and Sohrab Ismail-Beigi. Self-doping in boron sheets from first principles: A route to structural design of metal boride nanostructures. *Physical Review B*, 80(13):134113, October 2009. 3, 92, 94, 108, 111
- [13] Evgeni S. Penev, Somnath Bhowmick, Arta Sadrzadeh, and Boris I. Yakobson. Polymorphism of Two-Dimensional Boron. *Nano Letters*, 12(5):2441–2445, May 2012. 3, 92, 93, 94, 111
- [14] Yuanyue Liu, Evgeni S. Penev, and Boris I. Yakobson. Probing the Synthesis of Two-Dimensional Boron by First-Principles Computations. *Angewandte Chemie*, 125(11):3238–3241, March 2013. 3, 173
- [15] Zhuhua Zhang, Yang Yang, Guoying Gao, and Boris I. Yakobson. Two-Dimensional Boron Monolayers Mediated by Metal Substrates. *Angewandte Chemie International Edition*, 54(44):13022–13026, October 2015. 3, 93, 94, 95, 107, 108, 173
- [16] Giuseppe Grosso and Giuseppe Pastori Parravicini. *Solid State Physics*. Academic Press, December 2015. 7, 10
- [17] D. M. Ceperley and B. J. Alder. Ground State of the Electron Gas by a Stochastic Method. *Physical Review Letters*, 45(7):566–569, August 1980. 11
- [18] J. P. Perdew and Alex Zunger. Self-interaction correction to density-functional approximations for many-electron systems. *Physical Review B*, 23(10):5048–5079, May 1981. 11, 96, 114
- [19] John P. Perdew and Yue Wang. Accurate and simple analytic representation of the electron-gas correlation energy. *Physical Review B*, 45(23):13244–13249, June 1992. 12

- [20] John P. Perdew, Kieron Burke, and Matthias Ernzerhof. Generalized gradient approximation made simple. *Physical Review Letters*, 77(18):3865, 1996. 12, 57, 151
- [21] Axel D. Becke. A new mixing of Hartree–Fock and local density-functional theories. *The Journal of Chemical Physics*, 98(2):1372–1377, January 1993. 12
- [22] John P. Perdew, Matthias Ernzerhof, and Kieron Burke. Rationale for mixing exact exchange with density functional approximations. *The Journal of Chemical Physics*, 105(22):9982–9985, December 1996. 13
- [23] Jochen Heyd, Gustavo E. Scuseria, and Matthias Ernzerhof. Hybrid functionals based on a screened Coulomb potential. *The Journal of Chemical Physics*, 118(18):8207–8215, May 2003. 13, 57, 69
- [24] Aliaksandr V. Krukau, Oleg A. Vydrov, Artur F. Izmaylov, and Gustavo E. Scuseria. Influence of the exchange screening parameter on the performance of screened hybrid functionals. *The Journal of Chemical Physics*, 125(22):224106, December 2006. 13, 57, 69
- [25] Gregory H. Wannier. The Structure of Electronic Excitation Levels in Insulating Crystals. *Physical Review*, 52(3):191–197, August 1937. 13
- [26] Nicola Marzari, Arash A. Mostofi, Jonathan R. Yates, Ivo Souza, and David Vanderbilt. Maximally localized Wannier functions: Theory and applications. *Reviews of Modern Physics*, 84(4):1419–1475, October 2012. 15
- [27] Nicola Marzari and David Vanderbilt. Maximally localized generalized Wannier functions for composite energy bands. *Physical Review B*, 56(20):12847, 1997. 15, 23, 127
- [28] Alexey A. Soluyanov and David Vanderbilt. Computing topological invariants without inversion symmetry. *Physical Review B*, 83(23):235401, June 2011. 16, 18, 58
- [29] R. D. King-Smith and David Vanderbilt. Theory of polarization of crystalline solids. *Physical Review B*, 47(3):1651–1654, January 1993. 16
- [30] David Vanderbilt and R. D. King-Smith. Electric polarization as a bulk quantity and its relation to surface charge. *Physical Review B*, 48(7):4442–4455, August 1993. 16
- [31] R. Resta. Theory of the electric polarization in crystals. *Ferroelectrics*, 136(1):51–55, November 1992. 16

- [32] Ivo Souza, Nicola Marzari, and David Vanderbilt. Maximally localized Wannier functions for entangled energy bands. *Physical Review B*, 65(3):035109, December 2001. 17
- [33] Giovanni Pizzi, Valerio Vitale, Ryotaro Arita, Stefan Blügel, Frank Freimuth, Guillaume Géranton, Marco Gibertini, Dominik Gresch, Charles Johnson, Takashi Koiratsune, Julen Ibañez-Azpiroz, Hyungjun Lee, Jae-Mo Lihm, Daniel Marchand, Antimo Marrazzo, Yuriy Mokrousov, Jamal I. Mustafa, Yoshiro Nohara, Yusuke Nomura, Lorenzo Paulatto, Samuel Poncé, Thomas Ponweiser, Junfeng Qiao, Florian Thöle, Stepan S. Tsirkin, Małgorzata Wierzbowska, Nicola Marzari, David Vanderbilt, Ivo Souza, Arash A. Mostofi, and Jonathan R. Yates. Wannier90 as a community code: new features and applications. *Journal of Physics: Condensed Matter*, 32(16):165902, April 2020. 18, 25, 58, 127
- [34] QuanSheng Wu, ShengNan Zhang, Hai-Feng Song, Matthias Troyer, and Alexey A. Soluyanov. WannierTools: An open-source software package for novel topological materials. *Computer Physics Communications*, 224:405–416, March 2018. 18, 58
- [35] G. Binnig, H. Rohrer, Ch. Gerber, and E. Weibel. Surface Studies by Scanning Tunneling Microscopy. *Physical Review Letters*, 49(1):57–61, July 1982. 18
- [36] D. M. Eigler and E. K. Schweizer. Positioning single atoms with a scanning tunnelling microscope. *Nature*, 344(6266):524–526, April 1990. 18
- [37] J. Tersoff and D. R. Hamann. Theory and application for the scanning tunneling microscope. *Physical Review Letters*, 50(25):1998–2001, 1983. 19, 96, 98, 104, 115
- [38] J. Tersoff and D. R. Hamann. Theory of the scanning tunneling microscope. *Physical Review B*, 31(2):805–813, January 1985. 19
- [39] J. Bardeen. Tunnelling from a Many-Particle Point of View. *Physical Review Letters*, 6(2):57–59, January 1961. 19
- [40] C. Julian Chen. Tunneling matrix elements in three-dimensional space: The derivative rule and the sum rule. *Physical Review B*, 42(14):8841–8857, 1990. 21, 96, 98, 103, 104, 115
- [41] Leo Gross, Nikolaj Moll, Fabian Mohn, Alessandro Curioni, Gerhard Meyer, Felix Hanke, and Mats Persson. High-Resolution Molecular Orbital Imaging Using a p -Wave STM Tip. *Physical Review Letters*, 107(8):086101, August 2011. 21, 96, 102, 113

- [42] Gábor Mándi and Krisztián Palotás. Chen’s derivative rule revisited: Role of tip-orbital interference in STM. *Physical Review B*, 91(16), April 2015. 21
- [43] Wei Ku, Tom Berlijn, and Chi-Cheng Lee. Unfolding First-Principles Band Structures. *Physical Review Letters*, 104(21):216401, May 2010. 22, 23, 24, 129
- [44] Voicu Popescu and Alex Zunger. Extracting E versus k effective band structure from supercell calculations on alloys and impurities. *Physical Review B*, page 12, 2012. 23, 25
- [45] Lars Hedin. New Method for Calculating the One-Particle Green’s Function with Application to the Electron-Gas Problem. *Physical Review*, 139(3A):A796–A823, August 1965. 26, 30
- [46] Mark S. Hybertsen and Steven G. Louie. First-Principles Theory of Quasiparticles: Calculation of Band Gaps in Semiconductors and Insulators. *Physical Review Letters*, 55(13):1418–1421, September 1985. 26
- [47] Mark S. Hybertsen and Steven G. Louie. Electron correlation in semiconductors and insulators: Band gaps and quasiparticle energies. *Physical Review B*, 34(8):5390–5413, October 1986. 26, 31, 34, 35, 37, 38, 151
- [48] F. Aryasetiawan and O. Gunnarsson. The GW method. *Reports on Progress in Physics*, 61(3):237–312, March 1998. 29, 30, 32
- [49] Henrik Bruus and Karsten Flensberg. *Many-body quantum theory in condensed matter physics: an introduction*. Oxford University Press, 2004. 29
- [50] Stephen L. Adler. Quantum Theory of the Dielectric Constant in Real Solids. *Physical Review*, 126(2):413–420, April 1962. 34
- [51] Nathan Wiser. Dielectric Constant with Local Field Effects Included. *Physical Review*, 129(1):62–69, January 1963. 34
- [52] S. B. Zhang, D. Tománek, Marvin L. Cohen, Steven G. Louie, and Mark S. Hybertsen. Evaluation of quasiparticle energies for semiconductors without inversion symmetry. *Physical Review B*, 40(5):3162–3168, August 1989. 36
- [53] Jack Deslippe, Georgy Samsonidze, David A. Strubbe, Manish Jain, Marvin L. Cohen, and Steven G. Louie. BerkeleyGW: A Massively Parallel Computer Package for the Calculation of the Quasiparticle and Optical Properties of Materials and Nanostructures. *Computer Physics Communications*, 183(6):1269–1289, June 2012. 36, 44, 46, 151, 160

- [54] Michael Rohlfing and Steven G. Louie. Electron-hole excitations and optical spectra from first principles. *Physical Review B*, 62(8):4927–4944, August 2000. 38, 39, 40, 41, 42, 151
- [55] P. Umari, Geoffrey Stenuit, and Stefano Baroni. Optimal representation of the polarization propagator for large-scale *GW* calculations. *Physical Review B*, 79(20):201104, May 2009. 48
- [56] Feliciano Giustino, Marvin L. Cohen, and Steven G. Louie. *GW* method with the self-consistent Sternheimer equation. *Physical Review B*, 81(11):115105, March 2010. 48
- [57] Murilo L. Tiago and James R. Chelikowsky. Optical excitations in organic molecules, clusters, and defects studied by first-principles Green’s function methods. *Physical Review B*, 73(20):205334, May 2006. 48
- [58] Fabien Bruneval and Xavier Gonze. Accurate *GW* self-energies in a plane-wave basis using only a few empty states: Towards large systems. *Physical Review B*, 78(8):085125, August 2008. 48
- [59] Wei Kang and Mark S. Hybertsen. Enhanced static approximation to the electron self-energy operator for efficient calculation of quasiparticle energies. *Physical Review B*, 82(19):195108, November 2010. 48, 49
- [60] Jack Deslippe, Georgy Samsonidze, Manish Jain, Marvin L. Cohen, and Steven G. Louie. Coulomb-hole summations and energies for *GW* calculations with limited number of empty orbitals: A modified static remainder approach. *Physical Review B*, 87(16):165124, April 2013. 48, 151
- [61] Georgy Samsonidze, Manish Jain, Jack Deslippe, Marvin L. Cohen, and Steven G. Louie. Simple Approximate Physical Orbitals for *GW* Quasiparticle Calculations. *Physical Review Letters*, 107(18):186404, October 2011. 50, 151
- [62] Sohrab Ismail-Beigi. Truncation of periodic image interactions for confined systems. *Physical Review B*, 73(23):233103, June 2006. 52, 53, 151
- [63] Felipe H. da Jornada, Diana Y. Qiu, and Steven G. Louie. Nonuniform sampling schemes of the Brillouin zone for many-electron perturbation-theory calculations in reduced dimensionality. *Physical Review B*, 95(3):035109, January 2017. 53, 160, 165, 169

- [64] Stephen Eltinge and Sohrab Ismail-Beigi. Structure and binding of stanene on the $\text{Al}_2\text{O}_3(0001)$ surface. *arXiv:2009.00684 [cond-mat]*, September 2020. 55, 91
- [65] Alessandro Molle, Joshua Goldberger, Michel Houssa, Yong Xu, Shou-Cheng Zhang, and Deji Akinwande. Buckled two-dimensional Xene sheets. *Nature Materials*, 16(2):163–169, January 2017. 56, 71
- [66] Ji-Kai Lyu, Shu-Feng Zhang, Chang-Wen Zhang, and Pei-Ji Wang. Stanene: A Promising Material for New Electronic and Spintronic Applications. *Annalen der Physik*, 531(10):1900017, October 2019. 56
- [67] Sumanta Kumar Sahoo and Kung-Hwa Wei. A Perspective on Recent Advances in 2D Stanene Nanosheets. *Advanced Materials Interfaces*, 6(18):1900752, September 2019. 56, 76
- [68] Yandong Ma, Ying Dai, Meng Guo, Chengwang Niu, and Baibiao Huang. Intriguing Behavior of Halogenated Two-Dimensional Tin. *The Journal of Physical Chemistry C*, 116(23):12977–12981, June 2012. 56
- [69] Jun Zheng, Feng Chi, and Yong Guo. Spin-current diodes based on germanene and stanene subjected to local exchange fields. *Applied Physics Letters*, 113(11):112404, September 2018. 56, 71
- [70] E. G. Marin, D. Marian, G. Iannaccone, and G. Fiori. Tunnel-Field-Effect Spin Filter from Two-Dimensional Antiferromagnetic Stanene. *Physical Review Applied*, 10(4):044063, October 2018. 56, 71
- [71] William G. Vandenberghe and Massimo V. Fischetti. Imperfect two-dimensional topological insulator field-effect transistors. *Nature Communications*, 8(1):14184, April 2017. 56, 71
- [72] Amirali Abbasi. Modulation of the electronic properties of pristine and AlP-codoped stanene monolayers by the adsorption of CH_2O and CH_4 molecules: a DFT study. *Materials Research Express*, 6(7):076410, April 2019. 56, 71
- [73] Amirali Abbasi. Theoretical Investigation of The interaction Between Noble Metals (Ag, Au, Pd, Pt) and Stanene Nanosheets: A DFT Study. *Journal of Inorganic and Organometallic Polymers and Materials*, 29(6):1895–1915, November 2019. 56, 71
- [74] Huisheng Zhang, Zhe Wang, and Xiaohong Xu. Room temperature quantum spin Hall insulator: Functionalized stanene on layered PbI_2 substrate. *Applied Physics Letters*, 111(7):072105, August 2017. 56, 71

- [75] Shu-Chun Wu, Guangcun Shan, and Binghai Yan. Prediction of Near-Room-Temperature Quantum Anomalous Hall Effect on Honeycomb Materials. *Physical Review Letters*, 113(25):256401, December 2014. 56
- [76] Filipe Matusalem, Friedhelm Bechstedt, Marcelo Marques, and Lara K. Teles. Quantum spin Hall phase in stanene-derived overlayers on passivated SiC substrates. *Physical Review B*, 94(24):241403(R), December 2016. 56
- [77] Ping Li. Stanene on a SiC(0001) surface: a candidate for realizing quantum anomalous Hall effect. *Physical Chemistry Chemical Physics*, 21(21):11150–11157, 2019. 56, 76
- [78] Yong Xu, Peizhe Tang, and Shou-Cheng Zhang. Large-gap quantum spin Hall states in decorated stanene grown on a substrate. *Physical Review B*, 92(8):081112(R), August 2015. 56, 76, 86
- [79] Junji Yuhara, Yuya Fujii, Kazuki Nishino, Naoki Isobe, Masashi Nakatake, Lede Xian, Angel Rubio, and Guy Le Lay. Large area planar stanene epitaxially grown on Ag(111). *2D Materials*, 5(2):025002, January 2018. 56, 77, 90, 91
- [80] Tsuyoshi Ogikubo, Hiroki Shimazu, Yuya Fujii, Koichi Ito, Akio Ohta, Masaaki Araidai, Masashi Kurosawa, Guy Le Lay, and Junji Yuhara. Continuous Growth of Germanene and Stanene Lateral Heterostructures. *Advanced Materials Interfaces*, 7(10):1902132, May 2020. 56
- [81] Yani Liu, Nan Gao, Jincheng Zhuang, Chen Liu, Jiaou Wang, Weichang Hao, Shi Xue Dou, Jijun Zhao, and Yi Du. Realization of Strained Stanene by Interface Engineering. *The Journal of Physical Chemistry Letters*, 10(7):1558–1565, April 2019. 56, 90, 91
- [82] Wenhui Pang, Kazuki Nishino, Tsuyoshi Ogikubo, Masaaki Araidai, Masashi Nakatake, Guy Le Lay, and Junji Yuhara. Epitaxial growth of honeycomb-like stanene on Au(111). *Applied Surface Science*, 517:146224, March 2020. 56, 90, 91
- [83] Jian Gou, Longjuan Kong, Hui Li, Qing Zhong, Wenbin Li, Peng Cheng, Lan Chen, and Kehui Wu. Strain-induced band engineering in monolayer stanene on Sb(111). *Physical Review Materials*, 1(5):054004, October 2017. 56
- [84] Feng-feng Zhu, Wei-jiong Chen, Yong Xu, Chun-lei Gao, Dan-dan Guan, Can-hua Liu, Dong Qian, Shou-Cheng Zhang, and Jin-feng Jia. Epitaxial growth of two-dimensional stanene. *Nature Materials*, 14(10):1020–1025, August 2015. 56, 76, 78, 82, 86, 90, 91, 111

- [85] Jinmei Li, Tao Lei, Jiaou Wang, Rui Wu, Jiali Zhao, Lei Zhao, Yuxuan Guo, Haijie Qian, and Kurash Ibrahim. Anisotropic Electronic Structure and Interfacial Chemical Reaction of Stanene/Bi₂Te₃. *The Journal of Physical Chemistry C*, 124(8):4917–4924, February 2020. 56, 80, 90
- [86] Jinmei Li, Tao Lei, Jiaou Wang, Rui Wu, Haijie Qian, and Kurash Ibrahim. In-plane crystal field constrained electronic structure of stanene. *Applied Physics Letters*, 116(10):101601, March 2020. 56, 90
- [87] Jialiang Deng, Bingyu Xia, Xiaochuan Ma, Haoqi Chen, Huan Shan, Xiaofang Zhai, Bin Li, Aidi Zhao, Yong Xu, Wenhui Duan, Shou-Cheng Zhang, Bing Wang, and J. G. Hou. Epitaxial growth of ultraflat stanene with topological band inversion. *Nature Materials*, 17(12):1081–1086, December 2018. 56, 90, 91, 111
- [88] Yunyi Zang, Tian Jiang, Yan Gong, Zhaoyong Guan, Chong Liu, Menghan Liao, Ke-jing Zhu, Zhe Li, Lili Wang, Wei Li, Canli Song, Ding Zhang, Yong Xu, Ke He, Xucun Ma, Shou-Cheng Zhang, and Qi-Kun Xue. Realizing an Epitaxial Decorated Stanene with an Insulating Bandgap. *Advanced Functional Materials*, 28(35):1802723, August 2018. 56
- [89] Cai-Zhi Xu, Yang-Hao Chan, Peng Chen, Xiaoxiong Wang, David Flototto, Joseph Andrew Hlevyack, Guang Bian, Sung-Kwan Mo, Mei-Yin Chou, and Tai-Chang Chiang. Gapped electronic structure of epitaxial stanene on InSb(111). *Physical Review B*, 97(3):035122, January 2018. 56
- [90] Xiaohu Zheng, Jian-Feng Zhang, Bingbing Tong, and Rui-Rui Du. Epitaxial growth and electronic properties of few-layer stanene on InSb(111). *2D Materials*, 7(1):011001, October 2019. 56, 90, 91
- [91] Hui Wang, S. T. Pi, J. Kim, Z. Wang, H. H. Fu, and R. Q. Wu. Possibility of realizing quantum spin Hall effect at room temperature in stanene/Al₂O₃(0001). *Physical Review B*, 94(3):035112, July 2016. 57, 61, 62, 76, 90
- [92] Masaaki Araidai, Masashi Kurosawa, Akio Ohta, and Kenji Shiraishi. First-principles study on adsorption structure and electronic state of stanene on α -alumina surface. *Japanese Journal of Applied Physics*, 56(9):095701, September 2017. 57, 61
- [93] Paolo Giannozzi, Stefano Baroni, Nicola Bonini, Matteo Calandra, Roberto Car, Carlo Cavazzoni, Davide Ceresoli, Guido L. Chiarotti, Matteo Cococcioni, Ismaila Dabo, Andrea Dal Corso, Stefano de Gironcoli, Stefano Fabris, Guido Fratesi, Ralph Gebauer, Uwe Gerstmann, Christos Gougoussis, Anton Kokalj, Michele Lazzeri,

- Layla Martin-Samos, Nicola Marzari, Francesco Mauri, Riccardo Mazzarello, Stefano Paolini, Alfredo Pasquarello, Lorenzo Paulatto, Carlo Sbraccia, Sandro Scandolo, Gabriele Sclauzero, Ari P. Seitsonen, Alexander Smogunov, Paolo Umari, and Renata M. Wentzcovitch. QUANTUM ESPRESSO: a modular and open-source software project for quantum simulations of materials. *Journal of Physics: Condensed Matter*, 21(39):395502, September 2009. 57, 96, 98, 104, 113, 114, 150
- [94] P. Giannozzi, O. Andreussi, T. Brumme, O. Bunau, M. Buongiorno Nardelli, M. Calandra, R. Car, C. Cavazzoni, D. Ceresoli, M. Cococcioni, N. Colonna, I. Carnimeo, A. Dal Corso, S. de Gironcoli, P. Delugas, R. A. DiStasio, A. Ferretti, A. Floris, G. Fratesi, G. Fugallo, R. Gebauer, U. Gerstmann, F. Giustino, T. Gorni, J. Jia, M. Kawamura, H.-Y. Ko, A. Kokalj, E. Küçükbenli, M. Lazzeri, M. Marsili, N. Marzari, F. Mauri, N. L. Nguyen, H.-V. Nguyen, A. Otero-de-la Roza, L. Paulatto, S. Poncé, D. Rocca, R. Sabatini, B. Santra, M. Schlipf, A. P. Seitsonen, A. Smogunov, I. Timrov, T. Thonhauser, P. Umari, N. Vast, X. Wu, and S. Baroni. Advanced capabilities for materials modelling with Quantum ESPRESSO. *Journal of Physics: Condensed Matter*, 29(46):465901, November 2017. 57, 96, 113, 114, 150
- [95] G. Kresse and J. Furthmüller. Efficiency of ab-initio total energy calculations for metals and semiconductors using a plane-wave basis set. *Computational Materials Science*, 6(1):15–50, July 1996. 57, 69
- [96] Stefan Grimme. Semiempirical GGA-type density functional constructed with a long-range dispersion correction. *Journal of Computational Chemistry*, 27(15):1787–1799, November 2006. 58, 61, 62
- [97] Vincenzo Barone, Maurizio Casarin, Daniel Forrer, Michele Pavone, Mauro Sami, and Andrea Vittadini. Role and effective treatment of dispersive forces in materials: Polyethylene and graphite crystals as test cases. *Journal of Computational Chemistry*, 30(6):934–939, April 2009. 58
- [98] Stefan Grimme, Jens Antony, Stephan Ehrlich, and Helge Krieg. A consistent and accurate *ab initio* parametrization of density functional dispersion correction (DFT-D) for the 94 elements H–Pu. *The Journal of Chemical Physics*, 132(15):154104, April 2010. 58, 61, 62
- [99] Axel D. Becke and Erin R. Johnson. Exchange-hole dipole moment and the dispersion interaction revisited. *The Journal of Chemical Physics*, 127(15):154108, October 2007. 58, 61, 62

- [100] A. Otero-de-la Roza and Erin R. Johnson. Van der Waals interactions in solids using the exchange-hole dipole moment model. *The Journal of Chemical Physics*, 136(17):174109, May 2012. 58, 61, 62
- [101] Liang Fu and C. L. Kane. Topological insulators with inversion symmetry. *Physical Review B*, 76(4):045302, July 2007. 58, 59, 67
- [102] Peizhe Tang, Pengcheng Chen, Wendong Cao, Huaqing Huang, Seymour Cahangirov, Lede Xian, Yong Xu, Shou-Cheng Zhang, Wenhui Duan, and Angel Rubio. Stable two-dimensional dumbbell stanene: A quantum spin Hall insulator. *Physical Review B*, 90(12):121408(R), September 2014. 65, 66, 76
- [103] Jing Wang, Yong Xu, and Shou-Cheng Zhang. Two-dimensional time-reversal-invariant topological superconductivity in a doped quantum spin-Hall insulator. *Physical Review B*, 90(5):054503, August 2014. 71
- [104] Stephen D. Albright, Ke Zou, Claudia Lau, Stephen Eltinge, Hawoong Hong, Sohrab Ismail-Beigi, Frederick J. Walker, and Charles H. Ahn. Identifying crystal structures and chemical reactions at the interface of stanene on Bi_2Te_3 . *Journal of Applied Physics*, 128(16):165301, October 2020. 74, 77, 78, 86
- [105] K. I. Bolotin, K. J. Sikes, Z. Jiang, M. Klima, G. Fudenberg, J. Hone, P. Kim, and H. L. Stormer. Ultrahigh electron mobility in suspended graphene. *Solid State Communications*, 146(9-10):351–355, June 2008. 75
- [106] Lei Liao, Yung-Chen Lin, Mingqiang Bao, Rui Cheng, Jingwei Bai, Yuan Liu, Yongquan Qu, Kang L. Wang, Yu Huang, and Xiangfeng Duan. High-speed graphene transistors with a self-aligned nanowire gate. *Nature*, 467(7313):305–308, September 2010. 75
- [107] B. Radisavljevic, A. Radenovic, J. Brivio, V. Giacometti, and A. Kis. Single-layer MoS_2 transistors. *Nature Nanotechnology*, 6(3):147–150, March 2011. 75
- [108] Danfeng Li, Kyuho Lee, Bai Yang Wang, Motoki Osada, Samuel Crossley, Hye Ryoung Lee, Yi Cui, Yasuyuki Hikita, and Harold Y. Hwang. Superconductivity in an infinite-layer nickelate. *Nature*, 572(7771):624–627, August 2019. 75
- [109] Ivan Božović and Charles Ahn. A new frontier for superconductivity. *Nature Physics*, 10(12):892–895, December 2014. 75
- [110] Jian-Feng Ge, Zhi-Long Liu, Canhua Liu, Chun-Lei Gao, Dong Qian, Qi-Kun Xue, Ying Liu, and Jin-Feng Jia. Superconductivity above 100 K in single-layer FeSe films on doped SrTiO_3 . *Nature Materials*, 14(3):285–289, March 2015. 75

- [111] Ke Zou, Subhasish Mandal, Stephen D. Albright, Rui Peng, Yujia Pu, Divine Kumah, Claudia Lau, Georg H. Simon, Omur E. Dagdeviren, Xi He, Ivan Božović, Udo D. Schwarz, Eric I. Altman, Donglai Feng, Fred J. Walker, Sohrab Ismail-Beigi, and Charles H. Ahn. Role of double TiO_2 layers at the interface of $\text{FeSe}/\text{SrTiO}_3$ superconductors. *Physical Review B*, 93(18):180506, May 2016. 75
- [112] Rui Peng, Ke Zou, M. G. Han, Stephen D. Albright, Hawoong Hong, Claudia Lau, H. C. Xu, Yimei Zhu, F. J. Walker, and C. H. Ahn. Picoscale structural insight into superconductivity of monolayer $\text{FeSe}/\text{SrTiO}_3$. *Science Advances*, 6(15):eaay4517, April 2020. 75
- [113] Qimiao Si, Rong Yu, and Elihu Abrahams. High-temperature superconductivity in iron pnictides and chalcogenides. *Nature Reviews Materials*, 1(4):16017, April 2016. 75
- [114] M. König, S. Wiedmann, C. Brune, A. Roth, H. Buhmann, L. W. Molenkamp, X.-L. Qi, and S.-C. Zhang. Quantum Spin Hall Insulator State in HgTe Quantum Wells. *Science*, 318(5851):766–770, November 2007. 75
- [115] Philipp Leubner, Lukas Lunczer, Christoph Brüne, Hartmut Buhmann, and Laurens W. Molenkamp. Strain Engineering of the Band Gap of HgTe Quantum Wells Using Superlattice Virtual Substrates. *Physical Review Letters*, 117(8):086403, August 2016. 75
- [116] X. Qian, J. Liu, L. Fu, and J. Li. Quantum spin Hall effect in two-dimensional transition metal dichalcogenides. *Science*, 346(6215):1344–1347, December 2014. 75
- [117] Shujie Tang, Chaofan Zhang, Dillon Wong, Zahra Pedramrazi, Hsin-Zon Tsai, Chun-jing Jia, Brian Moritz, Martin Claassen, Hyejin Ryu, Salman Kahn, Juan Jiang, Hao Yan, Makoto Hashimoto, Donghui Lu, Robert G. Moore, Chan-Cuk Hwang, Choongyu Hwang, Zahid Hussain, Yulin Chen, Miguel M. Ugeda, Zhi Liu, Xiaoming Xie, Thomas P. Devereaux, Michael F. Crommie, Sung-Kwan Mo, and Zhi-Xun Shen. Quantum spin Hall state in monolayer $1\text{T}'\text{-WTe}_2$. *Nature Physics*, 13(7):683–687, July 2017. 75
- [118] Junwei Liu, Timothy H. Hsieh, Peng Wei, Wenhui Duan, Jagadeesh Moodera, and Liang Fu. Spin-filtered edge states with an electrically tunable gap in a two-dimensional topological crystalline insulator. *Nature Materials*, 13(2):178–183, December 2013. 75

- [119] Ilan T. Rosen, Eli J. Fox, Xufeng Kou, Lei Pan, Kang L. Wang, and David Goldhaber-Gordon. Chiral transport along magnetic domain walls in the quantum anomalous Hall effect. *npj Quantum Materials*, 2(1):69, December 2017. 75
- [120] K. Yasuda, M. Mogi, R. Yoshimi, A. Tsukazaki, K. S. Takahashi, M. Kawasaki, F. Kagawa, and Y. Tokura. Quantized chiral edge conduction on domain walls of a magnetic topological insulator. *Science*, 358(6368):1311–1314, December 2017. 75
- [121] Qing Lin He, Lei Pan, Alexander L. Stern, Edward C. Burks, Xiaoyu Che, Gen Yin, Jing Wang, Biao Lian, Quan Zhou, Eun Sang Choi, Koichi Murata, Xufeng Kou, Zhijie Chen, Tianxiao Nie, Qiming Shao, Yabin Fan, Shou-Cheng Zhang, Kai Liu, Jing Xia, and Kang L. Wang. Chiral Majorana fermion modes in a quantum anomalous Hall insulator–superconductor structure. *Science*, 357(6348):294–299, July 2017. 75
- [122] Ke Zou, Stephen D. Albright, Omur E. Dagdeviren, M. D. Morales-Acosta, Georg H. Simon, Chao Zhou, Subhasish Mandal, Sohrab Ismail-Beigi, Udo D. Schwarz, Eric I. Altman, Frederick J. Walker, and Charles H. Ahn. Revealing surface-state transport in ultrathin topological crystalline insulator SnTe films. *APL Materials*, 7(5):051106, May 2019. 75
- [123] T. V. Menshchikova, I. P. Rusinov, P. Golub, I. Yu. Sklyadneva, R. Heid, A. Isaeva, V. M. Kuznetsov, and E. V. Chulkov. Two- and one-dimensional quantum spin Hall states in stanene-functionalized GaTe and InTe matrices. *Journal of Materials Chemistry C*, 7(26):7929–7937, 2019. 76
- [124] Junfeng Gao, Gang Zhang, and Yong-Wei Zhang. Exploring Ag(111) Substrate for Epitaxially Growing Monolayer Stanene: A First-Principles Study. *Scientific Reports*, 6(1), September 2016. 76, 90
- [125] Celal Yelgel. Tunable electronic properties of van der Waals heterostructures composed of stanene adsorbed on two-dimensional, graphene-like nitrides. *Journal of Applied Physics*, 125(15):155301, April 2019. 76, 90
- [126] Menghan Liao, Yunyi Zang, Zhaoyong Guan, Haiwei Li, Yan Gong, Kejing Zhu, Xiao-Peng Hu, Ding Zhang, Yong Xu, Ya-Yu Wang, Ke He, Xu-Cun Ma, Shou-Cheng Zhang, and Qi-Kun Xue. Superconductivity in few-layer stanene. *Nature Physics*, 14(4):344–348, April 2018. 77, 90
- [127] Joseph Falson, Yong Xu, Menghan Liao, Yunyi Zang, Kejing Zhu, Chong Wang, Zetao Zhang, Hongchao Liu, Wenhui Duan, Ke He, Haiwen Liu, Jurgen H. Smet,

- Ding Zhang, and Qi-Kun Xue. Type-II Ising pairing in few-layer stanene. *Science*, 367(6485):1454–1457, March 2020. 77
- [128] Namrata Bansal, Yong Seung Kim, Eliav Edrey, Matthew Brahlek, Yoichi Horibe, Keiko Iida, Makoto Tanimura, Guo-Hong Li, Tian Feng, Hang-Dong Lee, Torgny Gustafsson, Eva Andrei, and Seongshik Oh. Epitaxial growth of topological insulator Bi_2Se_3 film on Si(111) with atomically sharp interface. *Thin Solid Films*, 520(1):224–229, October 2011. 77
- [129] Liang He, Faxian Xiu, Yong Wang, Alexei V. Fedorov, Guan Huang, Xufeng Kou, Murong Lang, Ward P. Beyermann, Jin Zou, and Kang L. Wang. Epitaxial growth of Bi_2Se_3 topological insulator thin films on Si(111). *Journal of Applied Physics*, 109(10):103702, May 2011. 77
- [130] U. Köhler, O. Jusko, G. Pietsch, B. Müller, and M. Henzler. Strained-layer growth and islanding of germanium on Si(111)-(7×7) studied with STM. *Surface Science*, 248(3):321–331, June 1991. 77
- [131] S. I. Stenin and A. I. Toropov. Molecular Beam Epitaxy of Semiconductor, Metal, and Dielectric Films. In Kh. S. Bagdasarov and É. L. Lube, editors, *Growth of Crystals*, pages 113–125. Springer US, Boston, MA, 1991. 77
- [132] Yasutomo Kajikawa, Makoto Nishigaichi, Masahiro Inoue, and Mitsunori Kayano. Effects of Bi Irradiation on the Molecular Beam Epitaxy Growth of GaSb on Ge(111) Vicinal Substrates. *physica status solidi (a)*, 217(3):1900425, February 2020. 77, 82
- [133] Thomas P. Debies and J. Wayne Rabalais. X-ray photoelectron spectra and electronic structure of Bi_2X_3 ($\text{X} = \text{O}, \text{S}, \text{Se}, \text{Te}$). *Chemical Physics*, 20(2):277–283, March 1977. 80
- [134] R. B. Shalvoy, G. B. Fisher, and P. J. Stiles. Bond ionicity and structural stability of some average-valence-five materials studied by x-ray photoemission. *Physical Review B*, 15(4):1680–1697, February 1977. 80
- [135] J. F. McGilp, P. Weightman, and E. J. McGuire. The $\text{N}_{6,7}\text{O}_{4,5}\text{O}_{4,5}$ Auger spectra of thallium, lead and bismuth. *Journal of Physics C: Solid State Physics*, 10(17):3445–3460, September 1977. 80
- [136] M. Horn-von Hoegen, F. J. Meyer zu Heringdorf, M. Kammler, C. Schaeffer, D. Reinking, and K. R. Hofmann. Bi surfactant mediated epitaxy of Ge on Si(111). *Thin Solid Films*, 343-344:579–582, April 1999. 82

- [137] Subham Naik, Gopal K. Pradhan, Shwetha G. Bhat, Bhaskar Chandra Behera, P. S. Anil Kumar, Saroj L. Samal, and D. Samal. The effect of Sn intercalation on the superconducting properties of 2H-NbSe_2 . *Physica C: Superconductivity and its Applications*, 561:18–23, June 2019. 87
- [138] Junji Yuhara, Naoki Isobe, Kazuki Nishino, Yuya Fujii, Lap Hong Chan, Masaaki Araidai, and Masashi Nakatake. Morphology and Electronic Structure of Sn-Intercalated $\text{TiS}_2(0001)$ Layers. *The Journal of Physical Chemistry C*, 123(36):22293–22298, September 2019. 87
- [139] F. Walker, E. Specht, and R. McKee. Film/substrate registry as measured by anomalous x-ray scattering at a reacted, epitaxial $\text{Cu/Si}(111)$ interface. *Physical Review Letters*, 67(20):2818–2821, November 1991. 88
- [140] Y. Uchida, N. Katsumata, and K. Ishida. Nickel-enhanced low-temperature epitaxial growth of silicon. *Thin Solid Films*, 427(1-2):294–297, March 2003. 88
- [141] R. A. McKee. Physical Structure and Inversion Charge at a Semiconductor Interface with a Crystalline Oxide. *Science*, 293(5529):468–471, July 2001. 88
- [142] Lennart Bengtsson. Dipole correction for surface supercell calculations. *Physical Review B*, 59(19):12301–12304, May 1999. 89, 151
- [143] A. Barfuss, L. Dudy, M. R. Scholz, H. Roth, P. Höpfner, C. Blumenstein, G. Landolt, J. H. Dil, N. C. Plumb, M. Radovic, A. Bostwick, E. Rotenberg, A. Fleszar, G. Bihlmayer, D. Wortmann, G. Li, W. Hanke, R. Claessen, and J. Schäfer. Elemental Topological Insulator with Tunable Fermi Level: Strained α -Sn on $\text{InSb}(001)$. *Physical Review Letters*, 111(15):157205, October 2013. 90
- [144] Dah-An Luh, Chia-Hsin Wang, and Yaw-Wen Yang. Growth of thin Sn films on $\text{Ag}(111)$ studied with low-energy electron diffraction and X-ray photoelectron spectroscopy. *Thin Solid Films*, 682:44–49, July 2019. 90
- [145] T. Osaka, H. Omi, K. Yamamoto, and A. Ohtake. Surface phase transition and interface interaction in the α -Sn/ $\text{InSb}\{111\}$ system. *Physical Review B*, 50(11):7567–7572, September 1994. 90
- [146] B. Roldan Cuenya, M. Doi, and W. Keune. Epitaxial growth and interfacial structure of Sn on $\text{Si}(111)-(7\times 7)$. *Surface Science*, 506(1-2):33–46, May 2002. 90
- [147] Rongting Wu, Ilya K. Drozdov, Stephen Eltinge, Percy Zahl, Sohrab Ismail-Beigi, Ivan Božović, and Adrian Gozar. Large-area single-crystal sheets of borophene on

- Cu(111) surfaces. *Nature Nanotechnology*, 14(1):44–49, January 2019. 92, 95, 98, 99, 100, 102, 103, 104, 108, 112, 114, 125
- [148] Xiaobao Yang, Yi Ding, and Jun Ni. *Ab initio* prediction of stable boron sheets and boron nanotubes: Structure, stability, and electronic properties. *Physical Review B*, 77(4):041402, January 2008. 92, 94
- [149] Andrew J. Mannix, Brian Kiraly, Mark C. Hersam, and Nathan P. Guisinger. Synthesis and chemistry of elemental 2D materials. *Nature Reviews Chemistry*, 1(2):0014, February 2017. 92
- [150] Andrew J. Mannix, Zhuhua Zhang, Nathan P. Guisinger, Boris I. Yakobson, and Mark C. Hersam. Borophene as a prototype for synthetic 2D materials development. *Nature Nanotechnology*, 13(6):444–450, June 2018. 92, 93
- [151] Zhuhua Zhang, Evgeni S. Penev, and Boris I. Yakobson. Two-dimensional materials: polyphony in B flat. *Nature Chemistry*, 8(6):525–527, 2016. 92, 93, 111, 172
- [152] Xiaojun Wu, Jun Dai, Yu Zhao, Zhiwen Zhuo, Jinlong Yang, and Xiao Cheng Zeng. Two-Dimensional Boron Monolayer Sheets. *ACS Nano*, 6(8):7443–7453, August 2012. 92, 94
- [153] Zhuhua Zhang, Yang Yang, Evgeni S. Penev, and Boris I. Yakobson. Elasticity, Flexibility, and Ideal Strength of Borophenes. *Advanced Functional Materials*, 27(9):1605059, March 2017. 92, 111
- [154] A. J. Mannix, X.-F. Zhou, B. Kiraly, J. D. Wood, D. Alducin, B. D. Myers, X. Liu, B. L. Fisher, U. Santiago, J. R. Guest, M. J. Yacaman, A. Ponce, A. R. Oganov, M. C. Hersam, and N. P. Guisinger. Synthesis of borophenes: Anisotropic, two-dimensional boron polymorphs. *Science*, 350(6267):1513–1516, December 2015. 92, 93, 98, 107, 108, 112
- [155] Baojie Feng, Jin Zhang, Qing Zhong, Wenbin Li, Shuai Li, Hui Li, Peng Cheng, Sheng Meng, Lan Chen, and Kehui Wu. Experimental realization of two-dimensional boron sheets. *Nature Chemistry*, 8(6):563–568, March 2016. 92, 93, 98, 108, 112
- [156] Baojie Feng, Jin Zhang, Ro-Ya Liu, Takushi Iimori, Chao Lian, Hui Li, Lan Chen, Kehui Wu, Sheng Meng, Fumio Komori, and Iwao Matsuda. Direct evidence of metallic bands in a monolayer boron sheet. *Physical Review B*, 94(4):041408, July 2016. 92, 93

- [157] G. E. Volovik. From standard model of particle physics to room-temperature superconductivity. *Physica Scripta*, T164:014014, December 2015. 94
- [158] Franz J. Giessibl. High-speed force sensor for force microscopy and profilometry utilizing a quartz tuning fork. *Applied Physics Letters*, 73(26):3956–3958, December 1998. 95, 96, 102
- [159] Hendrik J. Monkhorst and James D. Pack. Special points for Brillouin-zone integrations. *Physical review B*, 13(12):5188, 1976. 96, 114, 151
- [160] E. Bauer. Low energy electron microscopy. *Reports on Progress in Physics*, 57(9):895–938, September 1994. 96
- [161] James B. Hannon and Ruud M. Tromp. Low-Energy Electron Microscopy of Surface Phase Transitions. *Annual Review of Materials Research*, 33(1):263–288, August 2003. 96
- [162] Peter Sutter, Jerzy T. Sadowski, and Eli Sutter. Graphene on Pt(111): Growth and substrate interaction. *Physical Review B*, 80(24):245411, December 2009. 96
- [163] M. S. Altman. Trends in low energy electron microscopy. *Journal of Physics: Condensed Matter*, 22(8):084017, March 2010. 96
- [164] Prokop Hapala, Georgy Kichin, Christian Wagner, F. Stefan Tautz, Ruslan Temirov, and Pavel Jelínek. Mechanism of high-resolution STM/AFM imaging with functionalized tips. *Physical Review B*, 90(8), August 2014. 96, 113
- [165] Hongsheng Liu, Junfeng Gao, and Jijun Zhao. From Boron Cluster to Two-Dimensional Boron Sheet on Cu(111) Surface: Growth Mechanism and Hole Formation. *Scientific Reports*, 3(1):3238, December 2013. 107, 108
- [166] Timur R. Galeev, Qiang Chen, Jin-Chang Guo, Hui Bai, Chang-Qing Miao, Hai-Gang Lu, Alina P. Sergeeva, Si-Dian Li, and Alexander I. Boldyrev. Deciphering the mystery of hexagon holes in an all-boron graphene α -sheet. *Physical Chemistry Chemical Physics*, 13(24):11575, 2011. 108
- [167] Zhuhua Zhang, Andrew J. Mannix, Zhili Hu, Brian Kiraly, Nathan P. Guisinger, Mark C. Hersam, and Boris I. Yakobson. Substrate-Induced Nanoscale Undulations of Borophene on Silver. *Nano Letters*, 16(10):6622–6627, October 2016. 108
- [168] Xiaolong Liu, Zhuhua Zhang, Luqing Wang, Boris I. Yakobson, and Mark C. Hersam. Intermixing and periodic self-assembly of borophene line defects. *Nature Materials*, July 2018. 108, 112

- [169] K. S. Novoselov, A. K. Geim, S. V. Morozov, D. Jiang, M. I. Katsnelson, I. V. Grigorieva, S. V. Dubonos, and A. A. Firsov. Two-dimensional gas of massless Dirac fermions in graphene. *Nature*, 438(7065):197–200, November 2005. 111
- [170] Baojie Feng, Zijing Ding, Sheng Meng, Yugui Yao, Xiaoyue He, Peng Cheng, Lan Chen, and Kehui Wu. Evidence of Silicene in Honeycomb Structures of Silicon on Ag(111). *Nano Letters*, 12(7):3507–3511, July 2012. 111
- [171] Lei Meng, Yeliang Wang, Lizhi Zhang, Shixuan Du, Rongting Wu, Linfei Li, Yi Zhang, Geng Li, Haitao Zhou, Werner A. Hofer, and Hong-Jun Gao. Buckled Silicene Formation on Ir(111). *Nano Letters*, 13(2):685–690, February 2013. 111
- [172] Linfei Li, Shuang-zan Lu, Jinbo Pan, Zhihui Qin, Yu-qi Wang, Yeliang Wang, Geng-yu Cao, Shixuan Du, and Hong-Jun Gao. Buckled Germanene Formation on Pt(111). *Advanced Materials*, 26(28):4820–4824, July 2014. 111
- [173] M. E. Dávila, L. Xian, S. Cahangirov, A. Rubio, and G. Le Lay. Germanene: a novel two-dimensional germanium allotrope akin to graphene and silicene. *New Journal of Physics*, 16(9):095002, September 2014. 111
- [174] Miao Gao, Qi-Zhi Li, Xun-Wang Yan, and Jun Wang. Prediction of phonon-mediated superconductivity in borophene. *Physical Review B*, 95(2):024505, January 2017. 111
- [175] Baojie Feng, Jin Zhang, Suguru Ito, Masashi Arita, Cai Cheng, Lan Chen, Kehui Wu, Fumio Komori, Osamu Sugino, Koji Miyamoto, Taichi Okuda, Sheng Meng, and Iwao Matsuda. Discovery of 2D Anisotropic Dirac Cones. *Advanced Materials*, 30(2):1704025, January 2018. 111, 112
- [176] H. R. Jiang, Ziheng Lu, M. C. Wu, Francesco Ciucci, and T. S. Zhao. Borophene: A promising anode material offering high specific capacity and high rate capability for lithium-ion batteries. *Nano Energy*, 23:97–104, May 2016. 111
- [177] Vivekanand Shukla, John Wärmå, Naresh K. Jena, Anton Grigoriev, and Rajeev Ahuja. Toward the Realization of 2D Borophene Based Gas Sensor. *The Journal of Physical Chemistry C*, 121(48):26869–26876, December 2017. 111
- [178] Xu Sun, Xiaofei Liu, Jun Yin, Jin Yu, Yao Li, Yang Hang, Xiaocheng Zhou, Maolin Yu, Jidong Li, Guoan Tai, and Wanlin Guo. Two-Dimensional Boron Crystals: Structural Stability, Tunable Properties, Fabrications and Applications. *Advanced Functional Materials*, 27(19):1603300, May 2017. 111

- [179] Xiaolong Liu, Zonghui Wei, Itamar Balla, Andrew J. Mannix, Nathan P. Guisinger, Erik Luijten, and Mark C. Hersam. Self-assembly of electronically abrupt borophene/organic lateral heterostructures. *Science Advances*, 3(2):e1602356, February 2017. 112
- [180] Xiaolong Liu and Mark C. Hersam. Borophene-graphene heterostructures. *Science Advances*, 5(10):eaax6444, October 2019. 112
- [181] Rongting Wu, Adrian Gozar, and Ivan Božović. Large-area borophene sheets on sacrificial Cu(111) films promoted by recrystallization from subsurface boron. *npj Quantum Materials*, 4(1):40, December 2019. 112
- [182] Fang Zhao, Andrei Vrajitoarea, Qi Jiang, Xiaoyu Han, Aysha Chaudhary, Joseph O. Welch, and Richard B. Jackman. Graphene-Nanodiamond Heterostructures and their application to High Current Devices. *Scientific Reports*, 5(1):13771, November 2015. 117
- [183] Fucong Fei, Xiangyan Bo, Pengdong Wang, Jianghua Ying, Jian Li, Ke Chen, Qing Dai, Bo Chen, Zhe Sun, Minhao Zhang, Fanming Qu, Yi Zhang, Qianghua Wang, Xuefeng Wang, Lu Cao, Haijun Bu, Fengqi Song, Xiangang Wan, and Baigeng Wang. Band Structure Perfection and Superconductivity in Type-II Dirac Semimetal $\text{Ir}_{1-x}\text{Pt}_x\text{Te}_2$. *Advanced Materials*, 30(35):1801556, August 2018. 127
- [184] Alexey A. Soluyanov, Dominik Gresch, Zhijun Wang, QuanSheng Wu, Matthias Troyer, Xi Dai, and B. Andrei Bernevig. Type-II Weyl semimetals. *Nature*, 527(7579):495–498, November 2015. 127
- [185] G. E. Volovik. Black hole and hawking radiation by type-II Weyl fermions. *JETP Letters*, 104(9):645–648, November 2016. 127, 130
- [186] Huaqing Huang, Kyung-Hwan Jin, and Feng Liu. Black-hole horizon in the Dirac semimetal $\text{Zn}_2\text{In}_2\text{S}_5$. *Physical Review B*, 98(12):121110, September 2018. 127, 130
- [187] Kidae Shin, Stephen Eltinge, Sangjae Lee, Hyunki Shin, Juan Jjiang, Hawoong Hong, Bruce Davidson, Ke Zou, Sohrab Ismail-Beigi, Charles H. Ahn, and Frederick J. Walker. Polarity-driven atomic displacements at 2D $\text{Mg}_2\text{TiO}_4/\text{MgO}(001)$ oxide interface for hosting potential interlayer exciton states. In preparation. 132, 141, 143
- [188] Dmitrii Unuchek, Alberto Ciarrocchi, Ahmet Avsar, Kenji Watanabe, Takashi Taniguchi, and Andras Kis. Room-temperature electrical control of exciton flux

- in a van der Waals heterostructure. *Nature*, 560(7718):340–344, August 2018. 133, 148
- [189] G. Grosso, J. Graves, A. T. Hammack, A. A. High, L. V. Butov, M. Hanson, and A. C. Gossard. Excitonic switches operating at around 100 K. *Nature Photonics*, 3(10):577–580, October 2009. 133
 - [190] I. Schwartz, D. Cogan, E. R. Schmidgall, Y. Don, L. Gantz, O. Kenneth, N. H. Lindner, and D. Gershoni. Deterministic generation of a cluster state of entangled photons. *Science*, 354(6311):434–437, October 2016. 133
 - [191] I. Schwartz, E. R. Schmidgall, L. Gantz, D. Cogan, E. Bordo, Y. Don, M. Zielinski, and D. Gershoni. Deterministic Writing and Control of the Dark Exciton Spin Using Single Short Optical Pulses. *Physical Review X*, 5(1):011009, January 2015. 133
 - [192] M. M. Fogler, L. V. Butov, and K. S. Novoselov. High-temperature superfluidity with indirect excitons in van der Waals heterostructures. *Nature Communications*, 5(1):4555, December 2014. 133
 - [193] Zefang Wang, Daniel A. Rhodes, Kenji Watanabe, Takashi Taniguchi, James C. Hone, Jie Shan, and Kin Fai Mak. Evidence of high-temperature exciton condensation in two-dimensional atomic double layers. *Nature*, 574(7776):76–80, October 2019. 133
 - [194] Yu. E. Lozovik and V. I. Yudson. A new mechanism for superconductivity: pairing between spatially separated electrons and holes. *Zh. Eksp. Teor. Fiz.*, 71:738–753, 1976. 133
 - [195] L. V. Butov, A. C. Gossard, and D. S. Chemla. Macroscopically ordered state in an exciton system. *Nature*, 418(6899):751–754, August 2002. 133
 - [196] L. V. Butov. Excitonic devices. *Superlattices and Microstructures*, 108:2–26, August 2017. 133
 - [197] Keliang He, Nardeep Kumar, Liang Zhao, Zefang Wang, Kin Fai Mak, Hui Zhao, and Jie Shan. Tightly Bound Excitons in Monolayer WSe₂. *Physical Review Letters*, 113(2):026803, July 2014. 133
 - [198] Ziliang Ye, Ting Cao, Kevin O’Brien, Hanyu Zhu, Xiaobo Yin, Yuan Wang, Steven G. Louie, and Xiang Zhang. Probing excitonic dark states in single-layer tungsten disulphide. *Nature*, 513(7517):214–218, September 2014. 133

- [199] Pasqual Rivera, John R. Schaibley, Aaron M. Jones, Jason S. Ross, Sanfeng Wu, Grant Aivazian, Philip Klement, Kyle Seyler, Genevieve Clark, Nirmal J. Ghimire, Jiaqiang Yan, D. G. Mandrus, Wang Yao, and Xiaodong Xu. Observation of long-lived interlayer excitons in monolayer MoSe₂–WSe₂ heterostructures. *Nature Communications*, 6(1):6242, May 2015. 134
- [200] Bastian Miller, Alexander Steinhoff, Borja Pano, Julian Klein, Frank Jahnke, Alexander Holleitner, and Ursula Wurstbauer. Long-Lived Direct and Indirect Interlayer Excitons in van der Waals Heterostructures. *Nano Letters*, 17(9):5229–5237, September 2017. 134
- [201] Maurizia Palummo, Marco Bernardi, and Jeffrey C. Grossman. Exciton Radiative Lifetimes in Two-Dimensional Transition Metal Dichalcogenides. *Nano Letters*, 15(5):2794–2800, May 2015. 134
- [202] T. Kazimierczuk, D. Fröhlich, S. Scheel, H. Stolz, and M. Bayer. Giant Rydberg excitons in the copper oxide Cu₂O. *Nature*, 514(7522):343–347, October 2014. 134
- [203] E. Baldini, L. Chiodo, A. Dominguez, M. Palummo, S. Moser, M. Yazdi-Rizi, G. Auböck, B. P. P. Mallett, H. Berger, A. Magrez, C. Bernhard, M. Grioni, A. Rubio, and M. Chergui. Strongly bound excitons in anatase TiO₂ single crystals and nanoparticles. *Nature Communications*, 8(1):13, December 2017. 134
- [204] Edoardo Baldini, Adriel Dominguez, Tania Palmieri, Oliviero Cannelli, Angel Rubio, Pascal Ruello, and Majed Chergui. Exciton control in a room temperature bulk semiconductor with coherent strain pulses. *Science Advances*, 5(11):eaax2937, November 2019. 134
- [205] A. D. Caviglia, S. Gariglio, N. Reyren, D. Jaccard, T. Schneider, M. Gabay, S. Thiel, G. Hammerl, J. Mannhart, and J.-M. Triscone. Electric field control of the LaAlO₃/SrTiO₃ interface ground state. *Nature*, 456(7222):624–627, December 2008. 134
- [206] Kouros Kalantar-zadeh, Jian Zhen Ou, Torben Daeneke, Arnan Mitchell, Takayoshi Sasaki, and Michael S. Fuhrer. Two dimensional and layered transition metal oxides. *Applied Materials Today*, 5:73–89, December 2016. 134
- [207] Jiaxuan Wen, V. R. Saran Kumar Chaganti, Tristan K. Truttmann, Fengdeng Liu, Bharat Jalan, and Steven J. Koester. SrSnO₃ Metal-Semiconductor Field-Effect Transistor With GHz Operation. *IEEE Electron Device Letters*, 42(1):74–77, January 2021. 134

- [208] Hareesh Chandrasekar, Kaveh Ahadi, Towhidur Razzak, Susanne Stemmer, and Siddharth Rajan. High Current Density $\text{SmTiO}_3/\text{SrTiO}_3$ Field-Effect Transistors. *ACS Applied Electronic Materials*, 2(2):510–516, February 2020. 134
- [209] Junwoo Son, Pouya Moetakef, Bharat Jalan, Oliver Bierwagen, Nicholas J. Wright, Roman Engel-Herbert, and Susanne Stemmer. Epitaxial SrTiO_3 films with electron mobilities exceeding $30,000 \text{ cm}^2 \text{ V}^{-1} \text{ s}^{-1}$. *Nature Materials*, 9(6):482–484, June 2010. 134
- [210] Chenhao Jin, Eric Yue Ma, Ouri Karni, Emma C. Regan, Feng Wang, and Tony F. Heinz. Ultrafast dynamics in van der Waals heterostructures. *Nature Nanotechnology*, 13(11):994–1003, November 2018. 135
- [211] Simone Latini, Kirsten T. Winther, Thomas Olsen, and Kristian S. Thygesen. Inter-layer Excitons and Band Alignment in $\text{MoS}_2/\text{hBN}/\text{WSe}_2$ van der Waals Heterostructures. *Nano Letters*, 17(2):938–945, February 2017. 135
- [212] Pasqual Rivera, Hongyi Yu, Kyle L. Seyler, Nathan P. Wilson, Wang Yao, and Xiaodong Xu. Interlayer valley excitons in heterobilayers of transition metal dichalcogenides. *Nature Nanotechnology*, 13(11):1004–1015, November 2018. 135
- [213] Otfried Madelung. *Semiconductors: data handbook*. Springer, 2013. OCLC: 923745176. 135
- [214] J. B. Varley, A. Janotti, C. Franchini, and C. G. Van de Walle. Role of self-trapping in luminescence and p -type conductivity of wide-band-gap oxides. *Physical Review B*, 85(8):081109, February 2012. 135
- [215] Yi-Da Ho, Chia-Hui Su, and Cheng-Liang Huang. Intense Red Photoluminescence Emission of Sol-Gel-Derived Nanocrystalline Mg_2TiO_4 Thin Films. *Journal of the American Ceramic Society*, 97(2):358–360, February 2014. 135
- [216] Heinrich Hohl, Christian Kloc, and Ernst Bucher. Electrical and Magnetic Properties of Spinel Solid Solutions $\text{Mg}_{2-x}\text{Ti}_{1+x}\text{O}_4$; $0 \leq x \leq 1$. *Journal of Solid State Chemistry*, 125(2):216–223, September 1996. 135
- [217] V. S. Stubican and Rustum Roy. Mechanism of the precipitation of the spinel from $\text{MgO}-\text{Al}_2\text{O}_3$ solid solutions. *Journal of Physics and Chemistry of Solids*, 26(8):1293–1297, August 1965. 135
- [218] D. Hesse and H. Bethge. Formation of Mg_2TiO_4 epitaxial thin films on MgO by solid state reaction. *Journal of Crystal Growth*, 52:875–882, April 1981. 143

- [219] D. Hesse and H. Bethge. Solid state reactions for the epitaxial growth of spinel films. *Journal of Crystal Growth*, 65(1-3):69–76, December 1983. 143
- [220] F. Imai, K. Kunimori, T. Uchijima, and H. Nozoye. Interfacial reaction of MgO/TiO_x superlattice thin films. *Thin Solid Films*, 228(1-2):158–161, May 1993. 143
- [221] Divine P. Kumah, Ankit S. Disa, Joseph H. Ngai, Hanghui Chen, Andrei Malashevich, James W. Reiner, Sohrab Ismail-Beigi, Frederick J. Walker, and Charles H. Ahn. Tuning the Structure of Nickelates to Achieve Two-Dimensional Electron Conduction. *Advanced Materials*, 26(12):1935–1940, March 2014. 143
- [222] Sangjae Lee, Alex Taekyung Lee, Alexandru B. Georgescu, Gilberto Fabbri, Myung-Geun Han, Yimei Zhu, John W. Freeland, Ankit S. Disa, Yichen Jia, Mark P. M. Dean, Frederick J. Walker, Sohrab Ismail-Beigi, and Charles H. Ahn. Strong Orbital Polarization in a Cobaltate-Titanate Oxide Heterostructure. *Physical Review Letters*, 123(11):117201, September 2019. 143
- [223] Ankit S. Disa, Frederick J. Walker, and Charles H. Ahn. High-Resolution Crystal Truncation Rod Scattering: Application to Ultrathin Layers and Buried Interfaces. *Advanced Materials Interfaces*, 7(6):1901772, March 2020. 143
- [224] Yizhak Yacoby, Mukhles Sowwan, Edward Stern, Julie O. Cross, Dale Brewe, Ron Pindak, John Pitney, Eric M. Dufresne, and Roy Clarke. Direct determination of epitaxial interface structure in Gd_2O_3 passivation of GaAs. *Nature Materials*, 1(2):99–101, October 2002. 143
- [225] Jiachi Zhang, Minghui Yu, Qingsong Qin, Hongliang Zhou, Meijiao Zhou, Xuhui Xu, and Yuhua Wang. The persistent luminescence and up conversion photostimulated luminescence properties of nondoped Mg_2SnO_4 material. *Journal of Applied Physics*, 108(12):123518, December 2010. 148
- [226] Gaganpreet Kaur Behrh, Masahiko Isobe, Florian Massuyeau, Hélène Serier-Brault, Elijah E. Gordon, Hyun-Joo Koo, Myung-Hwan Whangbo, Romain Gautier, and Stéphane Jobic. Oxygen-Vacancy-Induced Midgap States Responsible for the Fluorescence and the Long-Lasting Phosphorescence of the Inverse Spinel $\text{Mg}(\text{Mg},\text{Sn})\text{O}_4$. *Chemistry of Materials*, 29(3):1069–1075, February 2017. 148
- [227] Bin Jiang, Fengfeng Chi, Xiantao Wei, Yonghu Chen, and Min Yin. A self-activated MgGa_2O_4 for persistent luminescence phosphor. *Journal of Applied Physics*, 124(6):063101, August 2018. 148

- [228] D. R. Hamann. Optimized norm-conserving Vanderbilt pseudopotentials. *Physical Review B*, 88(8):085117, August 2013. 150
- [229] Martin Schlipf and François Gygi. Optimization algorithm for the generation of ONCV pseudopotentials. *Computer Physics Communications*, 196:36–44, November 2015. 150
- [230] Peter E. Blöchl, Ove Jepsen, and Ole Krogh Andersen. Improved tetrahedron method for Brillouin-zone integrations. *Physical Review B*, 49(23):16223, 1994. 151
- [231] Robert D. Shannon, Ruth C. Shannon, Olaf Medenbach, and Reinhard X. Fischer. Refractive Index and Dispersion of Fluorides and Oxides. *Journal of Physical and Chemical Reference Data*, 31(4):931–970, December 2002. 166
- [232] R. L. Clendenen and H. G. Drickamer. Lattice Parameters of Nine Oxides and Sulfides as a Function of Pressure. *The Journal of Chemical Physics*, 44(11):4223–4228, June 1966. 166